Design of 1-3/0-3 viscoelastic composite layer for augmented active/ passive constrained layer damping of structural vibration

A
Thesis Submitted in
Partial Fulfillment of the Requirements
for the Degree of

DOCTOR OF PHILOSOPHY

by

Ambesh Kumar
(Roll No: 126103007)

DEPARTMENT OF MECHANICAL ENGINEERING
INDIAN INSTITUTE OF TECHNOLOGY GUWAHATI
GUWAHATI-781039, INDIA

June, 2018

Department of Mechanical Engineering
Indian Institute of Technology Guwahati
Guwahati-781039 INDIA

CERTIFICATE

It is certified that the work contained in the thesis entitled "**DESIGN OF 1-3/0-3 VISCOELASTIC COMPOSITE LAYER FOR AUGMENTED ACTIVE/ PASSIVE CONSTRAINED LAYER DAMPING OF STRUCTURAL VIBRATION**" submitted by **Ambesh Kumar (Reg. No. 126103007)** to the Indian Institute of Technology Guwahati for the award of the degree of Doctor of Philosophy has been carried out under my supervision in the Department of Mechanical Engineering, Indian Institute of Technology Guwahati. This work has not been submitted elsewhere for the award of any other degree or diploma.

(Dr. Satyajit Panda)
Associate Professor
Department of Mechanical Engineering
Indian Institute of Technology Guwahati
Guwahati-781039
INDIA

Declaration

I Ambesh Kumar (Roll no: 126103007) declare that the present written submission is my thoughts in my own words. I have adequately cited and referenced the original sources, where others ideas have been involved. I also declare that I have adhered to all principles of academic honesty and integrity and have neither fabricated nor falsified any idea/data/fact/source in my submission. I understand that any violation of the above will be cause for disciplinary action by the Institute and can also evoke penal action from the sources which have thus not been properly cited or from whom proper permission has not been taken when needed.

(**Ambesh Kumar**)

Date: **Roll No: 126103007**

Dedicated to

My parents and teachers

Acknowledgments

I would like to express my heartfelt gratitude towards all those who have immensely helped me during my journey of five years at IIT Guwahati and eventually assisted me to emerge as a researcher and a mature individual.

First and foremost, I must express my deepest sense of appreciation and respect for my thesis supervisor Dr. Satyajit Panda for providing me the opportunity to work under his supervision. His untiring guidance, constant encouragement, persistent patience and friendliness in the moment of difficulties was invaluable without which the following work would not have been possible.

I am also thankful to Prof. D Chakraborty, Prof. S Senthilvelan and Prof. A K Singh for their careful review and suggestions in their capacity as doctoral committee members. I am also grateful to past and present departmental heads Prof. P Mahanta, Prof. A K Dass and Prof. S K Dwivedy for providing me enough facilities during my Ph. D. program.

The financial support provided by the Ministry of Human Resource and Development, Government of India for research work at IIT Guwahati is gratefully acknowledged.

I express deepest gratitude to my parents Smt. Madhur Devi and Sri Dina Nath Jha for their constant love, support and encouragement. I would like to thank my wife Khushbu and son Atharv for their invaluable much needed patience and support during my research period. I would like to thank my whole family members for their love, encouragement and support towards my research work.

Finally, some of my friends have made my journey at IIT Guwahati more fabulous with their constant encouragement and supporting demeanour. I would be therefore grateful to my friends Sachin, Pavan, Manish, Shashi, Abhay, Purnendu and Pankaj.

Above all, I am thankful to the Almighty.

Date: **(Ambesh Kumar)**

Abstract

In this dissertation, two kinds of viscoelastic composite (VEC) layers are proposed by the names of 1-3 and 0-3 VEC layers. The 1-3 VEC layer is comprised of the inclusion of unidirectional graphite wafers or strips, while the other one (0-3 VEC) is composed of a rectangular array of thin rectangular graphite-wafers. The objective in these designs of the VEC layers is to augment the damping in the unconstrained layer damping (UCLD), passive constrained layer damping (PCLD) and active constrained layer damping (ACLD) treatments of structural vibration.

First, the1-3 VEC layer is employed as the damping layer in the UCLD and PCLD treatments of vibration of a substrate beam, and the corresponding damping mechanisms especially due to the graphite inclusions within the viscoelastic layer are investigated by developing a finite element (FE) model of the beam. The results reveal significantly enhanced magnitudes of the transverse shear and extensional strains within the viscoelastic phase for the presence of inclusions. So, the damping capacities of both the UCLD and PCLD treatments improve significantly. These observations motivate to extend the investigation for ACLD treatment of beams using the 1-3 VEC layer, and it is revealed that the active-passive damping in the ACLD treatment improves due to the use of 1-3 VEC layer instead of the conventional pure viscoelastic layer.

Next, the concept of 1-3 VEC layer is implemented to augment the constrained layer damping (CLD) of a circular cylindrical sandwich shell with the viscoelastic core. The graphite strips are axially inserted following the middle surface of the viscoelastic core, and a three-layered VEC core with the 1-3 connectivity of two phases is achieved. The sandwich shell is analysed by developing an FE model based on the layer-wise shear deformation theory, and it is observed that the passive damping in the overall shell arises mainly due to a transverse shear strain of the viscoelastic phase, but the damping increases significantly due to the inclusion of graphite strips. These strips are subsequently configured in an optimal manner for achieving improved damping in all modes of vibration of the shell within a frequency range of interest. The three-layered VEC is further utilized for the ACLD treatment of circular cylindrical shell where a new ACLD arrangement is proposed in layer-form using the vertically reinforced 1-3 piezoelectric composite layer with the printed patches of surface-electrodes. The main objective in this design of ACLD layer is to control all modes of vibration of the cylindrical shell effectively, and it is

substantiated through the FE analysis of the shell. It is found that the three-layered VEC improves the active-passive damping of the treatment while the proposed arrangement of electrode-patches serves to achieve the improved damping in all modes of vibration.

The improved damping due to the 1-3 VEC layer is achieved by the enhancement of the transverse shear and the extensional strains of the viscoelastic phase at a transverse plane of the principal material coordinate system. In contrast, for achieving similar enhancement of all strains in the viscoelastic phase, a new 0-3 VEC layer is designed, and its performance as the passively constrained damping layer over a substrate plate is investigated by deriving an FE model of the overall plate. It is observed that all strains in the viscoelastic phase of 0-3 VEC layer increase due to the inclusions, and it results in improved passive damping in the plate over that in the use of the 1-3 VEC or pure viscoelastic layer. This improved damping depends on geometrical properties of the 0-3 VEC layer, and thus its (0-3 VEC) optimal geometric configuration for maximum damping is addressed. The study is further extended for investigating the performance of the 0-3 VEC layer as the damping layer in ACLD treatment of plates. This reveals the same damping mechanisms as observed in the previous PCLD case, and it leads to an improved active-passive damping capacity of the ACLD treatment through an optimal geometric configuration of the 0-3 VEC layer.

Table of Contents

List of Figures

List of Tables

List of Symbols

List of symbols used throughout the thesis are listed. List of symbols less frequently used, or that have different meaning or different forms at different contexts, are defined where they are used.

$\boldsymbol{d}$	Global general displacement field vector
$\boldsymbol{d}^e$	Elemental nodal displacement vector
$\boldsymbol{D}$	Electrical displacement field vector
$\boldsymbol{E}$	Electric field vector
E	Young's modulus
h	Thickness of substrate beam/plate/shell
h_p	PFC layer thickness in shells
$\boldsymbol{I}$	Identity matrix
k	Number of layers
k_d	Feed back control gain
$\boldsymbol{K}$	Stiffness matrix
$\boldsymbol{L}$	Linear Operator matrices
$\bar{m}$	Mass per unit area
$\boldsymbol{M}$	Mass matrix
$\boldsymbol{N}$	Shape function matrix
$\boldsymbol{T}_t, \boldsymbol{T}_r$	Transformation vector
$\boldsymbol{P}_M^e$	Element mechanical load vector
δT_K	Variation of total kinetic energy
δT_P	Variation of total potential energy
u , v , w	Displacements components in coordinate directions
V	Applied voltage
$V_{\max}$	control voltage at peak point
$\dot{w}_s$	Sensing point velocity
$\boldsymbol{X}$	Global nodal displacement vector
ν	Poisson's ratio
ρ	Mass density
$\boldsymbol{\varepsilon}$	Strain vector
$\boldsymbol{\sigma}$	Stress vector
ω	Circular frequency

ω_0	Fundamental frequency of vibration
$u^k / v^k / w^k$	Displacement along $x / y / z$ direction within k^{th} layer
h_f^b / h_f^t	Thickness of inner/outer face layer of sandwich shell
h_d	Thickness of damping layer/core layer
h_c	Thickness of constraining layer
h_v	Thickness of top/bottom viscoelastic layer in three-layered core
θ_i / β_i	Rotation of normal to the middle plane of i^{th} layer with respect to y / x axes
$\varepsilon_x / \varepsilon_y / \varepsilon_z$	Normal strain along $x / y / z$ direction
$\varepsilon_{xy} / \sigma_{xy}$	In-plane shear strain/stress in the xy-plane
$\sigma_{xz} / \sigma_{yz}$	Transverse shear stress in xz / yz plane
σ_b / σ_s	Extensional/shear stress vector
C_b^k / C_s^k	Extensional/shear stiffness matrix for k^{th} layer
$\eta_i / \eta_i^e / \eta_i^s$	Total/extensional/transverse shear loss factor for i^{th} mode of vibration
m / n	Longitudinal/circumferential mode number
n_f	Number of graphite strips
r_c	Ratio between thicknesses of viscoelastic layer and core layer
$\alpha / \alpha^g / \alpha^v$	Total/viscoelastic/graphite circular span in each segment of circular shells
h_v^2	Thicknesses of middle layer in VEC layer
$u_0 / v_0 / w_0$	Displacement along $x / y / z$ direction at any point on reference surface
γ_i	Rate of change of thickness of i^{th} layer in the thickness direction
$\sigma_x / \sigma_y / \sigma_z$	Normal stress along $x / y / z$ direction
$\varepsilon_{xz} / \varepsilon_{yz}$	Transverse shear strain on xz / yz plane

$\boldsymbol{\varepsilon}_b$ / $\boldsymbol{\varepsilon}_s$	Extensional/shear strain vector
η / η_e / η_s	Total/extensional/transverse shear loss factor
ω	Operating frequency
$w''_{(m,n)}$	Weight for (m,n) mode
$\bar{\eta}$	Weighted average loss factor
$\eta_{(m,n)}$	Loss factor for (m,n) mode
$p(t)$	Transverse (radial) harmonic point load

Superscript:

e	Element
i	A State of deformation
s	Sensing point
v	Velocity
T	Transpose

Subscript:

e	Extensional
L	Linear
N	Nonlinear
s	Shear
q	Mode of vibration

Abbreviations:

UCLD	Unconstrained layer damping
FLD	Free layer damping
CLD	Constrained layer damping
PCLD	Passive constrained layer damping
ACLD	Active constrained layer damping
FE	Finite element
PFC	Piezoelectric fiber composite
VEC	Viscoelastic composite
VEM	Viscoelastic composite

Chapter 1

Introduction

Viscoelastic materials possess the inherent property of dissipating energy under a transient deformation. Based on this property, viscoelastic materials have long been utilized for suppression of structural vibrations. Generally, these materials are used in the form of a layer that is either freely attached to the surface of a host structure or constrained between a constraining layer and the host structure-surface. These two kinds of arrangements of a viscoelastic layer for passive damping of structural vibration are commonly known as unconstrained/free layer damping (UCLD) and constrained layer damping (CLD). In some references, a CLD is also called as a passive constrained layer damping (PCLD). The energy dissipation in a UCLD treatment occurs mainly due to alternate extension and compression of the viscoelastic layer, while the same in the CLD/PCLD treatment appears due to the transverse shear strains of the constrained viscoelastic layer under its transient deformations (Jones, 2001). In the quest for further development of viscoelastic damping treatment of structural vibration, the concept of active constrained layer damping (ACLD) emerged (Baz and Ro, 1993) where the passive constraining layer of the CLD/PCLD arrangement is replaced by the active constraining layer along with an appropriate controller. The active constraining layer not only constrains the motion of the viscoelastic layer but also acts as an actuator to control the transverse shear deformation of the constrained viscoelastic layer according to an appropriate control strategy. So, the damping capacity of the treatment improves, and also the damping treatment becomes adaptive to the changes in the characteristics of structural vibration. A substantial number of studies on these active and passive damping treatments of structural vibration have been reported in the literature on their mathematical modelling and experimental verification. The applications of these damping treatments in different engineering structures have also been addressed in the literature. Other than these fundamental studies and applications, various configurations of the damping treatments have been addressed in the literature for their augmented damping capacity.

In this introductory chapter, first, a brief introduction is presented on the viscoelastic materials, piezoelectric materials and piezoelectric composites. Next, a literature review on the uses of these materials in the UCLD, PCLD and ACLD treatments of structural vibration is presented. On the basis of this literature review, the scope of the present research has been identified, and the objectives of the present thesis are furnished. The contributions in the field of viscoelastic damping of structural vibration made towards the preparation of this dissertation have been delineated thereafter. In the end, the organization of the thesis is outlined.

1.1 Viscoelastic materials

The viscoelastic materials are basically long-chain polymers. Under an applied stress, the positions of some parts of the long polymer chain change. This rearrangement of parts of polymer chain results in time-dependent strain of the material and this phenomenon is commonly known as creep. During the rearrangement of parts of the polymer chain, a back stress develops, and when the magnitude of this back stress becomes equal to that of the applied stress, then the material does not undergo creep. As the applied stress is relieved, the back stress causes the material to return to its original form. The creep phenomenon indicates the viscous properties of the material while its (material) recovery into original form signifies elastic properties, and thus the material is identified by the name "viscoelasticity". For an elastic material, its linear constitutive behaviour can be described by the linear stress-strain curve as shown in Fig. 1.1(a). But, when this linear elastic behaviour is associated with the creep phenomenon for a viscoelastic material, the stress-strain curve encloses an area (Fig. 1.1(b)) that is proportional to the energy loss per cycle as the material undergoes cyclic oscillations (Jones, 2001). This enclosed curve is commonly known as a hysteresis loop. The stiffness or modulus of elasticity of the viscoelastic material can be obtained by the slope of the major axis of the ellipse, whereas the loss of energy or energy dissipation property is termed as the damping property. This damping property of a viscoelastic material is generally quantified by the parameters like loss factor, quality factor, damping ratio, etc. Of these, the most popular one is the loss factor that is defined as the ratio of the energy loss per radian (area of hysteresis loop/ 2π) divided by the peak strain energy in every cycle of operation (Ungar, 1964).

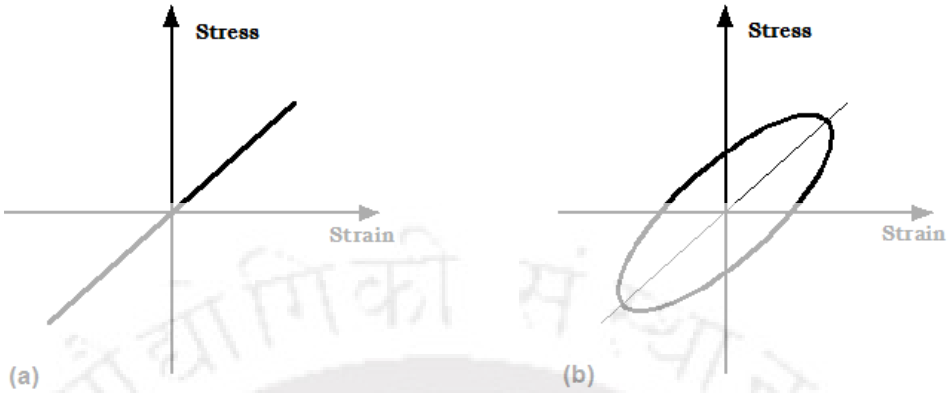

Fig. 1.1. Stress-strain plots for (a) linear elastic and (b) viscoelastic materials under the harmonic load at low-stress limits.

The modulus of elasticity and loss factor of a viscoelastic material usually vary with the operating frequency and temperature. The effects of operating temperature on the modulus of elasticity (G) and loss factor (η) are theoretically defined by dividing the whole temperature region in common applications into the glassy region (low temperature), transition region and rubbery region (high temperature) as shown in Fig. 1.2(a). The corresponding states of a viscoelastic material are called as glassy state, state of transition and rubbery state. The viscoelastic material possesses a high value of the modulus of elasticity at its glassy state. But, this material parameter starts to decrease steeply when the operating temperature increases beyond the state transition temperature (T_s), and the magnitude of the modulus of elasticity reaches a low value for the rubbery state of the material (Fig. 1.2(a)). In parallel to this variation of the modulus of elasticity, the loss factor also typically varies as shown in Fig. 1.2(a).

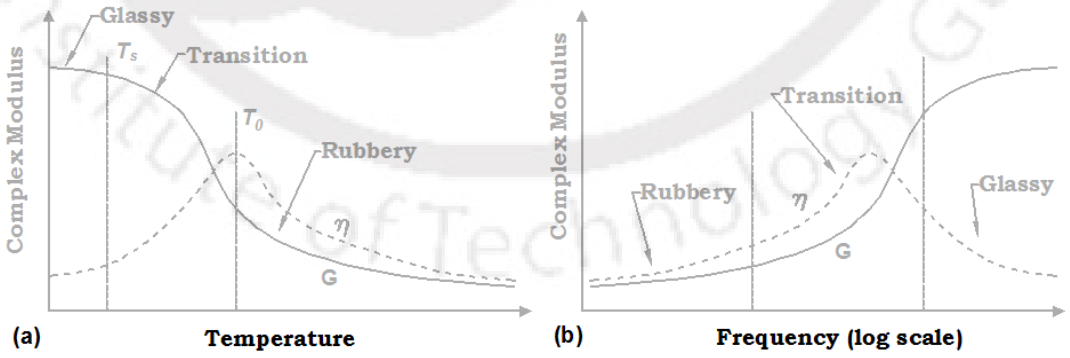

Fig. 1.2 Effects of (a) temperature and (b) frequency on the properties of a typical viscoelastic material.

Corresponding to these variations of the stiffness and damping properties of a viscoelastic material with the operating temperature, the material is usually characterized by some parameters as transition temperature, temperature of peak loss factor, low-temperature modulus, high-temperature modulus and width of the transition zone. Qualitatively, the effect of operating frequency on the mechanical behaviour of a viscoelastic material is almost opposite to that (behaviour) of the operating temperature as shown typically in Figs. 1.2(a)-(b)). With reference to these varied properties of a viscoelastic material, the important parameters in the characterization of the material within a frequency domain are commonly known as transition frequency, frequency of peak loss factor, low-frequency modulus, high-frequency modulus and width of the transition zone.

The commonly used viscoelastic materials for passive damping of structural vibration are, Paracril-BJ, Polymer Blend, butyl rubber, Viton-B, Styrene-butadiene rubber (SBR), Soundcoat N5, 3M-467, LD-400, etc. (Jones, 2001). For the theoretical formulation of the constitutive behavior of these viscoelastic materials in the frequency-domain or in the time-domain, various mathematical models are proposed in the literature, namely, Maxwell model, Voigt model, standard model , Kelvin chain model, generalized Maxwell model (Parke, 1966; Bert, 1973), Biot model (Biot, 1958), ADF model (Lesieutre and Bianchini, 1995), complex stiffness model (Scanlan, 1970), GHM model (Golla and Hughes, 1985), etc. Of these, the complex stiffness model is the frequently used one for the analysis of a viscoelastic material in the frequency domain, while GHM and ADF models are also widely utilized for similar analyses in the time-domain.

The complex stiffness model is established through the dynamic test where a viscoelastic material is considered to operate under a sinusoidal stress. Under the sinusoidal stress, the material would be in steady state motion with the sinusoidal strain. The strain appears with the same frequency but has a retarded phase (δ) (Chawla and Meyers, 1999). These stress and strain can be written in terms of their amplitudes (ε_0, σ_0), operating frequency (ω) and phase difference (δ) as (Chawla and Meyers, 1999),

$$\varepsilon = \varepsilon_0 \exp j(\omega t)\,,\ \ \sigma = \sigma_0 \exp j(\omega t + \delta)\,,\quad j = \sqrt{-1} \tag{1.1}$$

The stress and strain are related by the Hooke's law as given in Eq. (1.2), where the modulus of the material appears as a complex quantity.

$$E^* = \frac{\sigma}{\varepsilon} = \frac{\sigma_0}{\varepsilon_0}(\cos\delta + j\sin\delta) = (E' + jE'') \tag{1.2}$$

The real (E') and imaginary (E'') parts of the material modulus (E^*) are known as storage modulus and loss modulus, respectively. The ratio of loss modulus (E'') to storage modulus (E') is called as the loss factor (η). So, the complex constitutive relation (Eq. (1.2)) can also be written for a linear isotropic viscoelastic material as (Tomlinson, 1990),

$$E^* = E' + jE'' = E'(1 + j\eta) \tag{1.3}$$

$$G^* = (G' + jG'') = G'(1 + j\eta), \; E' = 2(1+\upsilon)G' \tag{1.4}$$

In Eqs. (1.3) and (1.4), the symbols G and υ represent shear modulus and Poisson's ratio, respectively. The measured complex properties (E', η) of a viscoelastic material are conventionally expressed through the temperature frequency nomogram that can be generated following a simple methodology based on the principle of temperature-frequency equivalence (Nashif, 1985, Jones, 2001).

The constitutive behaviour of a linear isotropic viscoelastic material in the time-domain is commonly expressed according to the following expression (Christensen, 1982),

$$\sigma(t) = \int_0^t E(t-\tau)\frac{\partial}{\partial\tau}\varepsilon(\tau)d\tau \tag{1.5}$$

where, $E(t)$ is the time-dependent relaxation modulus, $\varepsilon(\tau)$ is defined as zero for $t \le 0$. This equation in the time-domain may also be expressed in the complex-domain through the Laplace transform as (Golla and Hughes, 1985),

$$\tilde{\sigma}(s) = s\tilde{E}(s)\tilde{\varepsilon}(s) \tag{1.6}$$

In Eq. (1.6), $s\tilde{E}(s)$ is the material modulus function. This modulus function can also be written by the equality (Golla and Hughes, 1985) as, $s\tilde{E}(s) = E_o[1+h(s)]$, and it results in the constitutive relation as,

$$\tilde{\sigma}(s) = E_o[1+h(s)]\tilde{\varepsilon}(s) \tag{1.7}$$

where, E_o is the modulus of the material at equilibrium and $h(s)$ is the dissipation or relaxation function. Many mathematical representations of the

relaxation function ($h(s)$) are available in the literature (Adhikari and Woodhouse, 2003; Park et al., 1999). Among these different relaxation functions, the widely used ones are the GHM and ADF relaxation functions as given in Eqs. (1.8) and (1.9), respectively.

$$h(s) = G^{\infty}\left[1+\sum_{q=1}^{N}\alpha_q \frac{s^2+2\tilde{\xi}_q\tilde{\omega}_q s}{s^2+2\tilde{\xi}_q\tilde{\omega}_q s+\tilde{\omega}_q^2}\right] \tag{1.8}$$

$$h(s) = \sum_{q=1}^{N_v}\frac{\Delta_q s}{s+\Omega_q} \tag{1.9}$$

In Eq. (1.8), G^{∞} represents the modulus of the viscoelastic material in equilibrium; α_q, $\tilde{\xi}_q$ and $\tilde{\omega}_q$ are the GHM parameters which can be obtained by fitting the curve to experimental data for the modulus within a frequency-domain (McTavish and Hughes, 1992). In Eq. (1.9), Δ_q is the relaxation resistance and Ω_q is the inverse of the characteristic relaxation time at constant strain (Lesieutre and Bianchini, 1995). The GHM/ADF model is usually implemented by taking the equations of motion of a viscoelastic material system in the Laplace-domain, while a subsequent inverse Laplace transform of the solution is necessary for interpreting results in the time-domain.

1.2 Piezoelectric materials

In 1880, it was discovered by Pierre and Jacques Curie that the positive and negative charges are produced in certain portions of the surfaces of some crystals when they are deformed in particular directions, and the appearing charges are proportional to the applied load. Upon removal of the pressure, the charges disappear. This phenomenon of electric polarization or producing electricity as a consequence of mechanical strain/stress in certain materials is known as the direct piezoelectric effect. In a reverse way, the same materials become strained when an electric field is applied along the polarization direction, and this phenomenon is known as the converse piezoelectric effect. The materials which exhibit these two effects are commonly known as piezoelectric materials, and the phenomenon is termed as piezoelectricity (Cady, 1946). These direct and converse piezoelectric effects have been exploited for the development of distributed sensors and actuators particularly for active control of flexible structures.

Piezoelectric materials either exist naturally or are prepared synthetically. The natural piezoelectric materials include quartz, Rochelle salt, paraffin, bone, ammonium phosphate, etc. The synthetic piezoelectric materials include, lead zirconate titanate ($Pb(Zr,Ti)O_3$, commonly known as PZT), barium titanate, polyvinylidene fluoride (PVDF), lead lanthanum zirconate, lithium sulphate, etc. (Jalili, 2010). Of these, PZT and PVDF are the popular ones in active control of structural deformation/vibration. These synthetic piezoelectric materials are isotropic in nature at their raw stage where the dipoles (domains) are oriented randomly (Fig. 1.3(a)) with zero dipole density or polarization (Tiersten 1969, Choi and Han, 2016). Upon application of a strong electric field (about 10^6 V/m) in the presence of high temperature, the molecular dipoles align following the direction of the external electric field (Fig. 1.3 (b)), and this process is customarily known as poling.

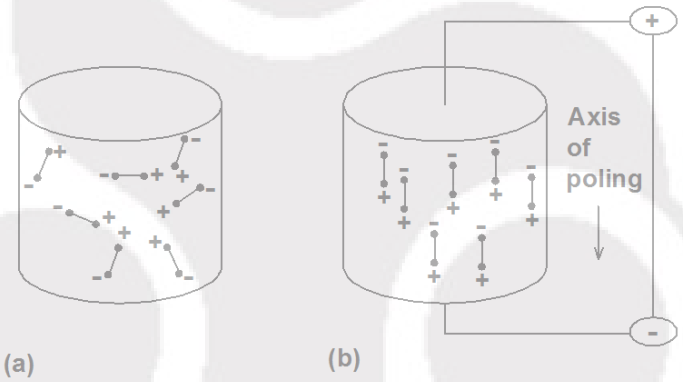

Fig.1.3 Schematic diagram of poling process for piezoelectric materials.

On removal of the applied electric field, a permanent reorientation of the molecular dipoles appears leading to the remanent polarization, and the material then becomes anisotropic in nature with the piezoelectricity behaviour. This phenomenon of polarization of a bulk piezoelectric material is generally described by a typical Hysteresis loop in a two-dimensional domain of the applied electric field (E) and polarization (P) as shown in Fig. 1.4(a). For a small magnitude of the applied electric field, polarization (P) is linearly related to the electric field (E) (part AB in Fig. 1.4(a)). Now, as the electric field increases, switching of molecular dipoles (domains) occurs following the direction of the applied field, and the polarization reaches to its saturation stage (P_S, point C in Fig 1.4(a)).

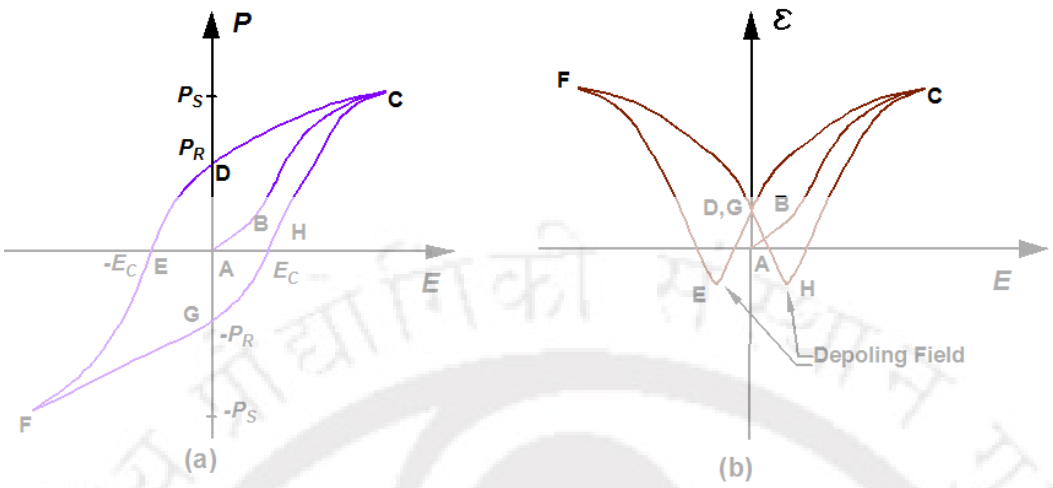

Fig. 1.4. (a) Hysteresis (electric field-polarization) loop of a typical piezoelectric material, (b) butterfly curve (electric field (E)-strain (ε)) of a piezoelectric material.

On removal of the applied electric field, back-switch of some of the domains occurs, and a non-zero polarization called as remanent polarization (P_R) appears for zero electric field. To achieve zero polarization, the electric field must be reversed to a finite value that is usually called as the coercive electric field ($-E_C$). As the electric field decreases beyond the coercive electric field, a negative maximum (saturation) polarization ($-P_S$) is reached, and a cycle continues as shown in Fig. 1.4(a). In parallel to the variation of polarization (Fig. 1.4(a)), the stain of the material also varies as shown in Fig 1.4(b). The curve in Fig. 1.4(b) is commonly known as butterfly curve due to its shape. For the decrease of electric field after reaching the maximum strain through the curve ABC, the strain decreases until the depoling takes place (point E, Fig. 1.4(b)) at the coercive electric field. For a further decrease of the electric field, the material expands until a physical strain limit (point G, Fig. 1.4(b)).

In the use of the piezoelectric materials for sensors and actuators, the maximum limit of the electric field is usually taken as the coercive electric field (point E or H, Fig. 1.4(b)). Moreover, in most of the applications, the linear constitutive behaviour of the piezoelectric materials is preferred and it lies at well below of the coercive electric field. If the applied electric field in operation exceeds the coercive electric field, then the depoling takes place, and material behaves differently. It is also essential that the operating temperature must not exceed a certain limit that is usually known as the Curie temperature (Chaudhry and Rogers, 1995). However, the constitutive behaviour of a linear

piezoelectric material under the operation at a constant temperature can be described by four field quantities, namely, stress (σ), strain (ε), electric displacement (D) and electric field (E). On the basis of these field quantities, four kinds of thermodynamic potentials can be defined as given in Eq. (1.10) (Chee, 2000) where the symbols U, H, F and G indicate internal energy, enthalpy, Helmholtz free energy and Gibbs free energy, respectively.

$$dH = \sigma d\varepsilon - DdE,\ dU = EdD + \sigma d\varepsilon,$$
$$dF = EdD - \varepsilon d\sigma,\ dG = -\varepsilon d\sigma - DdE, \quad (1.10)$$

These four kinds of piezoelectric constitutive formulations are utilized depending on the natural variables. In the structural applications of the piezoelectric materials, the natural variables are usually taken as strain (ε) and electric field (E), and thus the corresponding constitutive relations are derived using the thermodynamic potential H as (Chee, 2000),

$$\sigma = C\varepsilon - eE \quad (1.11)$$

$$D = e^{T}\varepsilon + \in E \quad (1.12)$$

where, C, e and $\in$ are the elastic, piezoelectric and permittivity matrices, respectively. Equations (1.11) and (1.12) correspond to the converse and direct piezoelectric effects, respectively for the linear piezoelectric behaviour under a constant temperature.

Piezoelectric sensors and actuators have been widely utilized for the last three decades for active control of deformation/vibration of flexible structures (Bailey and Hubbard, 1985; Crawley and de Luis, 1987; Baz and Poh, 1988; Tzou and Gadre, 1989; Crawley and Lazarus, 1991; Batra et al., 1996; Librescu et al., 1996; Chee et al., 1998; Balamurugan and Narayanan, 2001; Kapuria and Hagedorn, 2007; Kwak and Heo, 2007; Pradyumna and Gupta, 2011; Kundu et al., 2007; Araújo et al., 2016; Alibiegloo, 2017). These sensors/actuators are attached to or embedded in the host structure to have the self-sensing and self-controlling capabilities of the overall structure. This kind of assemblage of the overall structure requires sufficient conformability of the piezoelectric sensors/actuators especially for a host structure with a curved boundary surface or the complex geometry. The piezoelectric sensors/actuators would also have sufficient flexibility for their applications in control of the moderate or large amplitude of vibration of flexible structures. Along with these properties, a piezoelectric actuator would possess high strain energy density for its good actuation capability. The actuator would also be capable of providing

directional actuation. Concerning these required properties of a piezoelectric actuator, monolithic piezoelectric actuators possess high brittleness, high stiffness and low strain energy density. Monolithic piezoelectric actuators are also incapable in providing directional actuation. Because of these shortcomings, the piezoelectric fibre-reinforced composite (PFC) emerged. A PFC is made of piezoelectric fibres embedded in a polymer matrix. The polymer constituent provides sufficient flexibility and conformability of the composite while its (composite) electro-elastic properties are achieved due to the piezoelectric inclusions. A number of PFCs have been proposed by many researchers. Among many others, Smith and Auld (1991) first proposed a PFC that is comprised of vertically reinforced piezoelectric fibres within an epoxy matrix. This PFC produces the electrically induced actuation force along the thickness direction when an electric field is applied in the same direction. Later, Hagood and Bent (1993) proposed a new PFC that is comprised of horizontally reinforced piezoelectric fibres within an epoxy matrix. This PFC produces the electrically induced in-plane actuation force as an electric field is applied along the thickness direction. Subsequently, Bent (1997) proposed Active Fibre Composite (AFC). In AFC, the unidirectional piezoelectric fibres are aligned in the plane of the PFC lamina. But the poling direction of the fibres is their longitudinal direction so that this PFC produces the in-plane actuation force when the external electric field is applied along the longitudinal direction through a unique arrangement of electrodes (Interdigitated Electrodes (IDEs)). After the proposition of the AFC, a similar PFC was developed at NASA using the piezoelectric fibres of rectangular cross-section (High and Wilkie, 2003) instead of the fibres of circular cross-section (Bent, 1997). This PFC (High and Wilkie, 2003) is known as Macro-Fibre Composite (MFC), and it is a popular PFC actuator in the context of active control of structural vibration. Apart from these PFCs, Mallik and Ray (2003) designed a 1-3 PFC and derived its effective properties. Della and Shu (2008) derived the effective properties of 1-3 PFC having a porous non-piezoelectric matrix. Kapuria and Kumari (2011) estimated the effective electro-thermo-elastic properties of a PFC lamina and found that the dielectric ratio had significant effects on the electromechanical and electro-thermal coupling constants. Sakthivel and Arockiarajan (2012) proposed a 1-3-2 piezoelectric composite in which matrix and fibres possess piezoelectric properties. Kalamkarov and Savi (2012) proposed a piezoelectric composite that

is comprised of a periodic grid of generally orthotropic cylindrical reinforcements. Lin and Muliana (2013) analyzed the nonlinear electromechanical responses of piezoelectric composites comprising of nonlinear piezoelectric inclusions in a non-piezoelectric matrix. In all these available PFCs, the actuation force appears in the form of the electrically induced in-plane/transverse normal stress. However, the piezoelectric actuation in the form of the electrically induced transverse shear stress is also achieved by means of designing the Shear Actuated Fibre Composite (SAFC) (Raja and Ikeda, 2008).

A substantial number of studies on the development of piezoelectric composites have been observed in the literature. However, as the main concern of this dissertation does not lie within this context of the development of piezoelectric composites, the mostly used PFCs in active control of structural vibration are addressed in this section.

1.3 Passive damping of structural vibration

In many common structural vibration applications where cost is a prime factor along with reliability, passive damping serves as the vibration control mechanism, and it is usually achieved by the use of viscoelastic materials. Several techniques in the use of viscoelastic materials for suppression of structural vibration have been proposed in the literature such as vibration absorbers, UCLD treatment or free layer damping, CLD treatment, tuned damper, edge damping etc. (Grootenhuis, 1970; Nakra, 2000). Among these various techniques, the UCLD and CLD treatments are the popular ones for control for bending mode of vibration of thin-walled flexible structures. Extensive research on these damping treatments has been addressed in the literature. In the following sections, the damping mechanisms, as well as a literature review on each of these damping techniques, are presented.

1.3.1 *Unconstrained layer damping (UCLD) treatment*

In the UCLD treatment, a viscoelastic layer is freely attached to the surface of a flexible structure (substrate layer) as shown in Fig. (1.5(a)). As the overall structure undergoes bending deformation, the viscoelastic layer experiences extensional/compressional strain (Fig. 1.5(b)) that leads to the energy-dissipation from the overall structure. This damping treatment was proposed in 1952 (Oberst and Frankenfeld, 1952), and has been utilized substantially for passive damping of vibration of different engineering structures (Nakra, 1984;

Nakra, 1998; Rao, 2003; Sun and Kari, 2010). A good number of studies on the damping characteristics of this UCLD treatment have also been reported in the literature by many researchers. Among many others, Ungar and Edward (1964) reported that the thickness deformation could not be neglected for short and thick viscoelastic layer of UCLD arrangement. But, in general, the contribution of extensional strain of the viscoelastic layer to the overall passive damping is far greater than that of the thickness deformation/shear deformation of the same viscoelastic layer (Reddy, 1979). So, the energy dissipation in UCLD treatment mainly occurs due to alternate extension and compression of the viscoelastic layer.

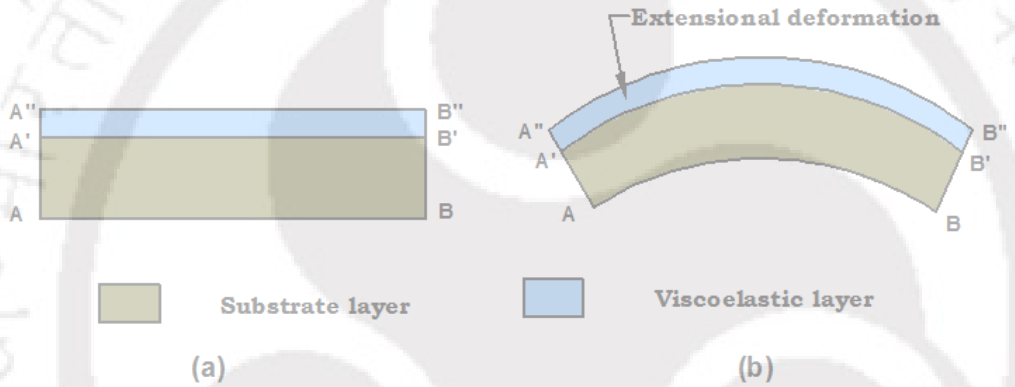

Fig. 1.5 Schematic diagrams of (a) undeformed and (b) deformed substrate layer integrated with a UCLD layer.

In a comparison study (Grootenhuis, 1970), it is revealed that the damping in the UCLD treatment is far lesser than that in the CLD treatment unless the viscoelastic layer possesses a high modulus of elasticity as well as high loss factor. Markus (1976) used the UCLD treatment for the cylindrical shell structures and found that the treatment yields lesser value of loss factor for the shell structures than that for beams and plates. Narayanan et al. (1981) analyzed the free vibration characteristics of open cross-section beams integrated with the UCLD treatment and found that the treatment is effective for the lower-order coupled mode. Mead (2007) presented a comparative study of different analytical methods for finding the loss factors in the UCLD treatment of beams and plates. Okazaki et al. (1994) studied the UCLD treatment of a shell structure using a thick viscoelastic layer and found the enhanced effects of shear and thickness deformations of the viscoelastic layer on the damping in the overall structure. Cortes and Elejabarrieta (2007) proposed a one-dimensional

homogenized formulation for UCLD treatment of beams to ease the analysis by reducing the number of degrees of freedom of the system. The same researchers (Cortes and Elejabarrieta, 2008) also found in a separate analytical study of beams with UCLD layer that the natural frequency is overestimated and the damping is underestimated if the shear deformations of the viscoelastic layer are neglected. Lumsdaine and Scott (1995, 1998) carried out a study on the shape optimization of UCLD layer for beam and plate structures and reported superior damping capacity of the UCLD layer for the optimized non-uniform thickness of the damping layer instead of its uniform thickness.

1.3.1.1 Literature on the use of UCLD treatment in different configurations

Apart from the aforesaid studies using a layer of UCLD treatment throughout the surface of the host structure, the partial UCLD treatment has also been addressed in the literature. Mead and Pearce (1961) suggested concentrated damping material around the location of the maximum bending moment for superior damping using the lesser mass of the damping material. Lunden (1979) demonstrated an optimal distribution of the material of UCLD treatment over the length of a beam element for effective damping of resonant vibration-amplitudes. Yildiz and Stevans (1985) also reported the optimal regions of the plates for addition of viscoelastic material in the UCLD treatment. In the same year, another study (Parthsarthy et al., 1985) revealed that the conversion of full to partial UCLD treatment (keeping the same mass of the damping material) results in superior damping provided that the damping material is to be concentrated in the areas of high extensional deformation. The effect of temperature on the optimal shape of the UCLD treatment is demonstrated by Cheng and Lapointe (1995). Roy and Ganeshan (1993, 1996) investigated the appropriate configuratiosn of partial UCLD treatment for beams and plates, and it was found that the configuration of the treatment significantly depends on the boundary conditions and the modes of vibration. It was also found in the same study (Roy and Ganeshan, 1996) that an optimal configuration of partial UCLD treatment for a particular mode of vibration may have detrimental effects on other modes of vibration. Ravi et al. (1996) proposed an efficient procedure for the analysis of plates with partial or full UCLD treatment. Lee and Hwang (2004) presented a methodology for optimal layout of partial UCLD treatment in effective damping of vibration of a beam where basically the viscoelastic material is located at the regions of high strain energy. Zang et al. (2010) presented an

optimal distribution of thickness of UCLD layer over the host structure-surface based on the mode-shapes of vibration and demonstrated the corresponding effectiveness of the UCLD treatment over its (UCLD) use with uniform thickness. El-sabbagh and Baz (2014) addressed the optimal distribution of viscoelastic material on the plate-surface with an objective of the maximum modal damping ratio. The same study also illustrates the optimization of the unit cell in case of the periodic damping treatment.

1.3.2 *Passive constrained layer damping (PCLD) treatment*

Although the UCLD treatment is easy to implement and also economically cheap passive damping arrangement, it possesses very low damping capacity that limits its applications in the suppression of structural vibration. In comparison to the UCLD treatment, a better passive damping treatment is the PCLD treatment (Swallow, 1939; Kerwin, 1959). This damping treatment is found to be very useful in automobile and aircraft engineering applications especially for door panels, floor panels, dash panels, brake covers, skin, stringers, frames of fuselage section in commercial aircraft (Rao, 2003), flutter suppression of aeronautical panels (Cunha-Filho et al., 2016). The damping (PCLD) treatment is also applied substantially in railway wheels (Jones and Thompson, 2000), outlet guide van (Tomlinsin 1990), computer hardware industry (Rao, 2003), squeal noise in trams (Merideno et al., 2014), machine tool (Marsh and Hale, 1998; Shi et al., 2017), spinning disks (Seubert et al., 2000), compression blades (Sun and Kari, 2010), etc.

The PCLD treatment is usually comprised of a viscoelastic layer which is constrained within the host structure-surface and a stiff constraining layer. A typical geometric configuration of the PCLD treatment is shown in Fig. 1.6(a) where a viscoelastic layer is constrained between the surface of the host structure and a constraining layer. As the overall structure undergoes bending deformation (Fig. 1.6(b)), the viscoelastic layer experiences transverse shear deformation/strain that leads to the energy-dissipation from the overall structure during its vibration. The constrained viscoelastic layer does not experience reasonable extensional strains, and thus the damping in the PCLD treatment arises mainly due to the transverse shear strain of the constrained viscoelastic layer. In some references, the PCLD treatment is called as the constrained layer damping (CLD), and it mainly arises in case of a sandwich structure with a viscoelastic core.

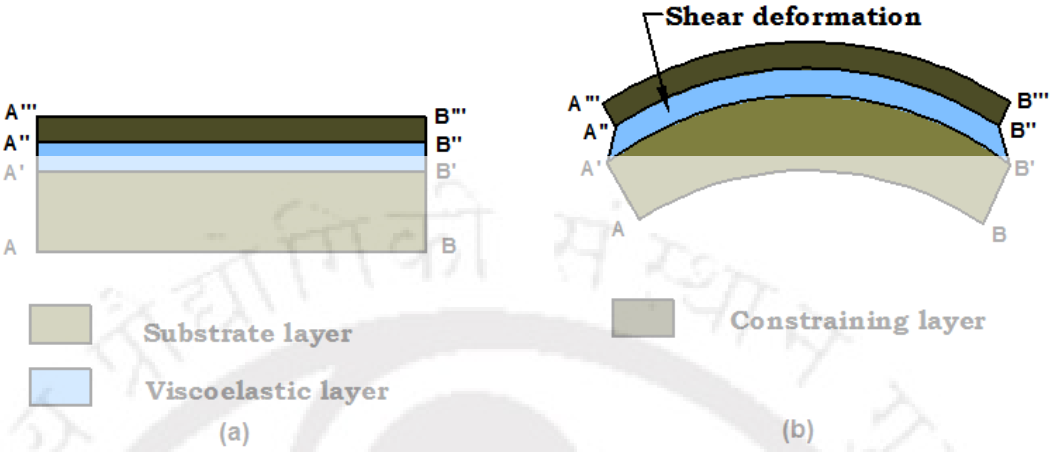

Fig. 1.6 Schematic diagrams of (a) undeformed and (b) deformed substrate layer integrated with a PCLD layer.

The PCLD/CLD treatment was first introduced by Swallow (1939) and its first mathematical formulation was addressed by Kerwin (1959) considering travelling sinusoidal waves of transverse displacements in beams. In the same year, Ross et al. (1959) proposed a model of CLD treatment where the relationship among the motions of component layers of CLD treatment and the loss factor was established. The analytical results in this study (Ross et al., 1959) were also verified experimentally by Yin et al. (1967). Subsequently, Mead and Markus (1969) derived a six-order differential equation in terms of transverse deflection for a variety of boundary conditions of beams. Besides the thin-walled flat structures (beams and plates), the PCLD/CLD treatment has also been utilized for suppression of vibration of thin-walled shell structures. Yu (1963) first analyzed the vibration of sandwich shells with the viscoelastic core. Later, Jones and Selerno (1966) presented an analysis of forced axisymmetric vibration of circular cylindrical sandwich shells with the viscoelastic core. Although cylindrical shells in these analyses are considered to have infinite length, later the analysis of a cylinder of finite length was presented by Pan (1969). Afterward, various theoretical and experimental studies on the PCLD treatment of thin-walled flexible structures appeared in the literature particularly for investigating its damping mechanisms and damping capacity for different kinds of structures.

Lu et al. (1979) presented an FE model of a three-layered viscoelastic sandwich plate, and it was also verified experimentally. Johnson and Kienholz (1982) derived an FE model of a three-layered viscoelastic laminate to compute

the modal damping ratio using the modal strain energy (MSE) method. The results of this work (Johnson and Kienholz, 1982) were verified by Shin and Maurer (1991) through the frequency response analysis of plates with PCLD layer, and it was reported that the numerical procedure might overestimate the damping in comparison to that obtained experimentally. Alam and Asnani (1984) derived the governing equations of motion for axisymmetric and non-axisymmetric vibration of a laminated shell with alternate elastic and viscoelastic layers. Sun et al. (1990) developed an FE model of a laminated beam using the offset beam elements for the stiff layers and the plane finite elements for the viscoelastic layer. In some mathematical models of plates with CLD/PCLD treatment, it was proposed to use the plane elements for face layers and the solid elements for viscoelastic layer (Johnson et al., 1991). Imaino and Harrison (1991) used MSE method in conjunction with the p-version FE method to evaluate the damping property of a beam with CLD treatment and found that the results differ significantly from those obtained with the conventional formulation. Wilson et al. (1992) also used MSE method combined with the p-version FE method and highlighted the advantages of the p-version FE method over the h-version FE method. Ramesh and Ganeshan (1992) presented a semi-analytical FE formulation based on the discrete layer theory for a laminated cylindrical shell with constrained viscoelastic layers. Yi and Hilton (1994) presented an FE model of viscoleastically damped composite structures for the analysis of damping in the time-domain. Kiehl and Jerzak (2001) and Meunier and Shenoi (2003) modelled the CLD treatment for beams and panels in the time-domain using the GHM method. Ramesh and Ganeshan (1994, 1995) derived an FE model of a circular cylindrical sandwich shell with the viscoelastic core and presented a comparative study on the utilization of different displacement theories for the damping analysis of the shell. Korjakin et al. (2001) developed a numerical model of a cylindrical sandwich shell with viscoelastic core using a specific sandwich shell finite element of 54 degrees-of-freedom. Cai et al. (2004) presented an analytical model of beams integrated with a PCLD patch where the longitudinal displacement of constraining layer is accounted. This consideration provides more accurate results for vibration of a beam with PCLD patch especially when a hard viscoelastic material is used as the damping layer. Zhang and Chen (2006) used three-dimensional solid elements to derive the FE model of laminated composites with the constrained

viscoelastic layers. Moreira and Rodrigues (2006) developed a facet-shell finite element using the generalized layer-wise formulation for laminated structures consisting of multiple viscoelastic layers. Alvelid and Enelund (2007) introduced an interface finite element to model the viscoelastic layer of a sandwich plate where the thickness deformations of the layers are accounted without increasing the degrees-of-freedom. Shin et al. (2009) investigated the viscoelastic damping in a laminated cylindrical shell with a constrained viscoelastic layer by developing an FE model using the layer-wise displacement theory. Manconi and Mace (2010) used wave finite element (WFE) method for analysis of laminated panels with the constrained viscoelastic layers and reported lesser computational time in comparison to that in the use of the conventional FE procedure. Ferreira et al. (2013) presented an FE model of the sandwich plates with the viscoelastic core based on the Carrera's Unified Formulation (CUF). Using this CUF, Filippi et al. (2016) also derived higher-order finite elements for the FE analysis of beams with CLD treatment. Xu (2015) derived an FE model of plates with CLD treatment and demonstrated simultaneous material layout and geometry optimization of the damping treatment. Apart from these FE formulations, matrix methods and wave propagation methods have also been utilized by many researchers to analyse the passive damping of vibration of circular cylindrical sandwich shells (Xiang et al., 2008; Lu et al., 2010; Zheng et al., 2014; Cao et al., 2011). For the analysis of the same structural elements (cylindrical sandwich shells), a few analytical models have also been developed in recent studies (Jin et al., 2015; Yang et al., 2015).

1.3.2.1 Literature on the importance of extensional/compressional strains in the viscoelastic layer of CLD/PCLD treatment

In most of the analyses of the PCLD/CLD treatment, extensional/compressional strains of the viscoelastic layer are not accounted for characterising the passive damping since the damping appears mostly due to the shear strain of the damping layer (Xie and Shepherd, 2009). However, it has also been shown in various studies that the compressional damping cannot be neglected especially for the damping treatment with a thick viscoelastic layer (Douglas, 1978; Douglus, 1986; Sylwan, 1987; Lee and Kim, 1996; Sisemore, 2002). Huang et al. (2001) reported that the relative thickness deformation (RTD) arises appreciably in case of the thicker viscoelastic layer or for partial CLD treatment of

structures. So, in these cases, the consideration of all the strains in the viscoelastic layer is inevitable for better accuracy of damping models.

1.3.2.2 Literature on the use of CLD/PCLD treatment in different configurations

In the quest of improved damping capacity of the CLD/PCLD treatment, it (CLD/PCLD) appeared with different geometric and/or material configurations. Plunkett and Lee (1970) presented an arrangement of improved CLD treatment that was achieved by cutting the constraining layer to the appropriate lengths. Trompette and Fatemi (1997) also reported a similar strategy where the elastic constraining layer is segmented in an optimal manner for appropriate distribution of shear strain within the constrained viscoelastic layer over the modes of vibration. Al-Ajmi and Bourisli (2008) used Genetic Algorithm (GA) to find the relative thickness and number of cuts in the segmented PCLD arrangement. Lepoittevin and Kress (2010) presented an optimal configuration of the segmented CLD arrangement for improved damping of all the modes of vibration of a beam element. Recently, Tian et al. (2016) investigated the effectiveness of segmentation of CLD treatment and reported that it could only be effective for a very thin viscoelastic layer.

Apart from the segmentation of constraining layer, Torvik and Strickland (1972) proposed a configuration of multilayer CLD treatment using segmented viscoelastic layer and unanchored constraining layer. The segmented viscoelastic layer in this CLD configuration undergoes enhanced shear strain, and it leads to the improved damping characteristics of the treatment. A similar work was also carried out by Alam and Asnani (1984a) by taking several CLD layers in a stack, and it was found that the damping in the structure increases when the number of CLD layers is increased as three, five and seven.

Lifshitz and Leibowitz (1987) computed the optimized thicknesses of constrained damping layers for a variety of boundary conditions and design constraints. Ganapati et al. (1999) reported that the damping property of a laminated beam element improves as the thickness of the viscoelastic layer of CLD arrangement increases especially for lower aspect ratios of the beam. A similar observation was found by Teng and Hu (2001). Additionally, they (Teng and Hu, 2001) also found that asymmetric viscoelastic sandwich laminates have lower damping efficiency compared to symmetric ones.

Rao and He (1993) carried out a parametric study on the damping characteristics of laminated composite beams with multiple viscoelastic layers and anisotropic constraining layers and demonstrated the effects of fibre orientations of composite laminas, thicknesses of different plies and thicknesses of viscoelastic layers on the damping property of the overall beam. Rao et al. (1997) also analyzed a laminated composite plate comprised of multiple damping layers and anisotropic constraining layers, and they reported a significant effect of the compliant layer on damping for higher modes of vibration. Maoût et al. (2011) optimized the stacking sequence, number of layers and relative thicknesses among the layers of a hybrid composite plate for its (plate) superior damping property. Zheng et al. (2014) observed in the shell structures that the effectiveness of PCLD treatment increases for the use of several constrained viscoelastic layers. Madeira et al. (2015) presented the optimal design of a sandwich panel with the viscoelastic core for the maximum modal damping using the minimum viscoelastic material. A similar optimization study on a sandwich beam element was also carried out by Hamdaoui et al. (2015).

Whittier (1959) introduced a standoff/spacer layer between the damping layer and the surface of host structure for improved damping in the CLD treatment. The standoff layer enhances the shear strain in the constrained viscoelastic layer, and that results in the improved damping capacity of the CLD treatment. Rogers and Parin (1995) experimentally verified the utility of this standoff/spacer layer. Garrison et al. (1994) also studied the utility of the standoff/spacer layer for the partial CLD treatment and found that the standoff layer facilitates to reduce the size of the CLD treatment without degradation of its damping capacity. Masti and Sainsbury (2005) suggested that incorporation of standoff layer within the partial CLD treatment can be a viable option for higher damping regardless of low weight and low surface area of the treatment.

In many engineering designs of vibrating structural elements, the constraints of mass and economic cost of the overall structure are imposed. In this circumstance, partial PCLD treatment may be an obvious choice, and thus an extensive research on this topic has been reported in the literature. Nokes and Nelson (1968) were among the earliest researchers to work on the partial PCLD, and they found that the loss factor for partial coverage is more than that for full coverage of the treatment. Markus (1974) also advocated for the partial PCLD treatment of beam. Lu (1977) proposed a partial CLD treatment in the

form of discretely distributed mass segments over the outer surface of a substrate shell and reported significant improvement of damping through this arrangement. El-Rehab and Wagner (1986) used thin axial strips to constrain the thin viscoelastic layer over the outer surface of a cylindrical shell. A similar shell was also analysed by Lu et al. (1991) considering the closely spaced axial strips. Lall et al. (1987, 1988) demonstrated the effect of size/coverage of the partial PCLD treatment on the passive damping of vibration of beam and plate structures. Marcelin et al. (1992) addressed the optimal size and location of partial CLD treatment for beam elements and also reported that the full CLD treatment is not always more efficient than the partial one. Cheng and Lapointe (1995) reported that the optimal distribution of partial CLD treatment over the surface of panels might result in indicative improvement of damping capacity of the treatment. Kung and Singh (1998) analysed a harmonically excited beam integrated with a number of patches of PCLD treatment and found much higher modal loss factor for the fixed-end patches in comparison to that for the free-end patches. Chen and Huang (1999) and Wang and Chen (2004) presented the partial CLD treatment of a cylindrical shell where the material of CLD is discontinuously distributed along the length of the shell but fully distributed over the circumference. For achieving the improved loss factor in the CLD treatment of a fluid-filled cylinder, the modal distributions of the thickness of constraining layer over the radial and circumferential coordinates of a cylindrical structure were recommended by Saravanan et al. (2000).

Chen and Huang (2001) proposed the partial CLD treatment of cylindrical shells in the form of the strip. The strips of CLD treatment are continuously distributed along the axial direction of the substrate cylinder. The same authors (Chen and Huang, 2002) also performed a study on the optimal PCLD patches for plates, and they observed that the maximum damping in the structure arises when the thickness of the constraining layer appears twice of that for the viscoelastic layer. Zheng et al. (2005) presented a GA based optimal layout of CLD patches over the surface of a cylindrical shell for effective damping of vibration. The same authors (Zheng et al., 2006a, 2006b) also performed a parametric study of a beam integrated with multiple PCLD patches and reported superior damping using multiple patches instead of one patch although the multiple patches are to be located at appropriate locations over the length of the beam. Granger and Ross (2009) studied the vibration of a beam with partial

PCLD treatment and found indicative effects of the length and thickness of the viscoelastic layer on the initial transient displacement of the overall beam. Kumar and Singh (2010) demonstrated the effectiveness of modal strain energy method in the optimal placement of CLD patches for damping characteristics in a wide frequency range. Cao et al. (2013) investigated the vibration and acoustic characteristics of a cylindrical shell integrated with two sets of rings of CLD treatment. This arrangement of CLD treatment was found to have significant damping capability in the suppression of radial vibration of the shell. Khalfi and Ross (2013) studied the effectiveness of partial CLD treatment to dampen out the bending waves in plates. The same authors (Khalfi and Ross, 2016) also performed a parametric study on the partial CLD treatment for a plate and suggested to locate the material of the treatment around the corners of the plate and also around the crests of mode shape of vibration.

1.4 Active constrained layer damping (ACLD) treatment

The viscoelastic damping of vibration of thin-walled structures is commonly achieved by UCLD and PCLD treatments. Extensive research on these passive damping treatments has been carried out by many researchers as presented in the foregoing sections. The PCLD treatment is the advanced one over the UCLD treatment, and a good damping of structural vibration can be obtained using the PCLD treatment. But, this passive damping (PCLD) treatment provides effective damping only under the operation at high frequency (Shi et al., 2004). This damping treatment (PCLD/CLD) is not also adaptive to the changes of vibration characteristics of a structure. So, the research on the use of viscoelastic materials along with the piezoelectric actuators has been carried out by many researchers especially for achieving adaptive viscoelastic damping and also enhanced damping at any operating frequency. The research in this direction leads to different hybrid damping treatments as Electro-Mechanical Surface Damping (EMSD) (Ghoneim, 1993, 1996; Hagood and Flotow, 1991), ACLD (Baz and Ro, 1995; Shi et al., 2004), Conventional Active Piezoelectric Damping Composite (CAPDC) (Gentilman et al., 1994; Reader and Sauter, 1993), Active Piezoelectric Damping Composite (APDC) (Arafa and Baz, 2000; Baz and Tempia, 2004), etc. Among the available hybrid damping treatments in the literature, the most popular one is the ACLD treatment as it is widely used in aircraft, naval and automobile industries (LaPlante, 1998; Kwak et al., 1999; Herdic et al., 2005). The arrangement for

this damping treatment is similar to that of the PCLD treatment, but the constraining layer is made of piezoelectric material along with a suitable controller. The piezoelectric constraining layer acts as an actuator mainly to control the transverse shear deformation of the constrained viscoelastic layer according to an appropriate control strategy. So, the viscoelastic damping enhances significantly. In some studies, the ACLD treatment is called as active-passive damping treatment since the damping arises through both the passive and active mechanisms. The ACLD treatment was proposed by Baz and Ro (1993). In this proposition of ACLD treatment (Baz and Ro, 1993), a viscoelastic layer is sandwiched between two piezoelectric layers. The piezoelectric layers are utilised as the sensor and actuator layers through a controller to control the transverse shear deformation of the constrained viscoelastic layer for having enhanced damping in the overall structure. Instead of using two piezoelectric layers, Shen (1993, 1994) utilised one piezoelectric layer to constrain the viscoelastic layer, while the control activities of the piezoelectric constraining layer were regulated by a controller and a point-sensor. Baz and Chen (1997) used a boundary control strategy for ACLD treatment of axisymmetric vibration of circular cylindrical shells. Their work was extended by Ray et al. (1997, 2001) for controlling the circumferential as well as longitudinal modes of vibration of thin shells using partial ACLD treatment. In some of the studies, this configuration is also called as smart constrained layer damping (SCLD) (Balamurgan and Narayanan, 2002). Azvine (1995) presented another arrangement of ACLD treatment where the piezoelectric layer is attached to the metallic constraining layer instead of using the piezoelectric layer as the constraining layer. In the early stage of evolution of ACLD treatment, its (ACLD) utility as a potential damping device was substantiated through a comparative study of the available active, passive and hybrid damping treatments (Chen and Baz, 1996, Veley and Rao, 1996, Tomlinson, 1996). In some of the studies, the uses of different control strategies for achieving superior damping capacity of the treatment are reported (Park and Baz, 1999, Gandhi and Munsky, 2000).

Various mathematical models of the ACLD treatment have been addressed in the literature especially for investigating the damping mechanisms and also for quantification of damping for different kinds of engineering structures. Nostrand et al. (1994) developed an FE model of a beam integrated with the ACLD treatment for the transient analysis of the overall beam. Lam et

al. (1995) used GHM model of viscoelastic material for transient analysis of beams with ACLD treatment. Saravanan et al. (2001) presented a semi-analytical model of circular cylindrical shells integrated with ACLD patches. Park and Baz (2001) developed FE models of plates with ACLD treatment based on the classical plate theory or layer-wise shear deformation theory and reported that the latter one provides more accurate results. Trindade et al. (2001) developed an FE model of sandwich beams using ADF model of viscoelastic material. Cento and Kawiecki (2002) presented an FE model of five-layered beam element using ADF model for sandwiched viscoelastic material. Sun and Tong (2004) carried out an FE analysis of beams with ACLD treatment and demonstrated the effects of incompatible transverse displacements of constraining layer and substrate beam on the closed-loop control activity in the treatment. Illaire and Kropp (2005) developed an analytical model for the ACLD treatment of beams to illustrate three damping mechanisms in the treatment as, (a) shearing of viscoelastic layer in open loop, (b) increment of the shear strain of viscoelastic layer due to the motion of the actuator and (c) decrease of total input power into the structure due to the forces applied by the actuator through the viscoelastic layer. Wang and Fang (2005) proposed spectral strip element method (SSEM) for FE model of beams integrated with ACLD layer and reported that the FE model provides accurate results even for less number of finite elements. Vasques et al. (2006) used the complex stiffness method to model the viscoelastic material and presented analytical as well as FE formulations for the vibration of beams consisting of elastic, viscoelastic and piezoelectric layers. Moita et al. (2011) proposed an efficient finite element for FE model of sandwich plates comprised of piezoelectric and viscoelastic layers. Datta and Ray (2016) presented an FE model of ACLD treatment for plates based on the fractional derivative model (FDM) of viscoelastic material.

1.4.1 *Literature on the ACLD treatment in different configurations*

In some studies on the ACLD treatment of structural vibration, the efficient utilization of the treatment using its minimum mass has been addressed. It physically arrives in the form of partial ACLD treatment. This partial ACLD treatment of flexible beams was introduced by Baz and Ro (1993). Subsequently, various studies on this topic arrived in the literature. Huang et al. (1996) presented optimal configurations of the partial ACLD and PCLD treatments. Ray and Baz (1997) carried out an optimization study to find the optimal size and

the optimal value of the velocity feedback control-gain for the partial ACLD treatment of plates with an objective of maximum active-passive damping. Ray and Reddy (2004) presented optimal control of cylindrical composite shells using ACLD patches. Li et al. (2008) found better damping performance of the ACLD treatment for beams by dividing the corresponding patch into two parts and placing them in an appropriate manner. Kumar and Singh (2009) performed a parametric study in order to find the optimal placement of ACLD and PCLD patches for vibration control of beams and found that damping can be enhanced considerably by proper choice of different parameters. Yuan et al. (2010) used ACLD treatment in the shape of the thin ring for control of vibration of cylindrical shells. They (Yuan et al., 2010) also subdivided the piezoelectric actuators in circumferential direction using the thin insulation layers. A similar work was carried out by Ni et al. (2013) where the effectiveness of the ACLD treatment at higher frequency-range of operation is discussed. Zheng et al. (2011) developed an FE model of the cylindrical shell structure integrated with the ACLD patches and discussed on the size and location of the patches for effective damping. Lu et al. (2017) presented the utility of the partial ACLD treatment for controlling the structural vibration in broad frequency-range of operation.

Apart from the partial ACLD treatment, it is utilized with other kinds of configurations mainly for its (ACLD) improved damping capacity along with compactness. Yellin and Shen (1996) proposed an ACLD configuration by the name of Self-sensing Active Constrained Layer (SACL) damping where the piezoelectric constraining layer acts in both the forms of sensor-layer and actuator-layer through the use of a bridge circuit. Lam et al. (1997) proposed two new configurations of hybrid damping treatment where the advantages of the piezoelectric (PZT) actuator and PCLD treatment are met. Lesieutre and Lee (1996) implemented the concept of the segmented constraining layer in the ACLD treatment for effective active-passive damping in long wavelength modes of vibration. Liao and Wang (1996) proposed a new configuration of ACLD treatment by the name of Enhanced Active Constrained Layer (EACL) damping treatment. The speciality of this design is the utilization of edge elements that significantly improve the active action of the piezoelectric constraining layer as well as the damping capacity of the treatment. This kind of ACLD treatment is subsequently studied by many researchers for further improvement of its

damping–capacity (Liao and Wang, 1997; Liu and Wang, 1998; Balamurugan and Narayanan, 2002; Gao and Liao, 2005). Liu and Wang (2000) introduced a Hybrid Constraining Layer (HCL) damping treatment using the concept of ACLD treatment. In this concept of HCL damping, passive and active materials are used together instead of pure piezoelectric material constraining layer for achieving improved damping characteristics of the ACLD treatment. The same authors (Liu and Wang, 2002) also integrated this concept of HCL damping treatment with the earlier concept of EACL damping treatment for attaining the advantages of both the treatments (EACL and HCL). Kumar et al. (2011) utilized a pre-stressed damping layer within the ACLD treatment and achieved enhanced damping-capacity of the treatment due to the initial stress within the constrained damping layer. The same authors (Kumar et al., 2011) also utilized the concept of stand-off-layer (Kumar et al., 2011a) and introduced a new configuration of ACLD treatment utilizing both the stand-off layer and edge anchors (Kumar, 2013). Plattenburg et al. (2015) presented a hybrid configuration of ACLD treatment where the constraining layers are comprised of both the active and passive patches. The different arrangements of the active-passive damping treatment along with the corresponding advantages and disadvantages are well summarized in (Benjeddou, 2001; Trindade and Benzeddou, 2002; Stanway et al., 2003). Recently, Koh (2016) carried out a comparison study on the damping capacities of ACLD treatment, Active-passive Constrained Layer Damping (APCLD) treatment, Active Control/Passive Constrained Layer Damping (AC/PCLD) treatment and Active Control/Passive Stand-Off Layer Damping (AC/PSOLD) treatment. It was observed from this study that the hybrid configurations like AC/PCLD and AC/PSOLD provide better damping treatment than that in the conventional ACLD treatment.

1.4.2 *ACLD treatment using piezoelectric composites*

In most of the studies on the ACLD treatment of structural vibration, the active constraining layer is made of monolithic piezoelectric materials. But, owing to several disadvantages in the structural use of monolithic piezoelectric actuators as mentioned in the earlier section, many researchers addressed the use of piezoelectric composites as the materials for the active constraining layer. Ray and Mallick, (2002) analyzed the performance of a piezoelectric fibre-reinforced composite (PFRC) in the ACLD treatment and found a better damping-capacity of the treatment for the use of the PFRC instead of the monolithic piezoelectric

materials. Ray and Reddy (2004a) investigated the active acoustic control of thin laminated composite plates using PFRC as the material for constraining layer in the ACLD treatment. The same authors (Ray and Reddy, 2005) also investigated the performance of PFRC patches as the constraining layers of ACLD treatment for active-passive damping of laminated composite shells. The performance of the vertically reinforced 1-3 PFRC layers as the active constraining layer of ACLD treatment was investigated by Ray and Pradhan (2006, 2007). Ray and Batra (2007) designed a nanotube-reinforced 1–3 piezoelectric composite (NRPEC) and investigated its performance for ACLD treatment of a laminated composite beam. The same authors (Ray and Batra, 2008) also studied the performance of the vertically/obliquely reinforced 1-3 PFRC in the ACLD treatment for suppression of vibration of functionally graded shells under the thermal environment. Panda and Ray (2009a, 2009b) presented the active control of geometrically nonlinear vibrations of functionally graded laminated composite plates using 1-3 PFRC in the ACLD treatment. Li and Narita (2013) presented the performance of PFRC material as the active constraining layer of ACLD treatment for cylindrical panels.

1.5 Research motivation and objectives

A literature review was performed with an objective of understanding the state-of-art research in the broad area of structural vibration control using viscoelastic materials. This literature survey reveals a substantial number of research reports on the passive damping of structural vibration using the viscoelastic materials in layer-form through the UCLD or CLD/PCLD arrangement. The CLD/PCLD treatment provides superior passive damping over that in the UCLD treatment (Kerwin, 1965). So, most of the available studies on the passive damping of structural vibration have been carried out using the CLD/PCLD arrangement. In these studies on the CLD treatment, the mathematical modelling and experimental verification of damping in the treatment have been addressed for different kinds of structures. Along with these theoretical and experimental studies, the research in the quest of improved damping capacity of the CLD treatment has also been reported using standoff/spacer layer (Whittier, 1959; Rogers and Parin, 1995; Masti and Sainsbury, 2005), segmented constraining layer (Plunkett and Lee, 1970), segmented damping layer (Trompette and Fatemi, 1997; Lepoittevin and Kress, 2010), multiple damping layers (Torvik and Strickland, 1972; Alam and Asnani,

1984a, 1984; Ramesh and Ganesan , 1993; Wan et al., 2016), partial PCLD (Nokes and Nelson, 1968; Wang and Chen, 2004; Zheng et al, 2005; Khalfi and Ross, 2016), closely spaced axial beams through VE layer (Lu et al., 1991), etc.

For further improvement of damping capacity of the CLD treatment, the concept of ACLD emerged (Baz and Ro, 1993). The damping in the ACLD treatment is indicatively higher than that in the CLD treatment (Baz and Ro, 1993), and thus exhaustive research on the ACLD treatment for various structures has been observed. Similar to the CLD treatment, several design modifications of the ACLD treatment have also been reported by many researchers, particularly for its (ACLD) improved damping capacity. In these design modifications, the popular ones are SACL damping (Yellin and Shen, 1996), segmented ACLD (Lesieutre and Lee, 1996), partial ACLD (Li et al., 2008; Yuan et al., 2010; Plattenburg et al., 2015), EACL damping (Liao and Wang, 1996; Kumar et al., 2011a), HCL damping (Liu and Wang, 2000), pre-compressed layer damping (Kumar et al., 2011) and ACLD with edge-anchors (Liao and Wang, 1997; Liu and Wang, 1998; Balamurugan and Narayanan, 2002). Through these studies, the CLD and ACLD treatments have gained the credential as the eminent means to exploit the damping properties of the viscoelastic materials in control of structural vibration. However, in all the available studies on the CLD and ACLD treatments, it is observed that the damping arises mainly due to the transverse shear strains of the constrained viscoelastic layer since the in-plane strains in the same damping layer appear with negligibly small magnitudes. If these in-plane strains appear with reasonable magnitudes along with the transverse shear strains within the constrained viscoelastic layer, then the damping capacity of the CLD/ACLD treatment is expected to improve. But, for this coincidental occurrence of transverse shear strains and in-plane strains with their reasonable magnitudes, it is required to distribute the stiffness and damping properties of the constrained layer in an appropriate manner. Although it is not an easy task, the foremost option is to tailor the properties of the constrained layer using the passive inserts in a predefined manner. It basically infers the design of viscoelastic composite (VEC) layer for the improved damping in the CLD and ACLD treatments. The research using such passive inserts within the viscoelastic layer of CLD or ACLD arrangement has not yet been reported in the literature. Thus, the main objective of this research is identified as the design of

VEC layers using the passive inserts for augmented CLD and ACLD treatments of basic structural elements like beams, plates and shells. These augmented CLD and ACLD treatments are aimed to arrive through the reasonable in-plane strains of the constrained damping layer along with its enhanced transverse shear strains.

In the application of CLD treatment for control of vibration of a structure within a range of operating frequency, generally, the modal damping does not appear in an adequate manner for all the modes of vibration within the frequency range. This discrepancy may be alleviated through the segmentation of constrained / constraining layer or CLD / PCLD layer in an appropriate manner (Plunkett and Lee, 1970; Lu et al., 1991; Zheng et al., 2005; Khalfi and Ross, 2016). However, a parallel strategy may be implemented without segmentation of the CLD treatment where it is required to distribute the stiffness and damping properties of the constrained layer in an optimal manner for the appearance of sufficient modal damping for any of the modes of vibration within a range of operating frequency. The research in this concern has not yet been reported in the literature. So, the second objective of the present research is identified as the design of a VEC layer in CLD treatment for improved modal damping according to a predefined relative importance of different modes of vibration within a frequency range of operation. Since the primary importance of damping is to reduce the amplitude of vibration at resonance, the relative importance of the modes of vibration would be based on the corresponding resonant amplitudes of vibration before the use of inclusions within the damping layer of CLD treatment.

In the ACLD treatment, the primary role of the piezoelectric constraining layer is to control the transverse shear deformation of the constrained viscoelastic layer for the effective active-passive damping of structural vibration. When this control of deformation is required to vary in space coordinates at any instant of time, the active constraining layer is to be segmented in the form of patches which act in different manners according to the requirement of varying control action in the space coordinates. This segmentation not only benefits the appropriate actuation of deformation of the constrained layer but also facilitates to overcome the discrepancy of poor flexibility and conformability of the piezoelectric actuator. However, with the advent of the flexible and conformable piezoelectric composites, the segmentation of the active constraining layer may

be avoided by the use of the patches of surface-electrodes. The variation of the control force in the space coordinates can then be achieved by supplying different electric fields through the patches of surface-electrodes according to the appropriate control strategy. The research in the line has not yet been addressed in the literature. So, another objective of this research is identified as the design of an ACLD treatment in layer-form using the patches of surface-electrodes for active-passive control of structural vibration within an operating frequency range.

In order to fulfil the aforesaid objectives in this research, the following theoretical studies have been carried out:

(a) Design of a 1-3 VEC layer for improved free/constrained layer damping treatment of beams.

(b) Active-passive damping treatment of beams using a new 1-3 VEC layer.

(c) Optimal passive damping in circular cylindrical sandwich shells with a three-layered VEC core.

(d) A design of ACLD treatment for vibration control of circular cylindrical shell structures using three-layered VEC.

(e) Augmented CLD treatment of plates through the optimal design of a new 0-3 VEC layer.

(f) Performance of a graphite wafer-reinforced viscoelastic composite layer for active-passive damping of plate vibration.

1.6 Contributions

The following contributions in the field of viscoelastic damping of structural vibration have been made towards the preparation of the dissertation.

1. A novel concept of 1-3 VEC layer is proposed for improved UCLD, PCLD and ACLD treatments of thin-walled flexible structures.

2. A novel concept of 0-3 VEC layer is proposed for improved PCLD and ACLD treatments of plates.

3. An optimal design of 1-3 VEC at the core of a circular cylindrical sandwich shell is presented for augmented passive damping of all the modes of vibration of the shell within an operating frequency range. This augmented damping over different modes of vibration can also be achieved as per the assigned relative importance of the modes.

4. A new design of ACLD treatment for circular cylindrical shell structures is presented using the 1-3 VEC layer, electrode-patches and velocity sensors. Through this design, it is possible to achieve augmented active-passive control of all the modes of vibration of the shell within an operating frequency-range of interest.

5. A strategy for the arrangement of electrode-patches over the surface of the piezoelectric constraining layer of the ACLD arrangement is proposed for effective active-passive control of all the modes of structural vibration.

6. The performance of the vertically reinforced 1-3 PFC actuator layer for active or active-passive control of circular cylindrical shells is presented using the electrode-patches over its (1-3 PFC) surfaces.

7. A geometrically nonlinear incremental thermo-visco-electro-elastic FE model of a circular cylindrical shell integrated with the actively constrained 1-3 VEC layer is developed for the analysis of its vibration characteristics under the thermal environment.

1.7 Organization of the thesis

A brief introduction of the viscoelastic materials, piezoelectric materials and piezoelectric composites is presented in Chapter 1. This is accompanied by a literature review on the uses of these materials for the UCLD, PCLD and ACLD treatments of structural vibration. On the basis of this literature review, the scope of the present research has been identified, and the objectives of the present thesis are outlined.

Chapter 2 deals with the design of a new 1-3 VEC layer for augmented UCLD and PCLD treatments of vibration of beam elements. The construction of the 1-3 VEC layer is first described, and then its arrangements for UCLD and

PCLD treatments of beams are demonstrated. Subsequently, an FE model of the beam is derived for identification of damping mechanisms and also for quantification of passive damping in the use of 1-3 VEC layer.

In Chapter 3, the new 1-3 VEC layer is utilized for ACLD treatment of vibration of beam elements. A similar analysis as done in Chapter 2 is carried out by deriving a closed-loop FE model of the beam. The results are illustrated mainly for substantiation of the utility of the new 1-3 VEC layer for augmented ACLD treatment of beams.

Next, in Chapter 4, the concept of 1-3 VEC layer is implemented for augmented passive damping of vibration of a circular cylindrical shell. A cylindrical sandwich shell is constructed with the core of three-layered VEC, and the passive damping within the shell is investigated through the development of an FE model based on the layer-wise shear deformation theory. The investigation is also extended in designing the three-layered VEC core for effective passive damping of all the modes of vibration of the sandwich shell.

Chapter 5 presents an ACLD arrangement for effective active-passive damping of several modes of vibration of a functionally graded circular cylindrical shell. The ACLD treatment is designed in the form of a layer over the outer surface of the substrate shell using the 1-3 VEC layer and the vertically reinforced 1-3 PFC layer with the printed patches of surface-electrodes. A closed-loop FE model of the overall shell is developed, and the active-passive damping in the overall shell is investigated with a special interest in controlling all the modes of vibration of the overall shell within a range of operating frequency.

In Chapter 6, a new 0-3 VEC layer is designed for augmented PCLD treatment of vibration of plates. The constructional features of the 0-3 VEC layer are first described, and then its performance in the PCLD treatment for plates is demonstrated by developing an FE model of the plates. The significant differences between the 1-3 VEC and the 0-3 VEC in their uses for PCLD treatment of plates are also presented.

The concept of 0-3 VEC layer is implemented for ACLD treatment of plates in Chapter 7. A closed-loop FE model of the plates is derived, and the active-passive damping characteristics of the treatment are investigated especially for the use of the new 0-3 VEC layer in the ACLD treatment.

Finally, the important conclusions from work carried out and the future scope of the present thesis work are outlined in Chapter 8. The list of references is provided at the end of the thesis.

Chapter 2

Design of a 1-3 VEC layer for improved free/constrained layer damping treatment of beams

2.1 Introduction

The literature survey in the previous chapter shows a substantial number of studies on the UCLD and PCLD treatments of thin-walled flexible structures. These studies reveal that the damping in the UCLD treatment mainly appears due to the extensional/compressional strain of the unconstrained viscoelastic layer, while the damping in the PCLD/CLD treatment arises due to the transverse shear strain of the constrained viscoelastic layer. No, if both the strains appear with reasonable magnitudes within the unconstrained /constrained viscoelastic layer, then the damping capacity of the UCLD/PCLD treatment may improve. But, it needs an appropriate distribution of stiffness and damping properties in the viscoelastic layer. Although it is not an easy task, the foremost option is to tailor the properties of the viscoelastic layer using the passive inserts within it (viscoelastic layer) in a predefined manner. It indicates the design of a viscoelastic composite layer for improved passive damping of UCLD/PCLD treatment of structural vibration. The research on the design of such a passive viscoelastic composite layer for improved UCLD/PCLD treatment of structural vibration has not yet been addressed in the literature. So, in this chapter (Kumar and Panda, 2016), a passive viscoelastic composite (VEC) layer is designed with an objective of simultaneous appearances of both the extensional and transverse shear strains within the VEC layer when it is used as a damping layer of UCLD/PCLD treatment. The prime intent of this study is to enhance the passive damping capacity of the UCLD/PCLD treatment through the use of presently designed VEC layer instead of the traditional monolithic viscoelastic material (VEM) layer.

In the following sections, first, the design of a 1-3 VEC layer is demonstrated. Next, its arrangement within the UCLD/PCLD treatment is presented considering a substrate beam. Subsequently, an FE model of the overall beam is derived for its static and dynamic flexure analyses. The static analysis examines the appearances of extensional and transverse shear strains within the presently designed VEC layer while it is used within the UCLD/PCLD

arrangement. The dynamic analysis substantiates the improvement in the damping capacities of both the UCLD and PCLD treatments due to the use of the present VEC layer instead of the traditional monolithic VEM layer. The dynamic analysis also addresses appropriate values of different geometrical parameters of 1-3 VEC layer for improved passive damping in the overall beam. It may be noted here that the notation 2-2 or 1-3 indicates the physical connectivity of the phase materials of a two-phase composite (Newnham, 1986), where the first number denotes the physical connectivity of the inclusion-phase (presently graphite) and the second number refers to the physical connectivity of the matrix phase (presently viscoelastic matrix).

2.2 Present VEC layer and its arrangements

In order to achieve both the extensional and transverse shear strains within the viscoelastic layer of UCLD/PCLD treatment, first a 2-2 viscoelastic composite (VEC) layer is designed as shown in Fig. 2.1(a). It (2-2 VEC) is made of graphite and viscoelastic constituent materials. All volumes for graphite-phase are considered to be identical in shape and size. These volumes are also uniformly spaced along the longitudinal (x) direction. Next, its (2-2 VEC) top and bottom surfaces are covered by two identical monolithic viscoelastic material (VEM) layers. The viscoelastic material is assumed to be perfectly bonded with the graphite-phase at all inter-phase surfaces. In order to achieve this, all three layers can be pressed into a single layer by the type of 1-3 VEC layer as shown in Fig. 2.1(b).

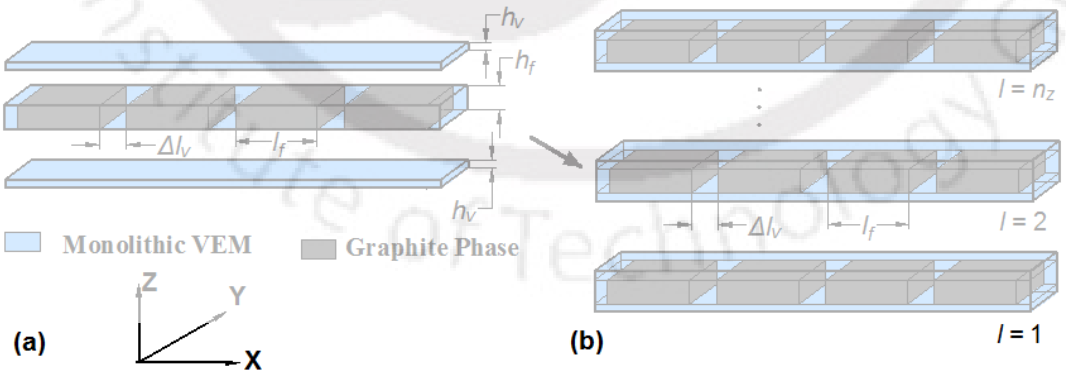

Fig. 2.1 Schematic diagrams of (a) 2-2 viscoelastic composite and pure VEM layers and (b) a number (n_z) of identical 1-3 viscoelastic composite (VEC) layers in the form of a laminate.

Figure 2.1(b) shows a number (n_z) of identical 1-3 VEC layers which can be staked into a 1-3 VEC laminate with uniform orientation of graphite phase-volumes. The geometrical properties of a 1-3 VEC layer are denoted by the parameters, h_v, h_f, Δl_v and l_f as shown in Fig. 2.1. Since the graphite-phase volumes are uniformly spaced in the longitudinal (x) direction, the number (n) of these volumes within certain length (L) can be computed by, $n = L/(l_f + \Delta l_v)$. The use of this 1-3 VEC layer/laminate as a damping layer of UCLD and PCLD arrangements is demonstrated in Figs. 2.2 and 2.3, respectively considering a substrate beam and one ($n_z = 1$) damping layer (1-3 VEC).

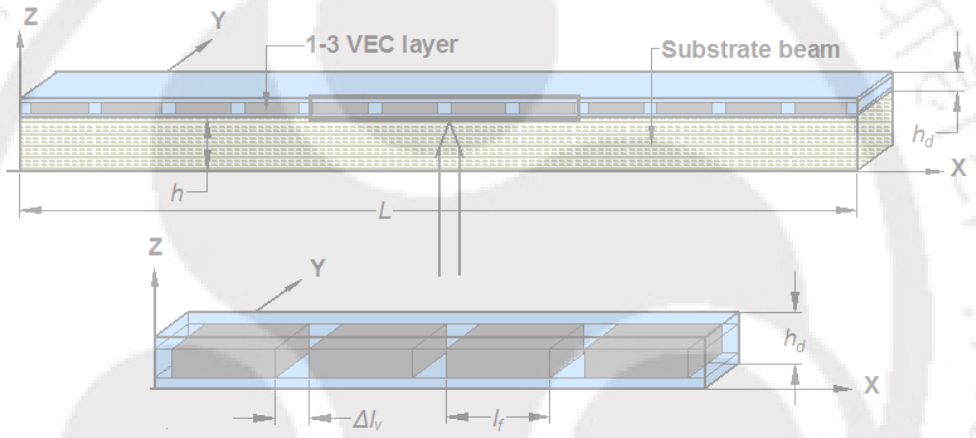

Fig. 2.2 Schematic diagram of a substrate beam integrated with a layer of UCLD treatment.

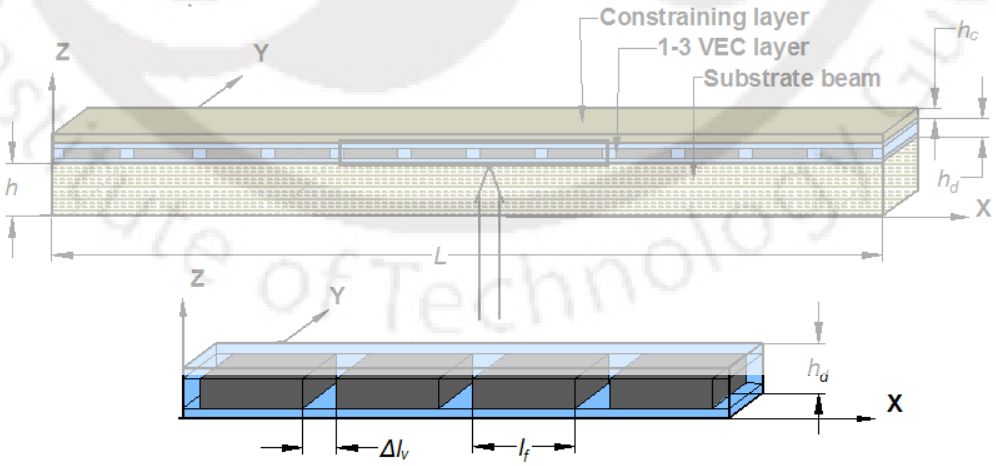

Fig. 2.3 Schematic diagram of a substrate beam integrated with a layer of PCLD treatment.

Basically, the damping layer in the conventional UCLD and PCLD arrangements is taken as the present 1-3 VEC layer instead of the traditional monolithic VEM layer. Under the bending deformation of the overall beam, the volume of viscoelastic material between two consecutive graphite-phase volumes of 2-2 VEC layer within the free (UCLD)/constrained (PCLD) 1-3 VEC layer is supposed to experience extensional deformation while the top/bottom VEM layer of the same VEC layer is supposed to undergo transverse shear deformation. So, both the extensional and transverse shear strains may appear simultaneously in a reasonable manner, and it may enhance the passive damping in the overall beam (Figs. 2.2 and 2.3). In order to substantiate this fact, the overall beam is analysed in the subsequent sections.

2.3 FE model of the overall beam

The geometrical and material properties of the overall beam (Figs. 2.2 and 2.3) do not vary along the transverse direction of xz-plane. The boundary conditions at the ends of the beam and the transverse mechanical load are also considered in the similar manner so that the three-dimensional beam can be represented at a plane in the form of a typical xz-plane. The overall beam is analysed considering such a typical xz-plane through a two-dimensional FE formulation. The state of strain and the state of stress at any point within a typical xz-plane of the beam (Figs. 2.2 and 2.3) can be written as,

$$\boldsymbol{\varepsilon}_e = \{\varepsilon_x \quad \varepsilon_z\}^{\mathrm{T}}, \quad \varepsilon_s = \gamma_{xz} \tag{2.1}$$

$$\boldsymbol{\sigma}_e = \{\sigma_x \quad \sigma_z\}^{\mathrm{T}}, \quad \sigma_s = \tau_{xz} \tag{2.2}$$

where, ε_x / σ_x and ε_z / σ_z are the normal strains/stresses along x and z directions, respectively; γ_{xz} / τ_{xz} is the shear strain/stress in the xz - plane. The subscripts e and s denote extensional and shear counterparts of the strain/stress vector, respectively. The linear strain displacement relations at any point within the overall beam can be written as,

$$\boldsymbol{\varepsilon}_e = \boldsymbol{L}_e \boldsymbol{d}, \ \varepsilon_s = \boldsymbol{L}_s \boldsymbol{d} \tag{2.3}$$

$$\boldsymbol{L}_e = \begin{bmatrix} \partial/\partial x & 0 \\ 0 & \partial/\partial z \end{bmatrix}, \ \boldsymbol{L}_s = \{\partial/\partial z \quad \partial/\partial x\}, \ \boldsymbol{d} = \{u \quad w\}^{\mathrm{T}} \tag{2.4}$$

where, u and w are the displacements along x and z directions at any point within the overall beam; $\boldsymbol{d}$ is a displacement vector. The constitutive relations for every phase-material within the overall beam can be written as,

$$\boldsymbol{\sigma}_e^k = \boldsymbol{C}_e^k \boldsymbol{\varepsilon}_e,\ \boldsymbol{\sigma}_s^k = \boldsymbol{C}_s^k \boldsymbol{\varepsilon}_s,\ k = 1,2,3,4. \tag{2.5}$$

where, the superscript k denotes substrate beam, viscoelastic phase, graphite phase and constraining layer as per its value as 1, 2, 3 and 4, respectively. It should be noted here that the viscoelastic material is modelled according to the complex stiffness method. So, the corresponding property matrices ($\boldsymbol{C}_e^k, \boldsymbol{C}_s^k$ for $k = 2$) are the complex stiffness matrices. The overall beam is considered to be subjected to a harmonic transverse mechanical load at the middle span ($x = L/2$) over its bottom surface ($z = 0$) such that the load is uniformly distributed with an intensity of p over the line (at middle span) is parallel to the y-axis. Accordingly, a typical xz-plane of the overall beam would be subjected to a harmonic transverse point-load (p) at its middle span ($x = L/2,\ z = 0$). Under this load on a typical xz-section, the principle of virtual work gives:

$$\delta T_P = \sum_{k=1}^{4} \left[\int_{A_k} \left\langle (\delta\boldsymbol{\varepsilon}_e)^{\mathrm{T}} \boldsymbol{\sigma}_e^k + (\delta\boldsymbol{\varepsilon}_s)^{\mathrm{T}} \boldsymbol{\sigma}_s^k \right\rangle dA_k \right] - (\delta w)\, p\big|_{\substack{x=L/2,\\ z=0}} \tag{2.6}$$

$$\delta T_K = \sum_{k=1}^{4} \left[\int_{A_k} \left(\{\delta\dot{u}\ \ \delta\dot{w}\}\, \rho^k\, \{\dot{u}\ \ \dot{w}\}^{\mathrm{T}} \right) dA_k \right] \tag{2.7}$$

where, δT_P and δT_K are the first variations of total potential energy and total kinetic energy respectively over the section of the beam at any instant of time (t), δ is the operator for first variation; ρ^k is the mass density for k^{th} material within the overall beam; A_k is the area of the k^{th} phase over a typical xz-plane of the overall beam. Substituting Eqs. (2.5), (2.3) and (2.4) in Eqs. (2.6) and (2.7), the following expressions for δT_P and δT_K can be obtained,

$$\delta T_P = \sum_{k=1}^{4} \left[\int_{A_k} (\delta\boldsymbol{d})^{\mathrm{T}} \left(\boldsymbol{L}_e^{\mathrm{T}} \boldsymbol{C}_e^k \boldsymbol{L}_e \boldsymbol{d} + \boldsymbol{L}_s^{\mathrm{T}} \boldsymbol{C}_s^k \boldsymbol{L}_s \boldsymbol{d} \right) dA_k \right] - (\delta w)\, p\big|_{\substack{x=L/2,\\ z=0}} \tag{2.8}$$

$$\delta T_K = \sum_{k=1}^{4} \left[\int_{A_k} \left\langle (\delta \dot{\boldsymbol{d}})^{\mathrm{T}} \rho^k \dot{\boldsymbol{d}} \right\rangle dA_k \right] \tag{2.9}$$

In order to derive the FE model, the sides of the rectangular domain of a typical xz-plane of the overall beam are divided in such a manner that the sides of every 9-node quadrilateral isoparametric element are in parallel to the axes (x and z) of the reference coordinate system. An element is considered to be made of the one of the phase materials. Figure 2.4 shows a similar FE mesh of a typical xz section of the beam along with a schematic diagram of 9-node quadrilateral isoparametric element.

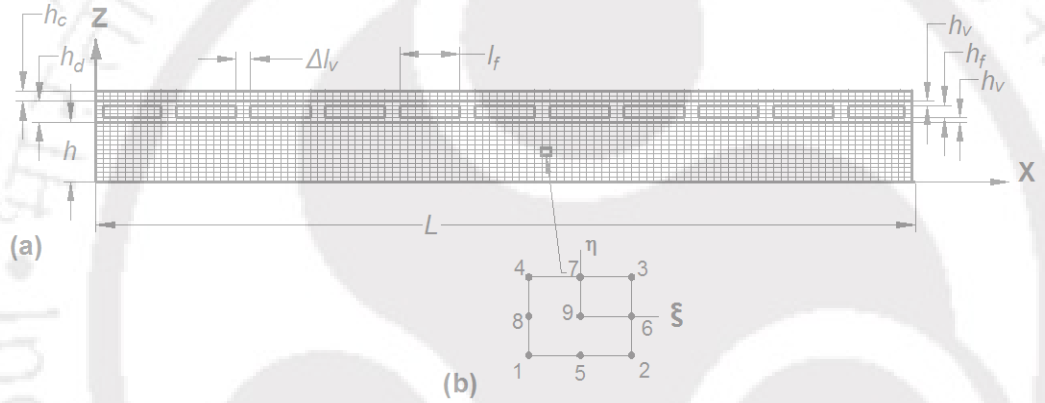

Fig. 2.4 (a) FE mesh of a typical xz - section of the beam with PCLD layer (b) a typical 9-node isoparametric element.

The displacement vector $(\boldsymbol{d})$ at a point within a typical element can be written as,

$$\boldsymbol{d} = \boldsymbol{N}\boldsymbol{d}^{\Delta} \tag{2.10}$$

where, $\boldsymbol{d}^{\Delta}$ is the elemental nodal displacement vector and $\boldsymbol{N}$ is the shape function matrix. The governing equations of motion of the overall beam are derived employing extended Hamilton's principle as,

$$\int_{t_1}^{t_2} \left(\delta T_K - \delta T_P \right) dt = 0 \tag{2.11}$$

Substituting Eqs. (2.8) and (2.9) in Eq. (2.11) and then using Eq. (2.10), the following simplified equations of motion for a typical element can be obtained,

$$\boldsymbol{M}^{\Delta}\ddot{\boldsymbol{d}}^{\Delta}+\left(\boldsymbol{K}_e^{\Delta}+\boldsymbol{K}_s^{\Delta}\right)\boldsymbol{d}^{\Delta}=\boldsymbol{P}^{\Delta}(t)$$

$$\boldsymbol{M}^{\Delta}=\int_{A_k^{\Delta}}\left(\boldsymbol{N}^{\mathrm{T}}\rho^{k}\boldsymbol{N}\right)dA_k^{\Delta},\ \boldsymbol{K}_e^{\Delta}=\int_{A_k^{\Delta}}\left(\boldsymbol{N}^{\mathrm{T}}\boldsymbol{L}_e{}^{\mathrm{T}}\boldsymbol{C}_e^{k}\boldsymbol{L}_e\boldsymbol{N}\right)dA_k^{\Delta},$$

$$\boldsymbol{K}_s^{\Delta}=\int_{A_k^{\Delta}}\left(\boldsymbol{N}^{\mathrm{T}}\boldsymbol{L}_s{}^{\mathrm{T}}\boldsymbol{C}_s^{k}\boldsymbol{L}_s\boldsymbol{N}\right)dA_k^{\Delta} \tag{2.12}$$

In Eq. (2.12), A_k^{Δ} is the elemental area within k^{th} material of an xz-plane of overall beam; $\boldsymbol{P}^{\Delta}(t)$ is the elemental mechanical load vector. Assembling the elemental equations of motion (Eq. (2.12)) for the whole domain of an xz-plane of overall beam, following global equations of motion can be obtained,

$$\boldsymbol{M}\ddot{\boldsymbol{X}}+\left(\boldsymbol{K}_e+\boldsymbol{K}_s\right)\boldsymbol{X}=\boldsymbol{P}(t),\ \ \boldsymbol{P}(t)=\boldsymbol{N}_p\,p(t) \tag{2.13}$$

where, $\boldsymbol{M}$ is the global mass matrix; $\boldsymbol{K}_e$ and $\boldsymbol{K}_s$ are the extensional and shear counterparts of the global stiffness matrix; $\boldsymbol{X}$ is the global nodal displacement vector; $\boldsymbol{P}(t)$ is the global mechanical load vector; $\boldsymbol{N}_p$ is a column matrix of the same size of $\boldsymbol{X}$, and it (N_p) represents the work-conjugate nodal transverse degree-of-freedom for the applied transverse point-load ($p(t)$). The transverse harmonic point-load is considered in the form of,

$$p(t)=p_0e^{j\omega t},\ \ j=\sqrt{-1} \tag{2.14}$$

where, p_0 is the amplitude of the mechanical excitation and ω is the angular frequency of operation. For the steady-state linear vibration of the overall beam, the nodal displacement vector$(\boldsymbol{X})$ can be written as (Meirovitch, 1997),

$$\boldsymbol{X}=\tilde{\boldsymbol{X}}e^{j\omega t},\ \ \tilde{\boldsymbol{X}}=\left(\boldsymbol{X}^{R}+j\boldsymbol{X}^{I}\right) \tag{2.15}$$

where, $\tilde{\boldsymbol{X}}$ is a complex nodal displacement vector and $\boldsymbol{X}^{R}/\boldsymbol{X}^{I}$ is its real/imaginary counterpart. Using Eq. (2.15) in Eq. (2.13), the following expression can be obtained,

$$\left[-\omega^{2}\boldsymbol{M}+\left(\boldsymbol{K}_e+\boldsymbol{K}_s\right)\right]\tilde{\boldsymbol{X}}=\boldsymbol{P}_0 \tag{2.16}$$

The solution of Eq. (2.16) provides complex nodal displacement vector ($\tilde{\boldsymbol{X}}$) and its absolute value is the nodal amplitude vector for the vibration of the overall beam.

2.4 Modal loss factor

The viscoelastic material is modelled using the complex stiffness method. So, the governing equations of motion (Eq. (2.13)) for free vibration of the overall beam can be written as,

$$\boldsymbol{M}\ddot{\boldsymbol{X}} + \left(\boldsymbol{K}^R + j\boldsymbol{K}^I\right)\boldsymbol{X} = 0$$

$$\boldsymbol{K}^R = \left(\boldsymbol{K}_e^R + \boldsymbol{K}_s^R\right),\ \boldsymbol{K}^I = \left(\boldsymbol{K}_e^I + \boldsymbol{K}_s^I\right) \tag{2.17}$$

In Eq. (2.17), superscripts R and I denote the real and the imaginary parts of the stiffness matrices ($\boldsymbol{K}_e$ and $\boldsymbol{K}_s$). According to the modal strain energy (MSE) method (Johnson and Kienholz, 1982), the natural frequency (ω_q) and loss factor (η_q) corresponding to q^{th} mode of vibration of the overall beam can be written as,

$$\omega_q^2 = (\boldsymbol{\varphi}_q^{\mathrm{T}}\boldsymbol{K}^R\boldsymbol{\varphi}_q)/(\boldsymbol{\varphi}_q^{\mathrm{T}}\boldsymbol{M}\boldsymbol{\varphi}_q) \tag{2.18}$$

$$\eta_q = (\boldsymbol{\varphi}_q^{\mathrm{T}}\boldsymbol{K}^I\boldsymbol{\varphi}_q)/(\boldsymbol{\varphi}_q^{\mathrm{T}}\boldsymbol{K}^R\boldsymbol{\varphi}_q) \tag{2.19}$$

where, $\boldsymbol{\varphi}_q$ is the nodal displacement vector for q^{th} mode-shape of the overall beam and it is basically an eigen vector of the following homogeneous equations of motion (Johnson and Kienholz, 1982),

$$\boldsymbol{M}\ddot{\boldsymbol{X}} + \boldsymbol{K}^R\boldsymbol{X} = 0 \tag{2.20}$$

The loss factor (η_q) for q^{th} mode of vibration is commonly called as the modal loss factor. Using Eq. (2.17) in Eq. (2.19), the modal loss factor (η_q) can be partitioned as,

$$\eta_q = \eta_q^e + \eta_q^s$$

$$\eta_q^e = (\boldsymbol{\varphi}_q^{\mathrm{T}}\boldsymbol{K}_e^I\boldsymbol{\varphi}_q)/(\boldsymbol{\varphi}_q^{\mathrm{T}}\boldsymbol{K}^R\boldsymbol{\varphi}_q)\ ,\ \eta_q^s = (\boldsymbol{\varphi}_q^{\mathrm{T}}\boldsymbol{K}_s^I\boldsymbol{\varphi}_q)/(\boldsymbol{\varphi}_q^{\mathrm{T}}\boldsymbol{K}^R\boldsymbol{\varphi}_q) \tag{2.21}$$

In Eq. (2.21), η_q^e and η_q^s appear due to the extensional and shear counterparts of the imaginary counterpart ($\boldsymbol{K}^I$) of the stiffness matrix. So, the quantities η_q^e

and η_q^s signify the loss/dissipation of energy due to extensional and transverse shear deformations of the damping layer, respectively for the q^{th} mode of vibration.

2.5 Results and discussions

In this section, first the extensional and transverse shear deformations of the presently designed 1-3 VEC layer are characterized through a bending analysis of the overall beam. This static analysis reveals the mechanisms of damping for the use of free/constrained 1-3 VEC layer. Next, a numerical analysis of modal loss factor of the overall beam is carried out for deciding appropriate geometrical configuration of the 1-3 VEC layer in order to achieve improved passive damping in the overall beam. Finally, the utility of the present VEC layer in the UCLD and PCLD treatments is substantiated through the evaluation of frequency responses of the overall beam under a steady state mechanical excitation. All these numerical studies are carried out by means of writing an FE code in the MATLAB software package corresponding to the aforesaid FE model of the overall beam.

The geometrical properties of the substrate beam (Figs. 2.2 and 2.3) are considered as, $L = 200$ mm, $h = 5$ mm. The ends ($x = 0, L$) of the substrate beam are considered to be constrained by either of the three kinds of boundary conditions namely clamped boundary conditions ($u|_{x=0} = 0$, $u|_{x=L} = 0$, $w|_{x=0} = 0$, $w|_{x=L} = 0$), clamped-free boundary conditions ($u|_{x=0} = 0$, $w|_{x=0} = 0$) and simply-supported boundary conditions ($w|_{x=0} = 0$, $w|_{x=L} = 0$, $u|_{x=0} = 0$). Unless otherwise mentioned, the ends of the substrate beam are constrained by clamped boundary conditions. The material for the substrate beam is considered as a unidirectional fiber-reinforced composite material having the properties of, E_L = 43.3 GPa, $E_T = 14.9$ GPa, $G_{LT} = 4.4$ GPa, $\nu_{LT} = 0.3$, $\rho = 1980$ kg/m^3, where the subscripts L and T signify the x- and z- directions, respectively. The material properties of the graphite in the VEC layer are, $E = 250$ GPa, $\nu = 0.3$, $\rho = 1400$ kg/m^3 (Jones, 1999), while the material for viscoelastic-phase is taken as Butyl Rubber (Jones, 2001). Generally, the material properties of this viscoelastic material vary with temperature and frequency. The present analysis is carried out within a narrow range of operating frequency (600-1000 Hz) around the

fundamental frequency of the beam at room temperature (35^{o} C). It is observed that the properties of the VEM (Butyl Rubber) insignificantly vary within this narrow range of frequency. So, for the sake of simplicity, average properties of the VEM over this narrow range of operating frequency are considered in evaluation of present numerical results which are, $E=20(1+0.9j)$ MPa, $\nu=0.49$, $\rho=920$ kg/m^3. In most of the available studies on the PCLD treatment of structural vibration, the material for the constraining layer is taken either as Steel ($E=$ 200 GPa, $\nu=0.3$, $\rho=7860$ kg/m^3) (Alvelid and Enelund, 2007; Martinez-Agirre and Elejabarrieta, 2010; Kumar et al, 2012) or as Aluminum ($E=$ 70 GPa, $\nu=0.3$, $\rho=2700$ Kg/m^3) (Xie and Shepard, 2009; Granger and Ross, 2009; Lepoittevin and Kress, 2010; Sher and Moreira, 2013). Presently, Steel is taken as the material for the constraining layer in the PCLD treatment and its thickness is considered as 0.5 mm.

In order to achieve sufficient numerical accuracy in the present FE results, a convergence study of the FE model is carried out considering the case of constrained 1-3 VEC layer. The FE mesh of a typical xz-plane of the overall beam (Fig. 2.3) is created by dividing its horizontal and vertical edges so that all elements are rectangular. The sides of every rectangular element are parallel to the reference coordinate (x and z) axes. With this kind of FE mesh, the fundamental frequency, modal loss factor and resonant-amplitude of the overall beam are computed for increasing number of (FE) elements. These results are illustrated in Table 2.1

Table 2.1 Convergence study for the present FE model of the overall beam.

$N_x \times N_z$	N_e	ω_0	η_{ω_0}	w/h
26 x 7	182	4584	0.288987	0.022210
46 x 9	414	4572	0.290928	0.022198
106 x 16	1696	4564	0.291224	0.022263
206 x 16	3296	4562	0.291215	0.022283
406 x 16	6496	4561	0.291227	0.022288
406 x 29	11774	4561	0.291229	0.022290
806 x 29	23374	4561	0.291230	0.022291

where, N_x and N_z are number of elements along x and z directions respectively; N_e is the total no of elements; ω_0 is the fundamental natural frequency (rad/s), η_{ω_0} is the modal loss factor at the fundamental mode, and

w/h is the dimensionless amplitude at the middle span $(L/2,0)$ of the beam for its vibration with fundamental natural frequency (ω_0).

Following this FE mesh convergence study, the number of elements in the FE model of the overall beam is chosen for computation of the following numerical results.

In order to verify the present FE formulation for the overall beam, its fundamental frequency and modal loss factor are computed considering unconstrained/constrained monolithic viscoelastic damping layer. These results are illustrated in Table 2.2 together with the similar results available in (Roy and Ganesan, 1996) and (Lall et al., 1988). It may be observed from this table that the present results are in good agreement with the earlier results (Roy and Ganesan, 1996; Lall et al., 1988) and this comparison verifies the present FE formulation.

Table 2.2 Verification of the present FE model of the substrate beam integrated with an unconstrained/constrained viscoelastic layer.

Parameters	UCLD		PCLD	
	Ref. (Roy and Ganesan, 1996)	Present FE results	Ref. (Lall et al., 1988)	Present FE results
ω_0	2891	2891.2	740.5	739.7
η	0.0024	0.0023	0.00448	0.00450

2.5.1 Analysis of strain

The characteristics of the extensional and the transverse shear strains within the unconstrained 1-3 VEC layer are interpreted through a bending analysis of the overall beam. This analysis is carried out considering both the 1-3 VEC and pure VEM layers separately as shown in Figs. 2.5(a) and 2.5(b), respectively. In these figures, the dimensions of the overall beam are considered as, L = 200 mm, h = 5 mm, h_f = 1 mm, h_v = 1 mm, l_f = 30 mm, h_d = 3 mm, Δl_v = 36 mm. The 1-3 VEC layer is considered to be comprised of two graphite-phase volumes and the overall beam is subjected to transverse load at its middle span. For unconstrained 1-3 VEC layer (Fig. 2.5(a)), Figs. 2.5(c) and 2.5(e) illustrate the distributions of the extensional (ε_x) and the transverse shear (γ_{xz}) strains, respectively over the xz-plane of the overall beam. Similar distributions of the

strains (ε_x and γ_{xz}) in case of the unconstrained pure VEM layer (Fig. 2.5(b)) are also presented in Figs. 2.5(d) and 2.5(f).

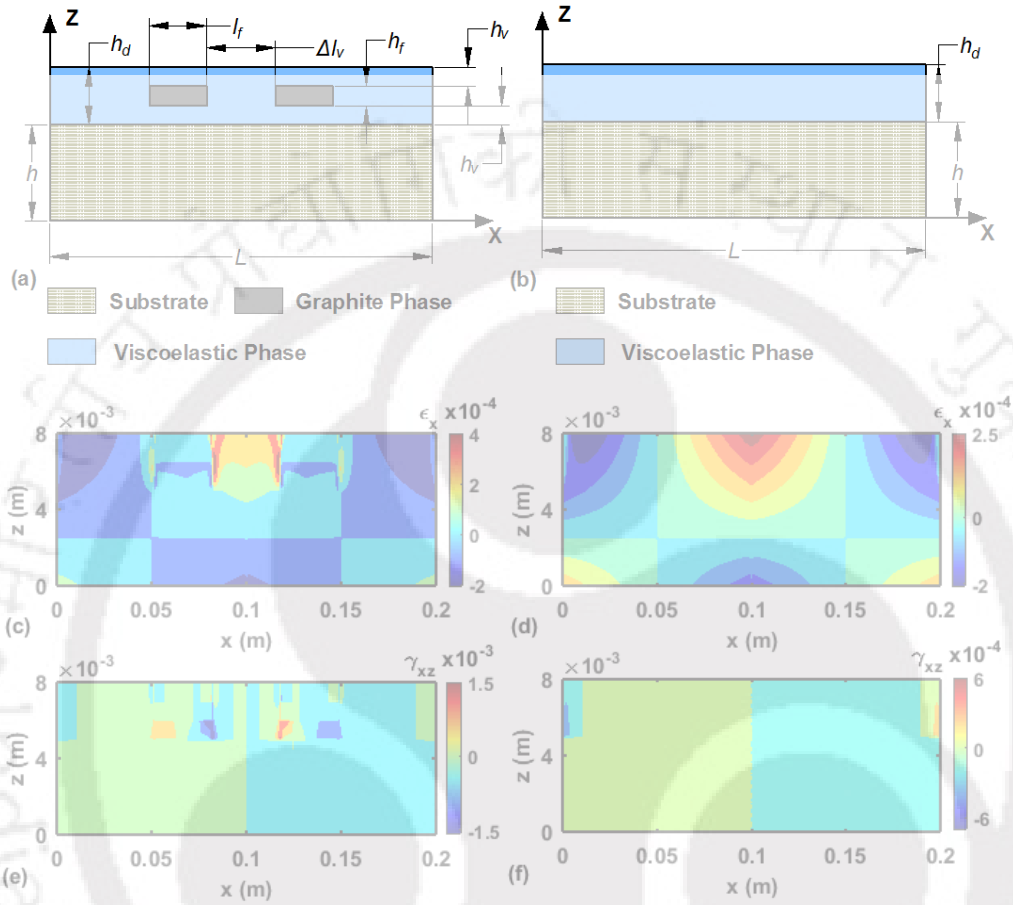

Fig. 2.5 Schematic diagram of a typical XZ-plane of the overall beam with unconstrained (a) 1-3 VEC layer or (b) pure VEM layer; distribution of extensional strain (ε_x) over the XZ-plane for unconstrained (c) 1-3 VEC layer or (d) pure VEM layer; distribution of shear strain (γ_{xz}) over the XZ-plane for unconstrained (e) 1-3 VEC layer or (f) pure VEM layer.

It may be observed from these figures (Figs. 2.5(a)-(f)) that the pure VEM layer is mainly subjected to extensional strain (Figs. 2.5(d) and 2.5(f)). But, it is possible to achieve transverse shear strain with reasonable magnitude along with the extensional strain within the unconstrained damping layer by introducing the graphite inclusions (Figs. 2.5(c) and 2.5(e)). The extensional strain in the 1-3 VEC layer appears between two consecutive graphite-phase volumes along x-direction while the transverse shear strain in the same layer mainly arises between the graphite-phase volumes and substrate beam. It may also be observed from Figs. 2.5(c)-(f) that the maximum values of ε_x and γ_{xz}

significantly increase due to the inclusion of graphite-phase volumes within the free/unconstrained viscoelastic layer. In case of a linear viscoelastic system, it is known that the cyclic dissipated energy is proportional to the cyclic stored energy (Ungar and Kerwin, 1962). So, the aforesaid increased magnitudes of strains due to the use of the 1-3 VEC layer may lead to the improvement in the dissipated energy by means of the increase of stored energy. However, this initial estimation is verified in the next section through the computation of modal loss factors.

In the cases of constrained damping layers (Figs. 2.6(a)-(b)), the distributions of extensional (ε_x) and shear (γ_{xz}) strains are illustrated in Figs. 2.6(c)-(f).

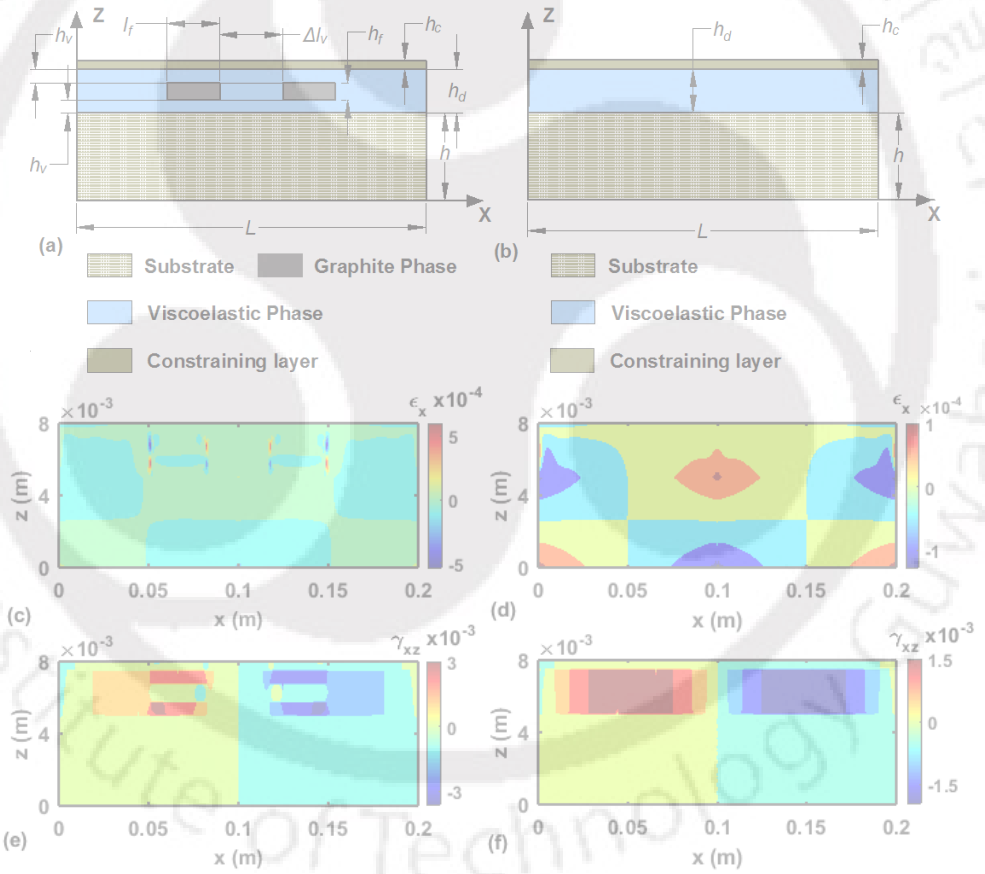

Fig. 2.6 Schematic diagram of a typical XZ-plane of the overall beam with constrained (a) 1-3 VEC layer or (b) pure VEM layer; distribution of extensional strain (ε_x) over the XZ-plane for constrained (c) 1-3 VEC layer or (d) pure VEM layer, distribution of shear strain (γ_{xz}) over the XZ-plane for constrained (e) 1-3 VEC layer or (f) pure VEM layer.

The dimensions of the overall beam are considered as, L = 200 mm, h = 5 mm, h_d = 2.5 mm, h_c = 0.5 mm, h_f = 0.5 mm, h_v = 1 mm, l_f = 30 mm, Δl_v = 36 mm. It may be observed from Figs. 2.6(d) and 2.6(f) that the pure VEM layer is mainly subjected to transverse shear strain while the extensional strain appears with very low magnitude. The magnitudes of these strains (ε_x, γ_{xz}) can be increased by the use of 1-3 VEC layer instead of the pure VEM layer (Figs. 2.6(c) and 2.6(e)). In this use, one zone of shear strain (Fig. 2.6(f)) is divided into two zones (Fig. 2.6(e)) along with its (γ_{xz}) improved magnitude. Also, the magnitude of the extensional strain (ε_x) increases (Figs. 2.6(c)-(d)).

These improvements in the magnitudes of the extensional and transverse shear strains imply improved energy dissipation from the overall beam during its vibration and it is verified in the subsequent sections through the dynamic analysis of the overall beam (Figs. 2.2 and 2.3).

2.5.2 Analysis of modal loss factor

The passive damping characteristics of the overall beam are studied in this section through the computation of modal loss factor. Basically, the influences of different geometric parameters in the design of 1-3 VEC layer (Fig. 2.1) on the damping characteristics of the overall beam are studied for selecting their (geometrical parameters) appropriate values. First, the case of unconstrained 1-3 VEC layer is studied (Fig. 2.2). Next, similar study is carried out for the constrained 1-3 VEC layer (Fig. 2.3).

2.5.2.1 Unconstrained 1-3 VEC layer (UCLD treatment)

The thickness (h_d) of the 1-3 VEC layer is considered either as 1.5 mm or as 3 mm. For every value of h_d, the thickness (h_v) of two pure VEM layers within the 1-3 VEC layer is varied and the corresponding variation of modal loss factor (η_q, $q=1$) is presented in Table 2.3. The variations of extensional (η_q^e) and shear (η_q^s) counterparts (Eq. (2.21)) of modal loss factor (η_q) are also illustrated in the same table (Table 2.3). It should be noted that the increase/decrease in the value of h_v causes the decrease/increase in the thickness (h_f) of intermediate 2-2 VEC layer since the total thickness (h_d) is kept at a constant value. For any

value of h_d, it may be observed from Table 2.3 that η_q^e decreases and η_q^s increases due to the increase of h_v. It may also be observed that the total loss factor (η_q) at a higher value of h_v arises mainly due to the transverse shear strain (γ_{xz}) of 1-3 VEC layer. At lower value of h_v, the loss factor (η_q) appears mainly due to the extensional strain (ε_x) of 1-3 VEC layer. So, the contributions of both the strains (ε_x, γ_{xz}) to the total damping (η_q) of the viscoelastic system depend on the thicknesses of the pure VEM and 2-2 VEC layers within the 1-3 VEC layer. From Table 2.3, an appropriate value of h_v for improved magnitude of loss factor (η_q) can be chosen between 0.05 mm and 0.15 mm in view of small rate of variation of η_q within these limits. Following the same, the value of h_v is taken as 0.1 mm for the subsequent results for UCLD treatment of beams.

Table 2.3 Variations of modal loss factor (η_q at the fundamental bending mode) and its counterparts (η_q^e, η_q^s) with the thickness (h_v) of pure VEM layers in the unconstrained 1-3 VEC layer ($\Delta l_v = 0.1$ mm, $h_v = 0.1$ mm, $n = 8$, $n_z = 1$, $L = 200$ mm, $h = 5$ mm**).**

1-3 VEC layer (UCLD treatment)						
h_v (mm)	h_d = 1.5 mm			h_d = 3.0 mm		
	η_q	η_q^e	η_q^s	η_q	η_q^e	η_q^s
0. 05	0.222	0.141	0.081	0.318	0.199	0.118
0. 10	0.217	0.118	0.099	0.327	0.161	0.165
0. 15	0.206	0.100	0.106	0.325	0.136	0.189
0. 20	0.194	0.086	0.108	0.318	0.118	0.200
0. 25	0.181	0.076	0.106	0.309	0.104	0.204
0. 30	0.168	0.067	0.101	0.299	0.094	0.205

It is evident from Table 2.3 and Fig. 2.5(c) that the extensional strain in the 1-3 VEC layer mainly appears at the horizontal (x-direction) gap (Δl_v) between two consecutive graphite-phase volumes. So, there may be certain effect of this dimension (Δl_v) on the modal loss factor (η_q) and it is studied considering a value of h_v as 0.1 mm.

Table 2.4 illustrates the variations of η_q at the fundamental bending mode and its two counterparts (η_q^e and η_q^s) with Δl_v for two different values of the thickness (h_d) of 1-3 VEC layer. It may be observed from Table 2.4 that the extensional counterpart of the loss factor (η_q^e) increases and shear counterpart of the loss factor (η_q^s) decreases with the increase of the gap (Δl_v). As a result, the total loss factor (η_q) first increases and then decreases after certain value of Δl_v. Since this optimal value of Δl_v insignificantly varies due to the change in the thickness (h_d) of 1-3 VEC layer (Table 2.4), a constant value of Δl_v can be chosen for all values of h_d which yields a value of η_q around its maximum value. In the present results, a value of Δl_v is taken as 0.1 mm (Table 2.4) for any value of the thickness (h_d) of 1-3 VEC layer.

Table 2.4 Variations of modal loss factor (η_q at the fundamental bending mode) and its counterparts (η_q^e, η_q^s) with the gap (Δl_v) between two consecutive graphite-phase volumes of unconstrained 1-3 VEC layer (h_v = 0.1 mm, n = 8, n_z = 1, L = 200 mm, h = 5 mm).

Δl_v (mm)	1-3 VEC layer (UCLD treatment)					
	h_d = 1.5 mm			h_d = 3.0 mm		
	η_q	η_q^e	η_q^s	η_q	η_q^e	η_q^s
0.025	0.210	0.053	0.157	0.301	0.061	0.240
0.050	0.223	0.100	0.122	0.325	0.120	0.204
0.075	0.222	0.114	0.108	0.328	0.145	0.183
0.100	0.217	0.118	0.099	0.327	0.161	0.165
0.125	0.210	0.117	0.093	0.323	0.171	0.152
0.150	0.202	0.114	0.088	0.317	0.177	0.140

The aforesaid results (Table 2.3 and Table 2.4) are evaluated considering eight graphite-phase volumes (n = 8) in 1-3 VEC layer. The variation of the number of graphite-phase volumes would have certain effect on the passive damping-capability of the 1-3 VEC layer. In order to verify this, the number of graphite-phase volumes in the 1-3 VEC layer is increased without alteration of its length (L) while the aforesaid values of h_v and Δl_v are maintained. The

corresponding results are furnished in Table 2.5 that shows that η_q^e increases and η_q^s decreases with the increasing number (n) of graphite-phase volumes. For $h_d = 1.5$ mm, the rate of increase of η_q^e is close to the rate of decrease of η_q^s. As a result, the total loss factor (η_q) does not vary indicatively. But the same does not occur for a higher thickness ($h_d = 3$ mm) of the VEC layer. In this case ($h_d = 3$ mm), the total loss factor (η_q) increases indicatively with increasing number of graphite-phase volumes. So, for the aforesaid values of h_v and Δl_v, the number of graphite-phase volumes within the 1-3 VEC layer may be increased as per the practical requirement in fabrication of the composite (VEC) layer.

Table 2.5 Variations of modal loss factor (η_q at fundamental bending mode) and its counterparts (η_q^e, η_q^s) with the number (n) of graphite-phase volumes in unconstrained 1-3 VEC layer (h_v = 0.1 mm, $\Delta l_v = 0.1$ mm, $n_z = 1$, L = 200 mm, h = 5 mm).

	1-3 VEC layer (UCLD treatment)					
n	$h_d = 1.5$ mm			$h_d = 3.0$ mm		
	η_q	η_q^e	η_q^s	η_q	η_q^e	η_q^s
2	0.213	0.054	0.159	0.263	0.049	0.214
3	0.221	0.080	0.141	0.299	0.080	0.219
4	0.222	0.095	0.126	0.311	0.103	0.208
5	0.221	0.106	0.116	0.317	0.123	0.195
10	0.213	0.119	0.094	0.329	0.177	0.153
15	0.208	0.121	0.087	0.341	0.201	0.139

Table 2.6 Variations of modal loss factor (η_q at fundamental bending mode) and its counterparts (η_q^e, η_q^s) with the number (n_z) of 1-3 VEC layers within a specified thickness (h_d) of unconstrained damping layer (h_v = 0.1 mm, Δl_v = 0.1mm, n = 8, L = 200 mm, h = 5 mm).

	1-3 VEC layer (UCLD treatment)						
	h_d = 1.5 mm				h_d = 3.0 mm		
n_z	η_q	η_q^e	η_q^s	n_z	η_q	η_q^e	η_q^s
1	0.217	0.118	0.099	1	0.327	0.161	0.165
2	0.200	0.089	0.111	5	0.279	0.068	0.211

Table 2.6 illustrates the magnitude of modal loss factor (η_q) when several 1-3 VEC layers are used in the form of a laminate (Fig. 2.1(b)) within certain thickness (h_d) for the damping layer. The results in this table (Table 2.6) show that the total loss factor (η_q) decreases as the number of 1-3 VEC layers increases within a specified thickness (h_d) of damping layer.

Table 2.7 illustrates the variations of modal loss factor η_q and its counterparts (η_q^e and η_q^s) for different boundary conditions at the ends of the substrate beam. It may be observed from this table that the loss factor and its counterparts significantly depend on the boundary conditions at the ends of the substrate beam. The unconstrained 1-3 VEC layer exhibits its maximum damping–capacity for the simply-supported boundary conditions among the three kinds of boundary conditions at the edges of the substrate beam. It may also be observed from Table 2.7 that the thickness of the unconstrained 1-3 VEC layer does not have much effect on its (VEC layer) damping-capacity when the ends of the substrate beam are supported by clamped-free boundary conditions.

Table 2.7 Modal loss factor (η_q at fundamental bending mode) and its counterparts (η_q^e, η_q^s) for different boundary conditions at the edges of the substrate beam (h_v = 0.1 mm, Δl_v = 0.1 mm, n = 8, n_z = 1, L = 200 mm, h = 5 mm).

Boundary condition	1-3 VEC layer (UCLD treatment)					
	h_d = 1.5 mm			h_d = 3 mm		
	η_q	η_q^e	η_q^s	η_q	η_q^e	η_q^s
Clamped-clamped	0.217	0.118	0.099	0.327	0.162	0.165
Simply-supported	0.312	0.192	0.120	0.360	0.188	0.172
Clamped-free	0.169	0.075	0.094	0.167	0.068	0.099

If the traditional pure VEM layer is used instead of the 1-3 VEC layer, then the damping characteristics of the overall beam is illustrated in Table 2.8 through the variation of modal loss factor (η_q) with the thickness of the pure VEM layer. Table 2.8 shows that the damping (η_q) in the overall beam arises mainly due to the extensional strain of the unconstrained pure VEM layer. Table

2.8 also shows that the passive damping in the overall beam increases with the increasing thickness of the pure VEM layer. However, for a specified thickness of the unconstrained damping layer (say, h_d = 3 mm), it may be observed from Table 2.8 and Table 2.3/2.4/2.5/2.6 that the passive damping in the overall beam significantly increases when 1-3 VEC layer is used instead of the conventional pure VEM layer.

Table 2.8 Variations of modal loss factor (η_q at fundamental bending mode) and its counterparts (η_q^e, η_q^s) with the thickness (h_d) of unconstrained pure VEM layer (L = 200 mm, h = 5 mm).

Pure VEM layer (UCLD Treatment)			
h_d (mm)	η_q	η_q^e	η_q^s
1.0	0.0007	0.0007	1.69e-05
1.5	0.0012	0.0012	4.17e-05
2.0	0.0018	0.0018	8.17e-05
2.5	0.0026	0.0025	14.4 e-05
3.0	0.0035	0.0033	22.8 e-05

This estimated difference in the uses of pure VEM layer and 1-3 VEC layer for UCLD treatment of beams is further substantiated through the numerical evaluation of frequency responses of the beam integrated either with the pure VEM layer or with the 1-3 VEC layer. These frequency responses are illustrated in Fig. 2.7 considering two different values of thickness of the damping layer (h_d = 1.5 mm and 3 mm). First the damping layer is considered to be made of pure VEM and the corresponding frequency response of the overall beam is evaluated. Then the 2-2 VEC layer is introduced within the same thickness (h_d) according to the present design of 1-3 VEC layer and the frequency responses are evaluated for different values of thickness (h_f) of 2-2 VEC layer. It may be observed from (Fig. 2.7) that the passive damping in the overall beam significantly increases if the pure VEM layer is substituted by the 1-3 VEC layer with identical thickness (h_d). This improved passive damping induced by the 1-3 VEC layer can further be increased by increasing the thickness (h_f) of its (VEC) 2-2 VEC layer. However, the results in Fig. 2.7 suggest 1-3 VEC layer instead of pure VEM layer for UCLD treatment of

structural vibration. In this use of 1-3 VEC layer, its appropriate geometric properties (as mentioned above) are to be maintained, and these properties can also be decided through an optimization algorithm.

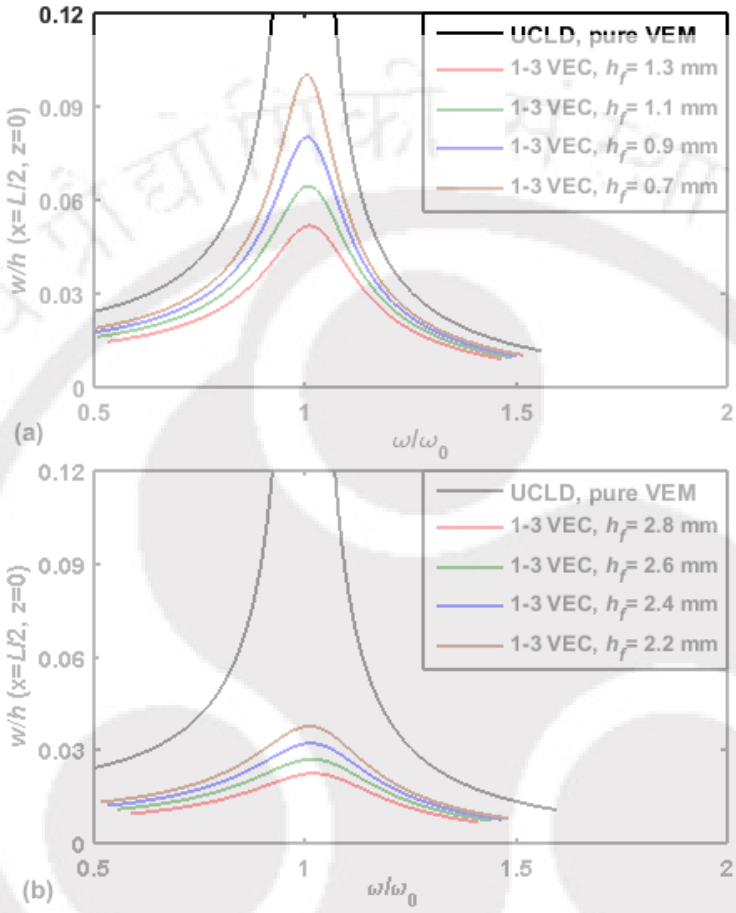

Fig. 2.7 Frequency responses of the substrate beam integrated either with pure VEM layer or with 1-3 VEC layer ((a) h_d = 1.5 mm, **(b)** h_d = 3.0 mm; p = 1000 N, Δl_v = 0.1 mm, n = 8, n_z = 1, L = 200 mm, h = 5 mm**).**

2.5.2.2 Constrained 1-3 VEC layer (PCLD treatment)

For the use of the 1-3 VEC layer as a constrained damping layer in PCLD treatment, the damping characteristics of the overall beam (Fig. 2.3) are studied in a similar manner as it is performed in the previous case of UCLD treatment. Table 2.9 illustrates the effect of the thickness (h_v) of two pure viscoelastic layers within the constrained 1-3 VEC layer (Fig. 2.1(a)) on the modal loss factor (η_q). Two different values of the thickness (h_d) of the constrained damping layer are considered for the numerical results. For the increasing thickness (h_v) of

pure VEM layers in 1-3 VEC layer, it may be observed from Table 2.9 that the shear counterpart (η_q^s) of modal loss factor first increases and then decreases while the extension counterpart (η_q^e) of the same decreases. As a result, the total loss factor (η_q) has its maximum value at certain thickness (h_v) of the VEM layers.

Table 2.9 Variations of modal loss factor (η_q at the fundamental bending mode) and its counterparts (η_q^e, η_q^s) with the thickness (h_v) of pure VEM layers within constrained 1-3 VEC layer ($\Delta l_v = 0.1$ mm, $n = 8$, $n_z = 1$, $L = 200$ mm, $h = 5$ mm).

	1-3 VEC layer (PCLD treatment)					
	h_d = 1.0 mm			h_d = 2.5 mm		
h_v (mm)	η_q	η_q^e	η_q^s	η_q	η_q^e	η_q^s
0.05	0.171	0.043	0.128	0.246	0.055	0.190
0.10	0.198	0.033	0.165	0.293	0.042	0.251
0.15	0.203	0.025	0.178	0.309	0.034	0.275
0.20	0.199	0.020	0.179	0.311	0.028	0.283
0.25	0.191	0.016	0.176	0.307	0.024	0.283
0.30	0.182	0.012	0.169	0.300	0.021	0.279

For the present configuration of the overall beam, this optimal value for the thickness (h_v) may be chosen between 0.10 mm and 0.20 mm (Table 2.9). According to this assessment, a particular value of h_v as 0.1 mm is selected at present while the effect of the gap (Δl_v) on the modal loss factor (η_q) is demonstrated in Table 2.10.

It may be observed from Table 2.10 that the increase in the value of Δl_v causes the decrease of the dissipated energy due to shear strain and also the increase of the same due to the extensional strain. Although the corresponding variations of η_q^s and η_q^e do not have much effect on the total loss factor (η_q), but it (η_q) has its maximum value at certain value of the gap (Δl_v). In the present case, an appropriate value for the gap (Δl_v) lies between 0.025 mm and 0.1 mm (Table 2.10). So, for evaluation of further numerical results for PCLD treatment

of beam, a value for the gap (Δl_v) is chosen as 0.1 mm in combination with a value of h_v as 0.1 mm.

Table 2.10 Variations of modal loss factor (η_q at the fundamental bending mode) and its counterparts (η_q^e, η_q^s) with the gap (Δl_v) between two consecutive graphite-phase volumes of the constrained 1-3 VEC layer (h_v = 0.1 mm, n = 8, n_z = 1, L = 200 mm, h = 5 mm).

1-3 VEC layer (PCLD treatment)						
Δl_v (mm)	h_d = 1.0 mm			h_d = 2.5 mm		
	η_q	η_q^e	η_q^s	η_q^e	η_q	η_q^s
0.025	0.203	0.021	0.183	0.294	0.029	0.264
0.050	0.205	0.033	0.172	0.298	0.052	0.246
0.075	0.202	0.034	0.168	0.294	0.059	0.235
0.100	0.198	0.033	0.165	0.289	0.062	0.227
0.125	0.195	0.032	0.163	0.284	0.063	0.221
0.150	0.192	0.031	0.162	0.279	0.063	0.217

The aforesaid results (Tables 2.9 and 2.10) for PCLD treatment of beam element are presented considering eight graphite-phase volumes within the whole span of the constrained 1-3 VEC layer. As the number of graphite-phase volumes increases within the same span of the 1-3 VEC layer, the corresponding variations in the modal loss factor (η_q) and its counterparts (η_q^e, η_q^s) are illustrated in Table 2.11 considering two different values of the thickness (h_d) of constrained damping layer.

It may be noted from Table 2.11 that the maximum value of total loss factor (η_q) appears at certain number of graphite-phase volumes and it occurs because of the opposite nature of variation of η_q^e with respect to the nature of variation of η_q^s. It may also be observed that the optimal number of graphite-phase volumes may vary with the thickness (h_d) of the constrained damping layer. However, a small rate of change of η_q with the increasing number of graphite-phase volumes (n) can be observed from Table 2.11, and this fact facilitates to choose any number of these volumes within the 1-3 VEC layer.

Table 2.11 Variations of modal loss factor (η_q at the fundamental bending mode) and its counterparts (η_q^e, η_q^s) with the number (n) of graphite-phase volumes of the constrained 1-3 VEC layer (h_v = 0.1 mm, Δl_v = 0.1mm, n_z = 1, L = 200 mm, h = 5 mm).

1-3 VEC layer (PCLD treatment)						
n	h_d = 1.0 mm			h_d = 2.5 mm		
1	η_q	η_q^e	η_q^s	η_q	η_q^e	η_q^s
2	0.208	0.017	0.191	0.272	0.022	0.250
3	0.209	0.025	0.184	0.290	0.034	0.256
4	0.207	0.029	0.178	0.293	0.042	0.251
5	0.205	0.031	0.173	0.294	0.050	0.244
10	0.195	0.033	0.162	0.284	0.065	0.219
15	0.190	0.031	0.159	0.287	0.072	0.215
20	0.188	0.029	0.158	0.287	0.075	0.212

Table 2.12 illustrates the variation of loss factor (η_q) when the number of 1-3 VEC layer increases within a specified thickness (h_d) of the constrained damping layer. It may be observed from Table 2.12 that the magnitude of loss factor (η_q) insignificantly vary as the number of 1-3 VEC layer increases within a specified thickness (h_d) of the constrained damping layer in the PCLD treatment.

Table 2.12 Variations of modal loss factor (η_q at the fundamental bending mode) and its counterparts (η_q^e, η_q^s) with the number (n_z) of 1-3 VEC layers within a specified thickness (h_d) of the constrained damping layer (h_v = 0.1 mm, Δl_v = 0.1mm, n = 8, L = 200 mm, h = 5 mm).

1-3 VEC layer (PCLD treatment)							
	h_d = 1.0 mm				h_d = 2.5 mm		
n_z	η_q	η_q^e	η_q^s	n_z	η_q	η_q^e	η_q^s
1	0.198	0.033	0.165	1	0.289	0.062	0.227
2	0.201	0.021	0.180	5	0.278	0.028	0.250

Table 2.13 demonstrates the variation in the damping-capacity of the constrained 1-3 VEC layer for different kinds of boundary conditions at the edges of the substrate beam. The characteristics of these results (Table 2.13) are

similar to those of the previous results for the unconstrained 1-3 VEC layer (Table 2.7). So, it may be concluded that the free or constrained 1-3 VEC layer possesses its maximum damping-capacity in case of the simply-supported boundary ends of the substrate beam.

Table 2.13 Modal loss factor (η_q at the fundamental bending mode) and its counterparts (η_q^e, η_q^s) for different boundary conditions at the edges of substrate beam (h_v = 0.1 mm, Δl_v = 0.1 mm, n = 8, n_z = 1, L = 200 mm, h = 5 mm).

Boundary condition	1-3 VEC layer (PCLD Treatment)					
	h_d = 1.0 mm			h_d = 2.5 mm		
	η_q	η_q^e	η_q^s	η_q	η_q^e	η_q^s
Clamped-clamped	0.198	0.033	0.165	0.289	0.062	0.227
Simply-supported	0.230	0.040	0.190	0.283	0.056	0.227
Clamped-free	0.163	0.017	0.146	0.162	0.026	0.136

For the use of the traditional pure VEM layer in place of the 1-3 VEC layer, the corresponding variations of loss factor (η_q) and its counterparts (η_q^e, η_q^s) with the thickness (h_d) of the constrained damping layer are demonstrated in Table 2.14.

Table 2.14 Variations of modal loss factor (η_q at the fundamental bending mode) and its counterparts (η_q^e, η_q^s) with the thickness (h_d) of constrained pure VEM layer in PCLD treatment (L = 200 mm, h = 5 mm).

Pure VEM layer (PCLD treatment)			
h_d (mm)	η_q	η_q^e	η_q^s
0.5	0.131	0.00011	0.131
1.0	0.135	0.00021	0.135
1.5	0.139	0.00031	0.138
2.0	0.143	0.00041	0.142
2.5	0.148	0.00049	0.147

It may be observed from this table (Table 2.14) that the loss factor (η_q) and its counterparts (η_q^e, η_q^s) increase with the increasing thickness of the constrained pure VEM layer. For any thickness of the constrained damping layer within the

PCLD arrangement, the magnitude of loss factor (η_q) caused by the pure VEM layer (Table 2.14) is significantly lesser than that caused by the 1-3 VEC layer (Table 2.9/2.10/2.11/2.12).

So, these results suggest 1-3 VEC layer instead of pure VEM layer for the PCLD treatment of structural vibration. Although this suggestion is achieved from the aforesaid analysis of modal loss factor, it is further verified through the computation of frequency responses of the overall beam (Fig. 2.3).

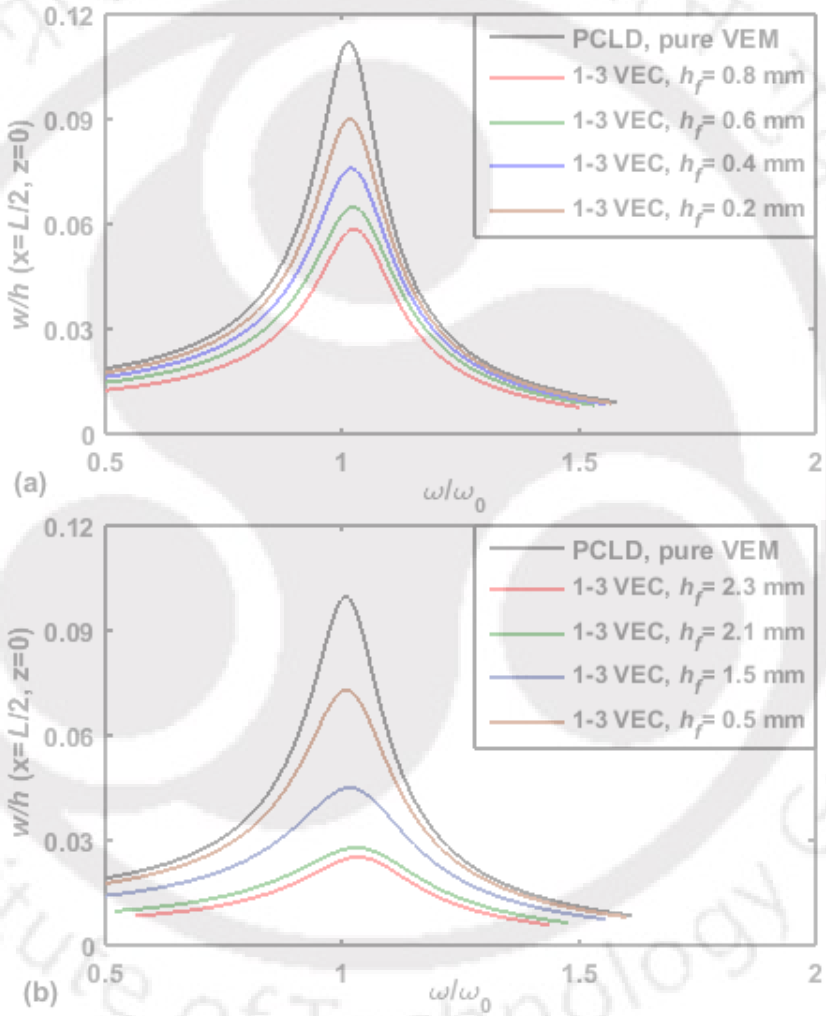

Fig. 2.8 Frequency responses of the substrate beam integrated with the PCLD layer ((a) h_d = 1.0 mm, **(b)** h_d = 2.5 mm; p = 1000 N, Δl_v = 0.1mm, n = 8, n_z = 1, L = 200 mm, h = 5 mm**).**

The harmonic mechanical excitation is considered as it is in the previous case of UCLD treatment. Also, similar strategy in consideration of pure VEM layer or 1-3 VEC layer is followed. Figure 2.8 illustrates these frequency responses for two

different values of the thickness (h_d) of the constrained damping layer. For any of the thickness (h_d), Fig. 2.8 shows an indicative increase of passive damping in the overall beam when the pure VEM layer is substituted by the present 1-3 VEC layer. So, the present results suggest 1-3 VEC layer instead of the conventional pure VEM layer for the PCLD treatment of structural vibration.

2.6 Summary

In this chapter, a 1-3 VEC layer is designed in combination of 2-2 VEC and pure VEM layers with an objective of the improved passive damping in the UCLD/PCLD treatment of structural vibration. The 1-3 VEC layer is utilized instead of the traditional monolithic VEM layer within the UCLD/PCLD arrangement, and the corresponding changes in the passive damping are studied considering a substrate beam integrated with a layer of UCLD/PCLD treatment. The study is carried out through the static as well as dynamic finite element (FE) analyses of the overall beam under the transverse mechanical load.

The static analysis exhibits mechanisms of passive damping in the UCLD and PCLD treatments for the use of 1-3 VEC layer. The corresponding numerical results reveal that the extensional and transverse shear strains in the viscoelastic phase increase indicatively due to the graphite inclusions. This observation infers improved passive damping in the UCLD/PCLD treatment, and it is subsequently substantiated through the dynamic analysis of the overall beam.

In the dynamic analysis, first a numerical analysis of modal loss factor of the overall beam is carried out with respect to various geometric parameters of 1-3 VEC layer and the appropriate values of these geometric parameters are decided for the improved damping capability of the constrained/unconstrained 1-3 VEC layer. Based on this geometric configuration of the 1-3 VEC layer, the passive damping in the overall beam is evaluated with and without considering the inclusions in the viscoelastic layer. These results reveal significant improvement in the passive damping capability of UCLD/PCLD treatment for the use of the graphite-inclusion in the form of a 1-3 VEC layer. So, the 1-3 VEC layer may be utilized instead of the pure VEM layer within the UCLD/PCLD treatment for accomplishing improved damping treatment of structural vibration.

Chapter 3

Active-passive damping treatment of beams using a new 1-3 VEC layer

3.1 Introduction

A new 1-3 VEC layer is proposed in the previous chapter for improved passive damping capacity of the UCLD/PCLD treatment of structural vibration. This 1-3 VEC layer is comprised of the graphite-wafers which are continuously distributed in one direction within the viscoelastic matrix. Under the bending deformation, high stiffness of the inclusions causes the viscoelastic phase within the axial gaps among the inserts to undergo extensional/compressional strain, while the viscoelastic phase between the stiff flat surfaces of the inserts and the constraining layer/substrate structure undergoes transverse shear deformation. These strains appear with reasonable magnitudes that are far ahead of the similar magnitudes in the absence of the stiff inclusions. So, an indicative improvement of passive damping in the UCLD/PCLD treatment of beams has been observed, and this observation motivates to extend the study on the use of the 1-3 VEC layer as a damping layer in the ACLD treatment of beams. So, in this chapter, the performance of the 1-3 VEC layer in the ACLD treatment of beams is investigated.

This study is carried out by taking the earlier configuration of the overall beam (Fig. 2.3) where the passive constraining layer is substituted by an active piezoelectric layer as shown in Fig. 3.1. The top and bottom surfaces of the active piezoelectric layer are fully electrode-surfaces and the external voltage is supplied across these electrodes according to the velocity feedback control strategy. A closed loop FE model of the overall beam (Fig. 3.1) is derived in the next section. Using this FE model, first, a bending analysis of the overall beam is carried out in the presence and the absence of the external voltage across the thickness of the piezoelectric constraining layer. This static analysis reveals the changes of the mechanisms of damping in the 1-3 VEC layer due to the use of active constraining layer instead of the earlier passive constraining layer (Chapter 2). Subsequently, the variations of damping capacity of the ACLD treatment with the different geometrical parameters in the arrangement of graphite-wafers within the 1-3 VEC layer are presented, and an appropriate

geometric configuration of the 1-3 VEC layer for effective ACLD treatment of the substrate beam is addressed. Based on this appropriate geometric configuration of the 1-3 VEC layer, the controlled frequency responses of the overall beam and the corresponding required control-voltages are evaluated, and the improvement of the control capability of the ACLD treatment due to the present 1-3 VEC layer is substantiated by evaluating similar responses without graphite-inclusions.

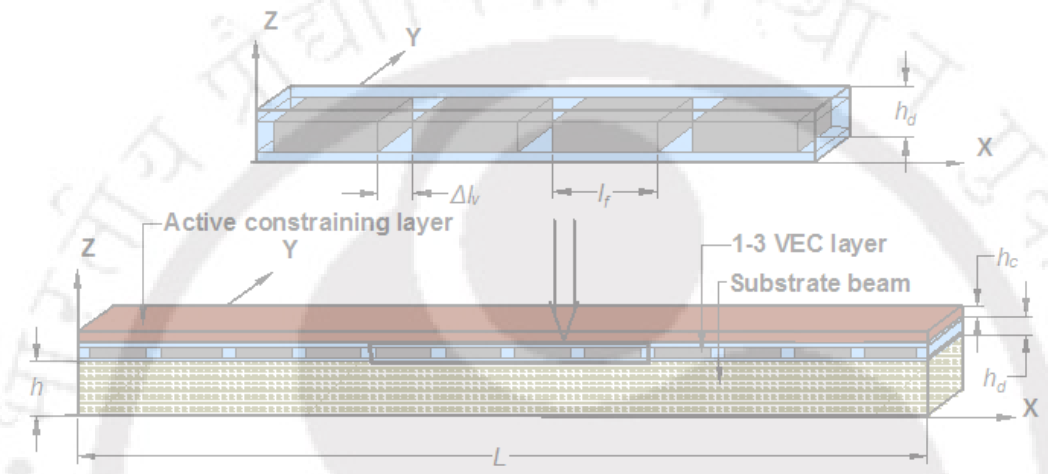

Fig. 3.1 Schematic diagram of a host beam integrated with actively constrained 1-3 VEC layer.

3.2 FE model of the overall beam

A coupled electro-elastic FE model of the overall beam (Fig. 3.1) is derived in this section. Similar to the previous beam (Fig. 2.3), the material and geometrical properties of the overall beam (Fig. 3.1) do not vary along the y-direction. The loading and boundary conditions are also considered in the same manner. So, the analysis of the overall beam can be carried out by considering a typical xz-plane as shown in Fig. 3.2. Corresponding to this plane of the overall beam, a two-dimensional coupled electro-elastic FE model is derived in this section for the analysis of active-passive damping in the overall beam. The length and height of the host beam are denoted by, L and h, respectively. The thickness of the constraining/constrained layer is denoted by, h_c / h_d. The number of graphite-wafers in the 1-3 VEC layer (Figs. 3.1 and 3.2) is denoted by n while the number of 1-3 VEC layers in case of its (1-3 VEC) use in the form of a laminate (Fig. 2.1) is denoted by, n_z. Other important geometrical parameters ($h_v, h_f, \Delta l_v, l_f$) of the 1-3 VEC layer are shown in Figs. 2.1 and 3.1.

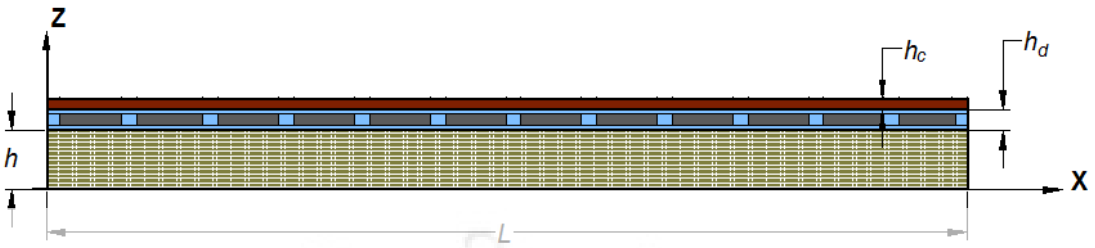

Fig. 3.2 Schematic diagram of a typical xz - plane of the overall beam (Fig. 3.1)

The state of strain and the state of stress can be defined according to Eqs. (2.1) and (2.2).

$$\boldsymbol{\varepsilon}_e = \{\varepsilon_x \;\; \varepsilon_z\}^{\mathrm{T}}, \quad \varepsilon_s = \gamma_{xz} \tag{2.1}$$

$$\boldsymbol{\sigma}_e = \{\sigma_x \;\; \sigma_z\}^{\mathrm{T}}, \quad \sigma_s = \tau_{xz} \tag{2.2}$$

The electric field vector ($\boldsymbol{E}$) and electric displacement vector ($\boldsymbol{D}$) at any point within the beam (Fig. 3.2) can be written as,

$$\boldsymbol{E} = \{E_X \;\; E_Z\}^{\mathrm{T}}, \;\; \boldsymbol{D} = \{D_X \;\; D_Z\}^{\mathrm{T}} \tag{3.1}$$

where, E_X / D_X and E_Z / D_Z are the electric field/displacement along the x and z directions, respectively. The strain-displacement relations can be written according to Eqs. (2.3) and (2.4), while the electric field-potential relations are presented in Eqs. (3.2) and (3.3).

$$\boldsymbol{\varepsilon}_e = \boldsymbol{L}_e \boldsymbol{d}, \;\; \varepsilon_s = \boldsymbol{L}_s \boldsymbol{d} \tag{2.3}$$

$$\boldsymbol{L}_e = \begin{bmatrix} \partial/\partial x & 0 \\ 0 & \partial/\partial z \end{bmatrix}, \;\; \boldsymbol{L}_s = \{\partial/\partial z \;\; \partial/\partial x\}, \;\; \boldsymbol{d} = \{u \;\; w\}^{\mathrm{T}} \tag{2.4}$$

$$\boldsymbol{E} = \boldsymbol{L}_p \phi \tag{3.2}$$

$$\boldsymbol{L}_p = \begin{Bmatrix} -\partial/\partial x \\ -\partial/\partial z \end{Bmatrix} \tag{3.3}$$

where, ϕ is the electric potential at any point in the overall beam. The constitutive relations for different materials within the overall beam (Fig. 3.2) can be written as,

$$\boldsymbol{\sigma}_e^k = \left(\boldsymbol{C}_e^k \boldsymbol{\varepsilon}_e - \boldsymbol{e}_e^k \boldsymbol{E}\right), \; \sigma_s^k = \left(C_s^k \varepsilon_s - \boldsymbol{e}_s^k \boldsymbol{E}\right)$$

$$\boldsymbol{D}^k = (\boldsymbol{e}_e^k)^{\mathrm{T}} \boldsymbol{\varepsilon}_e + (\boldsymbol{e}_s^k)^{\mathrm{T}} \varepsilon_s + \epsilon^k \boldsymbol{E} \tag{3.4}$$

where, k denotes the materials for substrate beam, viscoelastic phase, graphite-wafers and piezoelectric constraining layer according to its value as 1, 2, 3 and

4, respectively; $\boldsymbol{C}_e^k$ and C_s^k are the extensional and transverse shear counterparts of the stiffness matrix of k^{th} material; $\boldsymbol{e}_e^k$ and $\boldsymbol{e}_s^k$ are the extensional and shear counterparts of piezoelectric matrix of k^{th} material; ϵ^k is the dielectric matrix for the k^{th} material. The forms of these property matrices are given by,

$$\boldsymbol{C}_e^k = \begin{bmatrix} C_{11}^k & C_{13}^k \\ C_{13}^k & C_{33}^k \end{bmatrix}, C_s^k = C_{55}^k, \boldsymbol{e}_e^k = \begin{bmatrix} 0 & e_{31}^k \\ 0 & e_{33}^k \end{bmatrix}, \boldsymbol{e}_s^k = \begin{Bmatrix} e_{15}^k & 0 \end{Bmatrix}, \epsilon^k = \begin{bmatrix} \epsilon_{11}^k & 0 \\ 0 & \epsilon_{33}^k \end{bmatrix} \tag{3.5}$$

Similar to the previous analysis (Chapter 2), the viscoelastic phase ($k=2$) is modelled using the complex stiffness method. So, the stiffness matrices ($\boldsymbol{C}_e^k, C_s^k, k=2$) for the viscoelastic phase are complex matrices. Also, the piezoelectric matrices ($\boldsymbol{e}_e^k, \boldsymbol{e}_s^k$) for the substrate beam ($k=1$), viscoelastic phase ($k=2$) and graphite-wafers ($k=3$) are the null matrices. The overall beam is subjected to a similar load as that is considered in the previous analysis of the beam integrated with UCLD/PCLD layer. So, the xz-section of the overall beam (Fig. 3.2) is considered to be subjected to a transverse point-load ($p(t)$) at its middle point ($L/2, 0$). Under this load, the principle of virtual work gives,

$$\delta T_p = \left[\sum_{k=1}^{4} \int_{A_k} \left\langle (\delta\boldsymbol{\varepsilon}_e)^{\mathrm{T}} \boldsymbol{\sigma}_e^k + (\delta\varepsilon_s)\sigma_s^k - (\delta\boldsymbol{E})^{\mathrm{T}} \boldsymbol{D}^k \right\rangle dA_k \right] - (\delta w)\, p(t)\big|_{\substack{x=L/2, \\ z=0}} \tag{3.6}$$

$$\delta T_k = \left[\sum_{k=1}^{4} \int_{A_k} \left\langle (\delta\dot{\boldsymbol{d}})^{\mathrm{T}} \rho^k \dot{\boldsymbol{d}} \right\rangle dA_k \right] \tag{3.7}$$

where, δT_p and δT_k are the first variations of the total potential energy and the total kinetic energy respectively over the section of the smart beam at any instant of time (t), δ is an operator for the first variation and A_k is the area of k^{th} phase within the section (Fig. 3.2) of the beam; ρ_k is the mass density of k^{th} phase. For deriving the FE model of a typical xz-section of the beam, it (xz-section) is discretized using nine-node isoparametric elements such that the edges of every element are in parallel to the reference coordinate axes (x and z axes). A typical element is considered to be made of one of the phases within the

xz-section. The displacement vector ($\boldsymbol{d}$) and the electric potential (ϕ) at any point within a typical element can be expressed as follows,

$$\boldsymbol{d} = \boldsymbol{N}_d \, \boldsymbol{d}^{\Delta}, \; \phi = \boldsymbol{N}_{\phi} \, \boldsymbol{\phi}^{\Delta} \tag{3.8}$$

where, $\boldsymbol{d}^{\Delta}$ and $\boldsymbol{\phi}^{\Delta}$ are the elemental nodal displacement and electric potential vectors, respectively; N_d and N_{ϕ} are the corresponding shape-function matrices. The governing equations of motion of the overall beam are derived employing the extended Hamilton's principle as given in Eq. (2.11).

$$\int_{t_1}^{t_2} \left(\delta T_K - \delta T_P \right) dt = 0 \tag{2.11}$$

Substituting Eqs. (3.6), (3.7), (3.4, (2.3) and (3.2) in Eq. (2.11) and then using Eq. (3.8), the following simplified equations of motion for a typical element can be obtained,

$$\boldsymbol{M}^{\Delta} \ddot{\boldsymbol{d}}^{\Delta} + \boldsymbol{K}_{dd}^{\Delta} \, \boldsymbol{d}^{\Delta} - \boldsymbol{K}_{d\phi}^{\Delta} \, \boldsymbol{\phi}^{\Delta} = \boldsymbol{p}^{\Delta}(t), \; \boldsymbol{K}_{dd}^{\Delta} = (\boldsymbol{K}_{dde}^{\Delta} + \boldsymbol{K}_{dds}^{\Delta}), \; \boldsymbol{K}_{d\phi}^{\Delta} = (\boldsymbol{K}_{d\phi e}^{\Delta} + \boldsymbol{K}_{d\phi s}^{\Delta}) \tag{3.9}$$

$$\boldsymbol{K}_{\phi d}^{\Delta} \, \boldsymbol{d}^{\Delta} + \boldsymbol{K}_{\phi\phi}^{\Delta} \, \boldsymbol{\phi}^{\Delta} = 0, \; \boldsymbol{K}_{\phi d}^{\Delta} = (\boldsymbol{K}_{\phi d e}^{\Delta} + \boldsymbol{K}_{\phi d s}^{\Delta}) \tag{3.10}$$

The different matrices as appeared in Eqs. (3.9) and (3.10) are as follows,

$$\boldsymbol{M}^{\Delta} = \int_{A_k^{\Delta}} \left\langle N_d{}^{\mathrm{T}} \rho^k N_d \right\rangle dA_k^{\Delta}, \quad \boldsymbol{K}_{dde}^{\Delta} = \int_{A_k^{\Delta}} \left\langle N_d{}^{\mathrm{T}} (\boldsymbol{L}_e)^{\mathrm{T}} \boldsymbol{C}_e^k \boldsymbol{L}_e \boldsymbol{N}_d \right\rangle dA_k^{\Delta},$$

$$\boldsymbol{K}_{dds}^{\Delta} = \int_{A_k^{\Delta}} \left\langle N_d{}^{\mathrm{T}} (\boldsymbol{L}_s)^{\mathrm{T}} \boldsymbol{C}_s^k \boldsymbol{L}_s \boldsymbol{N}_d \right\rangle dA_k^{\Delta}, \quad \boldsymbol{K}_{d\phi e}^{\Delta} = \int_{A_k^{\Delta}} \left\langle N_d{}^{\mathrm{T}} (\boldsymbol{L}_e)^{\mathrm{T}} \boldsymbol{e}_e^k \boldsymbol{L}_p \boldsymbol{N}_{\phi} \right\rangle dA_k^{\Delta},$$

$$\boldsymbol{K}_{d\phi s}^{\Delta} = \int_{A_k^{\Delta}} \left\langle N_d{}^{\mathrm{T}} (\boldsymbol{L}_s)^{\mathrm{T}} \boldsymbol{e}_s^k \boldsymbol{L}_p \boldsymbol{N}_{\phi} \right\rangle dA_k^{\Delta}, \; \boldsymbol{K}_{\phi de}^{\Delta} = \int_{A_k^{\Delta}} \left\langle N_{\phi}{}^{\mathrm{T}} (\boldsymbol{L}_p)^{\mathrm{T}} (\boldsymbol{e}_e^k)^{\mathrm{T}} \boldsymbol{L}_e \boldsymbol{N}_d \right\rangle dA_k^{\Delta}$$

$$\boldsymbol{K}_{\phi d s}^{\Delta} = \int_{A_k^{\Delta}} \left\langle N_{\phi}{}^{\mathrm{T}} (\boldsymbol{L}_p)^{\mathrm{T}} (\boldsymbol{e}_s^k)^{\mathrm{T}} \boldsymbol{L}_s \boldsymbol{N}_d \right\rangle dA_k^{\Delta},$$

$$\boldsymbol{K}_{\phi\phi}^{\Delta} = \int_{A_k^{\Delta}} \left\langle N_{\phi}{}^{\mathrm{T}} (\boldsymbol{L}_p)^{\mathrm{T}} (\epsilon^k)^{\mathrm{T}} \boldsymbol{L}_p \boldsymbol{N}_{\phi} \right\rangle dA_k^{\Delta}, \; \boldsymbol{p}^{\Delta} = \left\langle N_d{}^{\mathrm{T}} \{0 \; p(t)\}^{\mathrm{T}} \right\rangle \Big|_{x=L/2, z=0} \tag{3.11}$$

where, A_k^{Δ} is the elemental area for a typical element within the k^{th} material. Assembling the elemental equations (Eqs. (3.9) and (3.10)) in the global space, the equations of motion of the overall beam can be obtained as,

$$\boldsymbol{M}\ddot{\boldsymbol{X}}_d + \boldsymbol{K}_{dd} \, \boldsymbol{X}_d - \boldsymbol{K}_{d\phi} \, \boldsymbol{X}_{\phi} = \boldsymbol{P}(t) \tag{3.12}$$

$$\boldsymbol{K}_{\phi d}\,\boldsymbol{X}_d + \boldsymbol{K}_{\phi\phi}\,\boldsymbol{X}_\phi = 0 \tag{3.13}$$

where, $\boldsymbol{M}$ is the global mass matrix; $\boldsymbol{K}_{dd}$ is the global stiffness matrix; $\boldsymbol{K}_{d\phi}$ and $\boldsymbol{K}_{\phi d}$ are the global electro-elastic coefficient matrices; $\boldsymbol{K}_{\phi\phi}$ is the global electrical coefficient matrix; $\boldsymbol{X}_d$ and $\boldsymbol{X}_\phi$ are the global nodal displacement and electric potential vectors; $\boldsymbol{P}(t)$ is the global mechanical load vector.

3.2.1 Implementation of control strategy

The external voltage is supplied across the top and bottom fully electrode-surfaces of the piezoelectric constraining layer according to the velocity feedback control strategy. The transverse velocity ($\dot{w}_s$) at the middle point ($x = L/2$, $z = (h + h_d + h_c)$, Fig. 3.1 or Fig. 3.2) of the beam is sensed by a velocity-sensor, and it ($\dot{w}_s$) is fed back to the surface-electrodes in the form of voltage (V) as,

$$V = -k_d \dot{w}_s,\; V = \left(\phi_t - \phi_b\right) \tag{3.14}$$

where, k_d is the velocity feedback control-gain; ϕ_t and ϕ_b are the applied electric potentials at the top and bottom surface-electrodes, respectively. These applied electric potentials (ϕ_t, ϕ_b) can directly be imposed in the FE model (Eqs. (3.12) and (3.13)) by specifying corresponding nodal electric potentials or elements of $\boldsymbol{X}_\phi$. For a specified nodal electric potential over the top/bottom surface of the piezoelectric constraining layer, the first variation of the corresponding element of $\boldsymbol{X}_\phi$ (say, $X_{\phi i}$) is zero ($\delta X_{\phi i} = 0$). Thus, the corresponding (i^{th}) rows of $\boldsymbol{K}_{\phi d}$ and $\boldsymbol{K}_{\phi\phi}$ are to be deleted while the columns ($\boldsymbol{P}^i_{d\phi}$ and $\boldsymbol{P}^i_{\phi\phi}$) of $\boldsymbol{K}_{d\phi}$ and $\boldsymbol{K}_{\phi\phi}$ with the same index (i) are to be removed for formation of electric potential load vector as,

$$\boldsymbol{M}\ddot{\boldsymbol{X}}_d + \boldsymbol{K}_{dd}\,\boldsymbol{X}_d - \boldsymbol{K}^r_{d\phi}\,\boldsymbol{X}^r_\phi = \boldsymbol{P}(t) + \boldsymbol{P}^i_{d\phi} X_{\phi i} \tag{3.15}$$

$$\boldsymbol{K}^r_{\phi d}\,\boldsymbol{X}_d + \boldsymbol{K}^r_{\phi\phi}\,\boldsymbol{X}^r_\phi = -\boldsymbol{P}^i_{\phi\phi} X_{\phi i} \tag{3.16}$$

where, $\boldsymbol{K}^r_{\phi d}$, $\boldsymbol{K}^r_{d\phi}$, $\boldsymbol{K}^r_{\phi\phi}$ and $\boldsymbol{X}^r_\phi$ are the reduced coefficient matrices and nodal electric potential vector after implementation of the specified value of $X_{\phi i}$.

For all the specified nodal electric potentials over the isopotential top ($\phi = \phi_t$) and bottom ($\phi = \phi_b$) surfaces of the constraining layer, Eqs. (3.15) and (3.16) can be written as,

$$\boldsymbol{M}\ddot{\boldsymbol{X}}_d + \boldsymbol{K}_{dd}\,\boldsymbol{X}_d - \boldsymbol{K}^r_{d\phi}\,\boldsymbol{X}^r_\phi = \boldsymbol{P}(t) + \boldsymbol{P}^t_{d\phi}\phi_t + \boldsymbol{P}^b_{d\phi}\phi_b,\ \boldsymbol{P}^t_{d\phi} = \sum_{s=1}^{N_t}\left(\boldsymbol{P}^i_{d\phi}\right)^s,\ \boldsymbol{P}^b_{d\phi} = \sum_{q=1}^{N_b}\left(\boldsymbol{P}^i_{d\phi}\right)^q, \quad (3.17)$$

$$\boldsymbol{K}^r_{\phi d}\,\boldsymbol{X}_d + \boldsymbol{K}^r_{\phi\phi}\,\boldsymbol{X}^r_\phi = -\boldsymbol{P}^t_{\phi\phi}\phi_t - \boldsymbol{P}^b_{\phi\phi}\phi_b,\ \boldsymbol{P}^t_{\phi\phi} = \sum_{s=1}^{N_t}\left(\boldsymbol{P}^i_{\phi\phi}\right)^s,\ \boldsymbol{P}^b_{\phi\phi} = \sum_{q=1}^{N_b}\left(\boldsymbol{P}^i_{\phi\phi}\right)^q \quad (3.18)$$

where, N_t and N_b are the numbers of nodes over the top and bottom surfaces of the constraining layer, respectively; i is the number of row of $\boldsymbol{X}_\phi$ corresponding to the electric potential at s^{th} or q^{th} node over the top or bottom surface, respectively of the piezoelectric layer. The electrode over the bottom surface of the piezoelectric constraining layer is considered to be grounded ($\phi_b = 0$). So, there would be no electric potential in the viscoelastic phase, graphite phase and substrate beam. Implementing this state of electric potential along with the displacement boundary conditions over the boundaries ($x = 0, L$) of the substrate beam, Eqs. (3.17) and (3.18) can be written as,

$$\boldsymbol{M}^{rr}\ddot{\boldsymbol{X}}^r_d + \boldsymbol{K}^{rr}_{dd}\,\boldsymbol{X}^r_d - \boldsymbol{K}^{rr}_{d\phi}\,\boldsymbol{X}^r_\phi = \boldsymbol{P}^r(t) + \boldsymbol{P}^{tr}_{d\phi}\phi_t \quad (3.19)$$

$$\boldsymbol{K}^{rr}_{\phi d}\,\boldsymbol{X}^r_d + \boldsymbol{K}^{rr}_{\phi\phi}\,\boldsymbol{X}^r_\phi = -\boldsymbol{P}^{tr}_{\phi\phi}\phi_t \quad (3.20)$$

Substituting the nodal electric potential vector ($\boldsymbol{X}^r_\phi$) from Eq. (3.20) into Eq. (3.19), we get the reduced equation as follows,

$$\boldsymbol{M}^{rr}\ddot{\boldsymbol{X}}^r_d + \boldsymbol{K}^{rr}\,\boldsymbol{X}^r_d = \boldsymbol{P}^r(t) + \boldsymbol{P}^r_\phi\phi_t \quad (3.21a)$$

$$\boldsymbol{K}^{rr} = \left\langle \boldsymbol{K}^{rr}_{dd} + \boldsymbol{K}^{rr}_{d\phi}(\boldsymbol{K}^{rr}_{\phi\phi})^{-1}\boldsymbol{K}^{rr}_{\phi d}\right\rangle,\ \boldsymbol{P}^r_\phi = \left\langle \boldsymbol{P}^{tr}_{d\phi} - \boldsymbol{K}^{rr}_{d\phi}(\boldsymbol{K}^{rr}_{\phi\phi})^{-1}\boldsymbol{P}^{tr}_{\phi\phi}\right\rangle \quad (3.21b)$$

$$\boldsymbol{X}^r_\phi = -(\boldsymbol{K}^{rr}_{\phi\phi})^{-1}(\boldsymbol{P}^{tr}_{\phi\phi}\phi_t + \boldsymbol{K}^{rr}_{\phi d}\,\boldsymbol{X}^r_d) \quad (3.22)$$

The velocity ($\dot{w}_s$) at the middle point of the beam can be expressed in terms of the global nodal velocity vector ($\dot{\boldsymbol{X}}^r_d$) through a transformation matrix ($\boldsymbol{N}_T$) as,

$$\dot{w}_s = \boldsymbol{N}_T\dot{\boldsymbol{X}}^r_d \quad (3.23a)$$

Using Eq. (3.23a) in Eq. (3.14), the applied electric potential (ϕ_t, $\phi_b = 0$) according to the control strategy can be expressed as,

$$\phi_t = -k_d \boldsymbol{N}_T \dot{\boldsymbol{X}}_d^r \tag{3.23b}$$

Introducing Eq. (3.23b) in Eqs. (3.21a), the following equations of motion can be obtained,

$$\boldsymbol{M}^{rr}\ddot{\boldsymbol{X}}_d^r + \boldsymbol{C}^{rr}\dot{\boldsymbol{X}}_d^r + \boldsymbol{K}^{rr}\boldsymbol{X}_d^r = \boldsymbol{P}^r(t), \boldsymbol{C}^{rr} = \boldsymbol{P}_\phi^r k_d \boldsymbol{N}_T \tag{3.24}$$

As mentioned earlier, the viscoelastic material is modelled by the complex stiffness method. So, the stiffness matrices (Eq. (3.4)) of the viscoelastic phase can be written as,

$$\boldsymbol{C}_e^k = (\boldsymbol{C}_{Re}^k + j\boldsymbol{C}_{Ie}^k), \boldsymbol{C}_s^k = (\boldsymbol{C}_{Rs}^k + j\boldsymbol{C}_{Is}^k),\ k = 2,\ j = \sqrt{-1} \tag{3.25}$$

where, R and I within the subscripts represent the real and imaginary counterparts of a complex stiffness matrix. Because of these complex stiffness matrices of the viscoelastic phase, Eq. (3.24) can be rewritten in terms of the real ($\boldsymbol{K}_R^{rr}$) and imaginary ($\boldsymbol{K}_I^{rr}$) counterparts of $\boldsymbol{K}^{rr}$ as,

$$\boldsymbol{M}^{rr}\ddot{\boldsymbol{X}}_d^r + \boldsymbol{C}^{rr}\dot{\boldsymbol{X}}_d^r + (\boldsymbol{K}_R^{rr} + j\boldsymbol{K}_I^{rr})\boldsymbol{X}_d^r = \boldsymbol{P}^r(t) \tag{3.26}$$

It may be noted here that the viscoelastic damping in the overall beam arises due to the imaginary counterpart ($\boldsymbol{K}_I^{rr}$) of the stiffness matrix ($\boldsymbol{K}^{rr}$).

3.3 Solution and estimation of damping in the overall beam

The applied transverse harmonic mechanical load is considered as, $\boldsymbol{P}(t) = \boldsymbol{P}_o e^{j\omega t}$ where $\boldsymbol{P}_o$ is the nodal load-amplitude vector and ω is the operating frequency. For linear vibration of the overall beam under this harmonic excitation, the steady state solution of Eq. (3.26) may be assumed as (Meirovitch, 1997), $\boldsymbol{X}_d^r = \bar{\boldsymbol{X}} e^{j\omega t}$ where $\bar{\boldsymbol{X}}$ is a complex nodal displacement vector. The absolute value of $\bar{\boldsymbol{X}}$ provides the nodal displacement-amplitude vector. Substituting this solution in Eq. (3.26), the governing equations of motion can be reduced as,

$$\left[-\omega^2\boldsymbol{M}^{rr} + j\omega\boldsymbol{C}^{rr} + \boldsymbol{K}_R^{rr} + j\boldsymbol{K}_I^{rr}\right]\bar{\boldsymbol{X}} = \boldsymbol{P}_0 \tag{3.27}$$

For the free vibration of the overall beam ($\boldsymbol{P}_0 = 0$), Eq. (3.27) represents a complex eigenvalue problem as,

$$\left\langle \boldsymbol{K}_R^{rr} + j(\boldsymbol{K}_{Ie}^{rr} + \boldsymbol{K}_{Is}^{rr} + \omega\boldsymbol{C}^{rr}) \right\rangle \boldsymbol{\psi}_i = \omega_i^2 \boldsymbol{M}^{rr}\boldsymbol{\psi}_i \tag{3.28}$$

In Eq. (3.28), $\boldsymbol{K}_{Ie}^{rr}$ and $\boldsymbol{K}_{Is}^{rr}$ are the extension and transverse shear counterparts of $\boldsymbol{K}_I^{rr}$; $\boldsymbol{\psi}_i$ is the complex nodal displacement vector for the i^{th} natural mode

having the complex natural frequency of ω_i. This natural frequency can be expressed as (Hu et al., 2008),

$$(\omega_i)^2 = (\omega_i^o)^2 \langle 1 + j\eta_i \rangle, \ \eta_i = \mathrm{Im}(\omega_i)^2 / \mathrm{Re}(\omega_i)^2 \tag{3.29}$$

where, ω_i^o is the natural frequency of the system; η_i is the corresponding modal loss factor; Im and Re indicate real and imaginary counterparts of a complex quantity. Now, if one assumes, $\boldsymbol{K}_{Is}^{rr} = \boldsymbol{0}$ and $\boldsymbol{K}_{Ie}^{rr} = \boldsymbol{0}$ in Eq. (3.28), the corresponding damping in the overall beam arises due to the modelling of the piezoelectric actuation force in the form of viscous damping force through the velocity feedback control strategy. Now, for the assumption of $\boldsymbol{K}_{Is}^{rr} \neq \boldsymbol{0}$ and $\boldsymbol{K}_{Ie}^{rr} = \boldsymbol{0}$, the active-passive damping (denoted by the modal loss factor η_s) appears due to the transverse shear strain of the viscoelastic phase and also due to the piezoelectric actuation force. The total active-passive damping (denoted by the modal loss factor η) in the overall beam arises due to the piezoelectric actuation force, transverse shear strain of viscoelastic phase and extensional strain of viscoelastic phase. The difference between η and η_s indicates the damping due to the extensional strain of the viscoelastic. In order to compute these modal loss factors (η and η_s), the complex quadratic eigenvalue problem (Eq. (3.28)) is solved by direct iteration method. The governing equations of motion (Eq. (3.28)) are written as,

$$\left\langle \boldsymbol{K}_R^{rr} + j(\boldsymbol{K}_{Ie}^{rr} + \boldsymbol{K}_{Is}^{rr} + \boldsymbol{C}^{rr}\omega_i^{prev}) \right\rangle \boldsymbol{\psi}_i = \left(\omega_i^{curr}\right)^2 \boldsymbol{M}^{rr} \boldsymbol{\psi}_i \tag{3.30}$$

where, the superscripts '*prev*' and '*curr*' represent the previous and present values, respectively of the complex frequency corresponding to two consecutive iterations. The iteration starts with $\omega_i^{prev} = 0$. Next, in every iteration, a complex linear eigenvalue problem is solved for ω_i^{curr} with an assigned value of ω_i^{prev} that is obtained from the previous iteration. If the value of ω_i^{curr} appears to that of ω_i^{prev} according to convergence criteria, the solution is identified as, $\omega_i^{curr} = \omega_i^{prev} = \omega_i$ and the iteration is terminated.

3.4 Results and discussions

In this section, the numerical results are presented for investigating the damping characteristics of the ACLD treatment of a substrate beam for using

the 1-3 VEC layer as the damping layer of the treatment. The geometrical and material properties of the substrate beam are not altered from those considered in the previous analysis (section 2.5). The thicknesses of the piezoelectric constraining layer and the constrained damping layer are taken as, 0.5 mm and 1 mm, respectively. The piezoelectric constraining layer is considered to be made of PZT5H (Smith and Auld, 1991) with the properties of, C_{11} = 151 GPa, C_{12} = 98 GPa, C_{13} = 96 GPa, C_{33} = 124 GPa, C_{44} = 24 GPa, ρ = 7500 kg/m^3, e_{31} = -5.1 C/m^2, e_{33} = 27 C/m^2, e_{15} = 17 C/m^2, ϵ_{11}=15.3×10^{-9} C/Vm, ϵ_{22}=15.1×10^{-9} C/Vm. The properties of the graphite-wafers within the 1-3 VEC layer are (Jones, 1999), E = 250 GPa, ν=0.3, ρ=1400 kg/m^3. The material for the viscoelastic-phase of 1-3 VEC layer is taken as Butyl Rubber (Jones, 2001). Similar to the previous analysis (section 2.5), the damping characteristics of the ACLD treatment are investigated within a narrow range of the operating frequency around the fundamental mode of vibration of the overall beam at the room temperature (35^o C). So, the average properties of the viscoelastic material within this frequency range are taken as, E=20(1+0.9j) MPa, ν=0.49, ρ=920 kg/m^3.

The FE mesh is generated by dividing the horizontal and vertical spans of ta typical xz-section (Fig. 3.2) of the overall beam in such a manner that every element is in the shape of a rectangle with its edges in parallel to the sides of the xz-section. Also, a typical element is made of one of the phase materials within the section. Using this FE mesh, the numerical results are evaluated after an FE mesh-convergence study where the natural frequency and the controlled transverse displacement-amplitude at the middle point of the beam are evaluated by increasing the number of elements. These results are illustrated in Table 3.1. On the basis of these results (Table 3.1), the FE mesh of a typical xz-section of the overall beam is decided for evaluation of the numerical results. In order to verify the present FE formulation, the natural frequencies of the overall beam are computed and compared with the similar results available in the literature (Yellin and Shen, 1996). This comparison is illustrated in Table 3.2. It may be observed from this table that the present results are in good agreement with the similar results available in (Yellin and Shen, 1996) thus verifying the present FE formulation.

Table 3.1 FE mesh-convergence study for the smart beam (h = 5 mm, L = 0.2 m, h_c = 0.5 mm, h_d = 2.5 mm, h_v = 0.1 mm, Δl_v = 0.1 mm, n = 8, n_z = 1, k_d = 100, p = 1.0 kN**).**

No. of elements	Fundamental frequency (rad/s)	Displacement-amplitude (mm) at fundamental resonant frequency
432	4121.88	0.131142
594	4121.19	0.131829
880	4115.87	0.132013
2376	4111.06	0.132081
4104	4110.64	0.132413
7866	4109.86	0.132795
14490	4109.72	0.132715

Table 3.2 Verification of present FE formulation.

Natural frequency	1st mode (Hz)	2ndmode (Hz)
Ref. (Yellin and Shen, 1996)	8.5	53
Present FE model	8.66	53.24

In order to verify the present iterative procedure for the solution of the complex quadratic eigenvalue problem (Eq. (3.28)), the overall beam is considered to operate under the aforesaid transverse harmonic load. Then, the variation of the transverse displacement-amplitude at the middle point of the beam is evaluated at every frequency of operation (around the fundamental natural frequency) through the solution of Eq. (3.27). This frequency response of the overall beam is utilized to estimate its modal loss factor using the half-power bandwidth method (ASTM, 2010). Similar results are also evaluated through the solution of the eigenvalue problem (Eq. (3.28)) using the present iterative procedure.

Table 3.3 Verification of the present iterative procedure for solving the complex quadratic eigenvalue problem (η_{iter} **: modal loss factor estimated by the present iterative procedure;** η_{resp} **: modal loss factor estimated by the half-power bandwidth method).**

	Monolithic viscoelastic layer		1-3 VCM	
k_d	η_{resp}	η_{iter}	η_{resp}	η_{iter}
0	0.0609	0.0608	0.1255	0.1243
100	0.09011	0.0907	0.1657	0.1642
200	0.1220	0.1208	0.2063	0.2045
300	0.1518	0.1511	0.2487	0.2458
400	0.182	0.1816	0.2911	0.2873
500	0.2140	0.2124	0.3374	0.3297

3.4.1 Analysis of strains in the actively constrained damping layer

A bending analysis of the overall beam (Fig. 3.1) is carried out in order to characterize the distributions of extensional and transverse shear strains within the actively constrained 1-3 VEC layer. The representative section (Fig. 3.2) of the overall beam is considered to be subjected to an upward transverse point-load at the middle point $(L/2,0)$ of its length, while the piezoelectric constraining layer is activated by supplying an external voltage across its thickness. The geometrical properties of the overall beam are considered as, L = 0.2 m, h = 5 mm, h_d = 1 mm, h_c = 0.5 mm, h_v = 0.3 mm, Δl_v = 36 mm, l_f = 30 mm, n = 2, n_z = 1. The 1-3 VEC layer is considered to be made of two $(n=2)$ graphite-wafers (Fig. 3.3(a)), and it is used instead of the traditional monolithic viscoelastic material layer (Fig. 3.3(b)). Corresponding to these configurations of the overall beam under bending deformation, the distributions of extensional (ε_x) and transverse shear (γ_{xz}) strains over the xz-section are illustrated in Figs. 3.3(c)-(f).

It may be observed from Figs. 3.3(c)-(d) that the maximum magnitude of the extensional strain in the viscoelastic phase increases when the constrained layer is made of 1-3 VEC instead of the monolithic viscoelastic material. This increase of extensional strain appears at the viscoelastic phase between any two consecutive graphite-wafers. Similar to these results, Figs. 3.3(e)-(f) illustrate the increase in the maximum magnitude of transverse shear strain for the inclusions of graphite-wafers within the constrained viscoelastic layer. So, both the shear and extensional strains within the constrained viscoelastic phase increase due to the inclusion of graphite-wafers under the active constraining layer. With reference to the earlier results (Fig. 2.5), the characteristics of strains within the 1-3 VEC layer do not change indicatively for the use of active constraining layer (Fig. 3.3) instead of the passive one (Fig. 2.5). The only changes of magnitudes of the strains within the viscoelastic phase appear for the alteration of the passive constraining layer into active one. So, similar to the PCLD treatment in the previous chapter, the active-passive damping-capacity of the ACLD treatment is expected to improve due to the inclusion of graphite-wafers in the constrained viscoelastic layer. This estimation is further quantified in the subsequent section through the evaluation of modal loss factors by solving the complex quadratic eigenvalue problem (Eq. (3.28)).

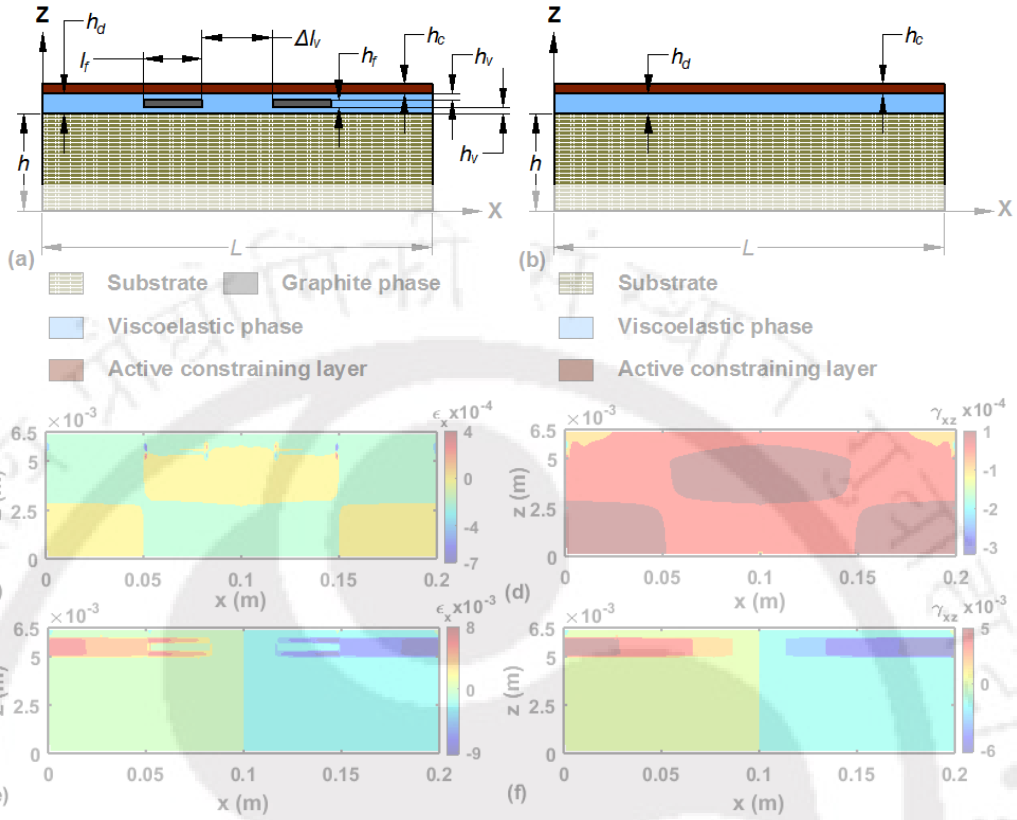

Fig. 3.3 Schematic diagram of xz-section of the overall beam (a) with or (b) without inclusions of graphite-wafers; distributions of extensional strain (ε_x) (c) with or (d) without graphite-inclusions; distributions of transverse shear strain (γ_{xz}) (e) with or (f) without graphite-inclusions (p = 1.0 kN, V = 200 volt).

3.4.2 Analysis of active-passive damping in the overall beam

Figure 3.4 illustrates the variations of the modal loss factors (η and η_s) with the velocity feedback control-gain (k_d) when the constrained damping layer is either made of 1-3 VEC or made of the pure viscoelastic material (VEM). The different geometric parameters of the 1-3 VEC layer are taken as, h_v = 0.1 mm, Δl_v = 0.1 mm, n_z = 1, n = 8. It may be observed from Fig. 3.4 that the damping in the overall beam significantly increases when the passive ($k_d = 0$) constraining layer becomes as an active ($k_d \neq 0$) layer. Also, this increase occurs at a steeper rate when the 1-3 VEC layer is utilized instead of the monolithic VEM layer. For any of the damping materials (pure VEM or 1-3 VEC), the difference in the magnitudes of η and η_s at any value of k_d implies the damping due to the extensional strain in the viscoelastic phase. So, in case of the pure VEM layer,

the active-passive damping in the overall beam appears due to the transverse shear strain of the viscoelastic phase (Fig. 3.4). In contrast, an indicative enhancement of active-passive damping in the ACLD treatment appears due to the extensional strain in the viscoelastic phase when the graphite-wafers are inserted within the viscoelastic layer in the form of 1-3 VEC layer. The damping in the ACLD treatment due to the transverse shear strain of the viscoelastic phase also increases for the graphite-inclusions. So, for the inclusion of graphite-wafers, the damping-capacity of the ACLD treatment increases due to the enhanced transverse shear strain in the viscoelastic phase and also due to the appearance of extensional strain in the same phase with a reasonable magnitude.

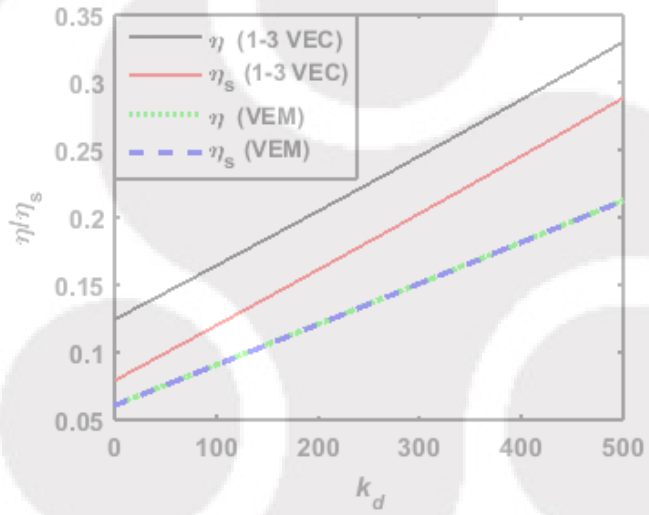

Fig. 3.4 Variations of modal loss factors (η, η_s) with the velocity feedback control-gain (k_d) (VEM: pure viscoelastic layer).

Figure 3.5 illustrates the variations of modal loss factors (η, η_s) with the thickness (h_v) of the top and bottom viscoelastic layers (Fig. 3.1 of Fig. 2.1) within the 1-3 VEC layer. The 1-3 VEC layer is comprised of eight graphite-wafers ($n=8$) with the gap (Δl_v) of 0.1 mm. Similar results in the absence of the graphite-wafers or for the pure VEM layer are also presented in the same figure (Fig. 3.5). In case of this pure VEM layer, there is no physical significance of the variation of h_v within a constant thickness of the constrained damping layer. So, the modal loss factors (η, η_s) have constant magnitudes for any value of h_v (Fig. 3.5). Also, the magnitude of η is almost equal to that of η_s. With reference

to these magnitudes of the modal loss factors (η , η_s), significantly higher magnitudes of the same damping parameters are obtained for the inclusion of graphite-wafers (Fig. 3.5).

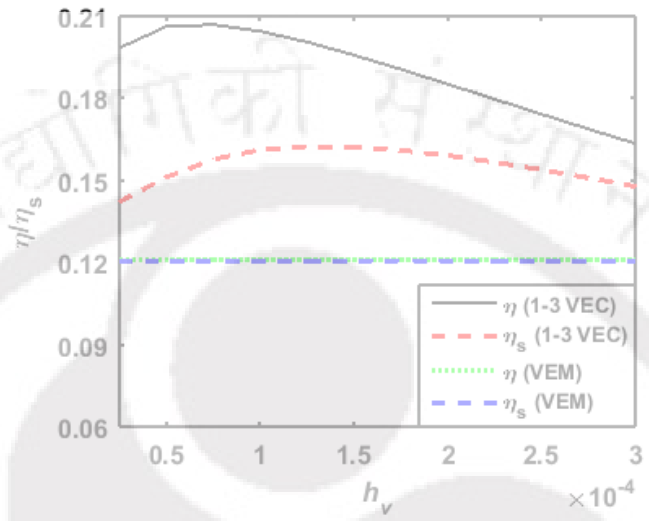

Fig. 3.5 Variations of modal loss factors (η , η_s) with the thickness (h_v , Fig. 3.1) of the top and bottom viscoelastic layers within the 1-3 VEC layer, (k_d = 200).

In fact, the transverse shear strain in the viscoelastic phase indicatively increases along with a reasonable magnitude of the extensional strain so that the active-passive damping in the overall beam increases. The main reason for this enhancement of damping or strains in the viscoelastic phase is the presence of the 2-2 VEC layer. As the thickness of the pure VEM layer in the 1-3 VEC layer increases with a constant thickness of the damping layer, the thickness of the 2-2 VEC layer decreases. So, both the extensional and transverse shear strains in the viscoelastic phase alter in such a manner that the corresponding active-passive damping in the overall beam first increases and then decreases (Fig. 3.5). This result indicates an optimum thickness (h_v) of the pure VEM layers within the 1-3 VEC layer, and it appears between 50 μm and 100 μm. On the basis of these limits, a value of h_v is considered as 100 μm for evaluation of the subsequent results.

The variations of the modal loss factors (η , η_s) with the axial gap (Δl_v) between any two consecutive graphite-wafers within the 1-3 VEC layer are illustrated in Fig. 3.6. The thickness (h_v) of the top/bottom VEM layer within the 1-3 VEC layer (Fig. 3.1) is taken as 0.1 mm. The gap (Δl_v) is increased gradually

with a constant number of graphite-wafers ($n = 8$) so that the dimension of every graphite-wafer in the x-direction decreases (Fig. 3.1). The numerical values of other geometric parameters of the 1-3 VEC layer are considered to be the same as those are taken for the previous result (Fig. 3.5).

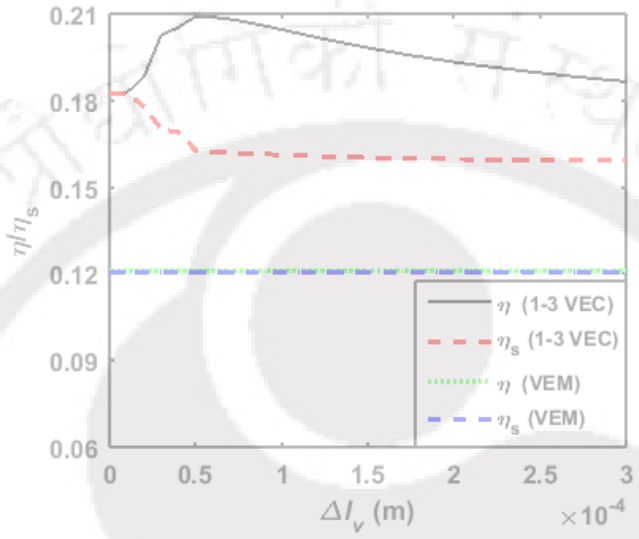

Fig. 3.6 Variations of modal loss factors (η, η_s) with the axial gap (Δl_v) between any two consecutive graphite-wafers in the 1-3 VEC layer, (k_d = 200).

It may be observed from Fig. 3.6 that the active-passive damping (η) in the overall beam significantly increases when a continuous graphite layer ($\Delta l_v = 0$) is divided into a certain number ($\Delta l_v \neq 0$) of graphite-wafers. For this division of graphite layer, the active-passive damping (η_s) due to the shear strain of the viscoelastic phase decreases while the damping ($\eta - \eta_s$) due to the extensional strain of the same phase increases. As a result, the total damping (η) in the overall beam first increases and then decreases for the gradual increment of the axial gap (Δl_v) from its zero-value. The overall result in Fig. 3.6 indicates a low value of the axial gap (Δl_v) within the 1-3 VEC layer for its better performance in the ACLD treatment, and it is presently considered as 0.1 mm for evaluating the subsequent results.

Figure 3.7 illustrates the variations of modal loss factors (η, η_s) with the number (n) of graphite-wafers in the 1-3 VEC layer. The thickness (h_v) and axial gap (Δl_v) within the 1-3 VEC layer are considered to have the same value as 0.1 mm. The number (n) of graphite-wafers along the x-direction is increased with

a constant gap (Δl_v = 0.1 mm) so that the dimension of the volumes in the same (x) direction decreases. The numerical values of other geometric parameters remain the same as those are considered in the previous result (Figs. 3.6). It may be observed from Fig. 3.7 that the characteristics in the variations of modal loss factors (η , η_s) with the number of graphite-wafers are close to those in the variations of the same parameters with the axial gap (Fig. 3.6). So, the 1-3 VEC damping layer could be configured either by changing the number (n) of graphite-wafers with a constant axial gap (Δl_v) or by changing the axial gap (Δl_v) with a constant number (n) of graphite-wafers.

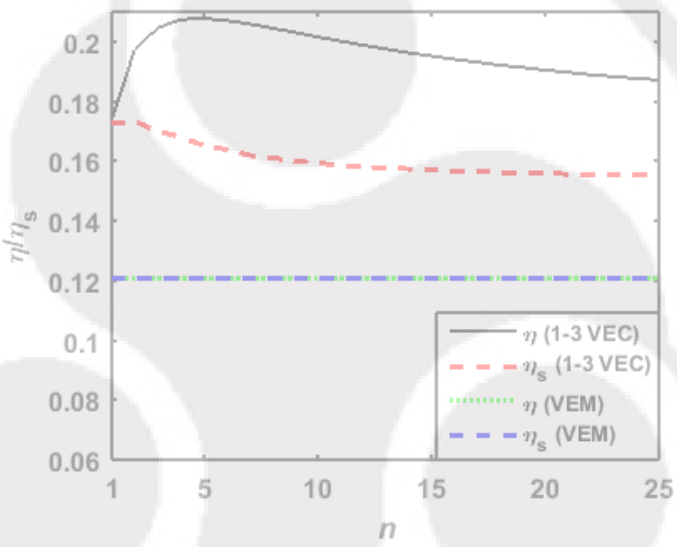

Fig. 3.7 Variations of modal loss factors (η , η_s) with the number (n) of graphite-wafers within the 1-3 VEC layer (k_d = 200).

In the foregoing results (Figs. 3.4-3.7), one (n_z = 1) 1-3 VEC layer is taken within the thickness (h_d) of the constrained damping layer. If several 1-3 VEC layers are used in the form of a laminate (Fig. 2.1(b)) within the same thickness of the damping layer, then the variations of modal loss factors (η , η_s) are demonstrated in Table 3.4. It may be observed from this table that the active-passive damping (η , η_s) in the overall beam decreases as the number of 1-3 layers increases within a specified thickness of the constrained damping layer. So, this result suggests one (n_z = 1) 1-3 VEC layer within the thickness of the damping layer of the ACLD treatment.

Table 3.4 Variations of modal loss factors (η, η_s) with the number (n_z) of 1-3 VEC layers within a specified thickness (h_d = 1 mm) of constrained damping layer (h_v = 0.1 mm, Δl_v = 0.1 mm, n = 8, k_d = 100).

n_z	η	η_s
1	0.2045	0.1611
2	0.1620	0.1435
3	0.1425	0.1345
4	0.1308	0.1279

3.4.3 Control capability of the present ACLD treatment

The aforesaid results (Figs. 3.4-3.7, Table 3.4) reveal the influences of different geometric parameters (n_z, n, h_v, Δl_v) of 1-3 VEC layer/laminate on the active-passive damping capacity of the ACLD treatment. These results may be utilized to configure the constrained 1-3 VEC layer for effective damping capacity of the ACLD treatment. Presently, the 1-3 VEC layer is configured as, n_z =1, n=8, h_v = 0.1 mm, Δl_v =0.1 mm. Using this geometric configuration of the 1-3 VEC layer, the overall beam is considered to operate under a transverse harmonic excitation at its (beam) middle span with the varying operating frequency around the fundamental natural frequency. The corresponding variations of the transverse displacement-amplitude at the middle point of the overall beam and the required control-voltage are illustrated in Figs. 3.8(a) and 3.8(b), respectively.

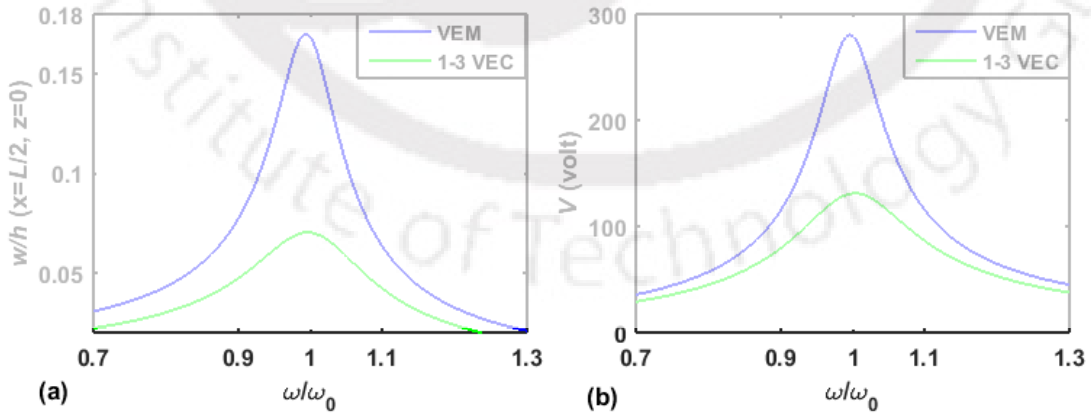

Fig. 3.8 Variations of (a) the transverse displacement-amplitude and (b) the corresponding control-voltage with the operating frequency (k_d = 100, p = 1.0 kN, ω_o is the fundamental natural frequency).

These figures (Figs. 3.8(a) and 3.8(b)) also contain the similar responses in the absence of the graphite-inclusions or for the pure VEM layer. It may be observed from Fig. 3.8(a) that the attenuation of the resonant transverse displacement-amplitude increases indicatively for the graphite-inclusions within the viscoelastic layer in the form of a 1-3 VEC layer. The maximum value of the required control-voltage also decreases indicatively (Fig. 3.8(b)). So, the present 1-3 VEC layer may be a potential damping layer for the ACLD treatment of structural vibration.

3.5 Summary

In this chapter, the active-passive damping capacity of the ACLD treatment for control of vibration of a simply-supported beam is investigated using a new 1-3 VEC damping layer. The 1-3 VEC layer is utilized instead of the traditional pure viscoelastic layer within the ACLD arrangement over the top surface of a substrate beam, and the corresponding changes in the active-passive damping characteristics of the treatment are studied through the static and dynamic banding analyses of the overall beam. The static analysis reveals enhanced magnitudes of transverse shear and extensional strains in the viscoelastic phase of the damping layer when the graphite-wafers are inserted within the viscoelastic damping layer in the form of a 1-3 VEC layer. These enhanced strains result in improved damping capacity of the ACLD treatment. The variations of this improved damping capacity of the ACLD treatment with the different geometrical parameters of the 1-3 VEC layer are evaluated, and an appropriate geometric configuration of the 1-3 VEC layer is decided for effective ACLD treatment of vibration of the simply-supported beam. Using this geometric configuration of the 1-3 VEC layer, the frequency responses of the overall beam are evaluated, and an indicative improvement of attenuation of transverse displacement-amplitude of the overall beam is observed due to the use of 1-3 VEC layer instead of the pure VEM layer within the ACLD treatment.

Chapter 4

Optimal passive damping in circular cylindrical sandwich shells with a three-layered VEC core

4.1 Introduction

In this chapter (Kumar and Panda, 2017), the concept of 1-3 VEC layer is utilized for improved PCLD/CLD treatment of vibration of a circular cylindrical shell. The overall cylindrical shell is constructed in the form of a cylindrical sandwich shell with the viscoelastic core where the thin graphite strips are inserted within the viscoelastic core following its middle surface. The identical graphite strips are oriented along the axial direction and distributed evenly around the circumference of the cylindrical shell. The physical model of this cylindrical viscoelastic composite damping layer is presented as a cylindrical laminate of three layers where two monolithic viscoelastic layers cover the top and bottom surfaces of the central viscoelastic composite layer. So, presently it is called as three-layered viscoelastic composite damping layer. In contrast to the available developments in the context of CLD treatment of shells, the contributions in this development lie in its two main objectives. The first objective is to achieve improved passive damping at all the modes of vibration of the cylindrical sandwich shell by the use of three-layered viscoelastic composite core instead of the traditional single-layered viscoelastic core. The second objective is to achieve this improvement of modal damping according to the assigned relative importance of excited modes within a frequency range of operation. It is observed in the use of single-layered viscoelastic core within an operating frequency-range that few modes are prominently excited to large resonant-amplitudes. So, it is required to provide sufficient damping to these modes in conjunction with the relative importance of corresponding resonant-amplitudes. This is now attempted by introducing the graphite-strips within the viscoelastic core in the form of three-layered viscoelastic composite core.

The graphite-strips are introduced with their optimal size and circumferential distribution by means of maximizing the weighted average loss factor of all the modal loss factors of excited modes within the operating frequency range. The relative importance (weights) of the excited modes within this weighted average loss factor is assigned in proportion to the resonant-

amplitudes appearing in the use of the single-layered viscoelastic core. This optimal configuration of the three-layered composite core is supposed to serve both the aforesaid objectives which are corroborated by an analysis of the sandwich shell. For this analysis, an FE model of the sandwich shell is developed based on the layer-wise shear deformation theory and Sander's shell theory. The numerical results are presented for substantiation of all the aforesaid objectives in the present design of a three-layered viscoelastic core or 1-3 VEC core for a circular cylindrical sandwich shell.

4.2 Present circular cylindrical sandwich shell and theoretical formulation

Figure 4.1(a) shows a schematic diagram of the circular cylindrical sandwich shell that is comprised of two face layers and a monolithic viscoelastic core. Following the middle surface of the viscoelastic core, thin graphite-stripes are embedded in the longitudinal direction as shown in Fig. 4.1(b). These inclusions of graphite-strips yield the pure viscoelastic core (Fig. 4.1(a) as a viscoelastic composite core (Fig. 4.1(b)). Its physical configuration is attributed by a laminate of two monolithic viscoelastic layers over the middle viscoelastic composite (VEC) layer (Fig. 4.1(c)). So, the laminate is presently called as a three-layered viscoelastic composite core. For inclusion of graphite-strips, the circumference of the core is divided into n_f number of equal segments with a circular span of α. Each segment contains one graphite-strip of circular span α^g along with the similar span α^v of viscoelastic phase (Fig. 4.1(b)). The thicknesses of the inner/outer viscoelastic layer and VEC layer are denoted by, h_v and h_v^2, respectively. The length, thickness and inner radius of the overall shell are denoted by, L, h and R, respectively. Within the total thickness (h) of the shell, the thicknesses of inner face layer, outer face layer and core are designated by, h_f^b, h_f^t and h_d, respectively. All the layers, as well as phase materials within the overall shell, are assumed to be perfectly bonded. For the mathematical modelling of the sandwich shell, its inner surface is taken as the reference surface. The origin of the reference curvilinear coordinate system (xyz) is located at one end of the reference surface such that the ends of the cylinder are denoted by the coordinates, $x=0$ and $x=L$. The x, y and z directions in the

curvilinear coordinate system (xyz) indicate axial, circumferential and outward radial directions, respectively as shown in Fig. 4.1.

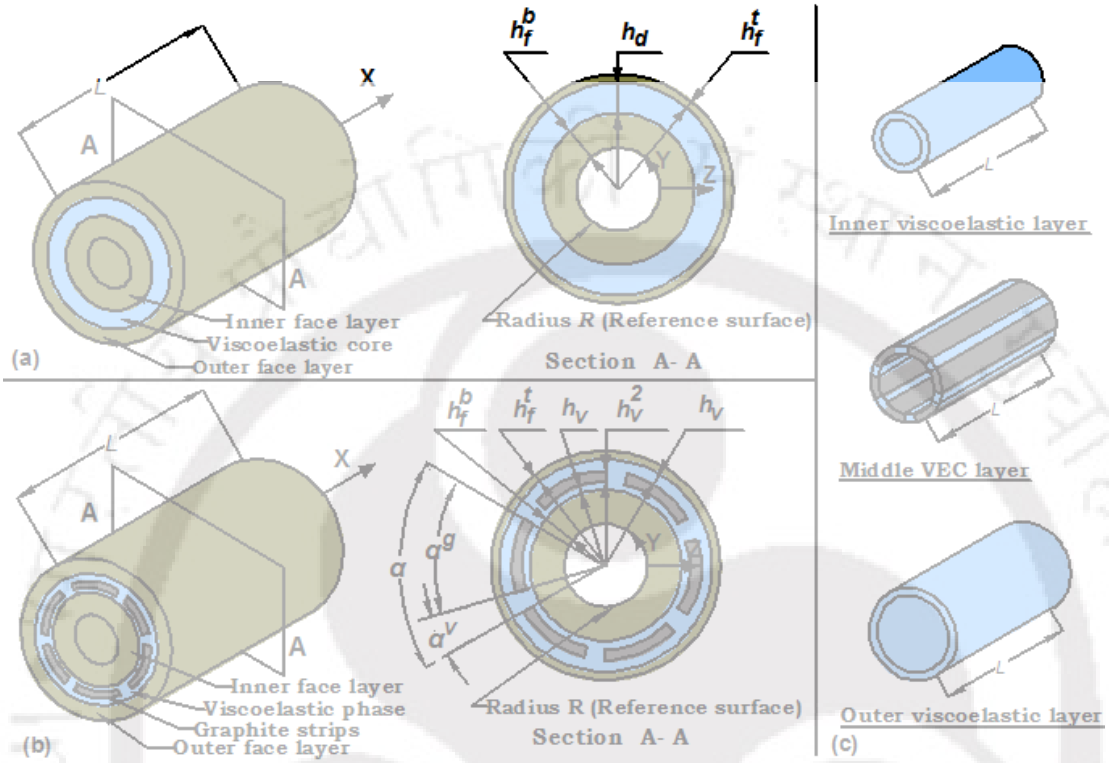

Fig. 4.1 Schematic diagrams of (a) sandwich shell with the single-layered viscoelastic core, (b) sandwich shell with three-layered viscoelastic composite core and (c) layers of the three-layered viscoelastic composite core.

With respect to the reference coordinate system, the kinematics of deformation of the overall shell is defined according to the layer-wise first order shear deformation theory (FSDT) as,

$$u^k(x,y,z)=u_0(x,y)+z_i^k\,\theta_i(x,y)\,,\quad v^k(x,y,z)=v_0(x,y)+z_i^k\,\beta_i(x,y)\,,$$

$$w^k(x,y,z)=w_0(x,y)+z_i^k\,\gamma_i(x,y) \qquad (4.1)$$

where, k/i represents the number of layers (five layers) starting from the innermost layer; repeated subscript (i) within a term represents summation over that subscript; u^k, v^k and w^k are the displacements along the x, y and z directions, respectively at any point within the k^{th} layer; u_0, v_0 and w_0 are the similar displacements at any point over the reference surface; θ_i and β_i represent the rotations of normal to the middle plane of i^{th} layer with respect to y and x axes, respectively; γ_i represents the rate of change of thickness of i^{th}

layer in the thickness direction; z_i^k stands for the thickness coordinates of different layers where the nonzero z_i^k are, $z_1^1 = z$; $z_1^2 = h_f^b$; $z_2^2 = (z - h_f^b)$; $z_1^3 = h_f^b$; $z_2^3 = h_v$; $z_3^3 = (z - h_f^b - h_v)$; $z_1^4 = h_f^b$; $z_2^4 = h_v$; $z_3^4 = h_v^2$; $z_4^4 = (z - h_f^b - h_v - h_v^2)$; $z_1^5 = h_f^b$; $z_2^5 = h_v$; $z_3^5 = h_v^2$; $z_4^5 = h_v$; $z_5^5 = (z - h_d - h_f^b)$. At any point within the k^{th} layer, the displacement components (u^k, v^k, w^k) can be written as,

$$\boldsymbol{d}^k = (\boldsymbol{d}_t + \boldsymbol{Z}_{dk}\boldsymbol{d}_r),\ \boldsymbol{d}^k = \left\{u^k \quad v^k \quad w^k\right\}^{\mathrm{T}},\ \boldsymbol{d}_t = \left\{u_0 \quad v_0 \quad w_0\right\}^{\mathrm{T}},$$

$$\boldsymbol{d}_r = \left\{(\boldsymbol{d}_{r1})^{\mathrm{T}} \quad (\boldsymbol{d}_{r2})^{\mathrm{T}} \quad (\boldsymbol{d}_{r3})^{\mathrm{T}} \quad (\boldsymbol{d}_{r4})^{\mathrm{T}} \quad (\boldsymbol{d}_{r5})^{\mathrm{T}}\right\}^{\mathrm{T}},\ \boldsymbol{d}_{ri} = \left\{\theta_i \quad \beta_i \quad \gamma_i\right\}^{\mathrm{T}}$$

$$\boldsymbol{Z}_{dk} = \left[z_{dk}^1 \quad z_{dk}^2 \quad z_{dk}^3 \quad z_{dk}^4 \quad z_{dk}^5\right],\ z_{dk}^i = \boldsymbol{I}_{(3\times3)} \otimes z_i^k \tag{4.2}$$

where, $\boldsymbol{I}_{(3\times}$ is the unit matrix of size (3×3) and $\otimes$ indicates Kronecker product. The displacement vector $(\boldsymbol{d}^k)$ can be defined by means of a generalized displacement vector $(\boldsymbol{d})$ as,

$$\boldsymbol{d}^k = (\boldsymbol{T}_t + \boldsymbol{Z}_{dk}\boldsymbol{T}_r)\boldsymbol{d}$$

$$\boldsymbol{d} = \left\{u_0 \quad v_0 \quad w_0 \quad \theta_1 \quad \theta_2 \quad \theta_3 \quad \theta_4 \quad \theta_5 \quad \beta_1 \quad \beta_2 \quad \beta_3 \quad \beta_4 \quad \beta_5 \quad \gamma_1 \quad \gamma_2 \quad \gamma_3 \quad \gamma_4 \quad \gamma_5\right\}^{\mathrm{T}} \tag{4.3}$$

where, $\boldsymbol{T}_t$ and $\boldsymbol{T}_r$ are the transformation matrices. The state of strain and the state of stress at any point within the overall shell can be written as,

$$\boldsymbol{\varepsilon}_b = \left\{\varepsilon_x \quad \varepsilon_y \quad \varepsilon_z \quad \varepsilon_{xy}\right\}^{\mathrm{T}},\ \boldsymbol{\varepsilon}_s = \left\{\varepsilon_{xz} \quad \varepsilon_{yz}\right\}^{\mathrm{T}},$$

$$\boldsymbol{\sigma}_b = \left\{\sigma_x \quad \sigma_y \quad \sigma_z \quad \sigma_{xy}\right\}^{\mathrm{T}},\ \boldsymbol{\sigma}_s = \left\{\sigma_{xz} \quad \sigma_{yz}\right\}^{\mathrm{T}} \tag{4.4}$$

where, ε_x / σ_x, ε_y / σ_y, ε_z / σ_z are the normal strains/stresses along the x, y and z directions respectively; $\varepsilon_{xy} / \sigma_{xy}$ is the in-plane shear strain/stress in the xy-plane; $\varepsilon_{yz} / \sigma_{yz}$ and $\varepsilon_{xz} / \sigma_{xz}$ are the transverse shear strains/stresses in the yz and xz-planes, respectively. According to Sander's strain-displacement relations for cylindrical shell (Reddy, 2004), the strain vectors for the displacement field (Eqs. (4.1)-(4.3)) can be written as,

$$\boldsymbol{\varepsilon}_b^k = (\boldsymbol{\varepsilon}_{bL} + \boldsymbol{z}_{Lk}^i \boldsymbol{\kappa}_{bL}^i),\ \boldsymbol{\varepsilon}_s^k = (\boldsymbol{\varepsilon}_{sL} + \boldsymbol{z}_{sk}^i \boldsymbol{\kappa}_s^i),$$

$$\boldsymbol{\varepsilon}_{bL}=\left\{\frac{\partial u_0}{\partial x}\quad\left(\frac{\partial v_0}{\partial y}+\frac{w_0}{R}\right)\quad 0\quad\left(\frac{\partial u_0}{\partial y}+\frac{\partial v_0}{\partial x}\right)\right\}^{\mathrm{T}},\quad \boldsymbol{\varepsilon}_{sL}=\left\{\frac{\partial w_0}{\partial x}\quad\frac{\partial w_0}{\partial y}-\frac{v_0}{R}\right\}^{\mathrm{T}},$$

$$\boldsymbol{\kappa}_{bL}^{i}=\left\{\frac{\partial\theta_i}{\partial x}\quad\frac{\partial\beta_i}{\partial y}\quad\gamma_i\quad\left(\frac{\partial\beta_i}{\partial x}+\frac{\partial\theta_i}{\partial y}\right)\right\}^{\mathrm{T}},\boldsymbol{\kappa}_{s}^{i}=\left\{\theta_i\quad\frac{\partial\gamma_i}{\partial x}\quad\beta_i\quad\frac{\partial\gamma_i}{\partial y}\right\}^{\mathrm{T}}\qquad(4.5)$$

where, the (m,n) elements $({}^{mn}z_{Lk}^{i},\ {}^{mn}z_{sk}^{i})$ of the matrices (z_{Lk}^{i}, z_{sk}^{i}) for z-coordinates are, ${}^{11}z_{Lk}^{i}=z_i^k$, ${}^{22}z_{Lk}^{i}=z_i^k$, ${}^{33}z_{Lk}^{i}=\partial z_i^k/\partial z$, ${}^{44}z_{Lk}^{i}=z_i^k$, ${}^{11}z_{sk}^{i}=\partial z_i^k/\partial z$, ${}^{12}z_{sk}^{i}=z_i^k$, ${}^{23}z_{sk}^{i}=\partial z_i^k/\partial z$, ${}^{24}z_{sk}^{i}=z_i^k$. In Eq. (4.5), the repeated superscript (i) indicates summation over that superscript. Equation (4.5) can also be written by expressing the layer-wise strain vectors $(\boldsymbol{\kappa}_{bL}^{i}, \boldsymbol{\kappa}_{s}^{i})$ in their generalized forms $(\boldsymbol{\kappa}_{bL}, \boldsymbol{\kappa}_{s})$ as follows,

$$\boldsymbol{\varepsilon}_b^k=(\boldsymbol{\varepsilon}_{bL}+\mathbf{Z}_L^k\boldsymbol{\kappa}_{bL}),\ \boldsymbol{\varepsilon}_s^k=(\boldsymbol{\varepsilon}_{sL}+\mathbf{Z}_s^k\boldsymbol{\kappa}_s),$$

$$\boldsymbol{\kappa}_{bL}=\left[(\boldsymbol{\kappa}_{bL}^{1})^{\mathrm{T}}\quad(\boldsymbol{\kappa}_{bL}^{2})^{\mathrm{T}}\quad(\boldsymbol{\kappa}_{bL}^{3})^{\mathrm{T}}\quad(\boldsymbol{\kappa}_{bL}^{4})^{\mathrm{T}}\quad(\boldsymbol{\kappa}_{bL}^{5})^{\mathrm{T}}\right]^{\mathrm{T}},$$

$$\boldsymbol{\kappa}_{s}=\left[(\boldsymbol{\kappa}_{s}^{1})^{\mathrm{T}}\quad(\boldsymbol{\kappa}_{s}^{2})^{\mathrm{T}}\quad(\boldsymbol{\kappa}_{s}^{3})^{\mathrm{T}}\quad(\boldsymbol{\kappa}_{s}^{4})^{\mathrm{T}}\quad(\boldsymbol{\kappa}_{s}^{5})^{\mathrm{T}}\right]^{\mathrm{T}}\qquad(4.6)$$

According to Eq. (4.6), the strain for every layer can be computed by specifying the corresponding matrices $(\mathbf{Z}_L^k, \mathbf{Z}_s^k)$ as given in Eq. (4.7),

$$\mathbf{Z}_L^1=\left[z_{L1}^1\quad 0\quad 0\quad 0\quad 0\right],\ \mathbf{Z}_s^1=\left[z_{s1}^1\quad 0\quad 0\quad 0\quad 0\right],$$

$$\mathbf{Z}_L^2=\left[z_{L2}^1\quad z_{L2}^2\quad 0\quad 0\quad 0\right],\ \mathbf{Z}_s^2=\left[z_{s2}^1\quad z_{s2}^1\quad 0\quad 0\quad 0\right],$$

$$\mathbf{Z}_L^3=\left[z_{L3}^1\quad z_{L3}^2\quad z_{L3}^3\quad 0\quad 0\right],\ \mathbf{Z}_s^3=\left[z_{s3}^1\quad z_{s3}^2\quad z_{s3}^3\quad 0\quad 0\right],$$

$$\mathbf{Z}_L^4=\left[z_{L4}^1\quad z_{L4}^2\quad z_{L4}^3\quad z_{L4}^4\quad 0\right],\ \mathbf{Z}_s^4=\left[z_{s4}^1\quad z_{s4}^2\quad z_{s4}^3\quad z_{s4}^4\quad 0\right],$$

$$\mathbf{Z}_L^5=\left[z_{L5}^1\quad z_{L5}^2\quad z_{L5}^3\quad z_{L5}^4\quad z_{L5}^5\right],\ \mathbf{Z}_s^5=\left[z_{s5}^1\quad z_{s5}^2\quad z_{s5}^3\quad z_{s5}^4\quad z_{s5}^5\right]\qquad(4.7)$$

All the materials within the domain of the overall shell are isotropic materials where the shear strains are not coupled with the extensional stresses. So, the constitutive relations for any of the phase materials within the overall shell can be written as,

$$\boldsymbol{\sigma}_b^k=\mathbf{C}_b^k\boldsymbol{\varepsilon}_b,\ \boldsymbol{\sigma}_s^k=\mathbf{C}_s^k\boldsymbol{\varepsilon}_s$$

$$\boldsymbol{C}_b^k = \frac{E^k}{\left(1+\nu^k\right)\left(1-2\nu^k\right)}\begin{bmatrix} 1-\nu^k & \nu^k & \nu^k & 0 \\ \nu^k & 1-\nu^k & \nu^k & 0 \\ \nu^k & \nu^k & 1-\nu^k & 0 \\ 0 & 0 & 0 & (0.5-\nu^k) \end{bmatrix},\ \boldsymbol{C}_s^k = \frac{E^k}{2\left(1+\nu^k\right)}\begin{bmatrix} 1 & 0 \\ 0 & 1 \end{bmatrix} \tag{4.8}$$

where, $\boldsymbol{C}_b^k$ and $\boldsymbol{C}_s^k$ are the stiffness matrices for isotropic materials corresponding to the strain vectors $\boldsymbol{\varepsilon}_b$ and $\boldsymbol{\varepsilon}_s$, respectively; E^k and ν^k are Young's modulus and Poisson's ratio, respectively for the k^{th} material/layer. It is to be noted here that the viscoelastic material (in layers, $k=2$, 3, 4) is modelled according to the complex stiffness method. So, the stiffness matrices ($\boldsymbol{C}_b^k, \boldsymbol{C}_s^k, k=2,3,4$) for this phase-material are in complex form. The ends of the overall cylindrical shell are considered as fixed ends while it is subjected to a transverse (radial) harmonic point-load ($p(t)$) at the middle span ($L/2,0,h/2$). For the corresponding vibration of the overall shell, the principle of virtual work gives,

$$\delta T_P = \int_0^{L}\int_0^{(2\pi R)}\left[\sum_{k=1}^{5}\int_{h_k}^{h_{k+1}}\left\langle(\delta\boldsymbol{\varepsilon}_b^k)^{\mathrm{T}}\boldsymbol{\sigma}_b^k + (\delta\boldsymbol{\varepsilon}_s^k)^{\mathrm{T}}\boldsymbol{\sigma}_s^k\right\rangle dz\right]dydx - (\delta w)p(t)\Big|_{\frac{L}{2},0,\frac{h}{2}} \tag{4.9}$$

$$\delta T_K = \int_0^{L}\int_0^{(2\pi R)}\left[\sum_{k=1}^{5}\int_{h_k}^{h_{k+1}}\left\langle\left\{\delta\dot{u}^k \quad \delta\dot{v}^k \quad \delta\dot{w}^k\right\}\rho^k\left\{\dot{u}^k \quad \dot{v}^k \quad \dot{w}^k\right\}^{\mathrm{T}}\right\rangle dz\right]dydx \tag{4.10}$$

where, δT_p and δT_k are the first variations of the total potential energy and the total kinetic energy respectively at any instant of time (t), δ is an operator for first variation; ρ^k is the mass density of the k^{th} layer; the dot over a parameter represents its (parameter) first-order derivative with respect to time (t); $\boldsymbol{\sigma}_b^k$ and $\boldsymbol{\sigma}_s^k$ represent the stress vectors ($\boldsymbol{\sigma}_b$, $\boldsymbol{\sigma}_s$) at any point in k^{th} layer; w (in Eq. (4.9)) is the displacement along transverse (radial) direction at the point ($L/2,0,h/2$) of applied load ($p(t)$).

4.3 FE model of the cylindrical sandwich shell

The FE model of the overall shell is derived by discretizing the cylindrical reference surface using nine-node isoparametric quadrilateral elements. The FE mesh is created by dividing the circumferential and longitudinal spans of the cylindrical reference surface such that every element is in the rectangular shape

with its edges in parallel to the circumferential and longitudinal directions. Since there is the discontinuity in the distribution of materials along the circumferential direction of middle layer ($k=3$, Figs. 4.1(b)-(c)), two kinds of elemental stacking sequence appear in the FE model. The first one is comprised of the middle viscoelastic layer while the other one is comprised of the middle graphite layer. The generalized displacement vector ($\boldsymbol{d}$) and strain vectors ($\boldsymbol{\varepsilon}_{bL}$, $\boldsymbol{\kappa}_{bL}$, $\boldsymbol{\varepsilon}_{sL}$, $\boldsymbol{\kappa}_{s}$) at a point in a typical element can be written in terms of elemental nodal displacement vector ($\boldsymbol{d}^e$) and shape function matrix ($\boldsymbol{N}_d$) as,

$$\boldsymbol{d}=\boldsymbol{N}_d\,\boldsymbol{d}^e,\ \boldsymbol{\varepsilon}_{bL}=\boldsymbol{B}_{bL}\boldsymbol{d}^e,\ \boldsymbol{\kappa}_{bL}=\boldsymbol{B}_{\kappa L}\boldsymbol{d}^e,\ \boldsymbol{\varepsilon}_{sL}=\boldsymbol{B}_{sL}\boldsymbol{d}^e,\ \boldsymbol{\kappa}_{s}=\boldsymbol{B}_{\kappa s}\boldsymbol{d}^e \tag{4.11}$$

where, the different strain-displacement matrices ($\boldsymbol{B}_{bL}, \boldsymbol{B}_{\kappa L}, \boldsymbol{B}_{sL}, \boldsymbol{B}_{ks}$) can be obtained from Eq. (4.5). Substituting Eqs. (4.8), (4.6) and (4.3) in Eqs. (4.9)-(4.10) and then using Eq. (4.11), the following expressions of δT_p^e and δT_k^e for a typical element can be obtained,

$$\delta T_P^e=\left(\delta d^e\right)^{\mathrm{T}}\left\langle \boldsymbol{K}_L^e\left(\boldsymbol{d}^e\right)-\boldsymbol{P}_M^e(\mathrm{t})\right\rangle,\ \delta T_K^e=\left(\delta\dot{\boldsymbol{d}}^e\right)^{\mathrm{T}}\boldsymbol{M}^e(\dot{\boldsymbol{d}}^e) \tag{4.12}$$

$$\boldsymbol{K}_L^e=\int_{A^e}\begin{bmatrix}\left(\boldsymbol{B}_{bL}\right)^{\mathrm{T}}\left(\boldsymbol{A}_b\boldsymbol{B}_{bL}+\boldsymbol{B}_{L1}\boldsymbol{B}_{\kappa L}\right)+\left(\boldsymbol{B}_{\kappa L}\right)^{\mathrm{T}}\left(\boldsymbol{B}_{L2}\boldsymbol{B}_{bL}+\boldsymbol{D}_L\boldsymbol{B}_{\kappa L}\right)\\+\left(\boldsymbol{B}_{sL}\right)^{\mathrm{T}}\left(\boldsymbol{A}_s\boldsymbol{B}_{sL}+\boldsymbol{B}_{s1}\boldsymbol{B}_{\kappa s}\right)+\left(\boldsymbol{B}_{ks}\right)^{\mathrm{T}}\left(\boldsymbol{B}_{s2}\boldsymbol{B}_{sL}+\boldsymbol{D}_s\boldsymbol{B}_{\kappa s}\right)\end{bmatrix}dA^e,$$

$$\boldsymbol{M}^e=\int_{A^e}\left\langle\left(\boldsymbol{N}_d\right)^{\mathrm{T}}\bar{\boldsymbol{m}}\boldsymbol{N}_d\right\rangle dA^e,$$

$$\bar{\boldsymbol{m}}=\sum_{k=1}^{5}\int_{h_k}^{h_{k+1}}\left\langle\left(\boldsymbol{T}_t\right)^{\mathrm{T}}\rho^k\boldsymbol{T}_t+\left(\boldsymbol{T}_t\right)^{\mathrm{T}}\rho^k\boldsymbol{Z}_{dk}\boldsymbol{T}_r+\left(\boldsymbol{T}_r\right)^{\mathrm{T}}\left(\boldsymbol{Z}_{dk}\right)^{\mathrm{T}}\rho^k\boldsymbol{T}_t+\left(\boldsymbol{T}_r\right)^{\mathrm{T}}\left(\boldsymbol{Z}_{dk}\right)^{\mathrm{T}}\rho^k\boldsymbol{Z}_{dk}\boldsymbol{T}_r\right\rangle dz \tag{4.13}$$

In Eq. (4.12), $\boldsymbol{P}_M^e(t)$ is the elemental nodal load vector. The different rigidity matrices ($\boldsymbol{A}_b, \boldsymbol{B}_{L1}, \boldsymbol{B}_{L2}, \boldsymbol{D}_L, \boldsymbol{A}_s, \boldsymbol{B}_{s1}, \boldsymbol{B}_{s2}, \boldsymbol{D}_s$) appearing in Eq. (4.13) are given in Eq. (4.14) where the third layer ($k=3$) is either made of graphite or made of viscoelastic material as per the elemental stacking sequences.

$$\boldsymbol{A}_b=\left(\sum_{k=1}^{5}\int_{h_k}^{h_{k+1}}\boldsymbol{C}_b^k dz\right),\ \boldsymbol{B}_{L1}=\left(\sum_{k=1}^{5}\int_{h_k}^{h_{k+1}}\boldsymbol{C}_b^k\boldsymbol{Z}_L^k dz\right),\ \boldsymbol{B}_{L2}=\left(\sum_{k=1}^{5}\int_{h_k}^{h_{k+1}}\left(\boldsymbol{Z}_L^k\right)^{\mathrm{T}}\boldsymbol{C}_b^k dz\right),$$

$$\boldsymbol{D}_L=\left(\sum_{k=1}^{5}\int_{h_k}^{h_{k+1}}\left(\boldsymbol{Z}_L^k\right)^{\mathrm{T}}\boldsymbol{C}_b^k\boldsymbol{Z}_L^k dz\right),\ \boldsymbol{A}_s=\left(\sum_{k=1}^{5}\int_{h_k}^{h_{k+1}}\boldsymbol{C}_s^k dz\right),\ \boldsymbol{B}_{s1}=\left(\sum_{k=1}^{5}\int_{h_k}^{h_{k+1}}\boldsymbol{C}_s^k\boldsymbol{Z}_s^k dz\right),$$

$$B_{s2}^{2}=\left(\sum_{k=1}^{5}\int_{h_k}^{h_{k+1}}\left(\boldsymbol{Z}_s^k\right)^{\mathrm{T}}\boldsymbol{C}_s^k dz\right),\ \boldsymbol{D}_s=\left(\sum_{k=1}^{5}\int_{h_k}^{h_{k+1}}\left(\boldsymbol{Z}_s^k\right)^{\mathrm{T}}\boldsymbol{C}_s^k\boldsymbol{Z}_s^k dz\right) \tag{4.14}$$

The governing equations of motion are derived employing the extended Hamilton's principle as given in Eq. (2.11).

$$\int_{t_1}^{t_2}\left(\delta T_K-\delta T_P\right)dt=0 \tag{2.11}$$

Introducing Eq. (4.12) in Eq. (2.11), the elemental governing equations of motion can be obtained. The assemblage of these elemental equations in the global space yields the governing equations of motion for the overall shell as,

$$\boldsymbol{M}\ddot{\boldsymbol{X}}+\boldsymbol{K}\,\boldsymbol{X}=\boldsymbol{P}_M(t),\ \boldsymbol{K}=\left(\boldsymbol{K}_e+\boldsymbol{K}_s\right) \tag{4.15}$$

where, $\boldsymbol{M}$ is the global mass matrix; $\boldsymbol{K}_e$ and $\boldsymbol{K}_s$ are the bending and transverse shear counterparts of the global stiffness matrix ($\boldsymbol{K}$); X is the global nodal displacement vector; $\boldsymbol{P}_M(t)$ is the global mechanical load vector.

4.4 Solution and estimation of damping

The complex stiffness of the viscoelastic material yields imaginary stiffness matrix ($\boldsymbol{K}$) of the overall shell, and thus it ($\boldsymbol{K}$) can be written as, $\boldsymbol{K}=(\boldsymbol{K}^R+j\boldsymbol{K}^I)$ where $\boldsymbol{K}^R=(\boldsymbol{K}_e^R+\boldsymbol{K}_s^R)$ and $\boldsymbol{K}^I=(\boldsymbol{K}_e^I+\boldsymbol{K}_s^I)$. Using this form of the stiffness matrix ($\boldsymbol{K}$), the equations of motion (Eq. (4.15)) can be written as,

$$\boldsymbol{M}\ddot{\boldsymbol{X}}+\left\langle(\boldsymbol{K}_e^R+\boldsymbol{K}_s^R)+j(\boldsymbol{K}_e^I+\boldsymbol{K}_s^I)\right\rangle\boldsymbol{X}=\boldsymbol{P}_M(t) \tag{4.16}$$

The transverse harmonic point-load is considered in the form of, $p(t)=p_0e^{j\omega t}$ ($j=\sqrt{-1}$) where p_0 is the amplitude of mechanical excitation with the operating frequency of ω. The corresponding solution (X) for the steady-state linear vibration of the overall shell can be written as (Meirovitch, 1997),

$$X=\tilde{X}e^{j\omega t},\quad \tilde{X}=\left(\boldsymbol{X}^R+j\boldsymbol{X}^I\right) \tag{4.17}$$

where, $\tilde{X}$ is a complex nodal displacement vector with the real and imaginary counterparts of $\boldsymbol{X}^R$ and $\boldsymbol{X}^I$, respectively. The solution (Eq. (4.17)) yields the governing equations (Eq. (4.16)) as,

$$\left[-\omega^2\boldsymbol{M}+\left\langle(\boldsymbol{K}_e^R+\boldsymbol{K}_s^R)+j(\boldsymbol{K}_e^I+\boldsymbol{K}_s^I)\right\rangle\right]\tilde{\boldsymbol{X}}=\boldsymbol{P}_0 \tag{4.18}$$

where, $\boldsymbol{P}_0$ is the nodal load-amplitude vector. The complex nodal displacement vector ($\tilde{\boldsymbol{X}}$) can be obtained by the solution of Eq. (4.18) and its absolute value provides the nodal displacement-amplitude vector for the steady state vibration of the shell. So, the frequency responses corresponding to the steady-state vibration of the overall shell under the transverse harmonic load can be evaluated by solving Eq. (4.18). Now, Eq. (4.18) also yields a complex eigenvalue problem for free vibration of the overall shell ($\boldsymbol{P}_0 = \boldsymbol{0}$) as,

$$\left\langle (\boldsymbol{K}_e^R + \boldsymbol{K}_s^R) + j(\boldsymbol{K}_e^I + \boldsymbol{K}_s^I) \right\rangle \boldsymbol{\psi}_i = \omega_i^2 \boldsymbol{M} \boldsymbol{\psi}_i \tag{4.19}$$

where, $\boldsymbol{\psi}_i$ is the nodal displacement vector for complex mode-shape of i^{th} mode of vibration and ω_i is the corresponding complex natural frequency. This complex natural frequency (ω_i) can also be expressed in terms of the natural frequency (ω_i^0) and modal loss factor (η_i) as given in Eq. (3.29).

$$(\omega_i)^2 = (\omega_i^0)^2 \left\langle 1 + j\eta_i \right\rangle, \ \eta_i = \mathrm{Im}(\omega_i)^2 / \mathrm{Re}(\omega_i)^2 \tag{3.29}$$

The modal loss factor (η_i) of the overall shell can be computed using Eq. (3.29). If the complex part ($\boldsymbol{K}^I = (\boldsymbol{K}_e^I + \boldsymbol{K}_s^I)$) of the stiffness matrix is considered as, $\boldsymbol{K}^I = \boldsymbol{K}_e^I$ ($\boldsymbol{K}_s^I = \boldsymbol{0}$) or $\boldsymbol{K}^I = \boldsymbol{K}_s^I$ ($\boldsymbol{K}_e^I = \boldsymbol{0}$), then the corresponding modal loss factor (η_i^e / η_i^s) appears due to the extensional or transverse shear counterpart of the strain vector. In this computation of modal loss factor, the complex eigenvalue problem (Eq. (4.19)) is to be solved. Alternatively, according to the MSE method (Johnson and Kienholz, 1982) as demonstrated in Section 2.4, the modal loss factor can also be computed by taking the real part ($\boldsymbol{K} = (\boldsymbol{K}_e^R + \boldsymbol{K}_s^R)$) of the stiffness matrix ($\boldsymbol{K}$) in solving the eigenvalue problem (Eq.(4.19)). In this method (MSE method), the natural frequency (ω_q) and modal loss factor (η_q) at a typical (q^{th}) mode of free vibration ($\boldsymbol{P}_M(t) = 0$) of the overall shell can then be obtained according to Eqs. (2.18) and (2.19).

$$\omega_q^2 = (\boldsymbol{\varphi}_q^{\mathrm{T}} \boldsymbol{K}^R \boldsymbol{\varphi}_q) / (\boldsymbol{\varphi}_q^{\mathrm{T}} \boldsymbol{M} \boldsymbol{\varphi}_q) \tag{2.18}$$

$$\eta_q = (\boldsymbol{\varphi}_q^{\mathrm{T}} \boldsymbol{K}^I \boldsymbol{\varphi}_q) / (\boldsymbol{\varphi}_q^{\mathrm{T}} \boldsymbol{K}^R \boldsymbol{\varphi}_q) \tag{2.19}$$

The modal loss factors (η_q^e / η_q^s) corresponding to the extensional/transverse shear counterpart of the strain vector can also be estimated using Eq. (2.21).

$$\eta_q = \eta_q^e + \eta_q^s$$

$$\eta_q^e = (\boldsymbol{\varphi}_q^{\mathrm{T}} \boldsymbol{K}_e^I \boldsymbol{\varphi}_q) / (\boldsymbol{\varphi}_q^{\mathrm{T}} \boldsymbol{K}^R \boldsymbol{\varphi}_q) \ , \ \eta_q^s = (\boldsymbol{\varphi}_q^{\mathrm{T}} \boldsymbol{K}_s^I \boldsymbol{\varphi}_q) / (\boldsymbol{\varphi}_q^{\mathrm{T}} \boldsymbol{K}^R \boldsymbol{\varphi}_q) \tag{2.21}$$

4.5 Results and discussions

In this section, the damping characteristics of the cylindrical sandwich shell are presented. First, the effects of different geometric parameters of the three-layered viscoelastic composite core on the damping characteristics of the overall shell are presented. Next, an optimal geometric configuration of the three-layered core is decided with an objective of improved damping over the conventional use of the single-layered viscoelastic core. The utility of this configuration is subsequently substantiated by means of evaluating the modal loss factors as well as the frequency responses of the sandwich shell for each of the single-layered and three-layered viscoelastic cores. The sandwich shell is presently taken in its symmetrical and unsymmetrical forms. For the symmetrical shell, the face layers are of equal thickness (h_f) of 2 mm within a total thickness (h) of 5 mm. In the unsymmetrical shell, the thicknesses of the outer and inner face layers are taken as 0.2 mm and 4 mm, respectively within a total thickness (h) of 5.2 mm. The length (L) and inner radius (R) for both the cylindrical shells are taken as 1 m and 0.5 m, respectively. The geometric parameters ($h_v, h_v^2, \alpha^v, n_f$) of the three-layered viscoelastic core are taken in different proportions for the present investigation on its damping-capacity. The face layers are considered to be made of Steel ($E = 210$ GPa, $\nu = 0.3$, $\rho = 7850$ kg/m^3) while the strips in VEC layer are made of graphite ($E = 250$ GPa, $\nu = 0.3$, $\rho = 1400$ kg/m^3 (Jones, 1999)). The material for the viscoelastic phase is considered to be made of butyl rubber (Jones, 2001). The properties of this viscoelastic material vary with the operating frequency and temperature. For the sake of simplicity in the present computation, the average properties are assumed for the operation of the overall shell around its lowest natural frequency at room temperature (35°C). These average properties are $E = 20(1+0.9j)$ MPa, $\nu = 0.49$ and $\rho = 920$ kg/m^3.

In order to verify the present FE formulation, the dimensionless natural frequencies (Ω) and modal loss factors (η) of the sandwich shell with single-

layered viscoelastic core are computed for its first five natural modes and plotted in Fig. 4.2 together with the similar results available in (Ramesh and Ganesan, 1994). The dimensionless natural frequency (Ω) is defined as (Ramesh and Ganesan, 1994), $\Omega = \rho_f t_f R\omega^2 / E_f$ (ρ_f and E_f are mass density and Young's modulus of face layers, respectively; R is the mean radius of the shell; ω is the natural frequency in rad/s; t_f and t_c are the thicknesses of face layer and core, respectively). It may be observed from this figure (Fig. 4.2) that the present results are in good agreement with the available FE results in (Ramesh and Ganesan, 1994) and it infers the accuracy of the present FE formulation in theoretical prediction of damping in the sandwich circular cylindrical shell with the viscoelastic core.

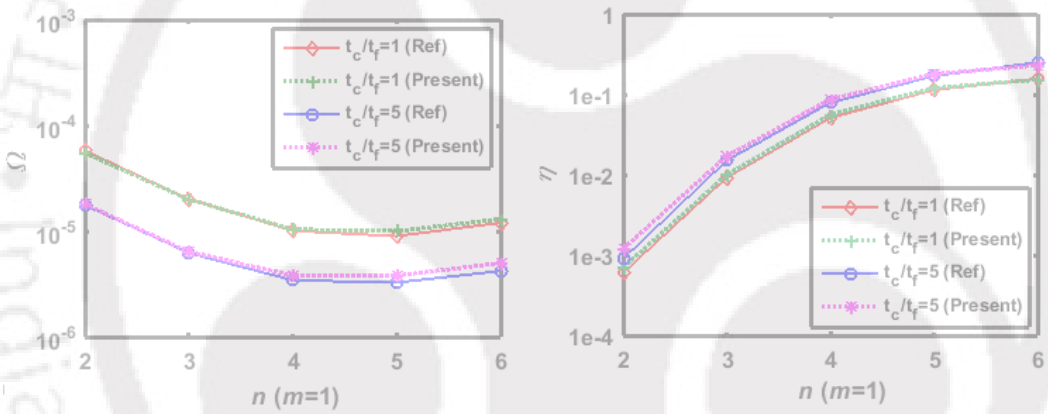

Fig. 4.2 Verification of the present FE formulation (m and n are the longitudinal and circumferential mode numbers, Ref: Ramesh and Ganesan, 1994).

It is known that the damping in a CLD treatment arises due to the strains in the constrained viscoelastic layer. So, a study on the distributions of extensional and transverse shear strains within the three-layered composite core is performed by taking a typical geometric configuration of the overall shell as, $L = 1$ m, $R = 0.5$ m, $h = 5.2$ mm, $h_f^b = 4$ mm, $h_f^t = 0.2$ mm, $h_d = 1$ mm, $h_v = 0.25$ mm, $h_v^2 = 0.5$ mm, $\alpha = 6^o$, $\alpha^g = 5^o$, $\alpha^v = 1^o$, $n_f = 60$. The overall shell (Fig. 4.1(a) or Fig. 4.1(b)) is considered to undergo bending deformation in the form of a typical bending mode-shape ($m = 1$, $n = 4$, m and n are the longitudinal and circumferential mode numbers). This bending mode of deformation is normalized for the maximum nodal transverse deflection of 0.1 and plotted in

Figs. 4.3(a) and 4.3(d) over the circumference of the shell for both the single-layered and three-layered cores, respectively. The corresponding distributions of extensional (ε_y) and transverses (γ_{yz}) shear strains at a cross-section (yz-plane at $x = L/2$) of the overall shell are evaluated. These results are then plotted over the circumference of the annular cross-section of the overall shell as presented in Figs. 4.3(b)-(c) and Figs. 4.3(e)-(f) for single-layered and three-layered cores, respectively. It may be observed from Fig. 4.3(e) that the extensional strain (ε_y) in the three-layered core appears with its indicative magnitudes at the circumferential gaps among the graphite strips. The maximum value of ε_y within the single-layered/three-layered core arises around the antinodes of the mode-shape (Figs. 4.3(b) and 4.3(e)).

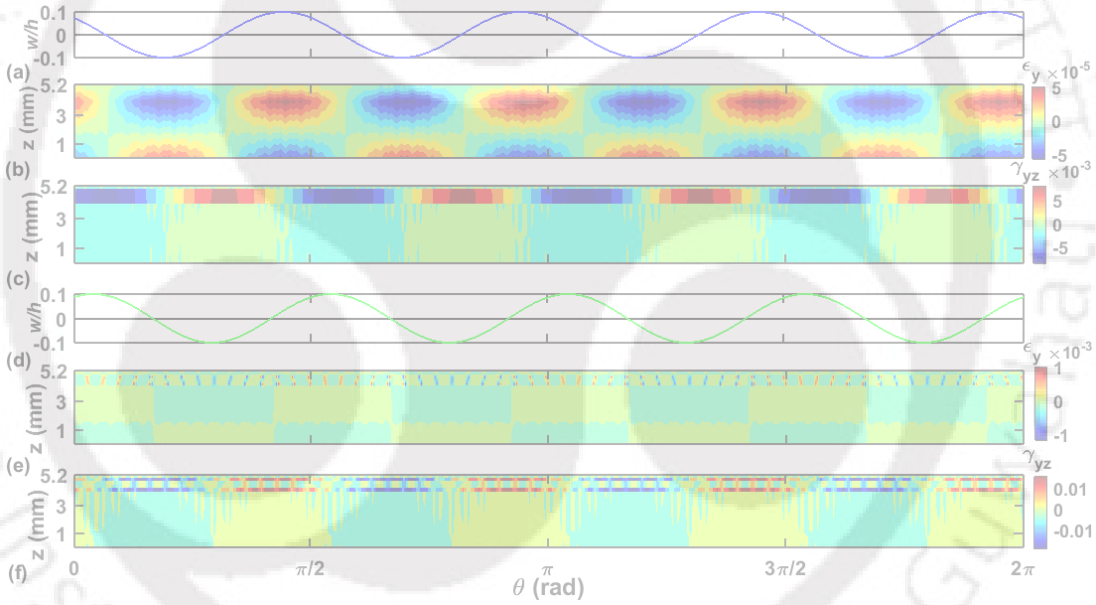

Fig 4.3 Mode shape ($m=1$, $n=4$) over the circumference of the shell for (a) single-layered/(d) three-layered core; distributions of ε_y for (b) single-layered/(e) three-layered core; distributions of γ_{yz} for (c) single-layered/(f) three-layered core.

It is important to observe that the maximum magnitude of ε_y increases due to the use of three-layered core instead of single-layered core. From Figs. 4.3(c) and 4.3(f), it may be observed that the transverse shear strain (γ_{yz}) appears with its maximum magnitude around the nodes of the mode-shape. The nature of distribution of γ_{yz} in single-layered core (Fig. 4.3(c)) is a known fact.

But, for the three-layered core (Fig. 4.3(f)), γ_{yz} appears with indicative magnitudes within the viscoelastic phase over the top and bottom surfaces of the graphite strips. Similar to the extensional strain, the maximum magnitude of shear strain also increases due to the use of the three-layered core instead of the single-layered core. These improvements in the magnitudes of strains (ε_y, γ_{yz}) within the core indicate enhanced damping in the overall shell. This initial observation is further substantiated by the subsequent dynamic analysis of the overall sandwich shell.

A narrow operating frequency-range around the lowest natural frequency of the sandwich shell is considered in the present study. This frequency-range includes first five natural bending modes as the natural frequencies of circular cylindrical shell structure are closely spaced in the frequency domain. All these natural modes are of fundamental longitudinal mode number ($m = 1$) while they are identified by the different circumferential mode numbers (n). The magnitudes of modal loss factors corresponding to these natural modes are computed either using complex mode-shapes (Eq. (4.19)) or using real mode-shapes (MSE method, Eq. (2.18)) of the shell. These results are furnished in Table 4.1 for both the symmetrical and unsymmetrical shells.

Table 4.1 Comparison of modal loss factor computed either using complex mode-shape (η_{CMS}) or using real mode-shape (η_{MSE}, MSE method) (Error (%) = $\left|(\eta_{CMS}-\eta_{MSE})/\eta_{CMS}\right|\times 100$, $r_c = h_v^2/h_d$).

Shell type	η /Error	$n=4$	$n=5$	$n=6$	$n=7$	$n=8$
Unsymmetrical shell (r_c=0.8, $\alpha^v = 1^o$, n_f=72)	η_{MSE}	0.0193	0.0241	0.0357	0.0499	0.0609
	η_{CMS}	0.0163	0.0194	0.0283	0.0399	0.0494
	Error (%)	18.40	24.23	26.14	25.06	23.28
Symmetrical shell (r_c=0.7, $\alpha^v = 2^o$, n_f=72)	η_{MSE}	0.0212	0.0573	0.1261	0.2070	0.2649
	η_{CMS}	0.0185	0.0513	0.1152	0.1912	0.2473
	Error (%)	14.59	11.69	9.46	8.26	7.12

It may be observed from this table that the assumption of real mode-shape (in MSE method) yields indicative errors in the estimation of modal loss factors. So, presently the modal loss factors are computed using complex mode-shapes according to Eq. (4.19).

The damping characteristics of the sandwich shell are studied based on the aforesaid natural modes. As an initial study, the modal loss factors ($\eta = \eta_q$, $\eta_s = \eta_q^s$, $\eta_e = \eta_q^e$) of the symmetrical and unsymmetrical cylindrical shells with single-layered viscoelastic core are evaluated for different values of core-thickness (h_d). Figures 4.4(a) and 4.4(b) demonstrate these results. The same results are also illustrated in Table 4.2.

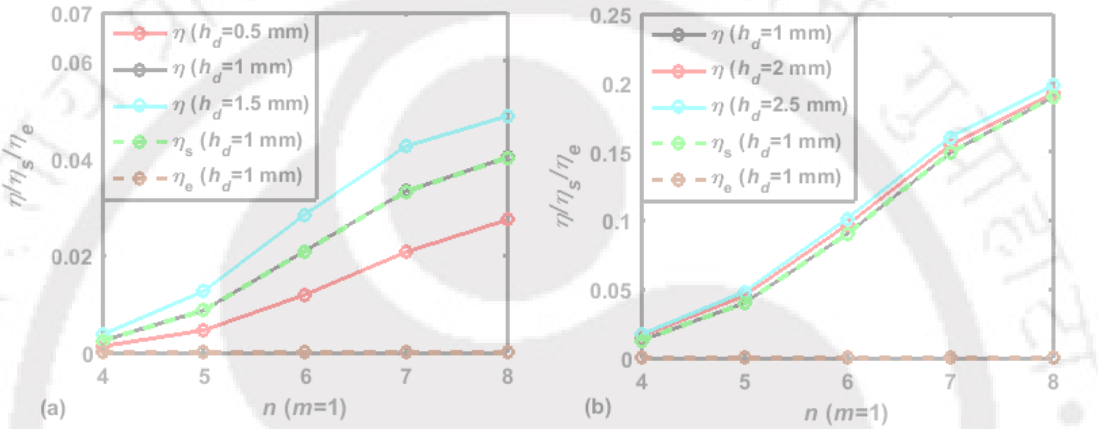

Fig. 4.4 Variations of modal loss factors ($\eta / \eta_s / \eta_e$) with the thickness (h_d) of single-layered viscoelastic core of (a) unsymmetrical ($h_f^b = 4$ mm, $h_f^t = 0.2$ mm) and (b) symmetrical ($h_f^b = h_f^t = 2$ mm) sandwich shells.

Table 4.2 Variation of the modal loss factor (η) with the thickness (h_c) of the single-layered viscoelastic core.

	η for unsymmetrical sandwich shell				
h_d (mm)	$n=4$	$n=5$	$n=6$	$n=7$	$n=8$
0.5	0.0013	0.0046	0.0119	0.0207	0.0273
1	0.0025	0.0087	0.0209	0.0332	0.0402
1.5	0.0037	0.0126	0.0284	0.0425	0.0487
	η for symmetrical sandwich shell				
h_d (mm)	$n=4$	$n=5$	$n=6$	$n=7$	$n=8$
1	0.0128	0.0398	0.0900	0.1490	0.1895
2	0.0158	0.0452	0.0966	0.1545	0.1920
2.5	0.0172	0.0480	0.1013	0.1604	0.1979

It may be observed from these figures and Table 4.2 that the magnitude of modal loss factor (η) at every natural mode of the unsymmetrical shell increases with the increasing thickness of the viscoelastic core. But, this change

occurs in an insignificant manner when the shell becomes a symmetrical shell (Fig. 4.4(b)). For any of these shells with a typical core-thickness of 1 mm, the corresponding variations of η_s and η_e (Fig. 4.4) indicate that the damping in the shell arises mainly due to the transverse shear deformation of the viscoelastic core. It is a known fact in case of the use of the single-layered viscoelastic core. Now, the improvement of damping for the use of the present three-layered core instead of the single-layered core is demonstrated in the subsequent results.

Figure 4.5(a) demonstrates the variations of modal loss factor at different natural modes of the unsymmetrical sandwich shell when the thickness of VEC layer within the three-layered core increases from its zero-value. The thickness (h_d) of the core is taken as 1 mm while the same (h_v^2) of VEC layer is varied in terms of a fraction ($r_c = h_v^2 / h_d$) of total core-thickness (h_d).

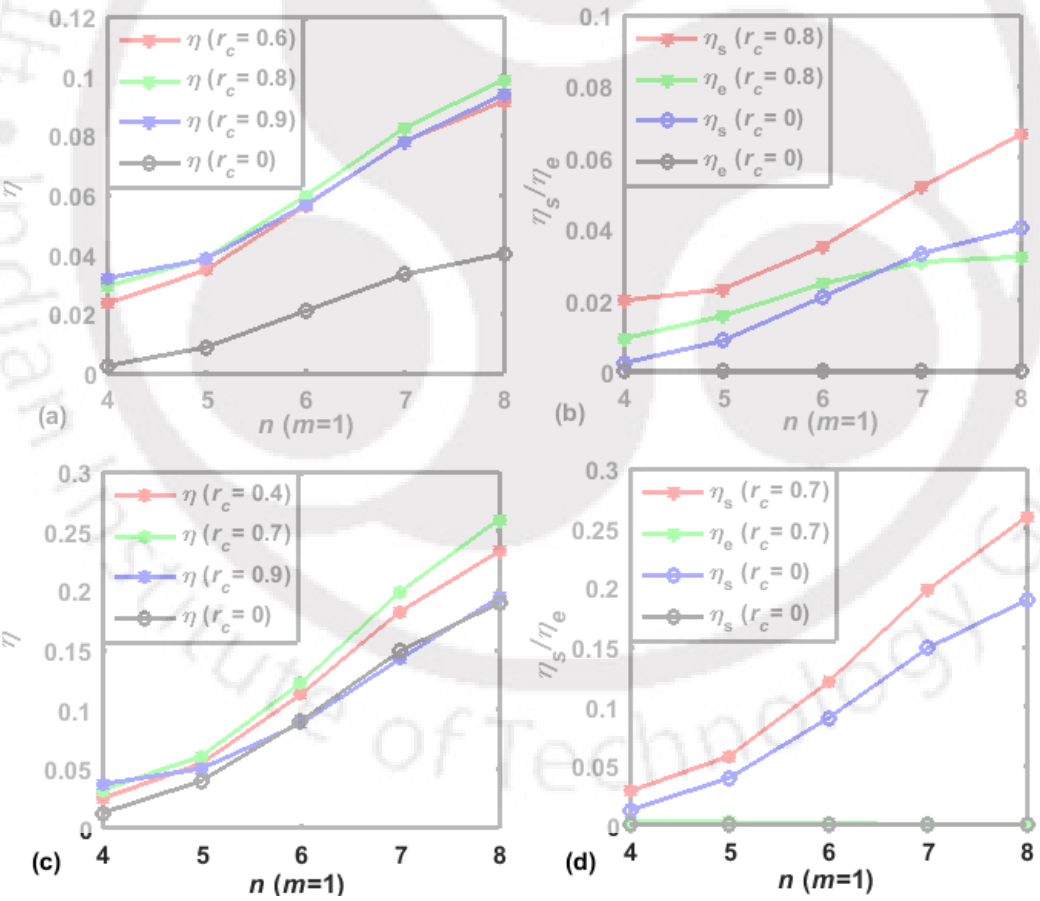

Fig. 4.5 Variations of modal loss factors ($\eta / \eta_s / \eta_e$) with the thickness of VEC layer ($\alpha^v = 0.01°, n_f = 72$) for (a)-(b) unsymmetrical and (c)-(d) symmetrical sandwich shells.

It may be observed from Fig. 4.5(a) that the damping in the overall shell significantly increases when the viscoelastic composite core ($r_c > 0$) is used instead of the pure viscoelastic core ($r_c = 0$). It may also be observed that the maximum damping in the overall shell appears at a certain thickness (h_v^2) of the VEC layer within the composite core ($r_c > 0$). This improvement of damping occurs due to the enhancement of both the transverse shear and extensional strains (Fig. 4.5(b)) in the core. Similar results for the symmetric sandwich shell are presented in Figs. 4.5(c)-(d). These results also show that the damping in the overall shell increases due to the use of VEC layer ($r_c > 0$) and the maximum damping appears at a certain thickness of VEC layer. But this increase of damping does not occur in such a significant manner as that appears in the unsymmetrical shell (Fig. 4.5(a)). The results, as given in Fig. 4.5, are also presented in Table 4.3. These results (Fig. 4.5 and Table 4.3) indicate improved damping in the cylindrical sandwich shells for the use of present three-layered viscoelastic core.

Table 4.3 Variation of the modal loss factor (η) with the thickness of VEC layer (r_c) in the three layered viscoelastic core.

	η for unsymmetrical sandwich shell				
r_c	$n=4$	$n=5$	$n=6$	$n=7$	$n=8$
0.6	0.0234	0.0347	0.0562	0.0781	0.0914
0.8	0.0292	0.0387	0.0596	0.0825	0.0987
0.9	0.0318	0.0385	0.0566	0.0778	0.0937
0	0.0025	0.0087	0.0209	0.0332	0.0402
	η for symmetrical sandwich shell				
r_c	$n=4$	$n=5$	$n=6$	$n=7$	$n=8$
0.4	0.0251	0.0545	0.1126	0.1820	0.2328
0.7	0.0323	0.0607	0.1221	0.1988	0.2599
0.9	0.0371	0.0502	0.0880	0.1424	0.1942
0	0.0128	0.0398	0.0900	0.1490	0.1895

Figure 4.6 illustrates the effect of the circumferential gap (α^v, Fig. 4.1(b)) between any two consecutive graphite-strips in VEC layer on the modal damping in unsymmetrical (Fig. 4.6(a))/symmetrical (Fig. 4.6(b)) sandwich shell. These results are also illustrated in Table 4.4. The circumferential gap (α^v) is increased with a constant number (n_f) of graphite-strips or gap (α) within the

VEC layer.

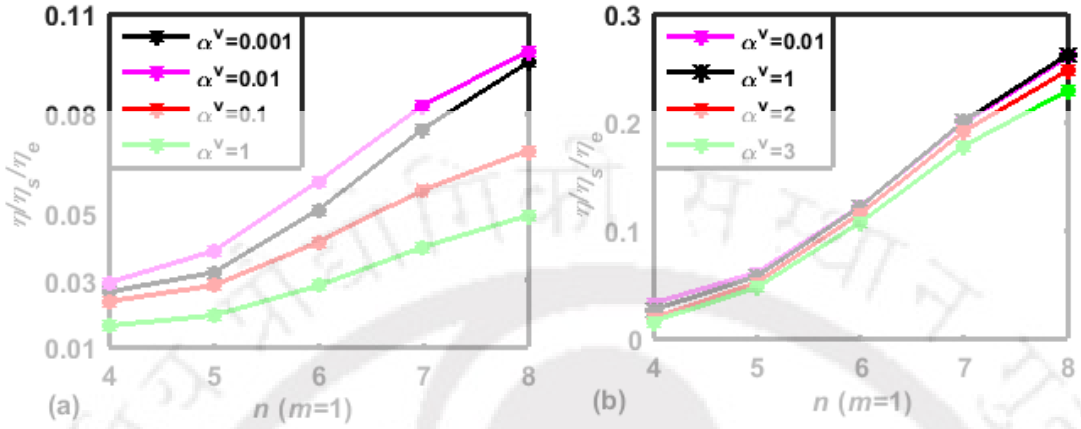

Fig. 4.6 Variations of modal loss factors ($\eta/\eta_s/\eta_e$) with the circumferential gap (α^v in degree) in the VEC layer for (a) unsymmetrical (r_c = 0.8, n_f =72) and (b) symmetrical (r_c = 0.7, n_f = 72) sandwich shells.

It may be observed from Fig. 4.6(a) or Table 4.4 that this gap (α^v) has an indicative influence on damping in the unsymmetrical shell (Fig. 4.6(a) or Table 4.4) and it (α^v) would be to its optimal value for achieving maximum damping-capacity of the three-layered viscoelastic core. In comparison to the unsymmetrical shell, the gap (α^v) has less influence on damping in the symmetric shell (Fig. 4.6(b) or Table 4.4).

Table 4.4 Variation of the modal loss factor (η) with the circumferential gap (α^v in degree) in the VEC layer.

α^v	η for unsymmetrical sandwich shell				
(degree)	$n=4$	$n=5$	$n=6$	$n=7$	$n=8$
0.001	0.0292	0.0387	0.0596	0.0825	0.0987
0.01	0.0264	0.0323	0.0511	0.0754	0.0953
0.1	0.0236	0.0284	0.0414	0.0571	0.0689
1	0.0163	0.0194	0.0283	0.0399	0.0494
α^v	η for symmetrical sandwich shell				
(degree)	$n=4$	$n=5$	$n=6$	$n=7$	$n=8$
0.01	0.0323	0.0607	0.1221	0.1988	0.2599
1	0.0260	0.0572	0.1216	0.2005	0.2619
2	0.0185	0.0513	0.1152	0.1912	0.2473
3	0.0154	0.0470	0.1069	0.1778	0.2286

Figure 4.7 represents similar results for the variation of number (n_f) of graphite-strips in the VEC layer. These results are also tabulated in Table 4.5.

The n_f is varied with a constant gap (α^v) between any two consecutive strips. It may be observed from Fig. 4.7 or Table 4.5 that the damping in the unsymmetrical sandwich shell at any of its natural modes varies with the number of graphite-strips while that does not appear in a significant manner for the symmetrical sandwich shell.

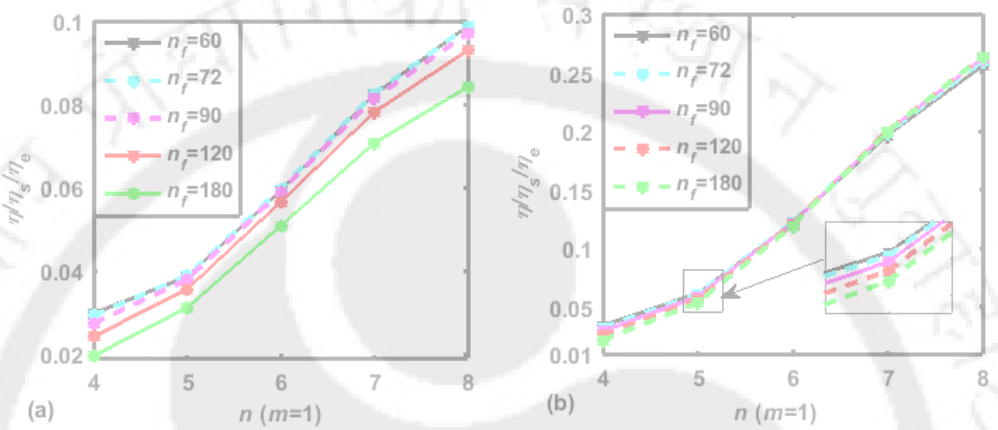

Fig. 4.7 Variations of modal loss factors ($\eta/\eta_s/\eta_e$) with the number (n_f) of graphite-strips within the VEC layer for (a) unsymmetrical (r_c =0.8, $\alpha^v = 0.01^o$) and (b) symmetrical (r_c =0.7, $\alpha^v = 0.01^o$) sandwich shells.

Table 4.5 Variation of the modal loss factor (η) with the number (n_f) of graphite-strips within the VEC layer.

	η for unsymmetrical sandwich shell				
n_f	$n=4$	$n=5$	$n=6$	$n=7$	$n=8$
60	0.0297	0.0385	0.0592	0.0823	0.0987
72	0.0292	0.0387	0.0596	0.0825	0.0987
90	0.0274	0.0379	0.0589	0.0814	0.0970
120	0.0241	0.0355	0.0564	0.0781	0.0929
180	0.0195	0.0311	0.0508	0.0706	0.0842
	η for symmetrical sandwich shell				
n_f	$n=4$	$n=5$	$n=6$	$n=7$	$n=8$
60	0.0340	0.0615	0.1215	0.1965	0.2557
72	0.0323	0.0607	0.1221	0.1988	0.2599
90	0.0295	0.0590	0.1217	0.1999	0.2623
120	0.0258	0.0565	0.1207	0.2001	0.2633
180	0.0217	0.0537	0.1193	0.1998	0.2636

4.5.1 Optimal geometric configuration of the three-layered viscoelastic composite core

The foregoing results (Figs. 4.5-4.7) indicate improved damping in the sandwich shell when the three-layered viscoelastic core is used instead of the traditional single-layered viscoelastic core of the same core-thickness. This improved damping appears mainly due to the inclusion of stiffer graphite-strips where the size and geometric arrangement of these strips are also important facts for this improved damping. So that, the corresponding geometric parameters (r_c, α^v, n_f) are very important factors in achieving improved damping over the damping in the use of the single-layered viscoelastic core. In order to raise this enhancement of damping to the maximum extent, the size and distribution of the inclusions in the three-layered viscoelastic core are to be made in an optimal manner. This infers the optimal values of the geometric parameters (r_c, α^v, n_f) for the objective of maximum damping. In case of the operation of the shell at a natural mode, the objective for this optimization problem may be taken as the maximization of the corresponding modal loss factor with respect to the geometric parameters (r_c, α^v, n_f). But, it is a little difficult to decide a similar objective in case of the operation of the shell under a dynamic load of varying operating frequency within a frequency range. Because, several resonances may appear at different natural modes and all these resonant-amplitudes are to be attenuated effectively by means of one geometric configuration of the three-layered core. Presently, it is attempted by defining a weighted average loss factor ($\bar{\eta}$) as,

$$\bar{\eta} = \sum_m \sum_n w''_{(m,n)} \eta_{(m,n)}, \quad w''_{(m,n)} = w_{(m,n)} / \sum_m \sum_n w_{(m,n)} \tag{4.20}$$

where, $\eta_{(m,n)}$ and $w''_{(m,n)}$ are the modal loss factor and the corresponding weight for the excited mode (m,n). The weights ($w''_{(m,n)}$) imply the relative importance of each of the quantity of the average quantity ($\bar{\eta}$). Note that, the main objective is to attenuate all the resonant-amplitudes effectively by means of superior damping over that in the use of the single-layered core. So, presently the relative importance ($w''_{(m,n)}$, weights) of the excited modes ($\eta_{(m,n)}$) is taken based on the resonant-amplitudes ($w_{(m,n)}$) appearing in the use of the single-layered core. For

the present FE model of the overall shell, the amplitude ($w_{(m,n)}$) at a resonant frequency is taken as the maximum one among all the nodal transverse displacement-amplitudes. For achieving maximum improvement of modal loss factors ($\eta_{(m,n)}$) at excited modes in accordance with these weights, the corresponding optimal values of the parameters (r_c, α^v, n_f) could be determined by maximization of average loss factor ($\bar{\eta}$) with respect to the same parameters. As a consequence, the number of excited modes (m,n) and the corresponding resonant-amplitudes ($w_{(m,n)}$) generally depend on the kind of applied load/excitation with varying frequency. So, the optimal configuration of the three-layered viscoelastic core is specific to the applied load/excitation with varying frequency. Presently, a transverse (radial) harmonic point-load with varying operating frequency (ω) (at a point ($L/2, 0^o$) on the outer surface of the shell) is considered for demonstrating the optimal values of the parameters (r_c, α^v, n_f) or optimal configuration of the three-layered core. Under this load, the frequency responses of the unsymmetrical and symmetrical sandwich shells with the single-layered viscoelastic core ($r_c = 0$) are evaluated within an operating frequency-range as illustrated in Fig. 4.8.

In Fig. 4.8, the maximum nodal transverse displacement-amplitude ($(w/h)_{\max}$) and the displacement-amplitude ($(w/h)_{\text{load point}}$) at the point of applied load are plotted at every frequency within the frequency range. The excited modes are of fundamental longitudinal mode numbers ($m=1$) while they are separated by the circumferential mode numbers (n). At every resonant frequency (Fig. 4.8), the maximum nodal transverse displacement-amplitude is almost equal to the transverse displacement-amplitude at the point of applied load. So, presently the resonant-amplitudes are taken at the point of applied load. In general, this kind of observation may not appear, and then the maximum nodal transverse displacement-amplitude is to be taken at every resonant frequency. However, for the present symmetrical/unsymmetrical shell, the excited modes ($m=1, n$) and the corresponding weights ($w''_{(m,n)}$) can be obtained from the responses in Fig. 4.8.

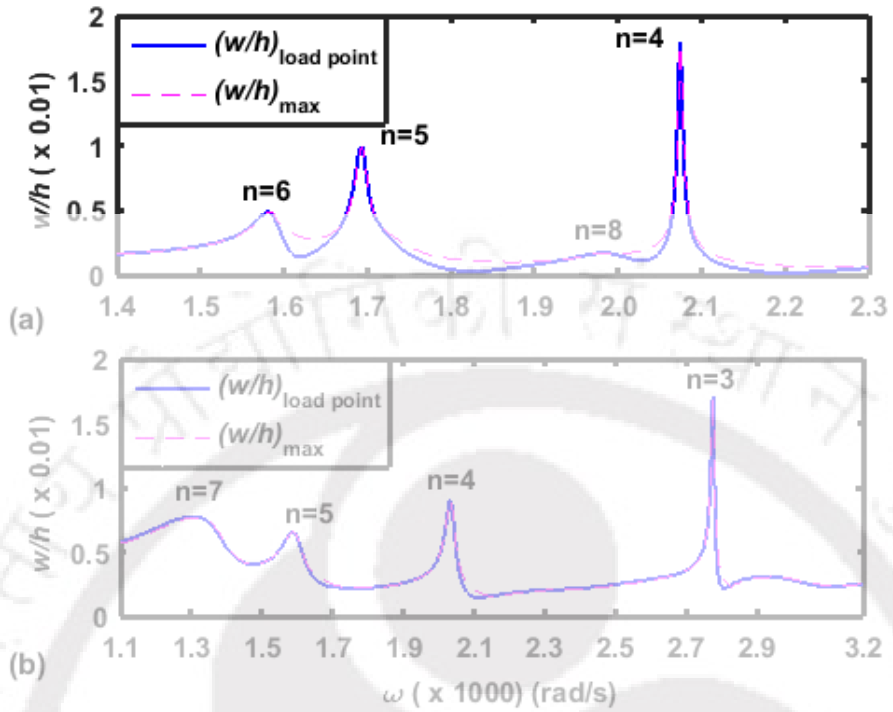

Fig. 4.8 Frequency responses of the (a) unsymmetrical and (b) symmetrical cylindrical sandwich shells comprised of the single-layered viscoelastic core.

Accordingly, the expressions of average loss factor ($\bar{\eta}$) are determined using Eq. (4.20) as,

$$\bar{\eta}\big|_{\substack{\text{unsymmetrical}\\ \text{shell}}} = w''_{(1,4)}\eta_{(1,4)} + w''_{(1,5)}\eta_{(1,5)} + w''_{(1,6)}\eta_{(1,6)} + w''_{(1,8)}\eta_{(1,8)} \tag{4.21}$$

$$\bar{\eta}\big|_{\substack{\text{symmetrical}\\ \text{shell}}} = w''_{(1,3)}\eta_{(1,3)} + w''_{(1,4)}\eta_{(1,4)} + w''_{(1,5)}\eta_{(1,5)} + w''_{(1,7)}\eta_{(1,7)} \tag{4.22}$$

For optimal geometric configuration of the three-layered core in each of the sandwich shells, these expressions of $\bar{\eta}$ are maximized within the physical bounds of the geometric parameters (r_c, α^v, n_f). The bounds of these parameters for a core-thickness (h_d) of 1 mm are chosen from the initial study (Figs. 4.5-4.7) as, $0.5 \le r_c \le 0.95$, $0.001^o \le \alpha^v \le 0.1^o$ and $50 \le n_f \le 100$ for the unsymmetrical shell. As per the present form of $\eta_{(m,n)}$ (Eqs. (4.21) and (4.22)) and FE formulation, the direct search method (Deb, 2012) is presently utilized for maximization of $\bar{\eta}$. This direct search method is presently utilized in its simplest type as Exhaustive Search Method (Deb, 2012) by means of generating a 3D mesh within the aforesaid axial limits (bounds) of the parameters. First, a coarse 3D mesh is generated, and the magnitudes of $\bar{\eta}$ at all the grid-points are

computed. These results are illustrated in Fig. 4.9(a) for the unsymmetrical sandwich shell.

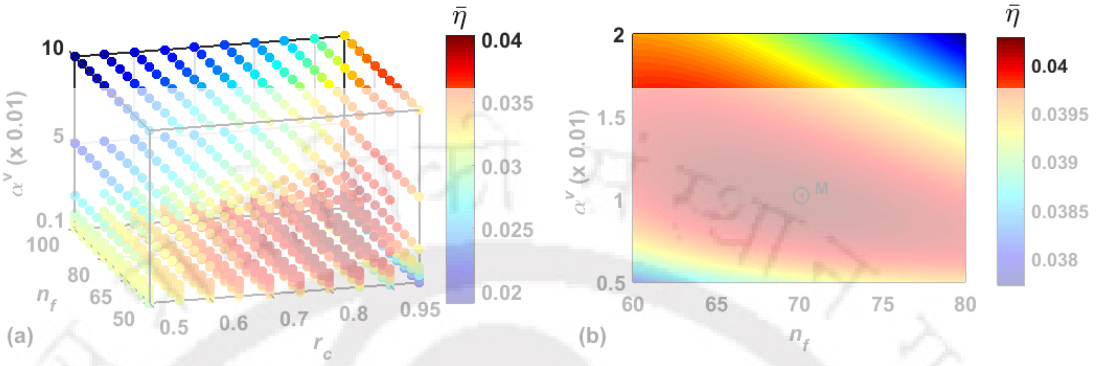

Fig. 4.9 (a) Variation of $\bar{\eta}$ for unsymmetrical sandwich shell at different grid points of 3D mesh with the axial direction of r_c, α_v, n_f; (b) contour plot of the variation of $\bar{\eta}$ in 2D plane of α_v and n_f at $r_c = 0.85$ (M-point for maximum $\bar{\eta}$).

At any set of values of α^v and n_f within their bounds, it may be observed from Fig. 4.9(a) that the magnitude of $\bar{\eta}$ reaches to its maximum value when the value of r_c is at its maximum limit ($r_c = 0.95$). This indicates a required thickness of pure viscoelastic layers within the three-layered core in few microns. As it may be difficult to achieve physically, presently a value of this parameter (r_c) is taken as 0.85 that is also very near to its maximum limit ($r_c = 0.95$). At this plane of r_c, the maximum magnitude of $\bar{\eta}$ is bracketed by a new set of bounds of other two parameters (α^v and n_f) as, $0.005^o \le \alpha^v \le 0.02^o$ and $60 \le n_f \le 80$ (Fig. 4.9(a)). Following these bounds of α^v and n_f over $r_c = 0.85$, a 2D fine mesh is created and the magnitudes of $\bar{\eta}$ are again evaluated at all the grid-points in order to plot a contour for the variation of $\bar{\eta}$ within the specified bounds around its ($\bar{\eta}$) maximum magnitude. Figure 4.9(b) illustrates this contour of $\bar{\eta}$ where the optimal values of the parameters are identified as, $\alpha^v = 0.01^o$ and $n_f = 70$ at the value of r_c as 0.85. The same procedure is followed for the optimal values of the parameters (r_c, α^v, n_f) in case of the symmetrical shell as illustrated in Figs. 4.10(a) and 4.10(b).

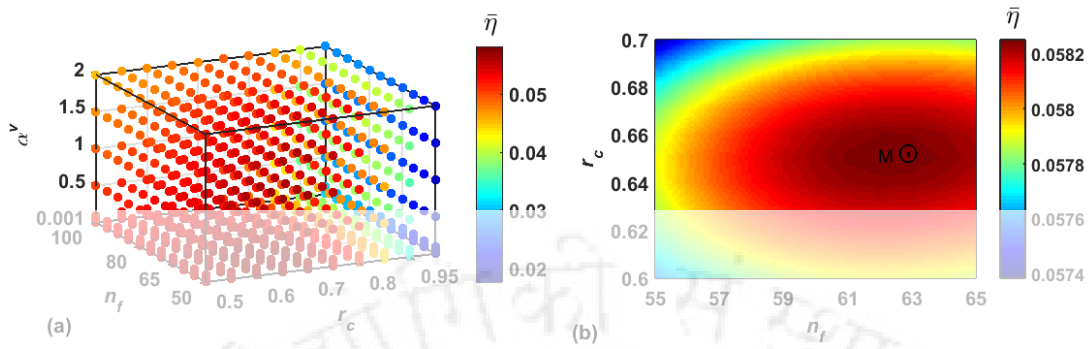

Fig. 4.10 (a) Variation of $\bar{\eta}$ for symmetrical sandwich shell at different grid points of 3D mesh with the axial direction of r_c, α_v, n_f; (b) contour plot of the variation of $\bar{\eta}$ in 2D plane of r_c and n_f at $\alpha_v = 0.01^o$ (M-point for maximum $\bar{\eta}$).

Unlike the unsymmetrical shell, the magnitude of $\bar{\eta}$ for the symmetrical shell approaches to its maximum value when the value of α^v is at its minimum limit ($\alpha^v = 0.001^o$, Fig. 4.10(a)). As it ($\alpha^v = 0.001^o$) may be difficult to achieve physically, a value of this parameter (α^v) is presently taken as, 0.01^o. At this plane ($\alpha^v = 0.01^o$), the bounds for other two parameters (r_c, n_f) around the maximum value of $\bar{\eta}$ are taken as, $0.6 \le r_c \le 0.7$ and $55 \le n_f \le 65$ (Fig. 4.10(a)). Within these bounds at the plane of $\alpha^v = 0.01^o$, the contour plot (Fig. 4.10(b)) for the variation of $\bar{\eta}$ shows the optimal values of the parameters as, r_c = 0.65 and n_f = 63.

Using this optimally configured three-layered viscoelastic composite core, the modal loss factors at the excited modes are evaluated. The corresponding improvements in the magnitudes of modal loss factors over the similar magnitudes in the use of single-layered core are tabulated in Table 4.6. The relative importance (weights) of the excited modes is also furnished in the same table. It may be observed from this table that the modal damping increases at all the modes for the use of the present three-layered viscoelastic core. More importantly, these improvements of modal loss factors appear following the same trend of relative importance (weights) of excited modes. Specifically, the maximum/minimum improvement of modal loss factor occurs at the mode of largest/smallest weight (Table 4.6). Thus, the resonant-amplitudes at the prominently excited modes (appearing in the use of single-layered core) could be

attenuated effectively by means of the optimally configured three-layered composite core.

Table 4.6 Weights ($w''_{(m,n)}$) and improvements of modal loss factors ($(\eta_{3L}-\eta_{1L})/\eta_{1L}$, subscripts $1L$ and $3L$ are for single-layered and three-layered viscoelastic cores) at different excited modes of symmetrical and unsymmetrical shells.

Natural Modes	$n=3$, $m=1$	$n=4$, $m=1$	$n=5$, $m=1$	$n=6$, $m=1$	$n=7$, $m=1$	$n=8$, $m=1$
Symmetrical sandwich shell						
$w''_{(m,n)}$	0.42	0.24	0.16	-------	0.18	-------
$(\eta_{3L}-\eta_{1L})/\eta_{1L}$	7.2	0.98	0.21	-------	0.26	-------
Unsymmetrical sandwich shell						
$w''_{(m,n)}$	-------	0.53	0.28	0.14	-------	0.05
$(\eta_{3L}-\eta_{1L})/\eta_{1L}$	-------	11.51	3.47	1.78	-------	1.43

For further corroboration of this utility of present three-layered core, the frequency responses of the symmetrical and unsymmetrical shells with optimally configured three-layered core are evaluated at the point of loading and plotted in Fig. 4.11.

It may be observed from this figure that the optimally configured three-layered core significantly attenuates all the resonant-amplitudes. Also, this attenuation of resonant-amplitudes occurs following the assigned relative importance (weights, Table 4.6) of the excited modes. So, the damping at any of the excited modes significantly increases when the three-layered viscoelastic core is used instead of single-layered viscoelastic core. Also, the damping characteristics of the single-layered core are indicatively refined by the use of optimally configured three-layered core in such a manner that the difference among the resonant-amplitudes (in the use of the single-layered core) reduces significantly (Fig. 4.11). With reference to this observation, it may be noted that the three-layered core indicatively reduces the fluctuation of vibration-amplitude in the operation of the structure under the excitation of varying frequency. This kind of advantage in the use of traditional single-layered viscoelastic core for passive damping treatment of a sandwich shell could not be achieved. So, the present three-layered viscoelastic composite core is a promising material for

damping of sandwich structures although it is to be used in its appropriate geometric configuration depending on the properties of the structural problem.

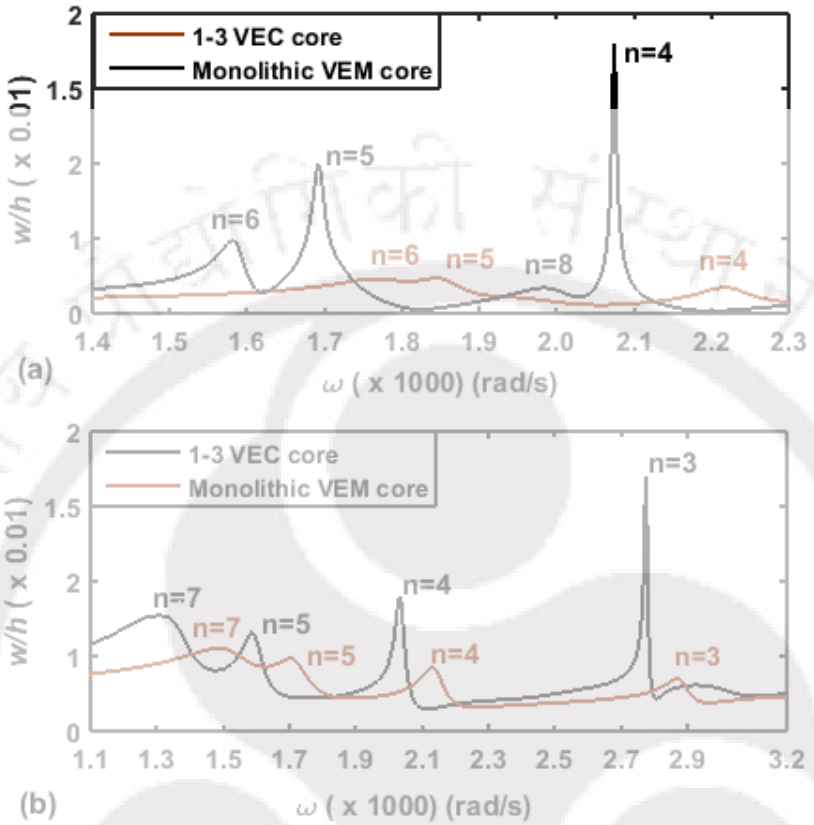

Fig. 4.11 Frequency responses of the (a) unsymmetrical and (b) symmetrical sandwich shells either comprised of the single-layered core or comprised of the three-layered core (modes with *m*=1).

4.6 Summary

A circular cylindrical sandwich shell with the three-layered viscoelastic composite core is proposed in this chapter, and its passive damping characteristics are analyzed. The new viscoelastic composite core is comprised of graphite-strips embedded longitudinally within the cylindrical monolithic viscoelastic core at its middle surface. The physical configuration of the composite core is attributed in the form of a cylindrical laminate of two monolithic viscoelastic layers over the inner and outer surfaces of the middle viscoelastic composite layer so that it is called as the three-layered viscoelastic composite core. The damping characteristics of the overall sandwich shell are analyzed by developing an FE model based on the layer-wise shear deformation theory and Sander's shell theory. The analysis reveals significantly improved passive damping in the sandwich shell for the use of the present three-layered

viscoelastic core instead of the traditional single-layered monolithic viscoelastic core. This improved damping arises due to the embedded graphite-strips which indicatively enhance transverse shear as well as extensional strains within the viscoelastic core. This enhancement of damping significantly depends on the size and circumferential distribution of the graphite-strips within the viscoelastic core. So, an optimal geometric configuration of the three-layered composite core is demonstrated for effective damping in the shell under its operation within a frequency range. A weighted average loss factor of modal loss factors of excited modes is taken as the objective function that is maximized for optimal size and distribution of the graphite strips. The weights of excited modes are taken based on the resonant-amplitudes appearing in the use of the traditional monolithic viscoelastic core. The numerical results corresponding to the use of this optimally configured three-layered core reveal significantly improved modal damping at any of the excited modes over the damping in the use of the traditional single-layered monolithic viscoelastic core. This improvement of damping at different excited modes of vibration appears following their (excited modes) assigned relative importance (weights). As these weights are taken in proportion to the resonant-amplitudes appearing in the use of single-layered core, the difference among these resonant-amplitudes significantly reduces due to the use of the optimally configured three-layered core. That infers reduced fluctuation of vibration-amplitude under a dynamic load of varying frequency. So, the present three-layered viscoelastic composite core is a promising material for damping of sandwich structures.

Chapter 5

A design of ACLD treatment for vibration control of circular cylindrical shell structures using three-layered VEC

5.1 Introduction

This chapter deals with the ACLD treatment of vibration of circular cylindrical shell structures (Panda and Kumar, 2016). In this context of ACLD treatment of cylindrical shell structures, an indicative number of studies have been reported in the literature (Chapter 1, Section 1.4). In all these and similar available studies, the constrained damping layer in the ACLD arrangement is taken as the monolithic viscoelastic material (VEM) layer, and the damping arises mainly through its (VEM layer) transverse shear strain. Unlike this conventional use of the monolithic VEM layer, the present three-layered VEC layer, as presented in Chapter 4, is supposed to experience enhanced transverse shear strains along with the reasonable extensional/compressional strains. So, an improved ACLD treatment of vibration of circular cylindrical shell structures may be obtained by the use of the present three-layered VEC instead of the traditional monolithic VEM layer, and it is investigated theoretically in this chapter.

Besides the design of the new three-layered VEC for ACLD treatment of shells, emphasis has also been placed in selection of piezoelectric material for the active constraining layer. A good actuation capability of piezoelectric material is the primary requirement in its selection as a material for the active constraining layer. Along with this requirement, flexibility and conformability of the piezoelectric constraining layer are other two important requirements particularly for the host structure of curved boundary surface. So, the uses of flexible polymer based piezoelectric fiber-reinforced composites (PFCs) in ACLD treatment have been reported in the literature (Ray and Reddy, 2005; Ray and Pradhan, 2006; Li and Narita, 2012). Different types of PFCs are proposed in the literature till the date (Chapter 1, Section 1.2). Among these PFCs, the continuous piezoelectric fiber-reinforced composites have superior actuation capability. But, most of these PFCs have not much flexibility and conformability because of the long, thin, brittle and continuous piezoelectric fibers. These shortcomings can be alleviated by their use in the patch-form. But it infers the use of the ACLD treatment in the patch-

form instead of its (ACLD) layer-form, and it may result its (ACLD) lesser damping/control capacity. Fortunately, only one type of the available continuous piezoelectric fiber-reinforced composites by the name of vertically reinforced 1-3 PFC (Smith and Auld, 1991) has sufficient flexibility and conformability. For the orientation of its fibers in the thickness direction, the fibers are of small length that facilitates to have its (1-3 PFC) sufficient flexibility and conformability. It has the primary actuation capability in the thickness mode of deformation while it also has good actuation capability in flexure mode of deformation (Ray and Pradhan, 2006). So, this PFC (Smith and Auld, 1991) can be used within the ACLD arrangement in the layer-form for control of vibration of a structure with curved boundary surface. Presently, this vertically reinforced 1-3 PFC is taken as the material of active constraining layer since the ACLD arrangement is considered in the layer-form for achieving its (ACLD) superior damping/control capability in control of vibration of circular cylindrical shell structures.

A common issue in the design of any structural piezoelectric control system is to control several modes of vibration of the overall smart structure effectively, and it is generally achieved by the use of the piezoelectric actuators in the form of the patches which are optimally/appropriately configured within the domain of the overall smart structure (Wang and Wang, 2000; Ray and Reddy, 2004; Bruant et al. 2010). Now, for the use of the piezoelectric actuator in the layer-form, it is a little difficult to achieve the same control activity as that is provided by the patches of the piezoelectric actuator. However, it may be achieved through the arrangement of the patches of surface-electrodes over the surfaces of the piezoelectric actuator layer, and the same is carried out in the present ACLD arrangement for control of several modes of vibration of circular cylindrical shell structure using the treatment in the layer-form. In this connection, a fruitful strategy for the arrangement of the electrode-patches over the surface of the actuator layer is proposed for effective control of several modes of vibration of the shell.

A host structure of thin-walled circular cylindrical shell is chosen at present because of its frequent applications in various engineering structures like aircraft fuselages, piping systems, naval halls of submarines, etc. In these applications, this structural element is subjected to dynamic mechanical loads while it may operate under high thermal environment. For structures under high thermal environment, the available studies (Shen, 2004; Pradyumna and Bandyopadhyay, 2010; Du and Li, 2013; Haghighi et al., 2014; Kulkarni et al.,

2015) recommend functionally graded materials (FGMs) (Koizumi, 1993) made of ceramic and metal constituents. So, the present circular cylindrical shell is considered to be made of FGM and the effect of its temperature on the damping characteristics of the present ACLD layer is also another objective of this study. The overall study is carried out in the following manner considering all the aforesaid aspects in the present ACLD treatment of vibration of an FG circular cylindrical shell.

First, an arrangement of ACLD layer throughout the outer surface of a FG circular cylindrical shell is demonstrated using three-layered VEC or 1-3 VEC layer, 1-3 PFC layer, velocity-sensors and electrode-patches. Subsequently, an electric potential function is assumed for the use of electrode-patches and a geometrically nonlinear coupled electro-visco-elastic incremental finite element (FE) model of the overall FG shell is developed. Using this FE model, the frequency responses of the overall shell in the absence or the presence of temperature within the FG shell are evaluated for the numerical analysis of its (overall shell) damping characteristics. In this numerical analysis, first the suitability of the present arrangement of electrode-patches over the surfaces of 1-3 PFC actuator/constraining layer is substantiated with reference to the objective of controlling several modes of vibration of the shell. Next, the utility of the present 1-3 VEC layer in the ACLD treatment is illustrated by using it (VEC layer) instead of the traditional monolithic VEM layer. This illustration also includes the effects of various geometric parameters in the design of 1-3 VEC layer on the active-passive damping characteristics of the ACLD treatment. Finally, the effects of temperature and material properties of the FG shell on the damping characteristics of the ACLD layer are furnished.

The major aspects of this study can be stated as: (a) design of 1-3 VEC damping layer for improved ACLD treatment of circular cylindrical shell structure, (b) effective control of several modes of vibration of the aforesaid structure using electrode-patches over the surface of active constraining layer of ACLD treatment, (c) a fruitful strategy in the arrangement of electrode-patches for achieving effective control of several modes of vibration using only one configuration of the electrode-patches.

5.2 Present FG circular cylindrical shell with ACLD layer

The component layers of the present three-layered VEC in the cylindrical coordinates are shown in Fig. 4.1(c). On the assemblage of these component

layers, a 1-3 VEC appears in the form of a thin cylinder as shown in Fig. 5.1. Using this 1-3 VEC as the material for constrained damping layer of ACLD treatment, the arrangement of the present FG circular cylindrical shell is illustrated in Fig. 5.2.

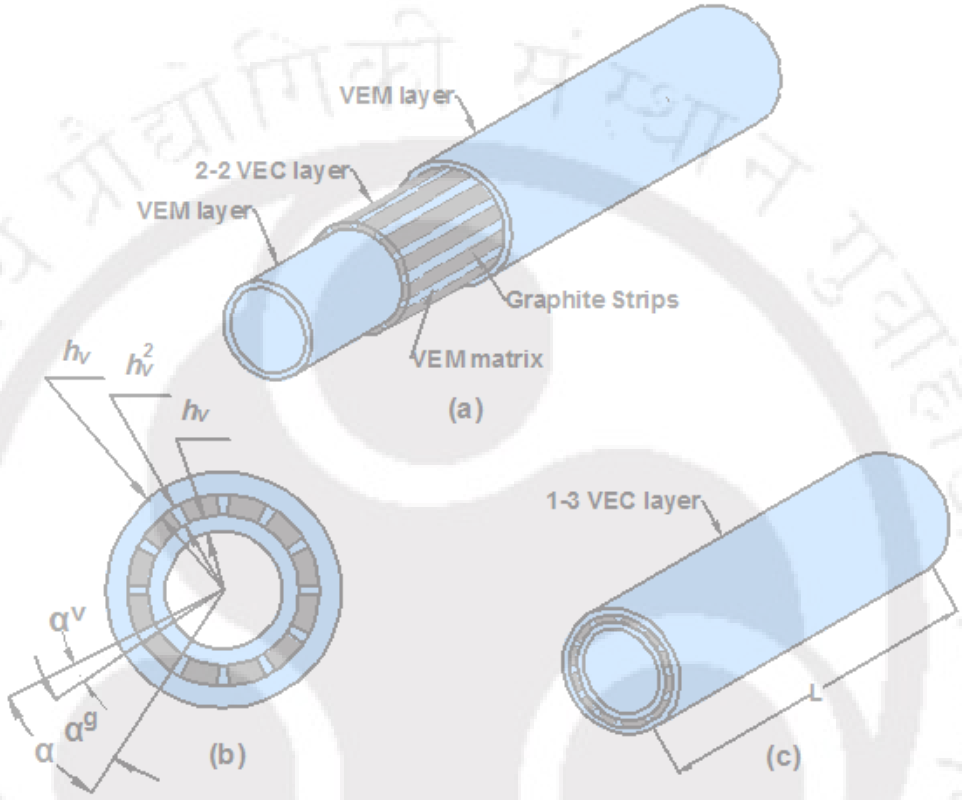

Fig. 5.1 Schematic diagrams of (a) component layers of 1-3 VEC layer (b) cross section of the laminated layers and (c) 1-3 VEC layer.

The substrate FG shell is made of two homogeneous and isotropic materials such as ceramic and metal. Its inner and outer surfaces are ceramic rich and metal rich surfaces, respectively. The inner surface is exposed to a high temperature (T_c) and the outer surface is always exposed to room temperature (T_m = 300 K) so that the ACLD arrangement (Fig. 5.2) is free from the thermal effect. The surfaces parallel to the inner and outer surfaces of the host FG shell are assumed as isothermal surfaces and the temperature varies in the radial/thickness direction only. The constraining layer is made of vertically/radially reinforced 1-3 PFC. Its piezoelectric fibers are aligned in the yz-plane of the curvilinear coordinate system and oriented along the thickness (z) direction. The inner surface of this PFC layer is considered to be fully electrode-surface that is also grounded to have zero electric potential. The outer surface of the same PFC layer is printed with

electrode-patches according to the following strategy. The external electric potential is supplied to these electrode-patches for activating the PFC layer.

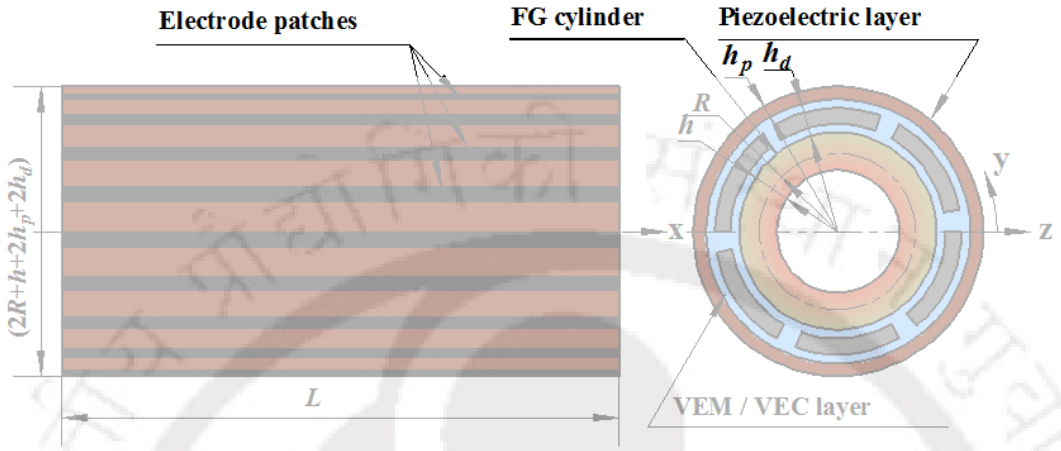

Fig. 5.2 Schematic diagram of a substrate FG shell integrated with the ACLD layer over its outer surface.

5.2.1 Arrangement of electrode-patches

The overall FG circular cylindrical shell is considered to operate under a mechanical harmonic excitation. The operating frequency is considered to be varied within a range of frequency. Since the natural frequencies of circular cylindrical shell element are closely spaced in the frequency-domain, several modes of vibration of the shell may appear within this specified range of the operating frequency. So, the actuator-layer is to be configured in an appropriate manner such that it could control all the modes of vibration effectively within the range of operating frequency of interest. In configuring this actuator-layer, it (actuator-layer) is primarily supposed to enhance the transverse shear strain within the constrained damping layer. Since this strain may not be distributed in uniform manner over the xy-plane especially for asymmetric bending modes, the actuator-layer has to act following the nature of the local strain. It implies the variation of the actuation force over the xy-plane of the curvilinear coordinate system (Fig. 5.2). This variation of actuation force is presently achieved by locating the electrodes in the form of patches while every electrode-patch is activated as per the local requirement of actuation. The locations of the electrode-patches can easily be decided following a mode-shape of vibration of the overall shell. But, since the mode of vibration of the overall shell changes during operation, it is a little difficult to determine the appropriate locations of the patches. Although a

suitable optimal algorithm may ease this difficulty, presently a new strategy is proposed in locating the electrode-patches for effective control of all the modes of vibration within a frequency-range of operation. The outer circumference of the PFC layer is divided into a number (n_e) of small identical segments ($\alpha_E(^o)$). Every segment is again divided into two parts among which one ($\alpha_E^p(^o)$) is printed with electrode and other one ($\alpha_E^g(^o)$) is left as it is. Every such printed electrode is continuously distributed in the longitudinal direction over the outer surface of the PFC layer as shown in Fig. 5.2. The number of circumferential divisions mainly depends on the maximum circumferential mode number (n) within the operating frequency-range. For a higher circumferential mode number (n), the number of circumferential divisions is to be increased. Presently, the modes of fundamental longitudinal mode number ($m=1$) are considered for the analysis. So, the electrode-patches are considered to have a length equal to that of the substrate cylinder. For higher longitudinal mode mummer ($m>1$), similar strategy could be followed as that is for the circumferential modes (n). With this configuration of the electrode-patches, the actuator-layer is supposed to act following the time-varying nature of local strain in the constrained layer around every electrode-patch. This is presently executed employing the velocity feedback control strategy by means of locating velocity sensors at the middle points of the electrode-patches. The electric potential to every electrode-patch is supplied according to its local velocity and the local actuation force around an electrode-patch is expected to enhance the transverse shear strain of the constrained layer at the same location.

5.3 Finite element formulation

In this section, a geometrically nonlinear coupled electro-visco-elastic incremental finite element model of the overall FG shell (Fig. 5.2) is derived. The overall shell is considered to be comprised of five layers as shown in Fig. 5.3. These layers are designated by the symbol k/i as per its value as 1, 2, 3, 4 and 5 for the host FG shell, first VEM layer, 2-2 VEC layer, second VEM layer and piezoelectric layer, respectively. Since the geometry of the graphite phase-volumes in the 2-2 VEC layer is defined in the macro-scale, it is not possible to treat it (VEC) as a macroscopically homogenized composite material. So, the analysis is carried out

considering the phases of VEC layer in explicit manner (macro-scale) as demonstrated in Fig. 5.3.

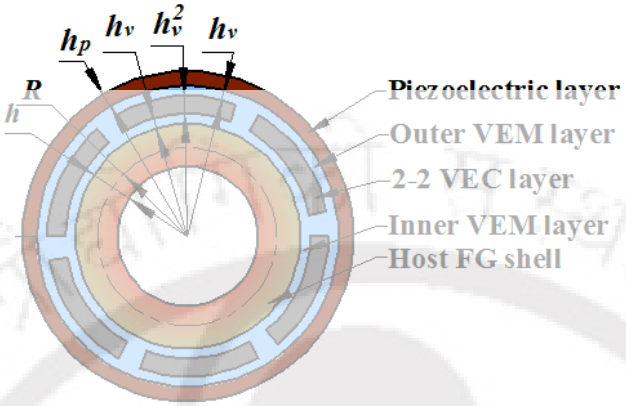

Fig. 5.3 Schematic diagram of a typical cross-section of the overall FG shell.

The middle surface of the host shell is taken as the reference surface, and the origin of the reference curvilinear coordinate system (xyz) is located at one end of the reference surface such that the ends of the cylinder are denoted by the coordinates $x=0$ and $x=L$. The axial, circumferential and radial directions of the shell are denoted by x, y and z axes of the curvilinear coordinate system (xyz). The overall shell is taken as a thin-walled shell and thus its kinematics of deformation is defined according to the layer-wise first order shear deformation theory (FSDT) as given in Eq. (4.1).

$$u^k(x,y,z)=u_0(x,y)+z_i^k\,\theta_i(x,y),\;\; v^k(x,y,z)=v_0(x,y)+z_i^k\,\beta_i(x,y),$$
$$w^k(x,y,z)=w_0(x,y)+z_i^k\,\gamma_i(x,y) \tag{4.1}$$

where, the thickness coordinates (z_i^k) for different layers are given in Table 5.1. The displacement components (u^k, v^k, w^k) at any point within the k^{th} layer can be written according to Eq. (4.2).

$$\boldsymbol{d}^k=(\boldsymbol{d}_t+\boldsymbol{Z}_{dk}\boldsymbol{d}_r),\;\; \boldsymbol{d}^k=\left\{u^k \quad v^k \quad w^k\right\}^{\mathrm{T}},\;\; \boldsymbol{d}_t=\left\{u_0 \quad v_0 \quad w_0\right\}^{\mathrm{T}}$$

$$\boldsymbol{d}_r=\left\{(\boldsymbol{d}_{r1})^{\mathrm{T}} \quad (\boldsymbol{d}_{r2})^{\mathrm{T}} \quad (\boldsymbol{d}_{r3})^{\mathrm{T}} \quad (\boldsymbol{d}_{r4})^{\mathrm{T}} \quad (\boldsymbol{d}_{r5})^{\mathrm{T}}\right\}^{\mathrm{T}},\;\; \boldsymbol{d}_{ri}=\left\{\theta_i \quad \beta_i \quad \gamma_i\right\}^{\mathrm{T}},$$

$$\boldsymbol{Z}_{dk}=\left[z_{dk}^1 \quad z_{dk}^2 \quad z_{dk}^3 \quad z_{dk}^4 \quad z_{dk}^5\right],\;\; z_{dk}^i=\boldsymbol{I}_{(3\times3)}\otimes z_i^k \tag{4.2}$$

According to Eq. (4.1), the displacement at every layer (k) can be obtained by specifying the corresponding matrix ($\boldsymbol{Z}_{dk}$). The layer-wise displacement vector ($\boldsymbol{d}^k$

) can then be expressed in terms of the generalized displacement vector ($\boldsymbol{d}$) as given in Eq. (4.3).

$$\boldsymbol{d}^k = (\boldsymbol{T}_t + \boldsymbol{Z}_{dk}\boldsymbol{T}_r)\boldsymbol{d}$$

$$\boldsymbol{d} = \{u_0 \quad v_0 \quad w_0 \quad \theta_1 \quad \theta_2 \quad \theta_3 \quad \theta_4 \quad \theta_5 \quad \beta_1 \quad \beta_2 \quad \beta_3 \quad \beta_4 \quad \beta_5 \quad \gamma_1 \quad \gamma_2 \quad \gamma_3 \quad \gamma_4 \quad \gamma_5\}^{\mathrm{T}} \quad (4.3)$$

Table 5.1 Thickness coordinates (z_i^k) of different layers.

Layer no.	z_1^k	z_2^k	z_3^k	z_4^k	z_5^k
k =1	z	0	0	0	0
k =2	$h/2$	$z-h/2$	0	0	0
k =3	$h/2$	h_v	$\left(z-h/2-h_v\right)$	0	0
k =4	$h/2$	h_v	h_v^2	$\left(z-h/2-h_v-h_v^2\right)$	0
k =5	$h/2$	h_v	h_v^2	h_v	$\left(z-h/2-2h_v-h_v^2\right)$

The state of strain and the state of stress at any point within the overall shell can be written according to Eq. (4.4).

$$\boldsymbol{\varepsilon}_b = \{\varepsilon_x \quad \varepsilon_y \quad \varepsilon_z \quad \varepsilon_{xy}\}^{\mathrm{T}}, \ \boldsymbol{\varepsilon}_s = \{\varepsilon_{xz} \quad \varepsilon_{yz}\}^{\mathrm{T}},$$

$$\boldsymbol{\sigma}_b = \{\sigma_x \quad \sigma_y \quad \sigma_z \quad \sigma_{xy}\}^{\mathrm{T}}, \ \boldsymbol{\sigma}_s = \{\sigma_{xz} \quad \sigma_{yz}\}^{\mathrm{T}} \quad (4.4)$$

The strain vectors (in Eq. (4.4)) can be written according to Sander's nonlinear strain-displacement relations for cylindrical shell (Reddy, 2004) as,

$$\boldsymbol{\varepsilon}_b^k = (\boldsymbol{\varepsilon}_{bL} + \boldsymbol{\varepsilon}_{bN} + z_{Lk}^i \boldsymbol{\kappa}_{bL}^i + z_{Nk}^i \boldsymbol{\kappa}_{bN}^i), \ \boldsymbol{\varepsilon}_s^k = (\boldsymbol{\varepsilon}_{sL} + z_{sk}^i \boldsymbol{\kappa}_s^i),$$

$$\boldsymbol{\varepsilon}_{bL} = \left\{\frac{\partial u_0}{\partial x} \quad \left(\frac{\partial v_0}{\partial y} + \frac{w_0}{R}\right) \quad 0 \quad \left(\frac{\partial u_0}{\partial y} + \frac{\partial v_0}{\partial x}\right)\right\}^{\mathrm{T}}, \ \boldsymbol{\varepsilon}_{sL} = \left\{\frac{\partial w_0}{\partial x} \quad \frac{\partial w_0}{\partial y} - \frac{v_0}{R}\right\}^{\mathrm{T}},$$

$$\boldsymbol{\varepsilon}_{bN} = \left\{\frac{1}{2}\left(\frac{\partial w_0}{\partial x}\right)^2 \quad \frac{1}{2}\left(\frac{\partial w_0}{\partial y} - \frac{v_0}{R}\right)^2 \quad 0 \quad \left(\frac{\partial w_0}{\partial y} - \frac{v_0}{R}\right)\frac{\partial w_0}{\partial x}\right\}^{\mathrm{T}},$$

$$\boldsymbol{\kappa}_{bL}^i = \left\{\frac{\partial \theta_i}{\partial x} \quad \frac{\partial \beta_i}{\partial y} \quad \gamma_i \quad \left(\frac{\partial \beta_i}{\partial x} + \frac{\partial \theta_i}{\partial y}\right)\right\}^{\mathrm{T}}, \ \boldsymbol{\kappa}_s^i = \left\{\theta_i \quad \frac{\partial \gamma_i}{\partial x} \quad \beta_i \quad \frac{\partial \gamma_i}{\partial y}\right\}^{\mathrm{T}},$$

$$\boldsymbol{\kappa}_{bN}^i = \left\{\frac{\partial w_0}{\partial x}\frac{\partial \gamma_i}{\partial x} \quad \left(\frac{\partial w_0}{\partial y} - \frac{v_0}{R}\right)\frac{\partial \gamma_i}{\partial y} \quad 0 \quad \left(\frac{\partial w_0}{\partial y} - \frac{v_0}{R}\right)\frac{\partial \gamma_i}{\partial x} + \frac{\partial w_0}{\partial x}\frac{\partial \gamma_i}{\partial y}\right\}^{\mathrm{T}},$$

$$\boldsymbol{z}_{Lk}^{i}=\begin{bmatrix} z_i^k & 0 & 0 & 0 \\ 0 & z_i^k & 0 & 0 \\ 0 & 0 & \dfrac{\partial z_i^k}{\partial z} & 0 \\ 0 & 0 & 0 & z_i^k \end{bmatrix},\ \boldsymbol{z}_{sk}^{i}=\begin{bmatrix} \dfrac{\partial z_i^k}{\partial z} & z_i^k & 0 & 0 \\ 0 & 0 & \dfrac{\partial z_i^k}{\partial z} & z_i^k \end{bmatrix},\ \boldsymbol{z}_{Nk}^{i}=\begin{bmatrix} z_i^k & 0 & 0 & 0 \\ 0 & z_i^k & 0 & 0 \\ 0 & 0 & 0 & 0 \\ 0 & 0 & 0 & z_i^k \end{bmatrix} \quad (5.1)$$

In Eq. (5.1), a repeated subscript or superscript (i) indicates summation over its range. Expressing the layer-wise strain vectors ($\boldsymbol{\kappa}_{bL}^{i}, \boldsymbol{\kappa}_{bN}^{i}, \boldsymbol{\kappa}_{s}^{i}$) in their generalized forms ($\boldsymbol{\kappa}_{bL}, \boldsymbol{\kappa}_{bN}, \boldsymbol{\kappa}_{s}$), the strain-displacement relations (Eq. (5.1)) can be rewritten as,

$$\boldsymbol{\varepsilon}_b^k=(\boldsymbol{\varepsilon}_{bL}+\boldsymbol{\varepsilon}_{bN}+\boldsymbol{Z}_L^k\boldsymbol{\kappa}_{bL}+\boldsymbol{Z}_N^k\boldsymbol{\kappa}_{bN}),\ \boldsymbol{\varepsilon}_s^k=(\boldsymbol{\varepsilon}_{sL}+\boldsymbol{Z}_s^k\boldsymbol{\kappa}_s),$$

$$\boldsymbol{\kappa}_{bL}=\left[(\boldsymbol{\kappa}_{bL}^1)^{\mathrm{T}}\quad(\boldsymbol{\kappa}_{bL}^2)^{\mathrm{T}}\quad(\boldsymbol{\kappa}_{bL}^3)^{\mathrm{T}}\quad(\boldsymbol{\kappa}_{bL}^4)^{\mathrm{T}}\quad(\boldsymbol{\kappa}_{bL}^5)^{\mathrm{T}}\right]^{\mathrm{T}},$$

$$\boldsymbol{\kappa}_{bN}=\left[(\boldsymbol{\kappa}_{bN}^1)^{\mathrm{T}}\quad(\boldsymbol{\kappa}_{bN}^2)^{\mathrm{T}}\quad(\boldsymbol{\kappa}_{bN}^3)^{\mathrm{T}}\quad(\boldsymbol{\kappa}_{bN}^4)^{\mathrm{T}}\quad(\boldsymbol{\kappa}_{bN}^5)^{\mathrm{T}}\right]^{\mathrm{T}},$$

$$\boldsymbol{\kappa}_{s}=\left[(\boldsymbol{\kappa}_{s}^1)^{\mathrm{T}}\quad(\boldsymbol{\kappa}_{s}^2)^{\mathrm{T}}\quad(\boldsymbol{\kappa}_{s}^3)^{\mathrm{T}}\quad(\boldsymbol{\kappa}_{s}^4)^{\mathrm{T}}\quad(\boldsymbol{\kappa}_{s}^5)^{\mathrm{T}}\right]^{\mathrm{T}} \quad (5.2)$$

According to Eq. (5.2), the strain at every layer can be obtained by specifying the corresponding matrices ($\boldsymbol{Z}_L^k, \boldsymbol{Z}_N^k, \boldsymbol{Z}_s^k$) as given in Eq. (5.3).

$$\boldsymbol{Z}_L^1=\left[z_{L1}^1\quad 0\quad 0\quad 0\quad 0\right],\ \boldsymbol{Z}_N^1=\left[z_{N1}^1\quad 0\quad 0\quad 0\quad 0\right],$$

$$\boldsymbol{Z}_s^1=\left[z_{s1}^1\quad 0\quad 0\quad 0\quad 0\right],\ \boldsymbol{Z}_L^2=\left[z_{L2}^1\quad z_{L2}^2\quad 0\quad 0\quad 0\right],$$

$$\boldsymbol{Z}_N^2=\left[z_{N2}^1\quad z_{N2}^2\quad 0\quad 0\quad 0\right],\ \boldsymbol{Z}_s^2=\left[z_{s2}^1\quad z_{s2}^2\quad 0\quad 0\quad 0\right],$$

$$\boldsymbol{Z}_L^3=\left[z_{L3}^1\quad z_{L3}^2\quad z_{L3}^3\quad 0\quad 0\right],\ \boldsymbol{Z}_N^3=\left[z_{N3}^1\quad z_{N3}^2\quad z_{N3}^3\quad 0\quad 0\right]$$

$$\boldsymbol{Z}_s^3=\left[z_{s3}^1\quad z_{s3}^2\quad z_{s3}^3\quad 0\quad 0\right],\ \boldsymbol{Z}_L^4=\left[z_{L4}^1\quad z_{L4}^2\quad z_{L4}^3\quad z_{L4}^4\quad 0\right],$$

$$\boldsymbol{Z}_N^4=\left[z_{N4}^1\quad z_{N4}^2\quad z_{N4}^3\quad z_{N4}^4\quad 0\right],\ \boldsymbol{Z}_s^4=\left[z_{s4}^1\quad z_{s4}^2\quad z_{s4}^3\quad z_{s4}^4\quad 0\right],$$

$$\boldsymbol{Z}_L^5=\left[z_{L5}^1\quad z_{L5}^2\quad z_{L5}^3\quad z_{L5}^4\quad z_{L5}^5\right],\ \boldsymbol{Z}_N^5=\left[z_{N5}^1\quad z_{N5}^2\quad z_{N5}^3\quad z_{N5}^4\quad z_{N5}^5\right],$$

$$\boldsymbol{Z}_s^5=\left[z_{s5}^1\quad z_{s5}^2\quad z_{s5}^3\quad z_{s5}^4\quad z_{s5}^5\right] \quad (5.3)$$

A thin piezoelectric composite (1-3 PFC) layer ($h_p \approx 200\,\mu\mathrm{m}$) is used at present for the constraining layer of ACLD arrangement. Generally, the top and bottom surfaces of a thin piezoelectric constraining layer are taken as fully

electrode-surfaces and the external voltage (V) is supplied across its thickness (h_p). Under this arrangement of electrodes, the components (E_x, E_y, E_z) of electric field ($\boldsymbol{E}$) could be assumed as (Ray and Pradhan, 2006), $E_x \approx 0$; $E_y \approx 0$ and $E_z = -V/h_p$. This assumption heads to decouple the electric potential field from the rest of the fields within the domain of the overall structure and the decoupled electro-elastic analysis could then be performed. But, this assumption for electric field (E) may not be an appropriate one in case of the present use of electrode-patches over the outer surface of the piezoelectric constraining layer. So, a coupled electro-elastic analysis is performed at present through the assumption of an electric potential function ($\phi(x,y,z)$). This potential function is considered within the domain of the constraining layer only since its (constraining layer) inner fully electrode-surface is grounded to have zero electric potential. The distribution of electric potential along the thickness direction (z) could be written in Taylor series as,

$$\phi(x,y,z) = \phi_0(x,y) + (\Delta z)\phi_1(x,y) + (\Delta z)^2\phi_2(x,y) + \ldots\ldots, \quad \Delta z = (z - z_0)$$

$$\phi_0(x,y) = \phi(x,y,z)\big|_{z_0}, \; \phi_1(x,y) = \frac{\partial\phi(x,y,z)}{\partial z}\bigg|_{z_0}, \; \phi_2(x,y) = \frac{1}{2}\frac{\partial^2\phi(x,y,z)}{\partial z^2}\bigg|_{z_0}, \ldots\ldots \tag{5.4}$$

The reference thickness coordinate (z_0) is taken as the thickness coordinate of the outer surface of the constraining layer and a quadratic distribution in the thickness coordinate is considered because of the thin piezoelectric (PFC) layer. For zero electric potential ($\phi = 0$) at the inner electrode-surface ($(z - z_0) = -h_p$), the quadratic distribution of electric potential ($\phi(x,y,z)$) can be expressed as,

$$\phi(x,y,z) = Z_1(z)\phi_0(x,y) + Z_2(z)\phi_1(x,y),$$

$$Z_1 = 1 - \left(\frac{z - z_o}{h_p}\right)^2, \; Z_2 = (z - z_o) + \frac{(z - z_o)^2}{h_p} \tag{5.5}$$

From Eq. (5.5), it may be noted that the electric potential at the outer surface ($z = z_0$, $Z_2 = 0$, $Z_1 = 1$) of the constraining layer is equal to $\phi_0(x,y)$. So, this parameter ($\phi_0(x,y)$) over the outer electrode-patches is to be specified to activate the constraining layer according to the control strategy. As per this form (Eq. (5.5)) of the electric potential field, a state of electric potential can be defined by the following generalized electric potential vector ($\boldsymbol{\phi}_v$),

$$\boldsymbol{\phi}_v = \begin{bmatrix} \phi_0 & \phi_1 \end{bmatrix}^{\mathrm{T}} \tag{5.6}$$

Also, the electric field ($\boldsymbol{E}$) can be expressed in the following form,

$$\boldsymbol{E} = \boldsymbol{Z}_E \boldsymbol{\phi}_E, \quad \boldsymbol{Z}_E = \begin{bmatrix} -Z_1 & 0 & -Z_2 & 0 & 0 & 0 \\ 0 & -Z_1 & 0 & -Z_2 & 0 & 0 \\ 0 & 0 & 0 & 0 & -\partial Z_1/\partial z & -\partial Z_2/\partial z \end{bmatrix},$$

$$\boldsymbol{\phi}_E = \left\{ \frac{\partial \phi_0}{\partial x} \quad \frac{\partial \phi_0}{\partial y} \quad \frac{\partial \phi_1}{\partial x} \quad \frac{\partial \phi_1}{\partial y} \quad \phi_0 \quad \phi_1 \right\}^{\mathrm{T}} \tag{5.7}$$

The material properties (P) of the host FG shell vary along the thickness direction according to a function of volume fractions and properties of the constituent materials as (Praveen and Reddy, 2001; Woo and Meguid, 2001),

$$p(z) = (p_c - p_m)\left[0.5 + (-1)^{\lambda} \, z/h \right]^r + p_m \tag{5.8}$$

where, p_c and p_m are the properties of ceramic and metal constituents; r is the power law exponent ($0 \le r \le \infty$) and λ is a positive integer. The odd/even value of λ signifies the outer surface of the host FG shell as metal-rich/ceramic-rich surface. All the material properties of the host FG shell like Young's modulus ($E(z)$), Poisson's ratio ($\nu(z)$), thermal conductivity ($k(z)$) and coefficient of thermal expansion ($\alpha(z)$) can be derived from Eq. (5.8) and the corresponding constitutive relations can be written as,

$$\boldsymbol{\sigma}_b^k = \boldsymbol{C}_b^k \left(\boldsymbol{\varepsilon}_b^k - \boldsymbol{\alpha} \Delta T \right), \quad \boldsymbol{\sigma}_s^k = \boldsymbol{C}_s^k \boldsymbol{\varepsilon}_s^k, \quad k = 1,$$

$$\boldsymbol{\alpha} = \left\{ \alpha_x(z) \quad \alpha_y(z) \quad \alpha_z(z) \quad 0 \right\}^{\mathrm{T}}, \quad \Delta T = T(z) - T_0 \tag{5.9}$$

where, C_b^k and C_s^k ($k = 1$) are the stiffness matrices as given in Eq. (5.10); $\alpha_x(z)$, $\alpha_y(z)$ and $\alpha_z(z)$ are the coefficients of thermal expansion along the x, y and z directions, respectively; $T(z)$ is the temperature distribution in the host FG shell along the thickness direction; T_0 is the reference temperature, and it is considered as the room temperature ($T_0 = 300$ K).

$$\boldsymbol{C}_b^k = \frac{E^k(z)}{\left(1+\nu^k(z)\right)\left(1-2\nu^k(z)\right)} \begin{bmatrix} 1-\nu^k(z) & \nu^k(z) & \nu^k(z) & 0 \\ \nu^k(z) & 1-\nu^k(z) & \nu^k(z) & 0 \\ \nu^k(z) & \nu^k(z) & 1-\nu^k(z) & 0 \\ 0 & 0 & 0 & 1/2-\nu^k(z) \end{bmatrix},$$

$$\boldsymbol{C}_s^k = \frac{E^k(z)}{\left(1+\nu^k(z)\right)\left(1-2\nu^k(z)\right)}\begin{bmatrix} 1/2-\nu^k(z) & 0 \\ 0 & 1/2-\nu^k(z) \end{bmatrix}, \quad k=1 \tag{5.10}$$

The temperature distribution ($T(z)$) across the thickness of the host FG shell can be obtained by the solution of the following one-dimensional steady state heat conduction equation,

$$-\frac{d}{dz}\left[k(z)\frac{dT(z)}{dz}\right]=0$$

$$T(z)\big|_{z=h/2}=T_c\,,\ T(z)\big|_{z=-h/2}=T_m \ \text{ for } \lambda=2$$

$$T(z)\big|_{z=h/2}=T_m\,,\ T(z)\big|_{z=-h/2}=T_c \ \text{ for } \lambda=1 \tag{5.11}$$

The solution of Eq. (5.11) is given by (Woo and Meguid, 2001),

$$T(z)=T_c-\frac{T_c-T_m}{\int_{-h/2}^{h/2}\frac{dz}{k(z)}}\int_{-h/2}^{z}\frac{dz}{k(z)} \ , \ \text{for } \lambda=2$$

$$T(z)=T_m-\frac{T_m-T_c}{\int_{-h/2}^{h/2}\frac{dz}{k(z)}}\int_{-h/2}^{z}\frac{dz}{k(z)} \ , \ \text{for } \lambda=1 \tag{5.12}$$

The material for the viscoelastic phase of the 1-3 VEC layer (Fig. 5.1 or Fig. 5.3) is considered as a linear isotropic viscoelastic material. The uniaxial isothermal stress-strain relation for such a viscoelastic material is given by (Christensen, 1982),

$$\sigma(t)=\int_0^t E(t-\tau)\frac{\partial}{\partial\tau}\varepsilon(\tau)d\tau \tag{5.13}$$

where, $E(t)$ is the time dependent relaxation modulus and $\varepsilon(\tau)$ is defined as zero for $t\le 0$. Following this stress-strain relation, the constitutive relations for the viscoelastic phase in 1-3 VEC layer can be written as,

$$\boldsymbol{\sigma}_b^k=\int_0^t \boldsymbol{C}_b^k E(t-\tau)\dot{\boldsymbol{\varepsilon}}_b^k(\tau)d\tau\,,\ \boldsymbol{\sigma}_s^k=\int_0^t \boldsymbol{C}_s^k G(t-\tau)\dot{\boldsymbol{\varepsilon}}_s^k(\tau)d\tau\,,\ k=2,3,4$$

$$G(t)=E(t)/2(1+\nu) \tag{5.14}$$

where, ν is the Poisson's ratio; $\boldsymbol{C}_b^k$ and $\boldsymbol{C}_s^k$ are the stiffness coefficient matrices as given in Eq. (5.15).

$$\boldsymbol{C}_b^k = \frac{1}{\left(1+\nu^k\right)\left(1-2\nu^k\right)}\begin{bmatrix} 1-\nu^k & \nu^k & \nu^k & 0 \\ \nu^k & 1-\nu^k & \nu^k & 0 \\ \nu^k & \nu^k & 1-\nu^k & 0 \\ 0 & 0 & 0 & 1/2-\nu^k \end{bmatrix},$$

$$\boldsymbol{C}_s^k = \begin{bmatrix} 1 & 0 \\ 0 & 1 \end{bmatrix} \; k = 2,3,4 \tag{5.15}$$

The constitutive relations for the graphite phase in the 2-2 VEC layer can be written as,

$$\boldsymbol{\sigma}_b^k = \boldsymbol{C}_b^k \boldsymbol{\varepsilon}_b^k, \; \boldsymbol{\sigma}_s^k = \boldsymbol{C}_s^k \boldsymbol{\varepsilon}_s^k, \; k = 3 \tag{5.16}$$

The forms of the stiffness matrices ($\boldsymbol{C}_b^k$ and $\boldsymbol{C}_s^k$ $(k=3)$) appearing in Eq. (5.16) are similar to those for the host FG cylinder (Eq. (5.10)) where the Young's modulus (E) and Poisson's ratio (ν) have constant values for the graphite phase. At a typical point on the xy-plane the third layer ($k=3$) is either made of viscoelastic material or made of graphite. So, this layer ($k=3$) is included in both the constitutive relations (Eqs. (5.14) and (5.16)). The constitutive relations for the vertically reinforced 1-3 PFC layer can be written as (Smith and Auld, 1991),

$$\boldsymbol{\sigma}_b^k = (\boldsymbol{C}_b^k \boldsymbol{\varepsilon}_b^k - \boldsymbol{e}_b E), \; \boldsymbol{\sigma}_s^k = (\boldsymbol{C}_s^k \boldsymbol{\varepsilon}_s^k - \boldsymbol{e}_s E),$$

$$\boldsymbol{D} = (\boldsymbol{e}_b^{\mathrm{T}} \boldsymbol{\varepsilon}_b^k + \boldsymbol{e}_s^{\mathrm{T}} \boldsymbol{\varepsilon}_s^k + \in E), \; k = 5 \tag{5.17}$$

where, $\boldsymbol{D}$ is the electric displacement vector; $\boldsymbol{C}_b^k$ and $\boldsymbol{C}_s^k$ $(k=5)$ are the elastic stiffness matrices; $\boldsymbol{e}_b$ and $\boldsymbol{e}_s$ are the piezoelectric matrices and $\in$ is the dielectric constant matrix. The forms of these property matrices are given in Eq. (5.18) where, C_{ij}^k, e_{ij} and $\in_{ij}$ are the elements of stiffness, piezoelectric and dielectric matrices, respectively.

$$\boldsymbol{C}_b^k = \begin{bmatrix} C_{11}^k & C_{12}^k & C_{13}^k & 0 \\ C_{12}^k & C_{22}^k & C_{23}^k & 0 \\ C_{13}^k & C_{23}^k & C_{33}^k & 0 \\ 0 & 0 & 0 & C_{66}^k \end{bmatrix}, \; \boldsymbol{C}_s^k = \begin{bmatrix} C_{55}^k & 0 \\ 0 & C_{44}^k \end{bmatrix}, \; k = 5$$

$$\boldsymbol{e}_b = \begin{bmatrix} 0 & 0 & e_{31} \\ 0 & 0 & e_{32} \\ 0 & 0 & e_{33} \\ 0 & 0 & 0 \end{bmatrix}, \boldsymbol{e}_s = \begin{bmatrix} e_{15} & 0 & 0 \\ 0 & e_{24} & 0 \end{bmatrix}, \boldsymbol{\epsilon} = \begin{bmatrix} \epsilon_{11} & 0 & 0 \\ 0 & \epsilon_{22} & 0 \\ 0 & 0 & \epsilon_{33} \end{bmatrix} \quad (5.18)$$

The overall shell is considered to be subjected to a harmonic transverse (radial) point-load ($p(t)$). Under this load, the principle of virtual work gives (Tierstien, 1969),

$$\delta T_p = \int_0^L \int_0^{(2\pi R)} \left[\sum_{k=1}^{5} \int_{h_k}^{h_{k+1}} \left\langle (\delta \boldsymbol{\varepsilon}_b^k)^{\mathrm{T}} \boldsymbol{\sigma}_b^k + (\delta \boldsymbol{\varepsilon}_s^k)^{\mathrm{T}} \boldsymbol{\sigma}_s^k \right\rangle dz - \int_{h_k}^{h_{k+1}} \left\langle (\delta \boldsymbol{E})^{\mathrm{T}} \boldsymbol{D} \right\rangle_{k=5} dz \right] dy dx \quad (5.19)$$
$$- (\delta w) p(t) \Big|_{x,y,z}$$

$$\delta T_K = \int_0^L \int_0^{(2\pi R)} \left[\sum_{k=1}^{5} \int_{h_k}^{h_{k+1}} \left\langle \left\{ \delta \dot{u}^k \quad \delta \dot{v}^k \quad \delta \dot{w}^k \right\} \rho^k \left\{ \dot{u}^k \quad \dot{v}^k \quad \dot{w}^k \right\}^{\mathrm{T}} \right\rangle dz \right] dy dx \quad (5.20)$$

where, δT_p and δT_k are the first variations of the total potential energy and the total kinetic energy respectively of the overall shell at any instant of time (t), δ is an operator for the first variation; ρ^k is the mass density of the k^{th} layer. For the steady state vibration of the overall FG shell with a circular frequency of ω, a state of vibration can be defined by specifying $\boldsymbol{d}, \boldsymbol{\phi}_v$ and ω. A new state of vibration ($\hat{\boldsymbol{d}}, \hat{\boldsymbol{\phi}}_v, \hat{\omega}$) can be defined by the increments ($\Delta \boldsymbol{d}$, $\Delta \boldsymbol{\phi}_v, \Delta\omega$) over a given state of vibration ($\boldsymbol{d}$, $\boldsymbol{\phi}_v, \omega$) as,

$$\hat{\boldsymbol{d}} = (\boldsymbol{d} + \Delta \boldsymbol{d}), \ \hat{\omega} = (\omega + \Delta\omega), \ \hat{\boldsymbol{\phi}}_v = (\boldsymbol{\phi}_v + \Delta \boldsymbol{\phi}_v),$$

$$\hat{\boldsymbol{d}} = \{ \hat{u}_0 \quad \hat{v}_0 \quad \hat{w}_0 \quad \hat{\theta}_1 \quad \hat{\theta}_2 \quad \hat{\theta}_3 \quad \hat{\theta}_4 \quad \hat{\theta}_5 \quad \hat{\beta}_1$$
$$\hat{\beta}_2 \quad \hat{\beta}_3 \quad \hat{\beta}_4 \quad \hat{\beta}_5 \quad \hat{\gamma}_1 \quad \hat{\gamma}_2 \quad \hat{\gamma}_3 \quad \hat{\gamma}_4 \quad \hat{\gamma}_5 \}^{\mathrm{T}},$$

$$\Delta \boldsymbol{d} = \{ \Delta u_0 \quad \Delta v_0 \quad \Delta w_0 \quad \Delta \theta_1 \quad \Delta \theta_2 \quad \Delta \theta_3 \quad \Delta \theta_4 \quad \Delta \theta_5 \quad \Delta \beta_1$$
$$\Delta \beta_2 \quad \Delta \beta_3 \quad \Delta \beta_4 \quad \Delta \beta_5 \quad \Delta \gamma_1 \quad \Delta \gamma_2 \quad \Delta \gamma_3 \quad \Delta \gamma_4 \quad \Delta \gamma_5 \}^{\mathrm{T}},$$

$$\hat{\boldsymbol{\phi}}_v = \{ \hat{\phi}_0 \quad \hat{\phi}_1 \}^{\mathrm{T}}, \ \Delta \boldsymbol{\phi}_v = \{ \Delta\phi_0 \quad \Delta\phi_1 \}^{\mathrm{T}} \quad (5.21)$$

The corresponding linearized incremental forms of the generalized strain vectors ($\boldsymbol{\varepsilon}_{bL}, \boldsymbol{\varepsilon}_{bN}, \boldsymbol{\kappa}_{bL}, \boldsymbol{\kappa}_{bN}, \boldsymbol{\varepsilon}_{sL}, \boldsymbol{\kappa}_s$) and the electric field vector ($\boldsymbol{\phi}_E$) can be expressed as,

$$\hat{\boldsymbol{\varepsilon}}_{bL} = \left(\boldsymbol{\varepsilon}_{bL} + \Delta\boldsymbol{\varepsilon}_{bL}\right),\ \hat{\boldsymbol{\varepsilon}}_{bN} = \left(\boldsymbol{\varepsilon}_{bN} + \Delta\boldsymbol{\varepsilon}_{bN}\right),$$

$$\hat{\boldsymbol{\kappa}}_{bL} = \left(\boldsymbol{\kappa}_{bL} + \Delta\boldsymbol{\kappa}_{bL}\right), \hat{\boldsymbol{\kappa}}_{bN} = \left(\boldsymbol{\kappa}_{bN} + \Delta\boldsymbol{\kappa}_{bN}\right),$$

$$\hat{\boldsymbol{\varepsilon}}_{sL} = \left(\boldsymbol{\varepsilon}_{sL} + \Delta\boldsymbol{\varepsilon}_{sL}\right),\ \hat{\boldsymbol{\kappa}}_{s} = \left(\boldsymbol{\kappa}_{s} + \Delta\boldsymbol{\kappa}_{s}\right),\ \hat{\boldsymbol{\phi}}_{E} = \left(\boldsymbol{\phi}_{E} + \Delta\boldsymbol{\phi}_{E}\right) \tag{5.22}$$

where, $\boldsymbol{\varepsilon}_{bL}, \boldsymbol{\varepsilon}_{bN}, \boldsymbol{\kappa}_{bL}, \boldsymbol{\kappa}_{bN}, \boldsymbol{\varepsilon}_{sL}$ and $\boldsymbol{\kappa}_{s}$ are the generalized strain vectors for the given state of deformation ($\boldsymbol{d}$) while $\Delta\boldsymbol{\varepsilon}_{bL}$, $\Delta\boldsymbol{\varepsilon}_{bN}$, $\Delta\boldsymbol{\kappa}_{bL}$, $\Delta\boldsymbol{\kappa}_{bN}$, $\Delta\boldsymbol{\varepsilon}_{sL}$ and $\Delta\boldsymbol{\kappa}_{s}$ are the corresponding linearized increments as given in Eq. (5.23). Similarly, $\boldsymbol{\phi}_{E}$ is the generalized electric field vector for a given state of electric potential ($\boldsymbol{\phi}_{v}$) and $\Delta\boldsymbol{\phi}_{E}$ is the corresponding increment as given in Eq. (5.24).

$$\Delta\boldsymbol{\varepsilon}_{bL} = \left\{ \frac{\partial\Delta u_0}{\partial x} \quad \left(\frac{\partial\Delta v_0}{\partial y} + \frac{\Delta w_0}{R}\right) \quad 0 \quad \left(\frac{\partial\Delta u_0}{\partial y} + \frac{\partial\Delta v_0}{\partial x}\right) \right\}^{\mathrm{T}},$$

$$\Delta\boldsymbol{\varepsilon}_{bN} = \left\{ \frac{\partial w_0}{\partial x}\frac{\partial\Delta w_0}{\partial x} \quad \left(\frac{\partial w_0}{\partial y} - \frac{v_0}{R}\right)\frac{\partial\Delta w_0}{\partial y} \quad 0 \quad \left(\frac{\partial w_0}{\partial y} - \frac{v_0}{R}\right)\frac{\partial\Delta w_0}{\partial x} + \frac{\partial w_0}{\partial x}\frac{\partial\Delta w_0}{\partial y} \right\}^{\mathrm{T}},$$

$$\Delta\boldsymbol{\varepsilon}_{sL} = \left\{ \frac{\partial\Delta w_0}{\partial x} \quad \left(\frac{\partial\Delta w_0}{\partial y} - \frac{\Delta v_0}{R}\right) \right\}^{\mathrm{T}},$$

$$\Delta\boldsymbol{\kappa}_{bL} = \left[\left(\Delta\boldsymbol{\kappa}_{bL}^{1}\right)^{\mathrm{T}} \quad \left(\Delta\boldsymbol{\kappa}_{bL}^{2}\right)^{\mathrm{T}} \quad \left(\Delta\boldsymbol{\kappa}_{bL}^{3}\right)^{\mathrm{T}} \quad \left(\Delta\boldsymbol{\kappa}_{bL}^{4}\right)^{\mathrm{T}} \quad \left(\Delta\boldsymbol{\kappa}_{bL}^{5}\right)^{\mathrm{T}} \right]^{\mathrm{T}},$$

$$\Delta\boldsymbol{\kappa}_{bL}^{i} = \left\{ \frac{\partial\Delta\theta_i}{\partial x} \quad \frac{\partial\Delta\beta_i}{\partial y} \quad \Delta\gamma_i \quad \left(\frac{\partial\Delta\beta_i}{\partial x} + \frac{\partial\Delta\theta_i}{\partial y}\right) \right\}^{\mathrm{T}},$$

$$\Delta\boldsymbol{\kappa}_{bN} = \left[\left(\Delta\boldsymbol{\kappa}_{bN}^{1}\right)^{\mathrm{T}} \quad \left(\Delta\boldsymbol{\kappa}_{bN}^{2}\right)^{\mathrm{T}} \quad \left(\Delta\boldsymbol{\kappa}_{bN}^{3}\right)^{\mathrm{T}} \quad \left(\Delta\boldsymbol{\kappa}_{bN}^{4}\right)^{\mathrm{T}} \quad \left(\Delta\boldsymbol{\kappa}_{bN}^{5}\right)^{\mathrm{T}} \right]^{\mathrm{T}},$$

$$\Delta\boldsymbol{\kappa}_{bN}^{i} = \begin{Bmatrix} \frac{\partial w_0}{\partial x}\frac{\partial\Delta\gamma_i}{\partial x} + \frac{\partial\Delta w_0}{\partial x}\frac{\partial\gamma_i}{\partial x} & \left(\frac{\partial w_0}{\partial y} - \frac{v_0}{R}\right)\frac{\partial\Delta\gamma_i}{\partial y} + \frac{\partial\gamma_i}{\partial y}\frac{\partial\Delta w_0}{\partial y} & \cdots \\ 0 & \left(\frac{\partial w_0}{\partial y} - \frac{v_0}{R}\right)\frac{\partial\Delta\gamma_i}{\partial x} + \frac{\partial w_0}{\partial x}\frac{\partial\Delta\gamma_i}{\partial y} + \frac{\partial\Delta w_0}{\partial x}\frac{\partial\gamma_i}{\partial y} + \frac{\partial\Delta w_0}{\partial y}\frac{\partial\gamma_i}{\partial x} \end{Bmatrix}^{\mathrm{T}}$$

$$\Delta\boldsymbol{\kappa}_{s} = \left[\left(\Delta\boldsymbol{\kappa}_{s}^{1}\right)^{\mathrm{T}} \quad \left(\Delta\boldsymbol{\kappa}_{s}^{2}\right)^{\mathrm{T}} \quad \left(\Delta\boldsymbol{\kappa}_{s}^{3}\right)^{\mathrm{T}} \quad \left(\Delta\boldsymbol{\kappa}_{s}^{4}\right)^{\mathrm{T}} \quad \left(\Delta\boldsymbol{\kappa}_{s}^{5}\right)^{\mathrm{T}} \right]^{\mathrm{T}},$$

$$\Delta\boldsymbol{\kappa}_{s}^{i} = \left\{ \Delta\theta_i \quad \frac{\partial\Delta\gamma_i}{\partial x} \quad \Delta\beta_i \quad \frac{\partial\Delta\gamma_i}{\partial y} \right\}^{\mathrm{T}}, \tag{5.23}$$

$$\Delta\boldsymbol{\phi}_E = \left\{ \frac{\partial \Delta\phi_0}{\partial x} \quad \frac{\partial \Delta\phi_0}{\partial y} \quad \frac{\partial \Delta\phi_1}{\partial x} \quad \frac{\partial \Delta\phi_1}{\partial y} \quad \Delta\phi_0 \quad \Delta\phi_1 \right\}^T \tag{5.24}$$

For deriving FE model of the overall shell, the reference cylindrical surface is discretized by the nine-node isoparametric quadrilateral elements. The FE mesh is generated by dividing the circumferential and longitudinal spans of the shell so that every element is in the rectangular shape with its edges in parallel to the circumferential and longitudinal directions. Since the graphite phase-volumes and electrode-patches are discontinuously arranged in the circumferential direction (Figs. 5.1 and 5.3), the FE mesh is generated in such a manner that the third layer ($k=3$) of a typical element is either made of graphite or made of viscoelastic material. Also, the top surface of a typical element is either fully electrode-surface or electrode-free surface. So, basically four kinds of elements appear in the FE mesh as shown in Fig. 5.4.

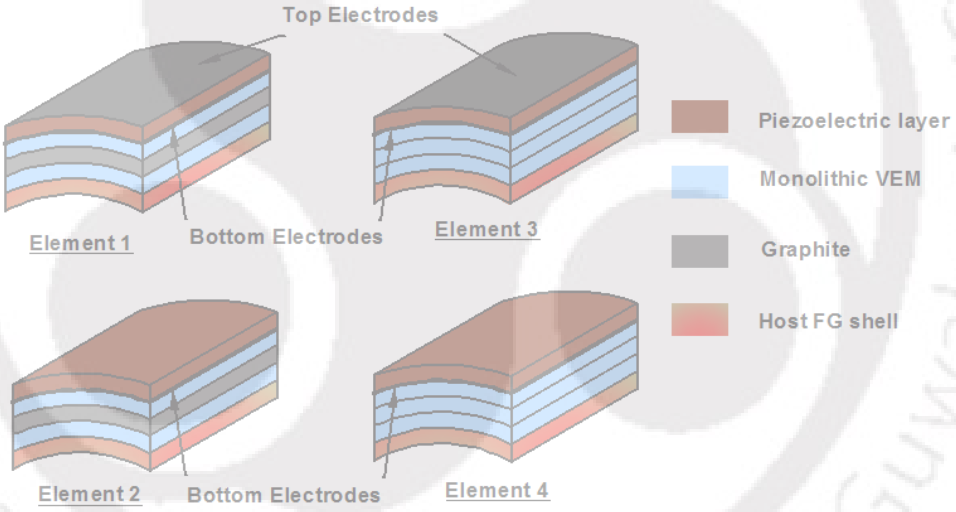

Fig. 5.4 Different elemental stacking sequences of layers along with the surface-electrodes over the inner and outer surfaces of the constraining layer.

Element 1 and Element 2 have the same stacking sequence that includes the third layer ($k=3$) as graphite phase-volume. Element 3 and Element 4 have similar stacking sequence but the third layer ($k=3$) is made of pure viscoelastic material. Element 1 and Element 3 are within a zone of electrode-patch over the outer surface of the constraining layer. Element 2 and Element 4 are outside of this zone of electrode-patch.

The generalized displacement and electric potential vectors at any point within a typical element can be written as,

$$\boldsymbol{d} = \boldsymbol{N}_d \boldsymbol{d}^e,\ \Delta\boldsymbol{d} = \boldsymbol{N}_d \Delta\boldsymbol{d}^e,\ \boldsymbol{\phi}_v = \boldsymbol{N}_\phi \boldsymbol{\phi}_v^e,\ \Delta\boldsymbol{\phi}_v = \boldsymbol{N}_\phi \Delta\boldsymbol{\phi}_v^e \tag{5.25}$$

where, $\boldsymbol{d}^e / \Delta\boldsymbol{d}^e$ is the elemental nodal displacement vector; $\boldsymbol{\phi}^e / \Delta\boldsymbol{\phi}^e$ is the elemental nodal electric potential vector; $\boldsymbol{N}_d / \boldsymbol{N}_\phi$ is the shape function matrix. In order to derive the elemental expressions of δT_P and δT_K, first Eqs. (5.9), (5.14), (5.16) and (5.17) are introduced in Eqs. (5.19) and (5.20) according to the elemental stacking sequence. Then, Eqs. (4.3), (5.2), (5.7) and their incremental forms (Eqs. (5.21) and (5.22)) are used along with the elemental equations (Eq. (5.25)) for the displacement and electric potential vectors. The resulting expressions of δT_P^e and δT_K^e for a typical element are obtained as follows,

$$\delta T_P^e = \left\langle \begin{array}{l} \delta\left(\Delta d^e\right)^T \left[\begin{array}{l} K_L^e\left(d^e + \Delta d^e\right) + K_N^e d^e + K_N^{\Delta e} \Delta d^e + \left(K_L^{ve} + K_{N2}^{ve}\right) \int_0^t E(t-\tau)\left(\dot{d}^e + \Delta\dot{d}^e\right) d\tau \\ + K_s^{ve} \int_0^t G(t-\tau)\left(\dot{d}^e + \Delta\dot{d}^e\right) d\tau - \left(K_{d\phi}^{Le} + K_{d\phi}^{Ne}\right)\left(\phi_v^e + \Delta\phi_v^e\right) \\ - P_T^{Le} - P_T^{Ne} - P_M^e(t) \end{array} \right] \\ - \delta\left(\Delta\phi_v^e\right)^T \left[K_{\phi d}^{Le}\left(d^e + \Delta d^e\right) + K_{\phi d}^{Ne} d^e + K_{\phi d}^{\Delta Ne} \Delta d^e + K_{\phi\phi}^e\left(\phi_v^e + \Delta\phi_v^e\right) \right] \end{array} \right\rangle \tag{5.26}$$

$$\delta T_K^e = \delta\left(\Delta\dot{d}^e\right)^T M^e\left(\dot{d}^e + \Delta\dot{d}^e\right) \tag{5.27}$$

$$K_N^e = \left(K_{N1}^e + K_{N2}^e + K_{NN,}^e\right),\ K_N^{\Delta e} = \left(K_{N1}^{\Delta e} + K_{N2}^{\Delta e} + K_{NN}^{\Delta e}\right),$$

$$K_L^e = \int_{A^e} \left[\begin{array}{l} B_{bL}{}^T\left(A_b B_{bL} + B_{L1} B_{\kappa L}\right) + B_{\kappa L}{}^T\left(B_{L2} B_{bL} + D_{L1} B_{\kappa L}\right) \\ + B_{sL}{}^T\left(A_s B_{sL} + B_{s1} B_{\kappa s}\right) + B_{ks}{}^T\left(B_{s2} B_{sL} + D_s B_{\kappa s}\right) \end{array} \right] dA^e,$$

$$K_{N1}^e = \int_{A^e} \left[B_{bL}{}^T\left(A_b B_{bN} + B_{N1} B_{\kappa N}\right) + B_{\kappa L}{}^T\left(B_{L2} B_{bN} + D_{N1} B_{\kappa N}\right) \right] dA^e,$$

$$K_{N2}^e = \int_{A^e} \left[B_{bN}^{\Delta}{}^T\left(A_b B_{bL} + B_{L1} B_{\kappa L}\right) + B_{\kappa N}^{\Delta}{}^T\left(B_{N2} B_{bL} + D_{N2} B_{\kappa L}\right) \right] dA^e,$$

$$K_{NN}^e = \int_{A^e} \left[B_{bN}^{\Delta}{}^T\left(A_b B_{bN} + B_{N1} B_{\kappa N}\right) + B_{\kappa N}^{\Delta}{}^T\left(B_{N2} B_{bN} + D_{N3} B_{\kappa N}\right) \right] dA^e,$$

$$K_{N1}^{\Delta e} = \int_{A^e} \left[B_{bL}{}^T\left(A_b B_{bN}^{\Delta} + B_{N1} B_{\kappa N}^{\Delta}\right) + B_{\kappa L}{}^T\left(B_{L2} B_{bN}^{\Delta} + D_{N1} B_{\kappa N}^{\Delta}\right) \right] dA^e,$$

$$K_{N2}^{\Delta e} = \int_{A^e} \left[B_{bN}^{\Delta}{}^T\left(A_b B_{bL} + B_{L1} B_{\kappa L}\right) + B_{\kappa N}^{\Delta}{}^T\left(B_{N2} B_{bL} + D_{N2} B_{\kappa L}\right) \right] dA^e,$$

$$K_{NN}^{\Delta e} = \int_{A^e} \left[B_{bN}^{\Delta}{}^T\left(A_b B_{bN}^{\Delta} + B_{N1} B_{\kappa N}^{\Delta}\right) + B_{\kappa N}^{\Delta}{}^T\left(B_{N2} B_{bN}^{\Delta} + D_{N3} B_{\kappa N}^{\Delta}\right) \right] dA^e,$$

$$\boldsymbol{K}_{L}^{ve}=\int_{A^e}\left[\boldsymbol{B}_{bL}{}^{T}\left(\boldsymbol{A}_{b}^{v}\boldsymbol{B}_{bL}+\boldsymbol{B}_{L1}^{v}\boldsymbol{B}_{\kappa L}\right)+\boldsymbol{B}_{\kappa L}{}^{\mathrm{T}}\left(\boldsymbol{B}_{L2}^{v}\boldsymbol{B}_{bL}+\boldsymbol{D}_{L1}^{v}\boldsymbol{B}_{\kappa L}\right)\right]dA^{e}$$

$$\boldsymbol{K}_{N2}^{ve}=\int_{A^e}\left[\boldsymbol{B}_{bN}^{\Delta}{}^{T}\left(\boldsymbol{A}_{b}^{v}\boldsymbol{B}_{bL}+\boldsymbol{B}_{L1}^{v}\boldsymbol{B}_{\kappa L}\right)+\boldsymbol{B}_{\kappa N}^{\Delta}{}^{T}\left(\boldsymbol{B}_{N2}^{v}\boldsymbol{B}_{bL}+\boldsymbol{D}_{N2}^{v}\boldsymbol{B}_{\kappa L}\right)\right]dA^{e},$$

$$\boldsymbol{K}_{s}^{ve}=\int_{A^e}\left[\boldsymbol{B}_{sL}{}^{T}\left(\boldsymbol{A}_{s}^{v}\boldsymbol{B}_{sL}+\boldsymbol{B}_{s1}^{v}\boldsymbol{B}_{\kappa s}\right)+\boldsymbol{B}_{\kappa s}{}^{\mathrm{T}}\left(\boldsymbol{B}_{s2}^{v}\boldsymbol{B}_{sL}+\boldsymbol{D}_{s}^{v}\boldsymbol{B}_{\kappa L}\right)\right]dA^{e},$$

$$\boldsymbol{K}_{d\phi}^{Le}=\int_{A^e}\left[\boldsymbol{B}_{bL}{}^{\mathrm{T}}\boldsymbol{A}_{be}^{1}\boldsymbol{B}_{E}+\boldsymbol{B}_{\kappa L}{}^{\mathrm{T}}\boldsymbol{B}_{be}^{1}\boldsymbol{B}_{E}+\boldsymbol{B}_{sL}{}^{\mathrm{T}}\boldsymbol{A}_{se}^{1}\boldsymbol{B}_{E}+\boldsymbol{B}_{\kappa s}\boldsymbol{B}_{se}^{1}\boldsymbol{B}_{E}\right]dA^{e},$$

$$\boldsymbol{K}_{d\phi}^{Ne}=\int_{A^e}\left[\boldsymbol{B}_{bN}^{\Delta}{}^{\mathrm{T}}\boldsymbol{A}_{be}^{1}\boldsymbol{B}_{E}+\boldsymbol{B}_{\kappa N}^{\Delta}{}^{\mathrm{T}}\boldsymbol{B}_{be}^{N1}\boldsymbol{B}_{E}\right]dA^{e},\quad \boldsymbol{P}_{T}^{Le}=\int_{A^e}\left[\boldsymbol{B}_{bL}{}^{\mathrm{T}}\boldsymbol{A}_{T}+\boldsymbol{B}_{\kappa L}{}^{\mathrm{T}}\boldsymbol{B}_{LT}\right]dA^{e},$$

$$\boldsymbol{P}_{T}^{Ne}=\int_{A^e}\left[\boldsymbol{B}_{bN}^{\Delta}{}^{\mathrm{T}}\boldsymbol{A}_{T}+\boldsymbol{B}_{\kappa N}^{\Delta}{}^{\mathrm{T}}\boldsymbol{B}_{NT}\right]dA^{e},\quad \boldsymbol{K}_{\phi\phi}^{e}=\int_{A^e}\left[\boldsymbol{B}_{E}{}^{\mathrm{T}}\boldsymbol{A}_{E}\boldsymbol{B}_{E}\right]dA^{e},$$

$$\boldsymbol{K}_{\phi d}^{Le}=\int_{A^e}\left[\boldsymbol{B}_{E}{}^{\mathrm{T}}\boldsymbol{A}_{be}^{2}\boldsymbol{B}_{bL}+\boldsymbol{B}_{E}{}^{\mathrm{T}}\boldsymbol{B}_{be}^{2}\boldsymbol{B}_{\kappa L}+\boldsymbol{B}_{E}{}^{\mathrm{T}}\boldsymbol{A}_{se}^{2}\boldsymbol{B}_{sL}+\boldsymbol{B}_{E}{}^{\mathrm{T}}\boldsymbol{B}_{se}^{2}\boldsymbol{B}_{\kappa s}\right]dA^{e},$$

$$\boldsymbol{K}_{\phi d}^{Ne}=\int_{A^e}\left[\boldsymbol{B}_{E}{}^{\mathrm{T}}\boldsymbol{A}_{be}^{2}\boldsymbol{B}_{bN}+\boldsymbol{B}_{E}{}^{\mathrm{T}}\boldsymbol{B}_{be}^{N2}\boldsymbol{B}_{\kappa N}\right]dA^{e},$$

$$\boldsymbol{K}_{\phi d}^{\Delta Ne}=\int_{A^e}\left[\boldsymbol{B}_{E}{}^{\mathrm{T}}\boldsymbol{A}_{be}^{2}\boldsymbol{B}_{bN}^{\Delta}+\boldsymbol{B}_{E}{}^{\mathrm{T}}\boldsymbol{B}_{be}^{N2}\boldsymbol{B}_{\kappa N}^{\Delta}\right]dA^{e},$$

$$\boldsymbol{M}^{e}=\int_{A^e}\left[\boldsymbol{N}_{d}^{T}\bar{\boldsymbol{m}}\boldsymbol{N}_{d}\right]dA^{e},$$

$$\bar{\boldsymbol{m}}=\sum_{k=1}^{5}\int_{h_k}^{h_{k+1}}\left[\boldsymbol{T}_{t}^{T}\rho^{k}\boldsymbol{T}_{t}+\boldsymbol{T}_{t}^{T}\rho^{k}\boldsymbol{Z}_{dk}\boldsymbol{T}_{r}+\boldsymbol{T}_{r}^{T}\boldsymbol{Z}_{dk}^{T}\rho^{k}\boldsymbol{T}_{t}+\boldsymbol{T}_{r}^{T}\boldsymbol{Z}_{dk}^{T}\rho^{k}\boldsymbol{Z}_{dk}\boldsymbol{T}_{r}\right]dz \tag{5.28}$$

where, A^e is the elemental area over the reference surface and $\boldsymbol{P}_{M}^{e}(t)$ is the point-load vector. The different strain-displacement matrices ($\boldsymbol{B}_{bL}$, $\boldsymbol{B}_{\kappa L}$, $\boldsymbol{B}_{sL}$, $\boldsymbol{B}_{ks}$, $\boldsymbol{B}_{bN}$, $\boldsymbol{B}_{\kappa N}$, $\boldsymbol{B}_{bN}^{\Delta}$, $\boldsymbol{B}_{\kappa N}^{\Delta}$, $\boldsymbol{B}_{E}$) appearing in Eq. (5.28) are obtained from the following elemental strain-displacement relations,

$$\boldsymbol{\varepsilon}_{bL}=\boldsymbol{B}_{bL}\boldsymbol{d}^{e},\ \boldsymbol{\kappa}_{bL}=\boldsymbol{B}_{\kappa L}\boldsymbol{d}^{e},\ \boldsymbol{\varepsilon}_{sL}=\boldsymbol{B}_{sL}\boldsymbol{d}^{e},$$

$$\boldsymbol{\kappa}_{S}=\boldsymbol{B}_{\kappa s}\boldsymbol{d}^{e},\ \boldsymbol{\varepsilon}_{bN}=\boldsymbol{B}_{bN}\boldsymbol{d}^{e},\boldsymbol{\kappa}_{bN}=\boldsymbol{B}_{\kappa N}\boldsymbol{d}^{e},$$

$$\Delta\boldsymbol{\varepsilon}_{bN}=\boldsymbol{B}_{bN}^{\Delta}\boldsymbol{d}^{e},\ \Delta\boldsymbol{\kappa}_{bN}=\boldsymbol{B}_{\kappa N}^{\Delta}\boldsymbol{d}^{e},\ \boldsymbol{\phi}_{E}=\boldsymbol{B}_{E}\boldsymbol{\phi}_{v}^{e} \tag{5.29}$$

Also, the different rigidity matrices ($\boldsymbol{A}_{b}$, $\boldsymbol{B}_{L1}$, $\boldsymbol{B}_{N1}$, $\boldsymbol{B}_{L2}$, $\boldsymbol{D}_{L1}$, $\boldsymbol{D}_{N1}$, $\boldsymbol{B}_{N2}$, $\boldsymbol{D}_{N2}$, $\boldsymbol{D}_{N3}$, $\boldsymbol{A}_{s}$, $\boldsymbol{B}_{s1}$, $\boldsymbol{B}_{s2}$, $\boldsymbol{D}_{s}$), coefficient rigidity matrices for viscoelastic layer ($\boldsymbol{A}_{b}^{v}$, $\boldsymbol{B}_{L1}^{v}$, $\boldsymbol{B}_{L2}^{v}$, $\boldsymbol{D}_{L1}^{v}$, $\boldsymbol{B}_{N2}^{v}$, $\boldsymbol{D}_{N2}^{v}$, $\boldsymbol{A}_{s}^{v}$, $\boldsymbol{B}_{s1}^{v}$, $\boldsymbol{B}_{s2}^{v}$, $\boldsymbol{D}_{s}^{v}$), electro-elastic coupling matrices ($\boldsymbol{A}_{be}^{1}$, $\boldsymbol{B}_{be}^{1}$, $\boldsymbol{A}_{se}^{1}$, $\boldsymbol{B}_{se}^{1}$, $\boldsymbol{B}_{be}^{N1}$, $\boldsymbol{A}_{be}^{2}$, $\boldsymbol{B}_{be}^{2}$, $\boldsymbol{A}_{se}^{2}$, $\boldsymbol{B}_{se}^{2}$, $\boldsymbol{B}_{be}^{N2}$), electrical rigidity matrix ($\boldsymbol{A}_{E}$) and thermo-elastic coupling vectors ($\boldsymbol{A}_{T}$, $\boldsymbol{B}_{LT}$, $\boldsymbol{B}_{NT}$) are given in Eqs. (5.30), (5.31) and (5.32).

For Element 1/ Element 2:

$$A_b = \left(\int_{h_k}^{h_{k+1}} C_b^k \mid_{k=1} dz + \int_{h_k}^{h_{k+1}} C_b^k \mid_{k=3} dz + \int_{h_k}^{h_{k+1}} C_b^k \mid_{k=5} dz \right),$$

$$A_b^v = \left(\int_{h_k}^{h_{k+1}} C_b^k \mid_{k=2} dz + \int_{h_k}^{h_{k+1}} C_b^k \mid_{k=4} dz \right),$$

$$A_s = \left(\int_{h_k}^{h_{k+1}} C_s^k \mid_{k=1} dz + \int_{h_k}^{h_{k+1}} C_s^k \mid_{k=3} dz + \int_{h_k}^{h_{k+1}} C_s^k \mid_{k=5} dz \right),$$

$$A_{sv} = \left(\int_{h_k}^{h_{k+1}} C_s^k \mid_{k=2} dz + \int_{h_k}^{h_{k+1}} C_s^k \mid_{k=4} dz \right),$$

$$B_{L1} = \left(\int_{h_k}^{h_{k+1}} C_b^k Z_L^k \mid_{k=1} dz + \int_{h_k}^{h_{k+1}} C_b^k Z_L^k \mid_{k=3} dz + \int_{h_k}^{h_{k+1}} C_b^k Z_L^k \mid_{k=5} dz \right),$$

$$B_{L1}^v = \left(\int_{h_k}^{h_{k+1}} C_b^k Z_L^k \mid_{k=2} dz + \int_{h_k}^{h_{k+1}} C_b^k Z_L^k \mid_{k=4} dz \right),$$

$$B_{L2} = \left(\int_{h_k}^{h_{k+1}} \left(Z_L^k\right)^T C_b^k \mid_{k=1} dz + \int_{h_k}^{h_{k+1}} \left(Z_L^k\right)^T C_b^k \mid_{k=3} dz + \int_{h_k}^{h_{k+1}} \left(Z_L^k\right)^T C_b^k \mid_{k=5} dz \right),$$

$$B_{L2}^v = \left(\int_{h_k}^{h_{k+1}} \left(Z_L^k\right)^T C_b^k \mid_{k=2} dz + \int_{h_k}^{h_{k+1}} \left(Z_L^k\right)^T C_b^k \mid_{k=4} dz \right),$$

$$D_{L1} = \left(\int_{h_k}^{h_{k+1}} \left(Z_L^k\right)^T C_b^k Z_L^k \mid_{k=1} dz + \int_{h_k}^{h_{k+1}} \left(Z_L^k\right)^T C_b^k Z_L^k \mid_{k=3} dz + \int_{h_k}^{h_{k+1}} \left(Z_L^k\right)^T C_b^k Z_L^k \mid_{k=5} dz \right),$$

$$D_{L1}^v = \left(\int_{h_k}^{h_{k+1}} \left(Z_L^k\right)^T C_b^k Z_L^k \mid_{k=2} dz + \int_{h_k}^{h_{k+1}} \left(Z_L^k\right)^T C_b^k Z_L^k \mid_{k=4} dz \right),$$

$$B_{s1} = \left(\int_{h_k}^{h_{k+1}} C_s^k Z_s^k \mid_{k=1} dz + \int_{h_k}^{h_{k+1}} C_s^k Z_s^k \mid_{k=3} dz + \int_{h_k}^{h_{k+1}} C_s^k Z_s^k \mid_{k=5} dz \right),$$

$$B_{s1}^v = \left(\int_{h_k}^{h_{k+1}} C_s^k Z_s^k \mid_{k=2} dz + \int_{h_k}^{h_{k+1}} C_s^k Z_s^k \mid_{k=4} dz \right),$$

$$B_{s2}^{2}=\left(\int_{h_k}^{h_{k+1}}\left(Z_s^k\right)^T C_s^k\,|_{k=1}\,dz+\int_{h_k}^{h_{k+1}}\left(Z_s^k\right)^T C_s^k\,|_{k=3}\,dz+\int_{h_k}^{h_{k+1}}\left(Z_s^k\right)^T C_s^k\,|_{k=5}\,dz\right),$$

$$B_{s2}^{v}=\left(\int_{h_k}^{h_{k+1}}\left(Z_s^k\right)^T C_s^k\,|_{k=2}\,dz+\int_{h_k}^{h_{k+1}}\left(Z_s^k\right)^T C_s^k\,|_{k=4}\,dz\right),$$

$$D_s=\left(\int_{h_k}^{h_{k+1}}\left(Z_s^k\right)^T C_s^k Z_s^k\,|_{k=1}\,dz+\int_{h_k}^{h_{k+1}}\left(Z_s^k\right)^T C_s^k Z_s^k\,|_{k=3}\,dz+\int_{h_k}^{h_{k+1}}\left(Z_s^k\right)^T C_s^k Z_s^k\,|_{k=5}\,dz\right),$$

$$D_s^{v}=\left(\int_{h_k}^{h_{k+1}}\left(Z_s^k\right)^T C_s^k Z_s^k\,|_{k=2}\,dz+\int_{h_k}^{h_{k+1}}\left(Z_s^k\right)^T C_s^k Z_s^k\,|_{k=4}\,dz\right),$$

$$B_{N1}=\left(\int_{h_k}^{h_{k+1}} C_b^k Z_N^k\,|_{k=1}\,dz+\int_{h_k}^{h_{k+1}} C_b^k Z_N^k\,|_{k=3}\,dz+\int_{h_k}^{h_{k+1}} C_b^k Z_N^k\,|_{k=5}\,dz\right),$$

$$B_{N2}=\left(\int_{h_k}^{h_{k+1}}\left(Z_N^k\right)^T C_b^k\,|_{k=1}\,dz+\int_{h_k}^{h_{k+1}}\left(Z_N^k\right)^T C_b^k\,|_{k=3}\,dz+\int_{h_k}^{h_{k+1}}\left(Z_N^k\right)^T C_b^k\,|_{k=5}\,dz\right),$$

$$B_{N2}^{v}=\left(\int_{h_k}^{h_{k+1}}\left(Z_N^k\right)^T C_b^k\,|_{k=2}\,dz+\int_{h_k}^{h_{k+1}}\left(Z_N^k\right)^T C_b^k\,|_{k=4}\,dz\right),$$

$$D_{N1}=\left(\int_{h_k}^{h_{k+1}}\left(Z_L^k\right)^T C_b^k Z_N^k\,|_{k=1}\,dz+\int_{h_k}^{h_{k+1}}\left(Z_L^k\right)^T C_b^k Z_N^k\,|_{k=3}\,dz+\int_{h_k}^{h_{k+1}}\left(Z_L^k\right)^T C_b^k Z_N^k\,|_{k=5}\,dz\right),$$

$$D_{N2}=\left(\int_{h_k}^{h_{k+1}}\left(Z_N^k\right)^T C_b^k Z_L^k\,|_{k=1}\,dz+\int_{h_k}^{h_{k+1}}\left(Z_N^k\right)^T C_b^k Z_L^k\,|_{k=3}\,dz+\int_{h_k}^{h_{k+1}}\left(Z_N^k\right)^T C_b^k Z_L^k\,|_{k=5}\,dz\right),$$

$$D_{N2}^{v}=\left(\int_{h_k}^{h_{k+1}}\left(Z_N^k\right)^T C_b^k Z_L^k\,|_{k=2}\,dz+\int_{h_k}^{h_{k+1}}\left(Z_N^k\right)^T C_b^k Z_L^k\,|_{k=4}\,dz\right),$$

$$D_{N3}=\left(\int_{h_k}^{h_{k+1}}\left(Z_N^k\right)^T C_b^k Z_N^k\,|_{k=1}\,dz+\int_{h_k}^{h_{k+1}}\left(Z_N^k\right)^T C_b^k Z_N^k\,|_{k=3}\,dz+\int_{h_k}^{h_{k+1}}\left(Z_N^k\right)^T C_b^k Z_N^k\,|_{k=5}\,dz\right) \tag{5.30}$$

For Element 3/ Element 4

$$A_b=\left(\int_{h_k}^{h_{k+1}} C_b^k\,|_{k=1}\,dz+\int_{h_k}^{h_{k+1}} C_b^k\,|_{k=5}\,dz\right),$$

$$A_b^v = \sum_{k=2}^{4} \int_{h_k}^{h_{k+1}} C_b^k dz\,,\; A_s = \left(\int_{h_k}^{h_{k+1}} C_s^k \mid_{k=1} dz + \int_{h_k}^{h_{k+1}} C_s^k \mid_{k=5} dz \right),$$

$$A_s^v = \sum_{k=2}^{4} \int_{h_k}^{h_{k+1}} C_s^k dz\;,\; B_{L1} = \left(\int_{h_k}^{h_{k+1}} C_b^k Z_L^k \mid_{k=1} dz + \int_{h_k}^{h_{k+1}} C_b^k Z_L^k \mid_{k=5} dz \right),$$

$$B_{L1}^v = \sum_{k=2}^{4} \int_{h_k}^{h_{k+1}} C_b^k Z_L^k dz\,,\; B_{L2} = \left(\int_{h_k}^{h_{k+1}} \left(Z_L^k\right)^T C_b^k \mid_{k=1} dz + \int_{h_k}^{h_{k+1}} \left(Z_L^k\right)^T C_b^k \mid_{k=5} dz \right),$$

$$B_{L2}^v = \sum_{k=2}^{4} \int_{h_k}^{h_{k+1}} \left(Z_L^k\right)^T C_b^k dz\,,\; D_{L1} = \left(\int_{h_k}^{h_{k+1}} \left(Z_L^k\right)^T C_b^k Z_L^k \mid_{k=1} dz + \int_{h_k}^{h_{k+1}} \left(Z_L^k\right)^T C_b^k Z_L^k \mid_{k=5} dz \right),$$

$$D_{L1}^v = \sum_{k=2}^{4} \int_{h_k}^{h_{k+1}} \left(Z_L^k\right)^T C_b^k Z_L^k dz\,,\; B_{s1} = \left(\int_{h_k}^{h_{k+1}} C_s^k Z_s^k \mid_{k=1} dz + \int_{h_k}^{h_{k+1}} C_s^k Z_s^k \mid_{k=5} dz \right),$$

$$B_{s1}^v = \sum_{k=2}^{4} \int_{h_k}^{h_{k+1}} C_s^k Z_s^k \mid_{k=1} dz\,,\; B_{s2} = \left(\int_{h_k}^{h_{k+1}} \left(Z_s^k\right)^T C_s^k \mid_{k=1} dz + \int_{h_k}^{h_{k+1}} \left(Z_s^k\right)^T C_s^k \mid_{k=5} dz \right),$$

$$B_{s2}^v = \sum_{k=2}^{4} \int_{h_k}^{h_{k+1}} \left(Z_s^k\right)^T C_s^k dz\,,\; D_s = \left(\int_{h_k}^{h_{k+1}} \left(Z_s^k\right)^T C_s^k Z_s^k \mid_{k=1} dz + \int_{h_k}^{h_{k+1}} \left(Z_s^k\right)^T C_s^k Z_s^k \mid_{k=5} dz \right),$$

$$D_s^v = \sum_{k=2}^{4} \int_{h_k}^{h_{k+1}} \left(Z_s^k\right)^T C_s^k Z_s^k dz\,,\; B_{N1} = \left(\int_{h_k}^{h_{k+1}} C_b^k Z_N^k \mid_{k=1} dz + \int_{h_k}^{h_{k+1}} C_b^k Z_N^k \mid_{k=5} dz \right),$$

$$B_{N2} = \left(\int_{h_k}^{h_{k+1}} \left(Z_N^k\right)^T C_b^k \mid_{k=1} dz + \int_{h_k}^{h_{k+1}} \left(Z_N^k\right)^T C_b^k \mid_{k=5} dz \right),\; B_{N2}^v = \sum_{k=2}^{4} \int_{h_k}^{h_{k+1}} \left(Z_N^k\right)^T C_b^k dz\,,$$

$$D_{N1} = \left(\int_{h_k}^{h_{k+1}} \left(Z_L^k\right)^T C_b^k Z_N^k \mid_{k=1} dz + \int_{h_k}^{h_{k+1}} \left(Z_L^k\right)^T C_b^k Z_N^k \mid_{k=5} dz \right),$$

$$D_{N2} = \left(\int_{h_k}^{h_{k+1}} \left(Z_N^k\right)^T C_b^k Z_L^k \mid_{k=1} dz + \int_{h_k}^{h_{k+1}} \left(Z_N^k\right)^T C_b^k Z_L^k \mid_{k=5} dz \right),$$

$$D_{N2}^v = \sum_{k=2}^{4} \int_{h_k}^{h_{k+1}} \left(Z_N^k\right)^T C_b^k Z_L^k dz\,,$$

$$D_{N3} = \left(\int_{h_k}^{h_{k+1}} \left(Z_N^k\right)^T C_b^k Z_N^k \mid_{k=1} dz + \int_{h_k}^{h_{k+1}} \left(Z_N^k\right)^T C_b^k Z_N^k \mid_{k=5} dz \right) \tag{5.31}$$

For Element 1/ Element 2/Element 3/ Element 4:

$$\boldsymbol{A}_{be}^{1}=\int_{h_k}^{h_{k+1}}\boldsymbol{e}_b\boldsymbol{Z}_E|_{k=5}\,dz\,,\ \boldsymbol{B}_{be}^{1}=\int_{h_k}^{h_{k+1}}\left(\boldsymbol{Z}_L^k\right)^T\boldsymbol{e}_b\boldsymbol{Z}_E|_{k=5}\,dz\,,$$

$$A_{se}^{1}=\int_{h_k}^{h_{k+1}}e_sZ_E|_{k=5}\,dz\,,\ B_{se}^{1}=\int_{h_k}^{h_{k+1}}(Z_s^k)^Te_sZ_E|_{k=5}\,dz\,,$$

$$B_{be}^{N1}=\int_{h_k}^{h_{k+1}}(Z_N^k)^Te_bZ_E|_{k=5}\,dz\,,\ A_{be}^{2}=\int_{h_k}^{h_{k+1}}(Z_E)^T(e_b)^T|_{k=5}\,dz\,,$$

$$B_{be}^{2}=\int_{h_k}^{h_{k+1}}\left(Z_E\right)^T\left(e_b\right)^TZ_L^k|_{k=5}\,dz\,,\ A_{se}^{2}=\int_{h_k}^{h_{k+1}}(Z_E)^T(e_s)^T|_{k=5}\,dz\,,$$

$$B_{se}^{2}=\int_{h_k}^{h_{k+1}}(\boldsymbol{Z}_E)^T\left(e_s\right)^TZ_s^k|_{k=5}\,dz\,,\ B_{be}^{N2}=\int_{h_k}^{h_{k+1}}(Z_E)^T\left(e_b\right)^TZ_N^k|_{k=5}\,dz\,,$$

$$A_E=\int_{h_k}^{h_{k+1}}(\boldsymbol{Z}_E)^T\,\epsilon^T\,Z_E\Big|_{k=5}\,dz\,,\ A_T=\int_{h_k}^{h_{k+1}}C_b^k\boldsymbol{\alpha}(z)\Delta T(z)|_{k=1}\,dz\,,$$

$$B_{LT}=\int_{h_k}^{h_{k+1}}(Z_L^k)^TC_b^k\boldsymbol{\alpha}(z)\Delta T(z)|_{k=1}\,dz\,,\ B_{NT}=\int_{h_k}^{h_{k+1}}(Z_N^k)^TC_b^k\boldsymbol{\alpha}(z)\Delta T(z)|_{k=1}\,dz \tag{5.32}$$

The forms of these matrices and vectors in Eqs. (5.30), (5.31) and (5.32) vary due to the variation of elemental stacking sequence of layers. So, these are presented according to the elemental stacking sequence (Fig. 5.4). It should be noted here that the temperature gradient across the thickness of the host FG shell causes thermal deformation of the overall shell. The coupling of this thermal deformation with the amplitude of vibration is accounted by geometrically nonlinear formulation while the overall shell is considered to vibrate with small displacement-amplitude. For this small time-varying displacement of the overall shell, the time-derivative of strain within the constitutive relation of linear viscoelastic material (Eq. (5.14)) is considered in linear form for the simplicity in deriving Eq. (5.26). The governing equations of motion of a typical element of the overall shell is derived employing the extended Hamilton's principle as given by Eq. (2.11)

$$\int_{t_1}^{t_2}\left(\delta T_K-\delta T_P\right)dt=0 \tag{2.11}$$

Substituting Eqs. (5.26) and (5.27) in Eq. (2.11), the elemental governing equations of motion can be obtained as,

$$\begin{aligned}
&\boldsymbol{M}^e(\ddot{\boldsymbol{d}}^e+\Delta\ddot{\boldsymbol{d}}^e)+\boldsymbol{K}_L^e\left(\boldsymbol{d}^e+\Delta\boldsymbol{d}^e\right)+\boldsymbol{K}_N^e\boldsymbol{d}^e+\boldsymbol{K}_N^{\Delta e}\Delta\boldsymbol{d}^e\\
&+\left(\boldsymbol{K}_L^{ve}+\boldsymbol{K}_{N2}^{ve}\right)\int_0^t E(t-\tau)\left(\dot{\boldsymbol{d}}^e+\Delta\dot{\boldsymbol{d}}^e\right)d\tau+\boldsymbol{K}_s^{ve}\int_0^t G(t-\tau)\left(\dot{\boldsymbol{d}}^e+\Delta\dot{\boldsymbol{d}}^e\right)d\tau\\
&-(K_{d\phi}^{Le}+K_{d\phi}^{Ne})(\boldsymbol{\phi}_v^e+\Delta\boldsymbol{\phi}_v^e)-\boldsymbol{P}_T^{Le}-\boldsymbol{P}_T^{Ne}-\boldsymbol{P}_M^e(t)=0
\end{aligned} \tag{5.33}$$

$$K_{\phi d}^{Le}\left(\boldsymbol{d}^e+\Delta\boldsymbol{d}^e\right)+\boldsymbol{K}_{\phi d}^{Ne}\boldsymbol{d}^e+\boldsymbol{K}_{\phi d}^{\Delta Ne}\Delta\boldsymbol{d}^e+\boldsymbol{K}_{\phi\phi}^e(\boldsymbol{\phi}_v^e+\Delta\boldsymbol{\phi}_v^e)=0 \tag{5.34}$$

The properties of the viscoelastic materials are usually characterized by the frequency and temperature dependent complex modulus. According to the GHM method (Golla and Hughes, 1985), this complex modulus is expressed in terms of a series of mini oscillators in the Laplace-domain as,

$$s\tilde{G}(s)=G^{\infty}\left[1+\sum_{q=1}^{N_v}\alpha_q\frac{s^2+2\tilde{\xi}_q\tilde{\omega}_q s}{s^2+2\tilde{\xi}_q\tilde{\omega}_q s+\tilde{\omega}_q^2}\right] \tag{5.35}$$

where, G^{∞} represents the modulus in equilibrium; N_v is the number of mini oscillators; α_q, $\tilde{\xi}_q$, $\tilde{\omega}_q$ are the GHM parameters which could be obtained by fitting the curve through experimental data for the modulus within a frequency-domain. This material modulus function ($s\tilde{G}(s)$) is introduced within the governing equations of motion (Eq. (5.33)) by taking those in the Laplace-domain. Subsequently, the resulting equations are expressed in the time-domain through inverse Laplace transform as,

$$\begin{aligned}
&\boldsymbol{M}^e(\ddot{\boldsymbol{d}}^e+\Delta\ddot{\boldsymbol{d}}^e)+\boldsymbol{K}_L^{te}\left(\boldsymbol{d}^e+\Delta\boldsymbol{d}^e\right)+\boldsymbol{K}_N^{te}\boldsymbol{d}^e+\boldsymbol{K}_N^{\Delta e}\Delta\boldsymbol{d}^e\\
&-\left(K_a^{Le}+K_a^{Ne}+K_a^{se}\right)\sum_{q=1}^{N_v}\alpha_q\left(z_q^e+\Delta z_q^e\right)\\
&-(K_{d\phi}^{Le}+K_{d\phi}^{Ne})(\boldsymbol{\phi}_v^e+\Delta\boldsymbol{\phi}_v^e)-\boldsymbol{P}_T^{Le}-\boldsymbol{P}_T^{Ne}-\boldsymbol{P}_M^e(t)=0\,,
\end{aligned}$$

$$\boldsymbol{K}_L^{te}=\boldsymbol{K}_L^e+\boldsymbol{K}_L^{ve}E^{\infty}\left(1+\sum_{q=1}^{N_v}\alpha_q\right)+\boldsymbol{K}_s^{ve}G^{\infty}\left(1+\sum_{q=1}^{N_v}\alpha_q\right),$$

$$\boldsymbol{K}_N^{te}=\boldsymbol{K}_N^e+\boldsymbol{K}_{N2}^{ve}E^{\infty}\left(1+\sum_{q=1}^{N_v}\alpha_q\right),$$

$$\boldsymbol{K}_a^{Le}=\boldsymbol{K}_L^{ve}E^{\infty}\,,\ \boldsymbol{K}_a^{se}=\boldsymbol{K}_s^{ve}G^{\infty}\,,\ \boldsymbol{K}_a^{Ne}=\boldsymbol{K}_{N2}^{ve}E^{\infty} \tag{5.36}$$

$$\left(\ddot{z}_q^e + \Delta\ddot{z}_q^e\right) + 2\tilde{\xi}_q\tilde{\omega}_q\left(\dot{z}_q^e + \Delta\dot{z}_q^e\right) + \tilde{\omega}_q^2\left(z_q^e + \Delta z_q^e\right) = \tilde{\omega}_q^2\left(\boldsymbol{d}^e + \Delta\boldsymbol{d}^e\right) \tag{5.37}$$

In Eqs. (5.36)-(5.37), z_q^e is the elemental nodal auxiliary/dissipation coordinate vector for q^{th} mini-oscillator; E^∞ is the Young's modulus of isotropic viscoelastic material in equilibrium. Equations (5.36), (5.34) and (5.37) are the elemental governing equations of motion in the time-domain. In order to express these equations in the frequency-domain, the harmonic balance method (HBM) is utilized through the following forms of nodal displacements ($\boldsymbol{d}^e$) and auxiliary coordinates (z_q^e),

$$\boldsymbol{d}^e = \boldsymbol{a}_0 + \sum_{s=1}^{F}\left\langle \boldsymbol{a}_s\cos(s\omega t) + \boldsymbol{b}_s\sin(s\omega t)\right\rangle \tag{5.38}$$

$$z_q^e = \boldsymbol{a}_{q0} + \sum_{s=1}^{F}\left\langle \boldsymbol{a}_{qs}\cos(s\omega t) + \boldsymbol{b}_{qs}\sin(s\omega t)\right\rangle \tag{5.39}$$

where, $\boldsymbol{a}_0 / \boldsymbol{a}_{q0}$ is the time-independent elemental nodal displacement/auxiliary (dissipation) coordinate vector; $\boldsymbol{a}_s / \boldsymbol{a}_{qs}$ and $\boldsymbol{b}_s / \boldsymbol{b}_{qs}$ are the elemental nodal displacement/auxiliary (dissipation) coordinate vectors for the amplitudes in s-th harmonic term. These solutions and their time derivatives can be written in the following forms,

$$\boldsymbol{d}^e = S^e X^e,\ \dot{\boldsymbol{d}}^e = \omega S_1^e X^e,\ \ddot{\boldsymbol{d}}^e = -\omega^2 S_2^e X^e,$$

$$z_q^e = S^e X_q^e,\ \dot{z}_q^e = \omega S_1^e X_q^e,\ \ddot{z}_q^e = -\omega^2 S_2^e X_q^e,$$

$$\Delta\boldsymbol{d}^e = S^e\Delta X^e,\ \Delta\dot{\boldsymbol{d}}^e = \left(\omega\, S_1^e\Delta X^e + \Delta\omega S_1^e X^e\right),$$

$$\Delta\ddot{\boldsymbol{d}}^e = \left(-\omega^2 S_2^e\Delta X^e - 2\omega\ \Delta\omega S_2^e X^e\right),$$

$$\Delta z_q^e = S^e\Delta X_q^e,\ \Delta\dot{z}_q^e = \left(\omega S_1^e\Delta X_q^e + \Delta\omega S_1^e X_q^e\right),$$

$$\Delta\ddot{z}_q^e = \left(-\omega^2 S_2^e\Delta X_q^e - 2\omega\Delta\omega S_2^e X_q^e\right),$$

$$\boldsymbol{X}^e = \left[\boldsymbol{a}_0^{\mathrm{T}}\quad \boldsymbol{a}_1^{\mathrm{T}}\quad \boldsymbol{b}_1^{\mathrm{T}}\quad .\ .\ .\quad \boldsymbol{a}_F^{\mathrm{T}}\quad \boldsymbol{b}_F^{\mathrm{T}}\right]^{\mathrm{T}},$$

$$\boldsymbol{X}_q^e = \left[\boldsymbol{a}_{q0}^{\mathrm{T}}\quad \boldsymbol{a}_{q1}^{\mathrm{T}}\quad \boldsymbol{b}_{q1}^{\mathrm{T}}\quad .\ .\ .\quad \boldsymbol{a}_{qF}^{\mathrm{T}}\quad \boldsymbol{b}_{qF}^{\mathrm{T}}\right]^{\mathrm{T}},$$

$$\Delta \boldsymbol{X}^e = \left[\Delta \boldsymbol{a}_0{}^{\mathrm{T}} \quad \Delta \boldsymbol{a}_1{}^{\mathrm{T}} \quad \Delta \boldsymbol{b}_1{}^{\mathrm{T}} \quad . \quad . \quad . \quad \Delta \boldsymbol{a}_F{}^{\mathrm{T}} \quad \Delta \boldsymbol{b}_F{}^{\mathrm{T}} \right]^{\mathrm{T}},$$

$$\Delta \boldsymbol{X}_q^e = \left[\Delta \boldsymbol{a}_{q0}{}^{\mathrm{T}} \quad \Delta \boldsymbol{a}_{q1}{}^{\mathrm{T}} \quad \Delta \boldsymbol{b}_{q1}{}^{\mathrm{T}} \quad . \quad . \quad . \quad \Delta \boldsymbol{a}_{qF}{}^{\mathrm{T}} \quad \Delta \boldsymbol{b}_{qF}{}^{\mathrm{T}} \right]^{\mathrm{T}} \tag{5.40}$$

The matrices (S^e, S_1^e, S_2^e) appearing in Eq. (5.40) are given in Eq. (5.41) where $\boldsymbol{I}$ and $\mathbf{0}$ are the unit and null matrices, respectively, and θ is equal to ωt.

$$S^e = \left[I \quad I\cos\theta \quad I\sin\theta \quad . \quad . \quad . \quad I\cos(F\theta) \quad I\sin(F\theta) \right],$$

$$S_1^e = \left[0 \quad -I\sin\theta \quad I\cos\theta \quad . \quad . \quad . \quad -F\times I\sin(F\theta) \quad F\times I\cos(F\theta) \right],$$

$$S_2^e = \left[0 \quad I\cos\theta \quad I\sin\theta \quad . \quad . \quad . \quad F^2\times I\cos(F\theta) \quad F^2\times I\sin(F\theta) \right] \tag{5.41}$$

For small increment over a given state, the terms $\Delta\omega \boldsymbol{S}_1^e \Delta \boldsymbol{X}^e$, $\Delta\omega \boldsymbol{S}_2^e \Delta \boldsymbol{X}^e$, $\Delta\omega \boldsymbol{S}_1^e \Delta \boldsymbol{X}_q^e$ and $\Delta\omega \boldsymbol{S}_2^e \Delta \boldsymbol{X}_q^e$ appearing in derivation of Eq. (5.40) are omitted. According to this form of solution, the nonlinear strain-displacement matrices ($\boldsymbol{B}_{bN}, \boldsymbol{B}_{\kappa N}, \boldsymbol{B}_{bN}^{\Delta}$, $\boldsymbol{B}_{\kappa N}^{\Delta}$) can be modified as,

$$B_{bN} = B_{bN}^t \, S^e{}^{\mathrm{T}}, \; B_{bN}^t = \left[B_{bN}^0 \quad B_{bN}^{a1} \quad B_{bN}^{b1} \ldots\ldots B_{bN}^{aF} \quad B_{bN}^{bF} \right],$$

$$B_{bN}^{\Delta} = B_{bN}^{\Delta t} \, S^e{}^{\mathrm{T}}, \; B_{bN}^{\Delta t} = \left[B_{bN}^{\Delta 0} \quad B_{bN}^{\Delta a1} \quad B_{bN}^{\Delta b1} \ldots\ldots B_{bN}^{\Delta aF} \quad B_{bN}^{\Delta bF} \right],$$

$$B_{\kappa N} = B_{\kappa N}^t \, S^e{}^{\mathrm{T}}, B_{\kappa N}^t = \left[B_{\kappa N}^0 \quad B_{\kappa N}^{a1} \quad B_{\kappa N}^{b1} \ldots\ldots B_{\kappa N}^{aF} \quad B_{\kappa N}^{bF} \right],$$

$$B_{\kappa N}^{\Delta} = B_{\kappa N}^{\Delta t} \, S^e{}^{\mathrm{T}}, \; B_{\kappa N}^{\Delta t} = \left[B_{\kappa N}^{\Delta 0} \quad B_{\kappa N}^{\Delta a1} \quad B_{\kappa N}^{\Delta b1} \ldots\ldots B_{\kappa N}^{\Delta aF} \quad B_{\kappa N}^{\Delta bF} \right] \tag{5.42}$$

where, $B_{bN}^0 / B_{bN}^{as} / B_{bN}^{bs}$, $B_{bN}^{\Delta 0} / B_{bN}^{\Delta as} / B_{bN}^{\Delta bs}$, $B_{\kappa N}^0 / B_{\kappa N}^{as} / B_{\kappa N}^{bs}$ and $B_{\kappa N}^{\Delta 0} / B_{\kappa N}^{\Delta as} / B_{\kappa N}^{\Delta bs}$ ($s = 1,2,3,\ldots,F$) are in similar forms of B_{bN}, B_{bN}^{Δ}, $B_{\kappa N}$ and $B_{\kappa N}^{\Delta}$, respectively while the same are the functions of $\boldsymbol{a}_0 / \boldsymbol{a}_s / \boldsymbol{b}_s$ as per their superscripts ($0 / as / bs$). Introducing Eqs. (5.40) and (5.42) in Eqs. (5.36), (5.34) and (5.37), the following expressions can be obtained,

$$\boldsymbol{K}_c^e \Delta \boldsymbol{X}^e - 2\omega\Delta\omega \boldsymbol{M}_c^e \boldsymbol{X}^e + \boldsymbol{K}_0^e \boldsymbol{X}^e - \left(\boldsymbol{K}_a^{Lce} + \boldsymbol{K}_a^{Nce} + \boldsymbol{K}_a^{sce} \right) \sum_{q=1}^{N_v} \alpha_q \left(\boldsymbol{X}_q^e + \Delta \boldsymbol{X}_q^e \right)$$

$$- \left(\boldsymbol{K}_{d\phi}^{Le} + \boldsymbol{K}_{d\phi}^{Nce} \right) \left(\boldsymbol{\phi}_v^e + \Delta \boldsymbol{\phi}_v^e \right) - \boldsymbol{P}_T^{Le} - \boldsymbol{P}_T^{Nce} - \boldsymbol{P}_M^e(t) = 0, \tag{5.43}$$

$$\boldsymbol{K}_{\phi d}^{0e} \boldsymbol{X}^e + \boldsymbol{K}_{\phi d}^{ce} \Delta \boldsymbol{X}^e + \boldsymbol{K}_{\phi\phi}^e \left(\boldsymbol{\phi}_v^e + \Delta \boldsymbol{\phi}_v^e \right) = 0 \tag{5.44}$$

$$\boldsymbol{K}_{0q}^{e}\boldsymbol{X}_{q}^{e}+\boldsymbol{K}_{cq}^{e}\Delta\boldsymbol{X}_{q}^{e}+\Delta\omega\boldsymbol{K}_{cq}^{0e}\boldsymbol{X}_{q}^{e}=\boldsymbol{K}_{q}^{ce}\left(\boldsymbol{X}^{e}+\Delta\boldsymbol{X}^{e}\right) \tag{5.45}$$

The forms of different matrices appearing in Eqs. (5.43), (5.44) and (5.45) are as follows,

$$\boldsymbol{K}_{c}^{e}=\left(-\omega^{2}\boldsymbol{M}^{e}\boldsymbol{S}_{2}^{e}+\boldsymbol{K}_{L}^{te}\boldsymbol{S}^{e}+\left\langle \boldsymbol{K}_{N1}^{\Delta te}(\boldsymbol{S}^{e})^{\mathrm{T}}+\boldsymbol{S}^{e}\boldsymbol{K}_{N2}^{\Delta te}+\boldsymbol{S}^{e}\boldsymbol{K}_{NN}^{\Delta te}(\boldsymbol{S}^{e})^{\mathrm{T}}\right\rangle \boldsymbol{S}^{e}\right),$$

$$K_{0}^{e}=\left(-\omega^{2}M^{e}S_{2}^{e}+K_{L}^{te}S^{e}+\left\langle \begin{matrix} K_{N1}^{te}(S^{e})^{\mathrm{T}}+S^{e}K_{N2}^{te}+S^{e}K_{NN}^{te}(S^{e})^{\mathrm{T}} \\ +S^{e}K_{N2}^{vte}E^{\infty}\left(1+\sum_{q=1}^{N_{v}}\alpha_{q}\right) \end{matrix}\right\rangle S^{e}\right),$$

$$M_{c}^{e}=M^{e}S_{2}^{e},\ K_{a}^{Lce}=K_{a}^{Le}S^{e},\ K_{a}^{sce}=K_{a}^{se}S^{e},$$

$$K_{a}^{Nce}=S^{e}K_{N2}^{vte}E^{\infty}S^{e},\ K_{d\phi}^{Nce}=S^{e}K_{d\phi}^{Nte},\ P_{T}^{Nce}=S^{e}P_{T}^{Nte} \tag{5.46}$$

$$K_{\phi d}^{0e}=\left\langle K_{\phi d}^{Le}+K_{\phi d}^{Nte}(S^{e})^{\mathrm{T}}\right\rangle S^{e},\quad K_{\phi d}^{ce}=\left\langle K_{\phi d}^{Le}+K_{\phi d}^{\Delta Nte}(S^{e})^{\mathrm{T}}\right\rangle S^{e} \tag{5.47}$$

$$K_{0q}^{e}=-\omega^{2}S_{2}^{e}+2\tilde{\xi}_{q}\tilde{\omega}_{q}\omega S_{1}^{e}+\tilde{\omega}_{q}{}^{2}S^{e},\ K_{cq}^{e}=K_{0q}^{e},$$

$$K_{cq}^{0e}=-2\omega S_{2}^{e}+2\tilde{\xi}_{q}\tilde{\omega}_{q}S_{1}^{e},\ K_{q}^{ce}=\tilde{\omega}_{q}{}^{2}S^{e} \tag{5.48}$$

In Eqs. (5.46), (5.47) and (5.48), the different nonlinear vectors and matrices (K_{N1}^{te}, K_{N2}^{te}, K_{NN}^{te}, K_{N2}^{vte}, $K_{N1}^{\Delta te}$, $K_{N2}^{\Delta te}$, $K_{NN}^{\Delta te}$, $K_{d\phi}^{Nte}$, P_{T}^{Nte}, $K_{\phi d}^{Nte}$, $K_{\phi d}^{\Delta Nte}$) are obtained by using modified forms (B_{bN}^{t}, $B_{bN}^{\Delta t}$, $B_{\kappa N}^{t}$, $B_{\kappa N}^{\Delta t}$) of the nonlinear strain-displacement matrices (B_{bN}, B_{bN}^{Δ}, $B_{\kappa N}$, $B_{\kappa N}^{\Delta}$) in the expressions (Eqs. (5.28)) of (K_{N1}^{e}, K_{N2}^{e}, K_{NN}^{e}, K_{N2}^{ve}, $K_{N1}^{\Delta e}$, $K_{N2}^{\Delta e}$, $K_{NN}^{\Delta e}$, $K_{d\phi}^{Ne}$, P_{T}^{Ne}, $K_{\phi d}^{Ne}$, $K_{\phi d}^{\Delta Ne}$). Assembling the elemental equations of motion (Eqs. (5.43)-(5.45)) in the global space, the following expressions can be obtained,

$$K_{c}\Delta X\ -2\omega\Delta\omega M_{c}X\ +K_{0}X\ -\left(K_{a}^{Lc}+K_{a}^{Nc}+K_{a}^{sc}\right)\sum_{q=1}^{N_{v}}\alpha_{q}\left(X_{q}+\Delta X_{q}\right)$$

$$-\left(K_{d\phi}^{L}+K_{d\phi}^{Nc}\right)\left(\phi_{v}+\Delta\phi_{v}\right)-P_{T}^{L}-P_{T}^{Nc}-P_{M}(t)=0 \tag{5.49}$$

$$\boldsymbol{K}_{\phi d}^{0}\boldsymbol{X}+\boldsymbol{K}_{\phi d}^{c}\Delta\boldsymbol{X}+\boldsymbol{K}_{\phi\phi}\left(\boldsymbol{\phi}_{v}+\Delta\boldsymbol{\phi}_{v}\right)=0 \tag{5.50}$$

$$\boldsymbol{K}_{0q}\boldsymbol{X}_{q}+\boldsymbol{K}_{cq}\Delta\boldsymbol{X}_{q}+\Delta\omega\boldsymbol{K}_{cq}^{0}\boldsymbol{X}_{q}=\boldsymbol{K}_{q}^{c}\left(\boldsymbol{X}+\Delta\boldsymbol{X}\right) \tag{5.51}$$

The inner fully electrode-surface of the constraining layer is grounded ($\phi(x,y,z)=0$) and the electric potentials (ϕ_{0}) at the electrode-patches over the outer surface of

the same constraining layer are supplied according to the velocity feedback control strategy. The transverse velocity at the middle point of every electrode-patch is sensed by a velocity sensor. This velocity is fed back to that electrode-patch in the form of electric potential as follows,

$$\phi_\ell = -k_d^\ell \dot{w}_\ell^m \tag{5.52}$$

where, ℓ denotes a patch among the n_e number of electrode-patches; ϕ_ℓ and k_d^ℓ are the applied electric potential and the velocity feedback control-gain, respectively over the ℓ^{th} electrode-patch; $\dot{w}_\ell^m$ is the transverse velocity at the middle point of ℓ^{th} electrode-patch. Using Eq. (5.40) in Eq. (5.52), the electric potential (ϕ_ℓ) over ℓ^{th} electrode-patch can be written as,

$$\begin{aligned}
&\left(\phi_\ell + \Delta\phi_\ell\right) = -k_d^\ell S_1^s \left(\omega w_\ell^m + \omega \Delta w_\ell^m + \Delta\omega w_\ell^m\right) \\
&w_\ell^m = \begin{bmatrix} w_\ell^{ma1} & w_\ell^{mb1} & . & . & . & . & w_\ell^{maF} & w_\ell^{mbF} \end{bmatrix}^{\mathrm{T}}, \\
&\Delta w_\ell^m = \begin{bmatrix} \Delta w_\ell^{ma1} & \Delta w_\ell^{mb1} & . & . & . & . & \Delta w_\ell^{maF} & \Delta w_\ell^{mbF} \end{bmatrix}^{\mathrm{T}}, \\
&S_1^s = \begin{bmatrix} -\sin(\theta) & \cos(\theta) & . & . & . & . & -F\sin(F\theta) & F\cos(F\theta) \end{bmatrix}
\end{aligned} \tag{5.53}$$

where, w_ℓ^{mas} / Δw_ℓ^{mas} and w_ℓ^{mbs} / Δw_ℓ^{mbs} ($s = 1,2,3,\ldots\ldots F$) are the displacement-amplitudes in s^{th}-harmonic. The electric potentials (ϕ_0) over the electrode-patches are specified as ϕ_ℓ. These specified electric potentials could be imposed directly over the equations of motion (Eqs. (5.49) and (5.50). For a specified nodal electric potential over the outer surface of the constraining layer, the first variation of the corresponding element (say, ϕ_{vj}) of $\boldsymbol{\phi}_v$ is zero ($\delta\phi_{vj}$ = 0). Thus, the corresponding (j^{th}) rows of $\boldsymbol{K}_{\phi d}^0$, $\boldsymbol{K}_{\phi d}^c$ and $\boldsymbol{K}_{\phi\phi}$ are to be deleted while the columns ($\boldsymbol{P}_{d\phi}^{Lj}$, $\boldsymbol{P}_{d\phi}^{Nj}$ and $\boldsymbol{P}_{\phi\phi}^{j}$) of $\boldsymbol{K}_{d\phi}^L$, $\boldsymbol{K}_{d\phi}^{Nc}$ and $\boldsymbol{K}_{\phi\phi}$ with the same index (j) are to be removed for formation of the electric potential load vector as,

$$\begin{aligned}
&\boldsymbol{K}_c \Delta\boldsymbol{X} \; - 2\omega\Delta\omega \boldsymbol{M}_c \boldsymbol{X} \; + \boldsymbol{K}_0 \boldsymbol{X} \; - \left(\boldsymbol{K}_a^{Lc} + \boldsymbol{K}_a^{Nc} + \boldsymbol{K}_a^{sc}\right) \sum_{q=1}^{N_v} \alpha_q \left(\boldsymbol{X}_q + \Delta\boldsymbol{X}_q\right) \\
&- \left(\boldsymbol{K}_{d\phi r}^L + \boldsymbol{K}_{d\phi r}^{Nc}\right)\left(\boldsymbol{\phi}_{vr} + \Delta\boldsymbol{\phi}_{vr}\right) - \left(\boldsymbol{P}_{d\phi}^{Lj} + \boldsymbol{P}_{d\phi}^{Nj}\right)\left(\phi_{vj} + \Delta\phi_{vj}\right) - \boldsymbol{P}_T^L - \boldsymbol{P}_T^{Nc} - \boldsymbol{P}_M(t) = 0
\end{aligned} \tag{5.54}$$

$$\boldsymbol{K}^{0}_{\phi dr}\boldsymbol{X}+\boldsymbol{K}^{c}_{\phi dr}\Delta\boldsymbol{X}+\boldsymbol{K}_{\phi\phi r}\left(\boldsymbol{\phi}_{vr}+\Delta\boldsymbol{\phi}_{vr}\right)+\boldsymbol{P}^{j}_{\phi\phi}\left(\phi_{vj}+\Delta\phi_{vj}\right)=0 \tag{5.55}$$

where, $\boldsymbol{K}^{L}_{d\phi r}$, $\boldsymbol{K}^{Nc}_{d\phi r}$, $\boldsymbol{K}^{0}_{\phi dr}$, $\boldsymbol{K}^{c}_{\phi dr}$, $\boldsymbol{K}_{\phi\phi r}$ and $\boldsymbol{\phi}_{vr}$ are the reduced coefficient matrices and nodal electric potential vector after implementation of the specified value of ϕ_{vj}. For all the specified nodal electric potentials over the electrode-patches, Eqs. (5.54) and (5.55) can be written as,

$$\begin{aligned}
&K_c\Delta X\ -2\omega\Delta\omega M_c X\ +K_0 X\ -\left(K^{Lc}_a+K^{Nc}_a+K^{sc}_a\right)\sum_{q=1}^{N_v}\alpha_q\left(X_q+\Delta X_q\right)\\
&-\left(K^{L}_{d\phi r}+K^{Nc}_{d\phi r}\right)\left(\boldsymbol{\phi}_{vr}+\Delta\boldsymbol{\phi}_{vr}\right)-\sum_{\ell=1}^{n_e}\left(P^{L\ell}_{d\phi}+P^{N\ell}_{d\phi}\right)\left(\phi_{\ell}+\Delta\phi_{\ell}\right)-P^{L}_{T}-P^{Nc}_{T}-P_M(t)=0,\\
&\left(P^{L\ell}_{d\phi}+P^{N\ell}_{d\phi}\right)=\sum_{n_l=1}^{N^{\ell}_t}\left\langle\left(P^{Lj}_{d\phi}\right)^{n_l}+\left(P^{Nj}_{d\phi}\right)^{n_l}\right\rangle
\end{aligned} \tag{5.56}$$

$$\boldsymbol{K}^{0}_{\phi dr}\boldsymbol{X}+\boldsymbol{K}^{c}_{\phi dr}\Delta\boldsymbol{X}+\boldsymbol{K}_{\phi\phi r}\left(\boldsymbol{\phi}_{vr}+\Delta\boldsymbol{\phi}_{vr}\right)+\sum_{\ell=1}^{n_e}\boldsymbol{P}^{\ell}_{\phi\phi}\left(\phi_{\ell}+\Delta\phi_{\ell}\right)=0,$$

$$\boldsymbol{P}^{\ell}_{\phi\phi}=\sum_{n_l=1}^{N^{\ell}_t}\left(P^{i}_{\phi\phi}\right)^{n_l} \tag{5.57}$$

In Eqs. (5.56) and (5.57), N^{ℓ}_t is the number of nodes over ℓ^{th} electrode-patch and j indicates the element of $\boldsymbol{\phi}_v$ for the electric potential at n_l^{th} mode. From Eqs. (5.56) and (5.57), the nodal electrical potentials ($\boldsymbol{\phi}_{vr}+\Delta\boldsymbol{\phi}_{vr}$) are condensed and the resulting expression is expressed as,

$$\begin{aligned}
&K^{t}_c\Delta X\ -2\omega\Delta\omega M_c X\ +K^{t}_0 X\ -\left(K^{Lc}_a+K^{Nc}_a+K^{sc}_a\right)\sum_{q=1}^{N_v}\alpha_q\left(X_q+\Delta X_q\right)\\
&-\sum_{\ell=1}^{n_e}P^{\ell}_{\phi}\left(\phi_{\ell}+\Delta\phi_{\ell}\right)-P^{L}_{T}-P^{Nc}_{T}-P_M(t)=0,\\
&K^{t}_c=K_c+\left(K^{L}_{d\phi r}+K^{Nc}_{d\phi r}\right)\left(K_{\phi\phi r}\right)^{-1}K^{c}_{\phi dr},\\
&\boldsymbol{K}^{t}_0=\boldsymbol{K}_0+\left(\boldsymbol{K}^{L}_{d\phi r}+\boldsymbol{K}^{Nc}_{d\phi r}\right)\left(\boldsymbol{K}_{\phi\phi r}\right)^{-1}\boldsymbol{K}^{0}_{\phi dr},\\
&\boldsymbol{P}^{\ell}_{\phi}=\left(\boldsymbol{P}^{L\ell}_{d\phi}+\boldsymbol{P}^{N\ell}_{d\phi}\right)-\left(\boldsymbol{K}^{L}_{d\phi r}+\boldsymbol{K}^{Nc}_{d\phi r}\right)\left(\boldsymbol{K}_{\phi\phi r}\right)^{-1}\boldsymbol{P}^{\ell}_{\phi\phi}
\end{aligned} \tag{5.58}$$

Introducing Eq. (5.53) in Eq. (5.58) and then using Galerkin procedure, the simplified forms of Eqs. (5.58) and (5.51) can be expressed as,

$$\boldsymbol{K}_{\Delta}\Delta\boldsymbol{X}-2\omega\Delta\omega\boldsymbol{M}\boldsymbol{X}+\boldsymbol{K}\boldsymbol{X}-\boldsymbol{K}_{a}\sum_{q=1}^{N_v}\alpha_q\left(\boldsymbol{X}_q+\Delta\boldsymbol{X}_q\right)$$

$$+\sum_{\ell=1}^{n_e}P_c^{\ell}k_d^{\ell}\left(\omega w_{\ell}^{m}+\omega\Delta w_{\ell}^{m}+\Delta\omega w_{\ell}^{m}\right)-P_T-P_M=0 \tag{5.59}$$

$$\text{where, } K_{\Delta}=\int_0^{2\pi}\left(S^T K_c^t\right)d\theta,\ \boldsymbol{K}=\int_0^{2\pi}\left(S^T K_0^t\right)d\theta,$$

$$\boldsymbol{M}=\int_0^{2\pi}\left(S^T M_c\right)d\theta,\ \boldsymbol{K}_a=\left(K_a^b+K_a^s\right),$$

$$K_a^b=\int_0^{2\pi}\left(S^T\left\langle K_a^{Lc}+K_a^{Nc}\right\rangle\right)d\theta,$$

$$K_a^s=\int_0^{2\pi}\left(S^T K_a^{sc}\right)d\theta,\ P_c^{\ell}=\int_0^{2\pi}\left(S^T P_{\phi}^{\ell}S_1^s\right)d\theta,$$

$$P_T=\int_0^{2\pi}\left(S^T\left\langle P_T^L+P_T^{Nc}\right\rangle\right)d\theta,\ P_M=\int_0^{2\pi}\left(S^T P_M(t)\right)d\theta \tag{5.59a}$$

$$K_q X_q+K_q^{\Delta}\Delta X_q+\Delta\omega K_q^0 X_q=K_q^d\left(X+\Delta X\right), \tag{5.60}$$

$$\text{where, } K_q=\int_0^{2\pi}\left(S^T K_{0q}\right)d\theta,\ K_q^{\Delta}=\int_0^{2\pi}\left(S^T K_{cq}\right)d\theta,$$

$$K_q^0=\int_0^{2\pi}\left(S^T K_{cq}^0\right)d\theta,\ K_q^d=\int_0^{2\pi}\left(S^T K_q^c\right)d\theta \tag{5.60a}$$

where, S is the global form of S^e and the limits of integration is taken for one period assuming periodic vibration of the overall shell. The transverse displacements (w_{ℓ}^{m}, Δw_{ℓ}^{m}) at the sensor points can be expressed in terms of the global nodal displacement vectors (X, ΔX) through a transformation matrix (N_T^{ℓ}) as,

$$w_{\ell}^{m}=N_T^{\ell}X,\ \Delta w_{\ell}^{m}=N_T^{\ell}\Delta X \tag{5.61}$$

Using Eq. (5.61) in Eq. (5.59), the following expression can be obtained,

$$\boldsymbol{K}_{\Delta}^{t}\Delta\boldsymbol{X}+\Delta\omega f^{\omega}-\boldsymbol{K}_{a}\sum_{q=1}^{N_v}\alpha_q\left(\boldsymbol{X}_q+\Delta\boldsymbol{X}_q\right)=-f_0+\boldsymbol{P}_T+\boldsymbol{P}_M$$

$$\boldsymbol{K}_{\Delta}^{t}=\left(\boldsymbol{K}_{\Delta}+\omega\boldsymbol{C}\right),\ f^{\omega}=\left(-2\omega\boldsymbol{M}+\boldsymbol{C}\right)\boldsymbol{X},$$

$$f_0=\left(\boldsymbol{K}+\omega\boldsymbol{C}\right)\boldsymbol{X},\ \boldsymbol{C}=\sum_{\ell=1}^{n_e}\boldsymbol{P}_c^{\ell}k_d^{\ell}\boldsymbol{N}_T^{\ell} \tag{5.62}$$

Equations (5.62) and (5.60) are expressed in the following form considering three (N_v=3) mini-oscillator terms in the GHM model of viscoelastic material,

$$\boldsymbol{K}_t \Delta \boldsymbol{X}_t + \Delta\omega \boldsymbol{f}_t = \boldsymbol{f}_{0t} + \boldsymbol{f}_{Pt} \tag{5.63}$$

$$K_t = \begin{bmatrix} K_\Delta^t & -K_a\alpha_1 & -K_a\alpha_2 & -K_a\alpha_3 \\ K_1^d & -K_1^\Delta & 0 & 0 \\ K_2^d & 0 & -K_2^\Delta & 0 \\ K_3^d & 0 & 0 & -K_3^\Delta \end{bmatrix}, \quad f_{0t} = \begin{Bmatrix} -f_0 + K_a(\alpha_1 X_1 + \alpha_2 X_2 + \alpha_3 X_3) \\ -K_1^d X_1 + K_1 X_1 \\ -K_2^d X_2 + K_2 X_2 \\ -K_3^d X_3 + K_3 X_3 \end{Bmatrix},$$

$$f_t = \begin{Bmatrix} f^\omega \\ -K_1^0 X_1 \\ -K_2^0 X_2 \\ -K_3^0 X_3 \end{Bmatrix}, \quad f_{Pt} = \begin{Bmatrix} P_T + P_M \\ 0 \\ 0 \\ 0 \end{Bmatrix}, \quad \Delta X_t = \begin{Bmatrix} \Delta X \\ \Delta X_1 \\ \Delta X_2 \\ \Delta X_2 \end{Bmatrix} \tag{5.64}$$

Equation (5.63) describes the equations of motion of the overall shell in terms of the nodal displacements and dissipation co-ordinates. These equations of motion are solved using an arc-length extrapolation method (Kumar et al. 2015a) for the numerical evaluation of frequency responses of the overall shell.

5.4 Numerical results and discussions

In this section, the frequency responses of the overall shell are evaluated under a mechanical harmonic excitation in the absence/presence of ceramic rich surface temperature (T_c). Through these frequency responses, first the suitability of the present arrangement of electrode–patches is substantiated for control of several modes of vibration of the shell using one configuration of the patches. Next, the utility of present 1-3 VEC layer for ACLD treatment of vibration of circular cylindrical shell is verified. Finally, the effect of temperature (T_c) on the damping characteristic of the present ACLD layer is presented. The geometrical properties of the host FG shell and the PFC layer are considered as, L = 1.0 m, R = 0.5 m, h = 4 mm, h_p =200 μm. Unless otherwise mentioned, the circumferential span (α_E^p) of electrode-patches is considered as 9° within the segments (α_E) of 10° (n_e = 36). The thickness (h_d) of the constrained monolithic VEM/1-3 VEC layer is considered as 250 μm unless it is not mentioned in other ways. The other geometric properties, h_v, h_v^2, α, α^v (Fig. 5.1) of the constrained 1-3 VEC layer

are varied for investigating their effects on the damping characteristics of the ACLD treatment. The host FG shell is considered to be made of Zirconium and Aluminum alloy having the temperature-dependent material properties as (Noda, 1999),

Aluminium alloy:

$$\begin{aligned} E(T) &= (74+23\times10^{-3}T-11\times10^{-5}T^2+51\times10^{-9}T^3)\ \text{GPa},\\ \alpha(T) &= (1.6\times10^{-5}+3.45\times10^{-8}T-3.3\times10^{-11}T^2+2.4\times10^{-14}T^3)\ \text{K}^{-1},\\ k(T) &= 218\ \text{W mK}^{-1} \end{aligned} \tag{5.65}$$

Zirconium:

$$\begin{aligned} E(T) &= (225-20\times10^{-2}T-90\times10^{-6}T^2+4\times10^{-9}T^3)\ \text{GPa},\\ \alpha(T) &= (1.48\times10^{-5}-2.2\times10^{-8}T+1.15\times10^{-11}T^2+4\times10^{-15}T^3)\ \text{K}^{-1},\\ k(T) &= (11\times10^{-1}+1.6\times10^{-5}T+19\times10^{-7}T^2-97\times10^{-11}T^3)\ \text{WmK}^{-1} \end{aligned} \tag{5.66}$$

The thermal conductivity ($k(T)$) of the ceramic constituent is taken as 1.5 WmK^{-1} since it (Eq. (5.66)) is weakly dependent on the temperature. The magnitude of Poisson's ratio for the host FG shell is taken as 0.33. The material properties at any point within the host FG shell can be determined from Eqs. (5.8), (5.65) and (5.66) after knowing the distribution of temperature from Eq. (5.12).

The piezoelectric fibers in the 1-3 PFC layer are considered to be oriented in the radial direction since it is now taken in the cylindrical coordinate frame. Corresponding to this construction of the PFC layer in the cylindrical coordinate frame, its effective electro-elastic properties for a fiber volume fraction of 60% are determined following an earlier work (Kumar et al. 2015b). These effective electro-elastic properties are, $C_{11}=C_{22}=13.056$ GPa, $C_{33}=$ 36.019 GPa, $C_{12}=$ 4.34 GPa, $C_{13}=C_{23}=$ 6.794 GPa, $C_{44}=C_{55}=$ 2.503 GPa, $C_{66}=$ 1.649 GPa, $e_{31}=e_{32}=$ -0.231 C/m^2, $e_{33}=$ 18.379 C/m^2, $e_{24}=e_{15}=$ 0.0215 C/m^2, $\in_{11}=\in_{22}=0.32\times10^{-9}$ C/Vm, $\in_{33}=8.11\times10^{-9}$ C/Vm, $\rho=$ 5069 kg/m^3. The properties of graphite phase-volumes within the 1-3 VEC layer are taken as, $E=$ 250 GPa, $\nu=0.3$, $\rho=1406$ kg/m^3 (Jones, 1998). The material for viscoelastic phase of 1-3 VEC layer is taken from a published report (Shi et al., 2004). This viscoelastic material has the GHM parameters with a model of three mini-oscillators (Eq. (5.35)) as, $G^{\infty}=3.877\times10^4$ N/m^2, $\alpha_1=2.3263\times10^4$, $\alpha_2=4.1977\times10^1$, $\alpha_3=3.5174\times10^1$, $\tilde{\omega}_1=6.6169\times10^6$,

$\tilde{\omega}_2 = 3.2854\times10^4$, $\tilde{\omega}_3 = 4.7515\times10^4$, $\tilde{\xi}_1 = 3.0787$, $\tilde{\xi}_2 = 1.4288\times10^2$, $\tilde{\xi}_3 = 6.1785\times10^2$, $\rho = 789.5$ kg/m^3. In case of the use of monolithic VEM layer instead of 1-3 VEC layer for the constrained layer of ACLD arrangement, the same viscoelastic material (Shi et al., 2004) is utilized.

The boundary ends ($x = 0, L$) of the overall shell are considered to be fully clamped ends while it operates under a transverse (radial) mechanical harmonic excitation ($p(t) = p_0 \cos(\omega t)$) at a point ($L/2, 0$) over its outer surface. The overall shell undergoes thermal deformation due to the heated ceramic rich inner surface of the host FG shell while it (overall shell) is considered to vibrate with small displacement-amplitude due to the mechanical excitation. The coupling between these thermal deformation and displacement-amplitude is accounted by the geometrically nonlinear formulation of the problem. The small amplitude of vibration could be achieved by the small amplitude of mechanical excitation (p_0) and this small displacement-amplitude could be assessed considering one term ($s = 1$) of the general expression of the solution (Eqs. (5.38) and (5.39)). Corresponding to this form of solution, the maximum transverse (radial) deflection at a point of the overall shell during its vibration at a frequency can be written as, ($w^0 + w^a$) where w^a is the amplitude of vibration with respect to the equilibrium position, w^0. These parameters are computed at the point of mechanical excitation and presented in the dimensionless forms as, $W = w^a / h$ and $W_0 = w^0 / h$. The ACLD arrangement is utilized to reduce the amplitude of vibration of the overall shell by inducing active-passive damping within it (overall shell). The maximum reduction of amplitude of vibration is observed to occur at the resonant frequency for any mode (m, n) of vibration where also the displacement-amplitude of vibration appears with its maximum value ($W^{m,n}_{peak} = (w^a_{max})^{m,n} / h$). So, the change of this parameter ($W^{m,n}_{peak}$) indicates the alteration of damping within the overall shell. The controlled frequency responses of the overall shell are evaluated considering uniform value of control-gains ($k_d^\ell = k_d$, $\ell = 1,2,3,\ldots\ldots n_e$) for all the electrode-patches. For a specified value of control-gain (k_d), the values of $W^{m,n}_{peak}$ at all locations of the velocity sensors over the electrode-patches are evaluated and the maximum one is taken for the computation of maximum control voltage (V_m).

In order to verify the present FE model for a circular cylindrical shell, the dimensionless natural frequencies of an isotropic circular cylindrical shell ($r = 0,\ h_d \approx 0,\ h_p \approx 0$) are computed and compared with the similar results available in the literature (Pradhan et al., 2000). This comparison is illustrated in Table 5.2 and this table shows a good agreement of the present results with the earlier results (Pradhan et al., 2000).

Table 5.2 Comparison of dimensionless natural frequency ($\Omega = \omega R\sqrt{(1-\nu^2)\rho / E}$) for an isotropic circular cylindrical shell with clamped-clamped ends ($L/R = 20$, $h/R = 0.002$, $\nu = 0.3$).

n ($m=1$)	Ω (Pradhan et al., 2000)	Ω (Present)
1	0.0342	0.0343
2	0.0119	0.0115
3	0.0072	0.0071
4	0.0089	0.0090
5	0.0136	0.0135

This comparison verifies the accuracy of the present finite element model for a circular cylindrical shell. In order to verify the present implementation of GHM method, the constrained monolithic VEM layer is modelled using the complex stiffness method. The corresponding frequency response of the overall shell at the point of loading is plotted in Fig. 5.5 and this response is compared with the similar response obtained by employing GHM method with single-term GHM expression ($q = 1$, Eq. (5.35)). It may be observed that the response obtained by implementing GHM method is in good agreement with the similar response obtained by the use of complex stiffness method. This comparison verifies the accuracy in the present implementation of GHM method. As this accuracy in the implementation of GHM method is achieved by single-term GHM expression, the same ($q = 1$, Eq. (5.35)) is also used in evaluation of further results.

The constrained viscoelastic damping layer introduces passive damping within the overall shell while the active/passive constraining layer mainly acts to enhance this damping. As this viscoelastic damping is the main issue in attenuation of vibration of the overall shell, it is necessary to verify the present formulation in modelling this damping accurately. This verification is presently carried out considering passive constraining layer of the damping treatment since a study using similar active constraining layer (with electrode-patches) is not

available in the literature. The host cylinder, viscoelastic layer and constraining layer are taken in similar manner as those are considered in an available report (Ramesh and Ganesan, 1994). The natural frequencies and modal loss factors of this cylinder are computed and furnished in Fig. 5.6 together with the similar results available in the same report (Ramesh and Ganesan, 1994).

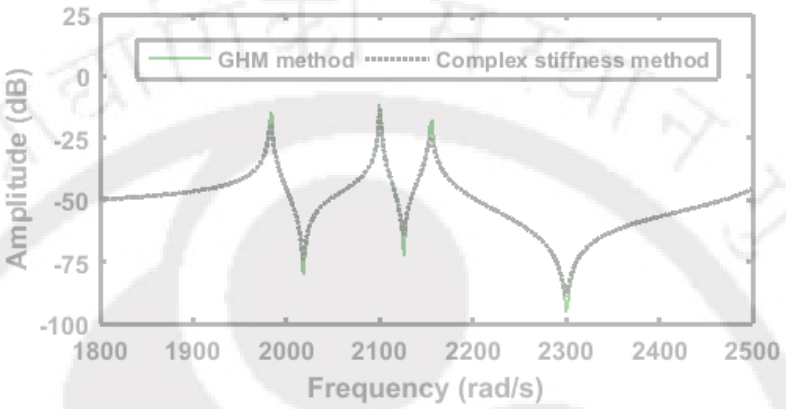

Fig. 5.5 Verification of the implementation of GHM method in the FE model of the overall circular cylindrical shell.

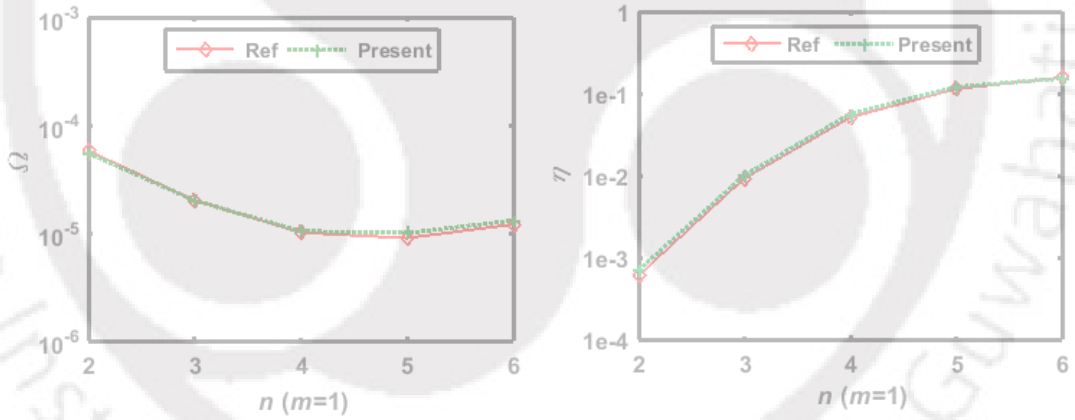

Fig. 5.6 Verifications of (a) dimensionless natural frequencies (Ω) and (b) viscoelastic damping (η: modal loss factor) within the overall circular cylindrical shell with reference to earlier results for an identical shell (Ref: Ramesh and Ganesan, 1994).

It may be observed from Fig. 5.6 that the present results are in excellent agreement with the earlier results (Ramesh and Ganesan, 1994) and it infers the accuracy of the present formulation in handling constrained layer damping for circular cylindrical shell structure.

A range of operating frequency is considered to study the damping characteristics of the present ACLD treatment of vibration of the overall shell. This

operating frequency-range includes first five asymmetric modes ($n>0$) of vibration of the shell as shown in Fig. 5.7.

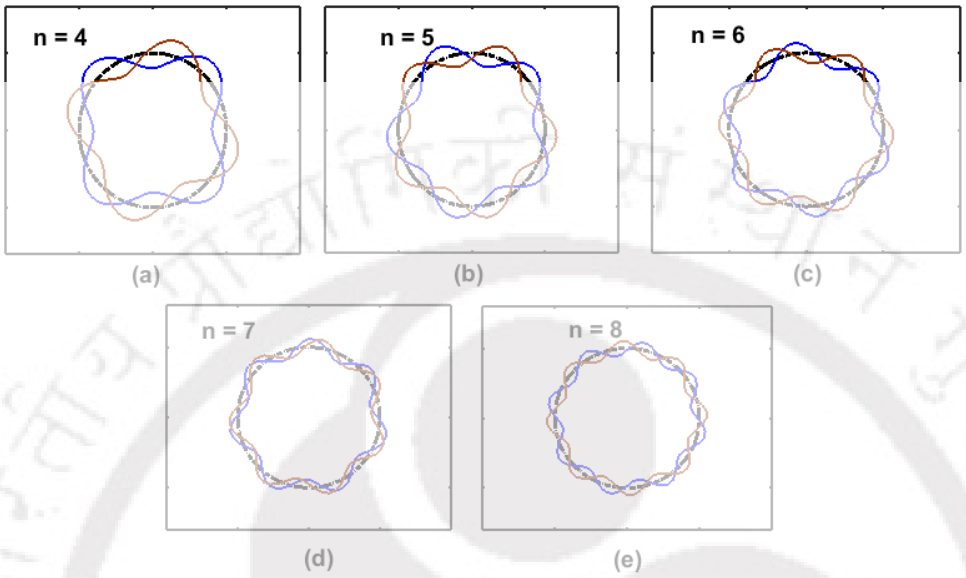

Fig. 5.7 First five asymmetric circumferential mode-shapes ($n>0$, $m=1$) of vibration of the FG circular cylindrical shell ($r=1$).

All the modes are of fundamental longitudinal mode number ($m=1$) while the circumferential mode number (n) varies from 4 to 8. The lowest natural frequency appears with the circumferential mode number (n) of 6 ($m=1$). For any asymmetric mode-shape ($n>0$) of circular cylindrical shell, it is known that there is a similar mode-shape that is orthogonal to the previous one with an angular shift of ($\pi/2n$) (Amabili, 2008). With reference to this phenomenon, the accuracy of the present FE model of the shell is again verified by plotting two orthogonal circumferential mode-shapes corresponding to every asymmetric mode ($n>0$) in Fig. 5.7.

For the FG circular cylindrical shell integrated with the 1-3 PFC layer only ($h_d \approx 0$), its frequency responses are illustrated in Fig. 5.8(a) for different values of control-gain (k_d) at room temperature ($T_c = T_m =$ 300 K). The corresponding variations of maximum control-voltage (V_m) are also illustrated in Fig. 5.8(b). The numbers within these figures (Fig. 5.8) indicate the circumferential mode numbers corresponding to the resonant frequencies and the dimensionless frequency (Ω) in the form as, $\Omega = \omega R\sqrt{(1-\nu^2)\rho_m / E_m}$ (ω is frequency in rad/s, ρ_m

is the density of metal constituent and E_m is young's modulus of metal constituent of FG material). It may be observed from Fig. 5.8 that the 1-3 PFC layer possesses good actuation-capability in control of bending modes of vibration of the shell even though it is primarily designed for control of thickness mode of deformation/vibration (Smith and Auld, 1991). It is interesting to observe that all the modes of vibration could be controlled effectively by the use of the present arrangement of electrode-patches.

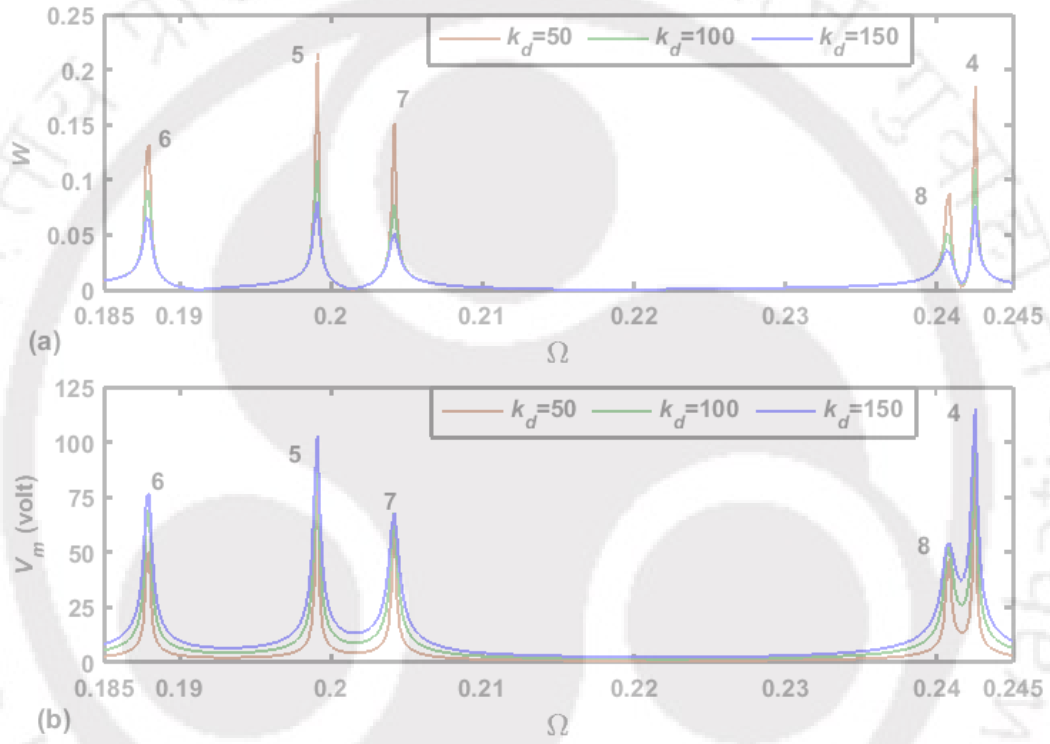

Fig. 5.8. (a) Frequency responses of the FG circular cylindrical shell ($r=1$) integrated with 1-3 PFC layer, (b) corresponding variations of maximum control-voltage (V_m) ($\alpha_E^p=9^\circ$, $\alpha_E=10^\circ$, $p_0=$ 20 N, $\lambda=1$, $r=1$, $h_d\approx 0$, $T_c=$ 300 K, $T_m=$ 300 K).

For an increase of control-gain (k_d), the amplitudes of all the modes of vibration decrease in almost uniform manner. This observation from Fig. 5.8(a) infers the suitability of present strategy for arrangement of electrode-patches in control of all the modes of vibration effectively using one configuration of electrode-patches. An increase of the control-gain (k_d) causes the reduction of displacement-amplitudes (Fig. 5.8(a)). But the corresponding required control-voltage does not increase indicatively (Fig. 5.8(b)). So, the amplitude of vibration corresponding to a mechanical excitation (p_0) could be controlled easily as per

the necessity in the design of the smart circular cylindrical shell. Figure 5.9 illustrates the frequency responses of the overall shell when the piezoelectric actuator-layer is either made of monolithic PZT-5H or made of 1-3 PFC. Since the fibers of 1-3 PFC are made of PZT-5H, the same material is chosen for the monolithic piezoelectric actuator-layer. It may be observed from Fig. 5.9 that the actuation-capability of the actuator-layer significantly decreases in expense of higher control-voltage when it (actuator) is made of 1-3 PFC instead of monolithic piezoelectric material. Despite this decrease of actuation-capability, the 1-3 PFC is presently used because of the requirements of high flexibility and conformability of the actuator-layer.

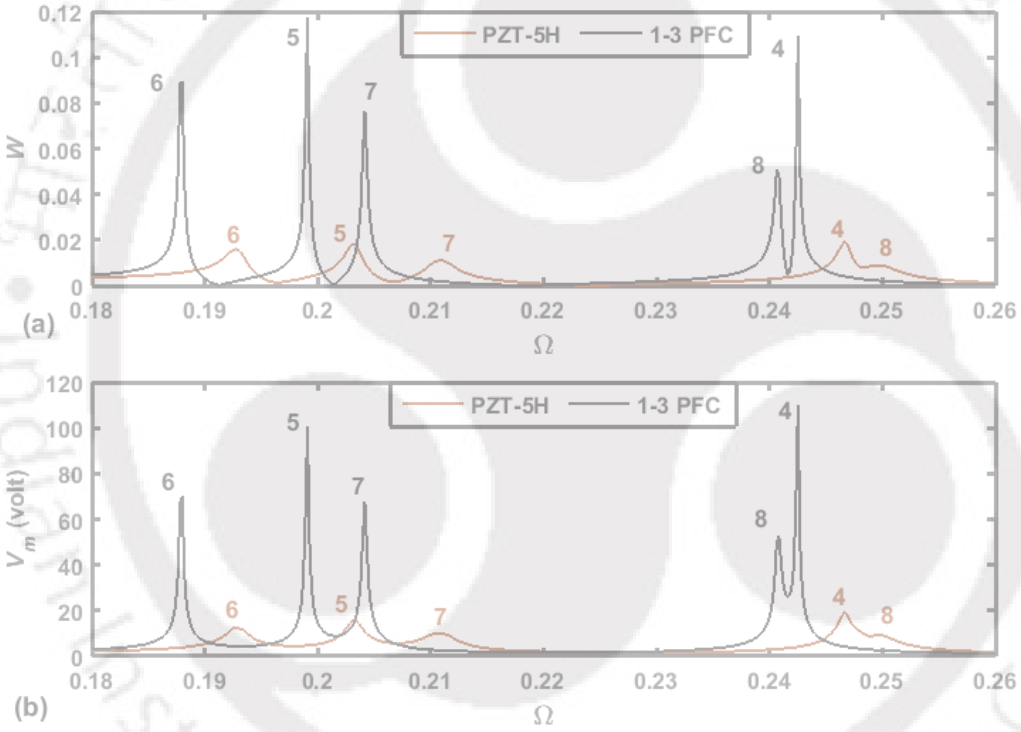

Fig. 5.9. (a) Frequency responses of the overall FG shell integrated with PZT-5H or 1-3 PFC layer, (b) corresponding variations of maximum control-voltage (V_m) ($\alpha_E^p = 9^o$, $\alpha_E = 10^o$, $p_0 =$ 20 N, $k_d = 100$, $\lambda = 1$, $r = 1$, $h_d \approx 0$, $T_c =$ 300 K, $T_m =$ 300 K, **the numbers indicate circumferential modes (** n **) of resonance).**

In the aforesaid (Figs. 5.8 and 5.9) arrangement of smart FG shell, a monolithic VEM layer is added in making the ACLD layer and the corresponding frequency responses of the overall shell are illustrated in Fig. 5.10(a) for two different values of thickness (h_d) of the constrained VEM layer. For any thickness of the constrained monolithic VEM layer, the characteristics of these responses (Fig. 5.10(a)) do not differ from those in Fig. 5.8(a). So, the present strategy of

arrangement of electrode-patches also goes well for effective ACLD treatment of several modes of vibration of the overall shell. The PFC layer induces significantly higher damping within the overall shell in expense of lesser control voltage (Figs. 5.8(b) and 5.10(b)) when it (PFC layer) is used in the form of ACLD layer (Fig. 5.10) instead of its direct use (Fig. 5.8). Although this observation of improved damping is a known fact (Ray and Pradhan, 2006), but the main intent here is to achieve further improvement in the damping characteristics of ACLD treatment by the use of present 1-3 VEC layer (Fig. 5.1).

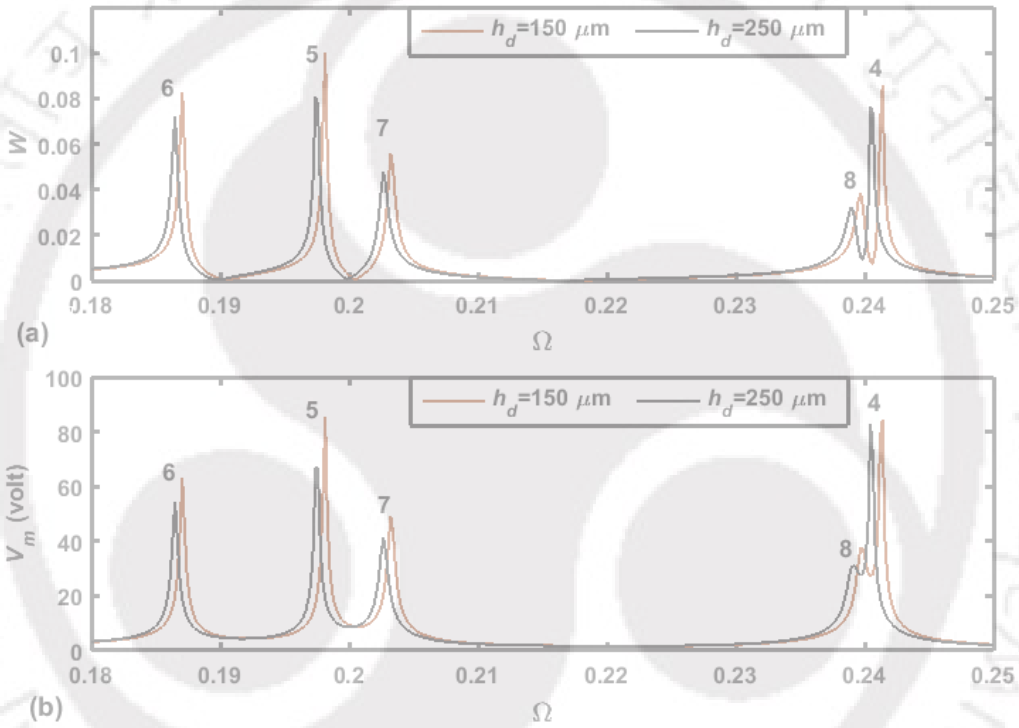

Fig. 5.10 (a) Frequency responses of the FG circular cylindrical shell ($r=1$) integrated with constrained monolithic VEM and 1-3 PFC constraining layers (ACLD layer), (b) corresponding variations of maximum control-voltage (V_m) ($\alpha_E^p=9^o$, $\alpha_E=10^o$, $p_0=20$ N, $k_d=100$, $\lambda=1$, $r=1$, $T_c=300$ K, $T_m=300$ K, the numbers indicate circumferential modes (n) of resonance).

For the use of the present 1-3 VEC layer instead of the conventional monolithic VEM layer within the ACLD arrangement, the corresponding change of damping within the overall shell is illustrated in Fig. 5.11. Figure 5.11(a) shows the frequency responses of the overall shell for different values of the thickness (h_v^2) of 2-2 VEC layer within a constant thickness ($h_d=250$ μm) of the constrained 1-3 VEC layer. The circumferential span (α^g) of graphite phase-volumes of 1-3

VEC layer is considered as 9^o within the segments (α) of 10^o ($n_g = 36$). First the thickness of the 2-2 VEC layer within the 1-3 VEC layer is considered as zero ($h_v^2 = 0$) so that whole constrained layer is a monolithic VEM layer. Next, the thickness of the 2-2 VEC layer is increased gradually within the constant thickness (h_d = 250 μm) of the 1-3 VEC layer.

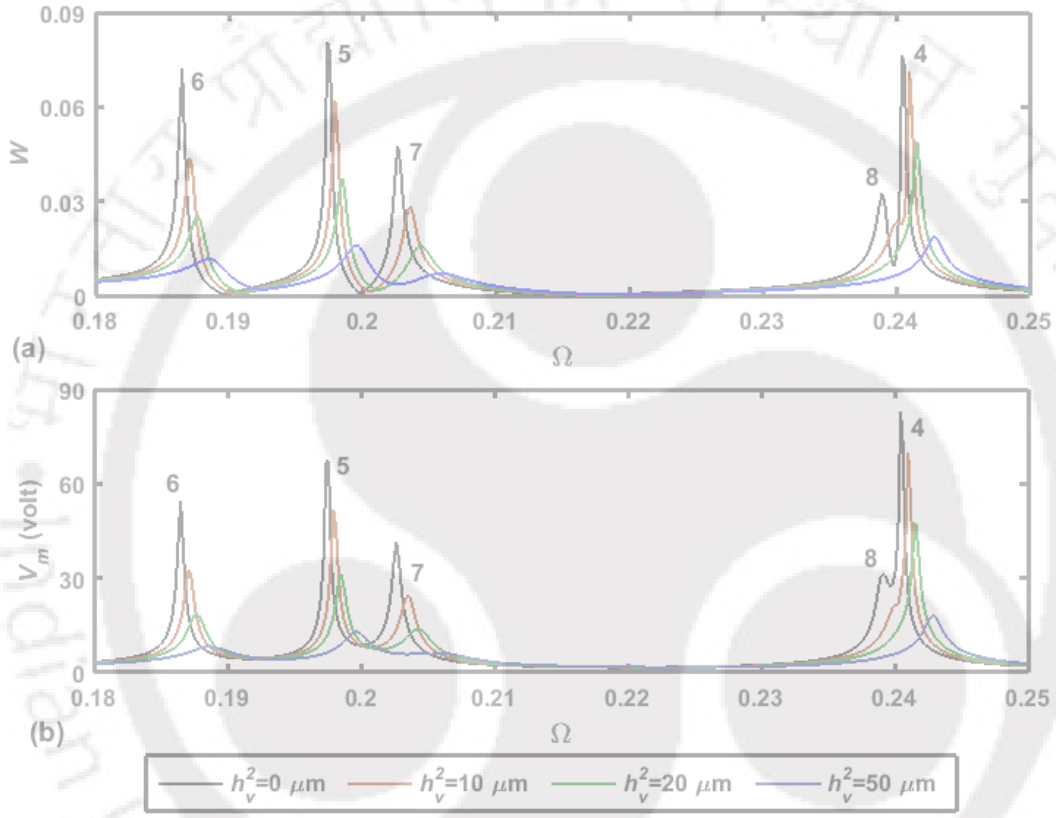

Fig. 5.11 (a) Frequency responses of the overall shell for different thickness (h_v^2) of 2-2 VEC layer within the constrained 1-3 VEC layer (h_d = 250 μm) of ACLD treatment, (b) corresponding variations of maximum control-voltage (V_m) ($\alpha_E^p = 9^o$, $\alpha_E = 10^o$, $\alpha^g = 9^o$, $\alpha = 10^o$, p_0 = 20 N, $k_d = 100$, $\lambda = 1$, $r = 1$, T_c = 300 K, T_m = 300 K, the numbers indicate circumferential modes (n) of resonance).

The corresponding frequency responses (Fig. 5.11(a)) reveal significant improvement of damping within the overall shell in expense of lesser control voltage (Fig. 5.11(b)) for the increase of thickness (h_v^2) of the 2-2 VEC layer from its (h_v^2) zero value. So, the control-capability of ACLD layer significantly improves for the use of the present 1-3 VEC layer instead of conventional monolithic VEM

layer. The results in Fig. 5.11 are evaluated for a particular value of the volume fraction index (r) of the host FG shell.

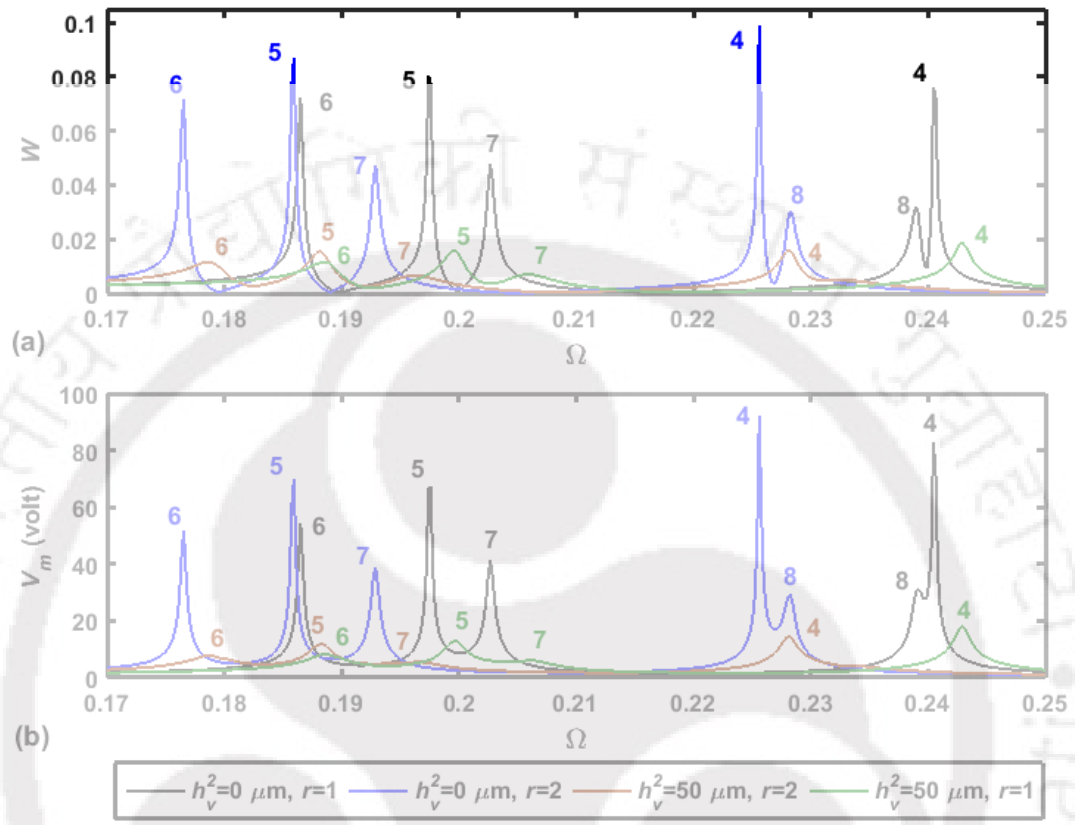

Fig. 5.12 (a) Frequency responses of the overall FG shell for different values of the volume fraction index (r) of host FG shell, (b) corresponding variations of maximum control-voltage (V_m) ($\alpha_E^p = 9^o$, $\alpha_E = 10^o$, $\alpha^g = 9^o$, $\alpha = 10^o$, $p_0 = 20$ N, $k_d = 100$, $\lambda = 1$, $T_c = 300$ K, $T_m = 300$ K, the numbers indicate circumferential modes (n) of resonance).

For two different values of the volume fraction index (r), similar responses (as in Fig. 5.11) are illustrated in Fig. 5.12. For every value of r, both the monolithic VEM layer ($h_v^2 = 0$) and 1-3 VEC layer ($h_v^2 = 50$ μm) are used separately within the same thickness ($h_d = 250$ μm) of the constrained layer. A higher value of volume fraction index causes the increase of metallic volume fraction in the FGM. So, the stiffness of the FG shell decreases and the frequency response of the overall FG shell shifts towards the lower frequency (Fig. 5.12). However, the responses in Fig. 5.12 reveal that the aforesaid improvement of damping characteristics of the ACLD layer due to the use of 1-3 VEC layer could be achieved for any value of the volume fraction index (r) of host FG shell.

In order to verify the sources of viscoelastic damping through the strains of the viscoelastic phase in the constrained layer, the frequency responses of the overall shell are evaluated considering either shear counterpart ($\boldsymbol{K}_a = \boldsymbol{K}_a^s$, $\boldsymbol{K}_a^b = \boldsymbol{0}$, Eq. (5.59)) or total damping ($\boldsymbol{K}_a = \boldsymbol{K}_a^s + \boldsymbol{K}_a^b$, Eq. (5.59)) for the dissipation coefficient matrix ($\boldsymbol{K}_a$). These responses are evaluated for each of the cases of monolithic VEM layer and 1-3 VEC layer. From these responses, the peak-amplitudes ($W_{peak}^{m,n}$) are noted in Table 5.3 for the modes (n = 4, 5, 6) with steep amplitudes. For any of these modes, it may be observed from this table that the damping (TSD) due to transverse shear strains of viscoelastic phase significantly increases for the use of 1-3 VEC layer instead of the monolithic VEM layer. The difference between TD and TSD signifies the contribution of other strain components in the damping. However, from these results, it may be concluded that the damping characteristics of the ACLD layer increase through all the strains in the viscoelastic phase although the overall (TD) improvement of damping occurs mainly due to the increase of transverse shear strain (TSD) of the viscoelastic phase of the constrained layer (Table 5.3).

Table 5.3 Peak-amplitudes ($W_{peak}^{m,n}$) of the different modes (m,n) of vibration corresponding to the damping due to transverse shear strains (TSD) and overall strain (TD) of the viscoelastic phase in the constrained layer ($\alpha_E^p = 9^o$, $\alpha_E = 10^o$, $\alpha^g = 9^o$, $\alpha = 10^o$, h_d = 250 μm, h_v^2 = 100 μm, p_0 = 20 N, $k_d = 100$, $\lambda = 1$, $r = 1$, T_c = 300 K, T_m = 300 K).

Constrained layer	$n = 4,\ m = 1$		$n = 5,\ m = 1$		$n = 6,\ m = 1$	
	TSD	TD	TSD	TD	TSD	TD
Monolithic VEM, $W_{peak}^{m,n}$	0.075	0.074	0.074	0.073	0.070	0.069
1-3 VEC, $W_{peak}^{m,n}$	0.011	0.009	0.012	0.010	0.009	0.008

Considering a particular thickness (h_v^2 = 100 μm) of the 2-2 VEC layer within the constrained 1-3 VEC layer (h_d = 250 μm), the frequency responses of the overall shell for different values of the control-gain (k_d) are plotted in Fig. 5.13. It may be observed from this figure that a significant amount of passive damping ($k_d = 0$) within the overall shell can be obtained by passively constrained 1-3 VEC layer.

Further improvement of damping in the overall shell is achieved by supplying the control voltage ($k_d \neq 0$, Fig. 5.13(b)) within its feasible range.

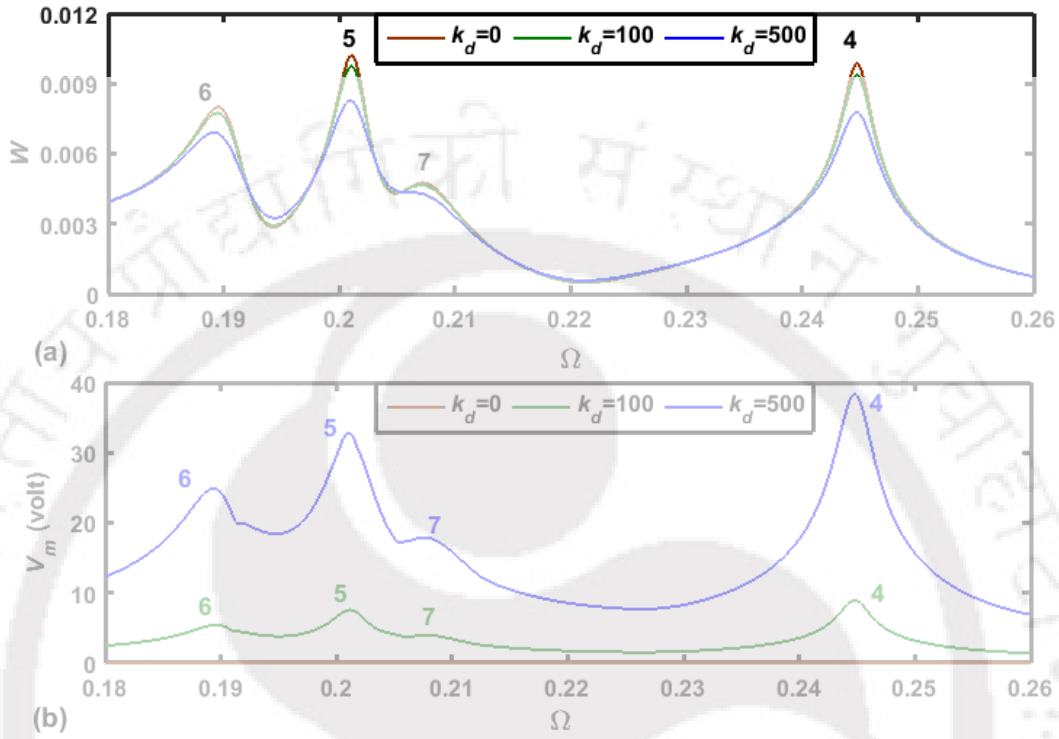

Fig. 5.13 (a) Frequency responses of the overall shell for different values of the control-gain (k_d), (b) corresponding variations of maximum control-voltage (V_m) ($\alpha_E^p = 9^o$, $\alpha_E = 10^o$, $\alpha^g = 9^o$, $\alpha = 10^o$, h_d = 250 μm, h_v^2 = 100 μm, p_0 = 20 N, $\lambda = 1$, $r = 1$, T_c = 300 K, T_m = 300 K, the numbers indicate circumferential modes (n) of resonance).

For achieving superior damping by means of increasing the value of control-gain, the required control-voltage increases. This increase of control-voltage limits the maximum value of k_d since the PFC layer operates within certain permissible value of applied voltage. It is a drawback in the use of PFC layer through the form of ACLD layer while similar drawback does not appear in its (PFC) direct use (Fig. 5.8(b)). Similar to Fig. 5.8(a), it may be observed from Fig. 5.13(a) that the amplitudes of all the modes of vibration decrease in almost uniform manner for an increase in the value of k_d. So, the present arrangement of electrode-patches and control strategy could also be utilized in case of the constrained 1-3 VEC layer within the ACLD arrangement.

For the use of monolithic PZT5H instead of 1-3 PFC as a material for active constraining layer within the ACLD arrangement, the corresponding increase of

damping in expense of lesser control-voltage is illustrated in Fig. 5.14. Although similar difference in the actuation capability is observed in case of the direct uses of the piezoelectric actuator-layers (Fig. 5.9), this difference reduces for their uses along with the 1-3 VEC layer (Fig. 5.14).

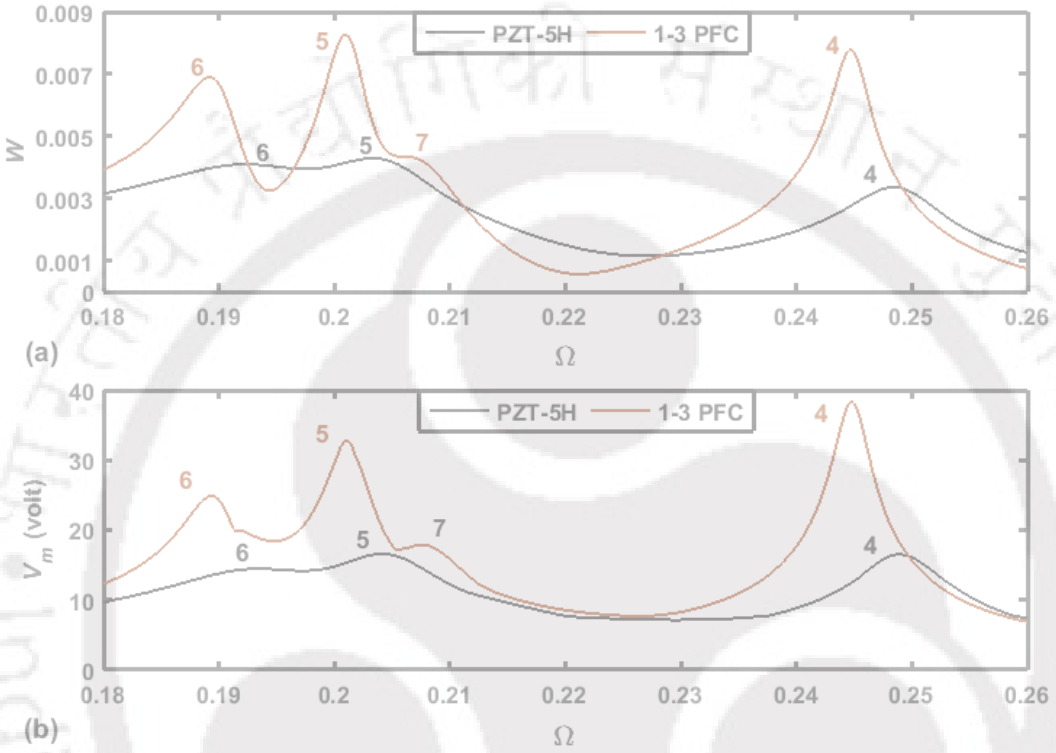

Fig. 5.14 (a) Frequency responses of the overall FG shell for the material of constraining layer either as PZT-5H or as 1-3 PFC, (b) corresponding variations of maximum control-voltage (V_m) ($\alpha_E^p = 9^o$, $\alpha_E = 10^o$, $\alpha^g = 9^o$, $\alpha = 10^o$, h_d = 250 μm, h_v^2 = 100 μm, p_0 = 20 N, $k_d = 500$, $\lambda = 1$, $r = 1$, T_c = 300 K, T_m = 300 K, the numbers indicate circumferential modes (n) of resonance).

In the foregoing results (Figs. 5.11-5.14, Table 5.3), the circumferential span (α^g) of graphite phase-volumes of the constrained 1-3 VEC layer is taken as 9^o within the circumferential segments (α) of 10^o. For the variation of the circumferential span (α^g) within the same segments (10^o), the corresponding variations of peak-amplitudes ($W_{peak}^{m,n}$) and maximum control voltage (V_m) are illustrated in Table 5.4 for the modes of vibration with steep displacement-amplitudes.

Table 5.4 Peak-amplitudes ($W_{peak}^{m,n}$) and corresponding maximum control-voltages (V_m) for different values of circumferential span (α^g) of graphite phase-volumes within a span ($\alpha = 10^o$) of circumferential segments (h_d = 250 μm, h_v^2 = 100 μm, $\alpha_E^p = 9^o$, $\alpha_E = 10^o$, p_0 = 20 N, $k_d = 500$, $\lambda = 1$, $r = 1$, T_c = 300 K, T_m = 300 K).

Parameters	$W_{peak}^{m,n}$ $(m=1)$				V_m (volt)			
$\alpha^g(^o)/\alpha^v(^o)$	$10^o/0^o$	$9^o/1^o$	$6^o/4^o$	$3^o/7^o$	$10^o/0^o$	$9^o/1^o$	$6^o/4^o$	$3^o/7^o$
$n=4$	0.0166	0.0078	0.0091	0.0134	83.4	38.3	45.9	66.8
$n=5$	0.0130	0.0083	0.0147	0.0244	55.0	32.8	55.6	97.0
$n=6$	0.0086	0.0069	0.0095	0.0145	31.28	24.8	31.6	53.6

For any of the modes, it may be observed from this table that the damping in the overall shell increases in expense of lesser control-voltage as the continuous ($\alpha^v = 0^o$) graphite phase-volume becomes discontinuous volumes ($\alpha^v > 0^o$). But this nature of variation of damping reverts at certain value of the span (α^g) of graphite phase-volumes within the segments ($\alpha = 10^o$). So, the circumferential span (α^g) of graphite volumes within a specified span (α) of segments would be taken carefully, and it may be decided in appropriate manner through an optimal algorithm. However, in case of the change of the span (α) of the circumferential segments with uniform gap ($\alpha^v = 1^o$) between any two consecutive graphite phase-volumes, the corresponding changes of damping in the overall shell and maximum control-voltage are illustrated in Table 5.5.

Table 5.5 Peak-amplitudes ($W_{peak}^{m,n}$) and corresponding maximum control-voltages (V_m) for different values of circumferential span (α) of segments ($\alpha^v = 1^o$, h_d = 250 μm, h_v^2 = 100 μm, $\alpha_E^p = 9^o$, $\alpha_E = 10^o$, p_0 = 20 N, $k_d = 500$, $\lambda = 1$, $r = 1$, T_c = 300 K, T_m = 300 K).

Parameters	$W_{peak}^{m,n}$ $(m=1)$		V_m (volt)	
n_g	36	18	36	18
$n=4$	0.0078	0.0101	38.3	49.7
$n=5$	0.0082	0.0093	32.5	36.4
$n=6$	0.0069	0.0073	24.9	26.1

In this result (Table 5.5), two different values of the span ($\alpha = 20^o$ ($n_g = 18$) and $\alpha = 10^o$ ($n_g = 36$)) are considered and its (α) maximum value is presently restricted to 20^o ($\alpha^v = 1^o$) because of the chance of lesser flexibility and conformability of the ACLD layer. It may be observed from Table 5.5 that an increase of the span (α) of segments causes the reduction of damping within the overall shell in expense of higher control-voltage. So, the span (α) of the circumferential segments is an important parameter in the design of the constrained 1-3 VEC layer.In the forgoing results, the circumferential span (α_E^p) of the electrode-patches is considered as 9^o within the circumferential segments (α_E) of 10^o. For the decrease of this span (α_E^p) within the same segments ($\alpha_E = 10^o$), the corresponding changes of peak-amplitudes ($W_{peak}^{m,n}$) and corresponding control-voltages (V_m) are illustrated in Table 5.6.

Table 5.6 Peak-amplitudes ($W_{peak}^{m,n}$) and corresponding maximum control-voltages (V_m) for different values of circumferential span (α_E^p) of the electrode-patches within a span ($\alpha_E = 10^o$) of circumferential segments (h_d = 250 μm, h_v^2 = 100 μm, $\alpha^g = 9^o, \alpha = 10^o$, p_0 = 20 N, k_d = 100, λ =1, r =1, T_c = 300 K, T_m = 300 K**).**

Parameters	$W_{peak}^{m,n}$ ($m=1$)			V_m (volt)		
$\alpha_E^p(^o)/\alpha_E^g(^o)$	$9^o/1^o$	$7^o/3^o$	$5^o/5^o$	$9^o/1^o$	$7^o/3^o$	$5^o/5^o$
$n=4$	0.0078	0.0069	0.0071	38.2	34.9	36.1
$n=5$	0.0083	0.0098	0.0100	32.8	39.6	43.5
$n=6$	0.0069	0.0070	0.0071	24.8	25.9	27.1

For any of the modes, it may be observed from this table that the peak-amplitude and the corresponding control-voltage insignificantly vary with the change of the circumferential span (α_E^p) of the electrode-patches. So, the circumferential span of the electrode-patches does not have much effect on the peak-amplitudes unless the corresponding span of segments (α_E) does not have too large value.

Figure 5.15 demonstrates the frequency responses of the overall shell when the properties of the host FG shell vary from stiffer inner surface to softer outer surface ($\lambda = 1$, inner ceramic to outer metallic) or from softer inner surface

to stiffer outer surface ($\lambda = 2$, inner metallic to outer ceramic). It may be observed from this figure that the ACLD layer provides higher damping when it is attached to the softer/metallic surface of the host FG shell. This observation facilitates to keep the ACLD layer free from thermal effect by attaching it to the metallic surface of the host FG shell while the ceramic rich surface of the FG shell is exposed to a high temperature. With this attachment of the present ACLD layer, the effect of the ceramic rich surface temperature on the control capability of the ACLD layer is demonstrated in the next section.

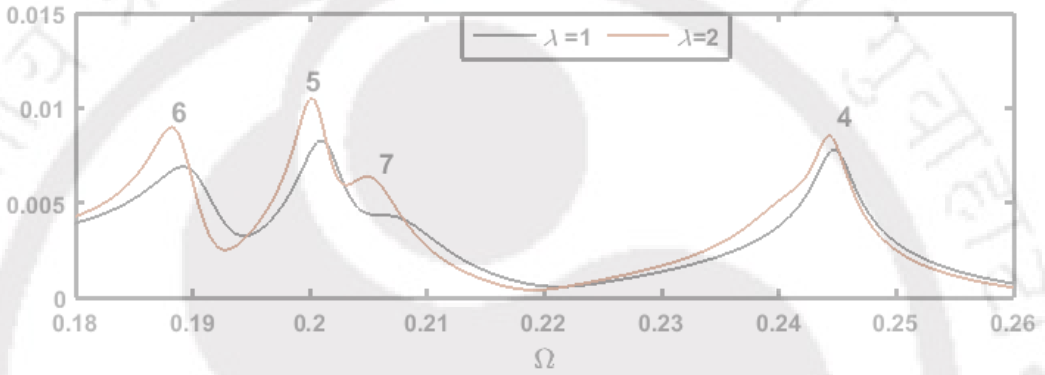

Fig. 5.15 Frequency responses of the overall shell when the properties of the host FG shell vary from stiffer inner surface to softer outer surface ($\lambda = 1$) or from softer inner surface to stiffer outer surface ($\lambda = 2$) ($\alpha_E^p = 9^o$, $\alpha_E = 10^o$, $\alpha^g = 9^o$, $\alpha = 10^o$, h_d = 250 μm, h_v^2 = 100 μm, p_0 = 20 N, $k_d = 500$, $r = 1$, T_c = 300 K, T_m = 300 K, the numbers indicate circumferential modes (n) of resonance).

5.4.1 Thermal effect

The temperature (T_c) over the inner ceramic rich surface of the host FG shell causes thermal deformation of the overall shell and it (overall shell) vibrates with respect to this thermal deformation due to the mechanical excitation. In order to account the coupling between the thermal deformation and the amplitude of vibration of the overall shell, the geometrically nonlinear formulation is carried out at present. Through this formulation, the deformation/vibration characteristics of the overall FG shell under the mechanical excitation in the presence of a temperature (T_c) are demonstrated here considering the fundamental mode of vibration ($m = 1$, $n = 6$).

Figure 5.16 illustrates the frequency responses ($W_t = (W + W_0)$) and the corresponding equilibrium position (W_0) of the overall shell for different ceramic

rich surface temperatures (T_c).At room temperature (T_c = 300 K), the overall shell vibrates with respect to zero equilibrium position ($W_0 = 0$). But, for a higher temperature ($T_c >$ 300 K), the equilibrium position (W_0) changes due to the thermal deformation of the overall shell and it (W_0) does not vary with the operating frequency as the temperature (T_c) remains constant during vibration.

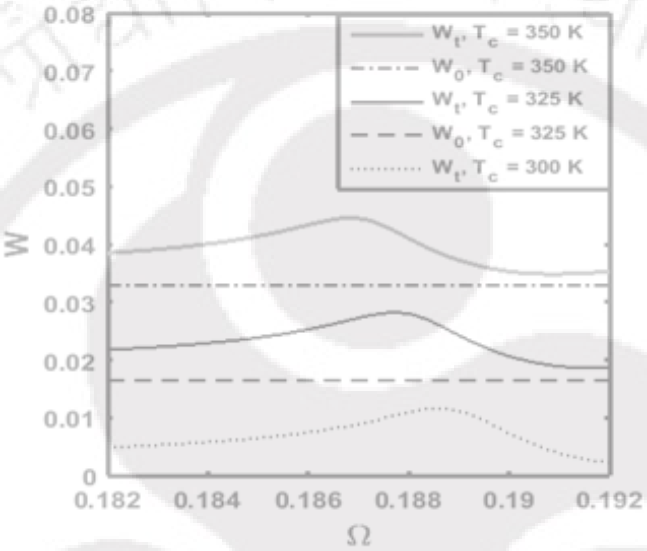

Fig. 5.16 Frequency responses ($W_t = (W + W_0)$) and the corresponding equilibrium position (W_0) for the fundamental mode ($m = 1,\ n = 6$) of vibration of the overall FG shell under different ceramic rich surface temperatures (T_c) ($\alpha_E^p = 9^o$, $\alpha_E = 10^o$, $\alpha^g = 9^o, \alpha = 10^o$, h_d = 250 μm, h_v^2 = 50 μm, p_0 = 20 N, $\lambda = 1$, $r = 1$, T_m = 300 K).

It may also be observed from Fig. 5.16 that the frequency response of the overall shell shifts towards the lower frequency due to the increase of temperature (T_c). It is basically due to a known fact of the decrease of natural frequency of vibration of a structure with the increase of temperature. For the present FG shell, this decrease of natural frequency with the increase of temperature is illustrated in Fig. 5.17 for two different values of the volume faction index (r).For any temperature, it may be observed that the natural frequency decreases as the volume fraction index (r) increases. Also, for any volume fraction index (r), the natural frequency of the overall shell linearly decreases with the increasing temperature (T_c).This decrease of natural frequency appears at a little higher rate for a higher value of volume fraction index (r). In fact, a higher value of r causes

increased volume fraction of metallic constituent so that the effective stiffness of the FG material decreases and also the natural frequency decreases. The increase of volume fraction of metallic constituent enhances the rise of temperature within the FG material corresponding to a specified rise of surface-temperature (T_c). This fact causes to decrease the natural frequency at a greater rate when the temperature (T_c) increases with a higher volume fraction index (r).

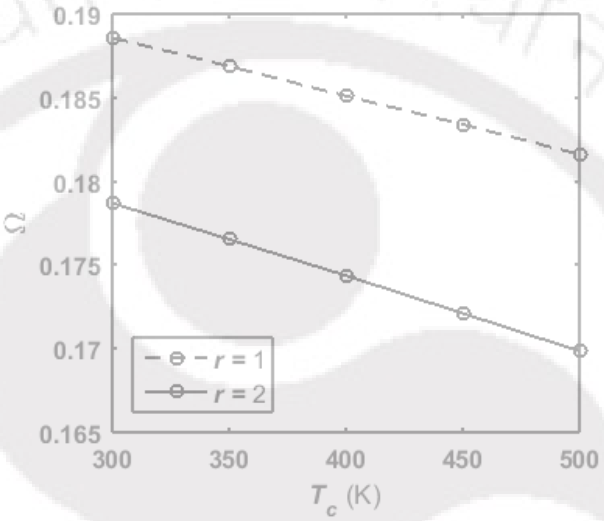

Fig. 5.17 Variation of dimensionless natural frequency (Ω for $m=1, n=6$) of the overall FG shell within a range of ceramic rich surface temperature (T_c).

The effect of temperature (T_c) on the control-capability of ACLD layer is demonstrated in Fig. 5.18 considering two values of the volume fraction index (r) of the host FG shell. The variations of displacement-amplitude ($W_{peak}^{m,n}$) at the fundamental resonance frequency and the corresponding maximum control-voltage are plotted in Figs. 5.18(a) and 5.18(b), respectively within a range of temperature (T_c). For any volume fraction index (r), the increase of peak-amplitude ($W_{peak}^{m,n}$) in Fig. 5.18(a) indicates the decrease of damping within the overall shell for the increase of temperature (T_c). The corresponding control-voltage (V_m) at a constant value of control-gain (k_d) either increases or decreases depending on the assigned value of volume fraction index (r). This difference in the nature of variation of control-voltage (V_m) with temperature (T_c) appears due to its (V_m) dependency on both the displacement-amplitude ($W_{peak}^{m,n}$) and frequency of vibration. The displacement-amplitude increases (Fig. 5.18(a)) and the

frequency of vibration decreases (Fig. 5.17) for a rise of temperature (T_c). So, the corresponding combined change appearing in the nature of variation of control-voltage (V_m) follow either the nature of variation of amplitude ($W_{peak}^{m,n}$) or the nature of variation of frequency. However, the quantitative measures of these variations (Fig. 5.18) of displacement-amplitude ($W_{peak}^{m,n}$) and control-voltage (V_m) appear in insignificant manner even though the corresponding variation of the thermal deformation/equilibrium position (W_0) occurs in significant manner (Fig. 5.19).

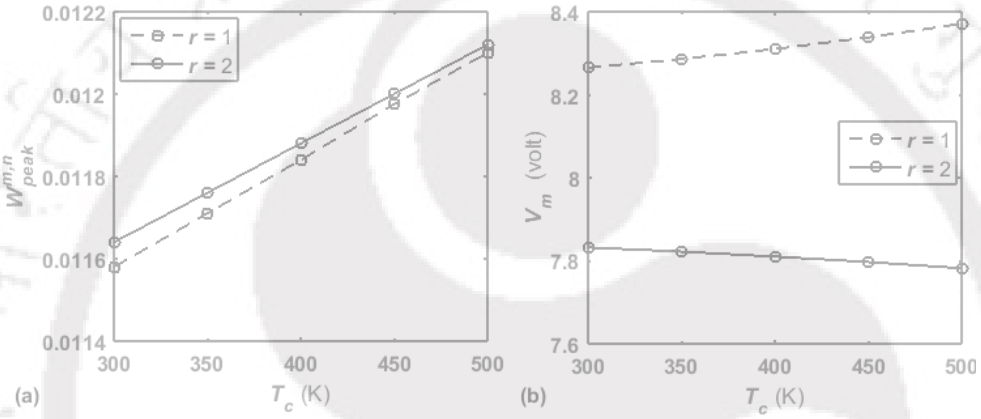

Fig. 5.18 Variations of (a) peak displacement-amplitude ($W_{peak}^{m,n}$) at the fundamental resonance ($m=1, n=6$) and (b) the corresponding maximum control-voltage (V_m) within a range of temperature (T_c) ($\alpha_E^p = 9^o$, $\alpha_E = 10^o$, $\alpha^g = 9^o$, $\alpha = 10^o$, h_d = 250 μm, h_v^2 = 50 μm, p_0 = 20 N, $\lambda = 1$, T_m = 300 K).

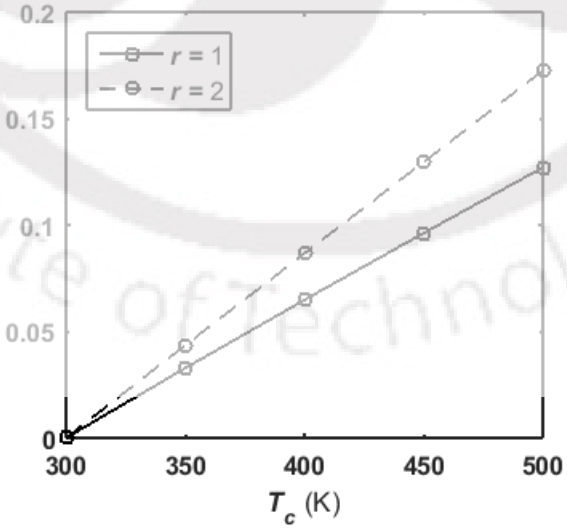

Fig. 5.19 Variation of the thermal deformation/equilibrium position (W_0) of the overall FG shell within a range of temperature (T_c).

So, the thermal deformation of the overall FG circular cylindrical shell has not much effect on the ACLD treatment of its (overall shell) vibration under mechanical excitation. Although this observation is presently obtained within a range of ceramic rich surface temperature ($300\,\mathrm{K} < T_c < 500\,\mathrm{K}$).

5.5 Summary

An ACLD arrangement for effective control of several modes of vibration of circular cylindrical shell structure is presented using the new 1-3 VEC layer as the constrained damping layer. The constrained 1-3 VEC layer is achieved by inserting graphite-strips through the middle surface of the conventionally constrained viscoelastic layer. The identical graphite-strips are in parallel to the axis of the substrate cylinder and uniformly distributed along the circumferential direction. The ACLD layer is considered to be distributed throughout the outer surface of the substrate circular cylindrical shell while its (ACLD) conformability with the curved host-surface is ensured by the use of the vertically/radially reinforced 1-3 PFC constraining layer. The surfaces of this active constraining layer are printed with electrode-patches for effective control of several modes of vibration of the shell by the use of the ACLD treatment in layer-form. A fruitful strategy for the arrangements of electrode-patches and velocity-sensors is presented for effective control of several modes of vibration of the shell within an operating frequency-range using the velocity feedback control strategy.

The substrate circular cylindrical shell is considered to be made of an FGM that is comprised of metal and ceramic constituents. The properties of this FG shell vary from its inner ceramic rich surface to its outer metal rich surface for the consideration of a high temperature at the inner concave surface of the overall shell. The overall FG shell is considered to vibrate under this temperature for an external mechanical harmonic excitation, and the corresponding controlled frequency responses are evaluated by developing a geometrically nonlinear electro-visco-elastic incremental finite element model. The small displacement-amplitude of vibration of the overall shell is considered due to the mechanical excitation in the presence of a high temperature at the inner concave surface, while the geometrically nonlinear formulation is carried out to account the coupling between the thermal deformation of the overall shell and its displacement-amplitude of vibration. The important observations obtained from the controlled frequency responses of the overall FG shell are summarized as

follows. These observations infer the utility of the present 1-3 VEC layer as well as the present ACLD layer for attenuation of several modes of vibration of a cylindrical shell structure within a range of operating frequency.

(a) The present strategy of arrangement of the patches of surface-electrode provides effective control of all the modes of vibration of the overall shell within an operating frequency-range of interest. It is not necessary to change the configuration of patches of surface-electrode for alteration of the mode of vibration.

(b) The 1-3 PFC constraining layer possesses good actuation capability in control of bending modes of vibration of the circular cylindrical shell structure even though it is primarily known as a material of distributed actuator for control of thickness mode of deformation/vibration of structures.

(c) In case of the use of actuator-layer without VEM/VEC layer, the required control-voltage insignificantly changes for reduction of displacement-amplitude by means of the increase of the control-gain at a specified mechanical excitation. This advantage is not achieved for the use the same actuator-layer with the VEM/VEC layer in the form of ACLD layer.

(d) The damping characteristics of the ACLD layer significantly increases for the use of the present 1-3 VEC layer instead of the traditional monolithic VEM layer. This improved ACLD treatment also holds for any value of the volume fraction index of the substrate FG shell.

(e) In the use of the 1-3 VEC layer instead of the traditional VEM layer, the improved ACLD treatment appears through the enhancement of all the strains in the viscoelastic phase of the constrained layer although the improved damping occurs mainly due to the enhanced transverse shear strains of the viscoelastic phase.

(f) The damping capacity of the 1-3 VEC layer significantly depends on the geometrical parameters in the arrangement of the graphite-strips. The study suggests optimal geometric configuration of the 1-3 VEC layer for its (VEC) superior damping capacity in the ACLD treatment.

(g) It is observed that the increase in the circumferential span of the graphite-strips (with a constant gap between any two consecutive graphite-strips) may not improve the damping characteristics of the 1-3 VEC layer.

(h) The temperature in the substrate FG shell does not have much effect on the damping characteristics of the ACLD layer even though it (FG shell) undergoes indicative thermal deformation.

(i) The overall FG shell vibrates under a mechanical excitation in the presence of a high temperature at its inner ceramic-rich surface. The equilibrium position of vibration of the overall shell is almost equal to its (overall shell) thermal deformation, and it (equilibrium) does not change indicatively with the operating frequency.

Chapter 6

Augmented CLD treatment of plates through the optimal design of a new 0-3 VEC layer

6.1 Introduction

In the PCLD/CLD and ACLD treatments using 1-3 VEC layer, the augmented damping arises due to the enhancement of certain strain components in the viscoelastic phase. These strain components lie in the transverse plane over which the graphite-inclusions are discontinuously distributed. However, in the quest of improved PCLD/CLD treatment of structural vibration through the enhancement of all the strain components in the viscoelastic phase, a new 0-3 VEC layer is designed in this chapter (Kumar et al., 2017a). In this concept of a 0-3 VEC layer, a rectangular array of the thin rectangular graphite-wafers is inserted through the middle surface of a pure viscoelastic layer. The geometrical construction of this VEC layer may be described by a stack of two pure viscoelastic layers over the top and bottom surfaces of a middle 1-3 VEC layer as shown in Fig. 6.1(a). As all the layers are combined into a single layer, a 0-3 VEC layer can be obtained. The performance of this 0-3 VEC layer as a damping layer in the CLD treatment is presently investigated by integrating the treatment over the top surface of a substrate plate as shown in Fig. 6.1(b) where multiple (n_z) VEC layers are taken within the thickness (h_d) of the constrained damping layer.

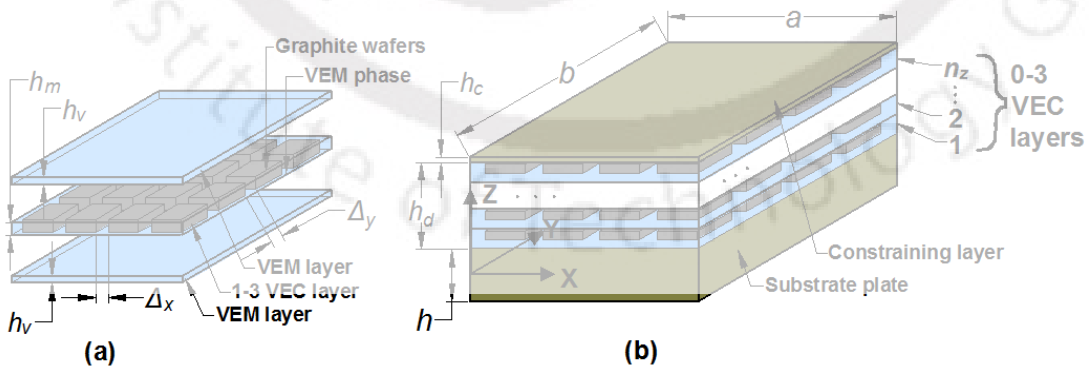

Fig. 6.1 Schematic diagrams of (a) the component layers of 0-3 VEC, (b) the CLD arrangement over the top surface of a substrate plate using 0-3 VEC layers.

As the overall plate undergoes bending deformation, the viscoelastic material within the in-plane axial gap between any two consecutive rectangular graphite-wafers is expected to experience extensional/compressional strain. Concurrently, the viscoelastic material in the transverse gap between any two successive horizontal surfaces of stiff elements suffers the transverse shear strains. So, the transverse shear and in-plane extensional strains are supposed to appear (with the reasonable magnitudes) within the constrained 0-3 VEC layers under the bending deformation of the overall plate (Fig. 6.1(b)). As this fact may augment the damping in the overall plate, the damping characteristics of the plate (Fig. 6.1(b)) are investigated through its static and dynamic flexural analyses as presented in the following sections by developing an FE model of the plate (Fig. 6.1(b)).

6.2 FE model of the plate

For the mathematical modelling of the overall plate, the origin of the rectangular coordinate system (xyz) is located at one corner of the middle plane of the substrate plate (Fig. 6.1(b)). In any of the 0-3 VEC layers, the number of graphite-wafers in the x/y direction is denoted by, n_x/n_y, while these inclusions are uniformly spaced in any direction (x/y). Every 0-3 VEC layer is assumed as a laminate of three layers as shown in Fig. 6.1(a). So, the total number of layers (N_L) in the overall laminated plate is, $N_L=(3n_z+2)$. The thin layers of the overall laminated plate are of different rigidities, and thus its kinematics of deformation is defined according to the layer-wise first-order shear deformation theory (FSDT) as given in Eq. (4.1). But, the deformation of thickness of the overall plate (Fig. 6.1(b)) is omitted, and the expressions in Eq. (4.1) are modified as follows,

$$u^k(x,y,z,t)=u_0(x,y,t)+z_i^k\,\alpha_i(x,y,t)\,,$$
$$v^k(x,y,z,t)=v_0(x,y,t)+z_i^k\,\beta_i(x,y,t)\,,$$
$$w^k(x,y,z,t)=w_0(x,y,t) \qquad (6.1)$$

where, u^k/u_0, v^k/v_0 and w^k/w_0 are the displacements along the x, y and z directions, respectively at any point within the k^{th} layer/over the xy-plane; i represents a layer and its repetition within a term indicates summation over the total number of layers; α_i/β_i is the rotation of the normal to the middle-plane

of i^{th} layer with respect to the y / x axis; z_i^k is the thickness coordinate as given in Eq. (6.2).

$$z_1^k = z \text{ or } (h_1/2) \text{ for } k=1 \text{ or } k>1$$

$$z_2^k = 0 \text{ or } (z-h_1/2) \text{ or } h_2 \text{ for } k<2 \text{ or } k=2 \text{ or } k>2$$

$$z_3^k = 0 \text{ or } (z-h_1/2-h_2) \text{ or } h_3 \text{ for } k<3 \text{ or } k=3 \text{ or } k>3$$

$$\ldots\ldots\ldots$$

$$\ldots\ldots\ldots$$

$$z_{(N_L-1)}^k = 0 \text{ or } (z-h_1/2-h_2-h_3-\ldots.-h_{(N_L-2)}) \text{ or } h_{(N_L-1)} \text{ for}$$

$$k<(N_L-1) \text{ or } k=(N_L-1) \text{ or } k>(N_L-1)$$

$$z_{N_L}^k = 0 \text{ or } (z-h_1/2-h_2-h_3-\ldots.-h_{N_{L-1}}) \text{ for } k<N_L \text{ or } k=N_L \qquad (6.2)$$

where, h_p ($p=1,2,3,\ldots,N_L$) represents the thickness of p^{th} layer. The displacement components (u^k, v^k, w^k) at any point within k^{th} layer can be written as,

$$\boldsymbol{d}^k = (\boldsymbol{d}_t + \boldsymbol{Z}_r^k \boldsymbol{d}_r),\ \boldsymbol{d}^k = \left\{u^k \quad v^k \quad w^k\right\}^T,\ \boldsymbol{d}_t = \left\{u_0 \quad v_0 \quad w_0\right\}^T,$$

$$\boldsymbol{d}_r = \left\{\alpha_1 \quad \beta_1 \quad \alpha_2 \quad \beta_2 \quad . \quad . \quad . \quad \alpha_{N_L} \quad \beta_{N_L}\right\}^T,$$

$$\boldsymbol{Z}_r^k = \left[\boldsymbol{Z}_1^k \quad \boldsymbol{Z}_2^k \quad \boldsymbol{Z}_3^k \quad \ldots \quad \boldsymbol{Z}_{N_L}^k\right],\ \boldsymbol{Z}_i^k = \begin{bmatrix} z_i^k & 0 & 0 \\ 0 & z_i^k & 0 \end{bmatrix}^T \qquad (6.3)$$

The displacement components can also be expressed in terms of a generalized displacement vector ($\boldsymbol{d}$) and the transformation matrices ($\boldsymbol{T}_t$ and $\boldsymbol{T}_r$) as follows,

$$\boldsymbol{d}^k = (\boldsymbol{T}_t + \boldsymbol{Z}_r^k \boldsymbol{T}_r)\boldsymbol{d},$$

$$\boldsymbol{d} = \left\{u_0 \quad v_0 \quad w_0 \quad \alpha_1 \quad \beta_1 \quad \alpha_2 \quad \beta_2 \quad \alpha_3 \quad \beta_3 \quad ..... \quad ..... \quad \alpha_{N_L} \quad \beta_{N_L}\right\}^T \qquad (6.4)$$

The strains/stresses at any point within the overall plate can be expressed under the plane stress assumption as,

$$\boldsymbol{\varepsilon}_b = \left\{\varepsilon_x \quad \varepsilon_y \quad \varepsilon_{xy}\right\}^T,\ \boldsymbol{\varepsilon}_s = \left\{\varepsilon_{xz} \quad \varepsilon_{yz}\right\}^T,$$

$$\boldsymbol{\sigma}_b = \left\{\sigma_x \quad \sigma_y \quad \sigma_{xy}\right\}^T,\ \boldsymbol{\sigma}_s = \left\{\sigma_{xz} \quad \sigma_{yz}\right\}^T \qquad (6.5)$$

where, the symbols ε / σ indicates strain/stress quantity; the subscripts x / xy, y / yz and z / xz indicate the quantities in the corresponding directions/planes.

According to Eq. (6.1), the strain-displacement relations for k^{th} layer can be written following Eqs. (4.5) and (4.6) as,

$$\boldsymbol{\varepsilon}_b^k = (\boldsymbol{\varepsilon}_{bL} + \boldsymbol{Z}_b^k \boldsymbol{\kappa}_b), \quad \boldsymbol{\varepsilon}_s^k = (\boldsymbol{\varepsilon}_{sL} + \boldsymbol{Z}_s^k \boldsymbol{\kappa}_s),$$

$$\boldsymbol{\kappa}_b = \left\{ \boldsymbol{\kappa}_b^1 \quad \boldsymbol{\kappa}_b^2 \quad .... \quad \boldsymbol{\kappa}_b^{N_L} \right\}^{\mathrm{T}}, \quad \boldsymbol{\kappa}_s = \left\{ \boldsymbol{\kappa}_s^1 \quad \boldsymbol{\kappa}_s^2 \quad .... \quad \boldsymbol{\kappa}_s^{N_L} \right\}^{\mathrm{T}},$$

$$\boldsymbol{\varepsilon}_{bL} = \left\{ \frac{\partial u_0}{\partial x} \quad \frac{\partial v_0}{\partial y} \quad \left(\frac{\partial u_0}{\partial y} + \frac{\partial v_0}{\partial x} \right) \right\}^{\mathrm{T}}, \quad \boldsymbol{\varepsilon}_{sL} = \left\{ \frac{\partial w_0}{\partial x} \quad \frac{\partial w_0}{\partial y} \right\}^{\mathrm{T}},$$

$$\boldsymbol{\kappa}_b^i = \left\{ \frac{\partial \alpha_i}{\partial x} \quad \frac{\partial \beta_i}{\partial y} \quad \left(\frac{\partial \alpha_i}{\partial y} + \frac{\partial \beta_i}{\partial x} \right) \right\}, \quad \boldsymbol{\kappa}_s^i = \left\{ \alpha_i \quad \beta_i \right\},$$

$$\boldsymbol{Z}_b^k = [\boldsymbol{z}_{b1}^k \quad \boldsymbol{z}_{b2}^k \quad .... \quad \boldsymbol{z}_{bN_L}^k], \quad \boldsymbol{Z}_s^k = [\boldsymbol{z}_{s1}^k \quad \boldsymbol{z}_{s2}^k \quad .... \quad \boldsymbol{z}_{sN_L}^k],$$

$$\boldsymbol{z}_{bi}^k = I_{3\times 3} \otimes z_i^k, \quad \boldsymbol{z}_{si}^k = I_{2\times 2} \otimes (\partial z_i^k / \partial z) \tag{6.6a}$$

where, $I_{m\times m}$ is a unit matrix of size $(m\times m)$ and the symbol $\otimes$ indicates the Kronecker product. The generalized strain vectors appearing in Eq. (6.6a) can be written as,

$$\boldsymbol{\varepsilon}_{bL} = \boldsymbol{L}_{bL}\boldsymbol{d}_t, \quad \boldsymbol{\kappa}_b = \boldsymbol{L}_{b\kappa}\boldsymbol{d}_r,$$
$$\boldsymbol{\varepsilon}_{sL} = \boldsymbol{L}_{sL}\boldsymbol{d}_t, \quad \boldsymbol{\kappa}_s = \boldsymbol{L}_{s\kappa}\boldsymbol{d}_r,$$

$$\boldsymbol{L}_{bL} = \begin{bmatrix} \partial/\partial x & 0 & 0 \\ 0 & \partial/\partial y & 0 \\ \partial/\partial y & \partial/\partial x & 0 \end{bmatrix}, \boldsymbol{l}_{b\kappa} = \begin{bmatrix} \partial/\partial x & 0 \\ 0 & \partial/\partial y \\ \partial/\partial y & \partial/\partial x \end{bmatrix},$$

$$\boldsymbol{L}_{sL} = \begin{bmatrix} 0 & 0 & \partial/\partial x \\ 0 & 0 & \partial/\partial y \end{bmatrix}, \quad \boldsymbol{l}_{s\kappa} = \begin{bmatrix} 1 & 0 \\ 0 & 1 \end{bmatrix},$$

$$\boldsymbol{L}_{b\kappa} = I_{(N_L\times N_L)} \otimes \boldsymbol{l}_{b\kappa}, \quad \boldsymbol{L}_{s\kappa} = I_{(N_L\times N_L)} \otimes \boldsymbol{l}_{s\kappa} \tag{6.6b}$$

The constitutive relations for the isotropic material within k^{th} layer can be written under the plane stress assumption as,

$$\boldsymbol{\sigma}_b^k = \boldsymbol{C}_b^k \boldsymbol{\varepsilon}_b^k, \quad \boldsymbol{\sigma}_s^k = \boldsymbol{C}_s^k \boldsymbol{\varepsilon}_s^k,$$

$$\boldsymbol{C}_b^k = \frac{E^k}{1-\left(\nu^k\right)^2} \begin{bmatrix} 1 & \nu^k & 0 \\ \nu^k & 1 & 0 \\ 0 & 0 & \frac{1}{2}\left(1-\nu^k\right) \end{bmatrix}, \quad \boldsymbol{C}_s^k = \frac{E^k}{2\left(1+\nu^k\right)} \begin{bmatrix} 1 & 0 \\ 0 & 1 \end{bmatrix} \tag{6.7}$$

where, E^k and ν^k are Young's modulus and Poisson's ratio, respectively. The overall plate is considered to operate under a transverse harmonic point-load ($p(t)$) at point ($a/2, b/2, -h/2$), and thus the principle of virtual work gives,

$$\delta T_P = \int_0^a \int_0^b \left[\sum_{k=1}^{N_L} \int_{h_k}^{h_{k+1}} \left\langle (\delta \boldsymbol{\varepsilon}_b^k)^{\mathrm{T}} \boldsymbol{\sigma}_b^k + (\delta \boldsymbol{\varepsilon}_s^k)^{\mathrm{T}} \boldsymbol{\sigma}_s^k \right\rangle dz \right] dy dx - (\delta w_0)\, p(t)\Big|_{\frac{a}{2},\frac{b}{2},-\frac{h}{2}} \tag{6.8}$$

$$\delta T_K = \int_0^a \int_0^b \left[\sum_{k=1}^{N_L} \int_{h_k}^{h_{k+1}} \left\langle \left\{ \delta \dot{u}^k \quad \delta \dot{v}^k \quad \delta \dot{w}^k \right\} \rho^k \left\{ \dot{u}^k \quad \dot{v}^k \quad \dot{w}^k \right\}^{\mathrm{T}} \right\rangle dz \right] dy dx \tag{6.9}$$

where, δT_P and δT_K are the first variations of the total potential energy and the total kinetic energy respectively at any instant of time (t), δ is an operator for the first variation; ρ^k is the mass density of k^{th} layer.

The FE mesh is generated by dividing the rectangular plane of the plate such that every nine-node quadrilateral isoparametric element is in the shape of a rectangle with the edges in parallel to the x and y axes. The 1-3 VEC layers of a typical element are made of graphite or viscoelastic material so that a typical element is comprised of isotropic layers although the overall plate is consisting of composite (0-3 VEC) layers. The different kinematic parameters at any point in a typical element can be expressed in terms of the shape function matrix ($\boldsymbol{N}$) and the elemental nodal displacement vector ($\boldsymbol{d}^e$) as,

$$\begin{gathered}
\boldsymbol{d} = \boldsymbol{N}\boldsymbol{d}^e, \quad d^k = (\boldsymbol{T}_t + \boldsymbol{Z}_r^k \boldsymbol{T}_r) N d^e, \\
\boldsymbol{\varepsilon}_{bL} = \boldsymbol{B}_{bL}\boldsymbol{d}^e, \quad \boldsymbol{\kappa}_b = \boldsymbol{B}_{\kappa b}\boldsymbol{d}^e, \\
\boldsymbol{\varepsilon}_{sL} = \boldsymbol{B}_{sL}\boldsymbol{d}^e, \quad \boldsymbol{\kappa}_s = \boldsymbol{B}_{\kappa s}\boldsymbol{d}^e \\
\boldsymbol{B}_{bL} = \boldsymbol{L}_{bL}\boldsymbol{T}_t\boldsymbol{N}, \quad \boldsymbol{B}_{\kappa b} = \boldsymbol{L}_{b\kappa}\boldsymbol{T}_r\boldsymbol{N}, \\
\boldsymbol{B}_{sL} = \boldsymbol{L}_{sL}\boldsymbol{T}_t\boldsymbol{N}, \quad \boldsymbol{B}_{\kappa s} = \boldsymbol{L}_{s\kappa}\boldsymbol{T}_r\boldsymbol{N}
\end{gathered} \tag{6.10}$$

Substituting Eqs. (6.7), (6.3) and (6.6a) in Eqs. (6.8) and (6.9) and then using Eq. (6.10a), the following elemental expressions can be obtained as,

$$\delta T_P^e = \left(\delta \boldsymbol{d}^e\right)^{\mathrm{T}} \left\{ \left(\boldsymbol{K}_b^e + \boldsymbol{K}_s^e \right) \boldsymbol{d}^e - \boldsymbol{P}_c^e\, p(t) \right\},$$

$$\delta T_K^e = \left(\delta \dot{\boldsymbol{d}}^e\right)^{\mathrm{T}} \boldsymbol{M}^e \dot{\boldsymbol{d}}^e,$$

$$\boldsymbol{K}_b^e = \int_{A^e} \left[\left(\boldsymbol{B}_{bL}\right)^{\mathrm{T}} \left(\boldsymbol{A}_b \boldsymbol{B}_{bL} + \boldsymbol{B}_{L1}\boldsymbol{B}_{\kappa b} \right) + \left(\boldsymbol{B}_{\kappa b}\right)^{\mathrm{T}} \left(\boldsymbol{B}_{L2}\boldsymbol{B}_{bL} + \boldsymbol{D}_L \boldsymbol{B}_{\kappa b} \right) \right] dA^e,$$

$$\boldsymbol{K}_s^e = \int_{A^e}\left[\left(\boldsymbol{B}_{sL}\right)^{\mathrm{T}}\left(\boldsymbol{A}_s\boldsymbol{B}_{sL}+\boldsymbol{B}_{s1}\boldsymbol{B}_{\kappa s}\right)+\left(\boldsymbol{B}_{\kappa s}\right)^{\mathrm{T}}\left(\boldsymbol{B}_{s2}\boldsymbol{B}_{sL}+\boldsymbol{D}_s\boldsymbol{B}_{\kappa s}\right)\right]dA^e\,,$$

$$\boldsymbol{M}^e = \int_{A^e}\left[\boldsymbol{N}^{\mathrm{T}}\left\langle(\boldsymbol{T}_t)^{\mathrm{T}}m_1\boldsymbol{T}_t+(\boldsymbol{T}_t)^{\mathrm{T}}\boldsymbol{m}_2\boldsymbol{T}_r+(\boldsymbol{T}_r)^{\mathrm{T}}\boldsymbol{m}_3\boldsymbol{T}_t+(\boldsymbol{T}_r)^{\mathrm{T}}\boldsymbol{m}_4\boldsymbol{T}_r\right\rangle\boldsymbol{N}\right]dA^e\,, \tag{6.11}$$

$$\boldsymbol{P}_c^e = \left\langle \boldsymbol{N}^{\mathrm{T}}\boldsymbol{T}_t^{\mathrm{T}}\{0\quad 0\quad 1\}^{\mathrm{T}}\right\rangle_{a/2,b/2,-h/2}$$

where, A^e is the elemental area and other parameters are given by,

$$\boldsymbol{A}_b = \sum_{k=1}^{N_L}\int_{h_k}^{h_{k+1}}\boldsymbol{C}_b^k dz\,,\quad \boldsymbol{B}_{L1} = \sum_{k=1}^{N_L}\int_{h_k}^{h_{k+1}}\boldsymbol{C}_b^k\boldsymbol{Z}_b^k dz\,,$$

$$\boldsymbol{B}_{L2} = \sum_{k=1}^{N_L}\int_{h_k}^{h_{k+1}}\left(\boldsymbol{Z}_b^k\right)^{\mathrm{T}}\boldsymbol{C}_b^k dz\,,\quad \boldsymbol{D}_L = \sum_{k=1}^{N_L}\int_{h_k}^{h_{k+1}}\left(\boldsymbol{Z}_b^k\right)^{\mathrm{T}}\boldsymbol{C}_b^k\boldsymbol{Z}_b^k dz\,,$$

$$\boldsymbol{A}_s = \sum_{k=1}^{N_L}\int_{h_k}^{h_{k+1}}\boldsymbol{C}_s^k dz\,,\quad \boldsymbol{B}_{s1} = \sum_{k=1}^{N_L}\int_{h_k}^{h_{k+1}}\boldsymbol{C}_s^k\boldsymbol{Z}_s^k dz\,,$$

$$\boldsymbol{B}_{s2} = \sum_{k=1}^{N_L}\int_{h_k}^{h_{k+1}}\left(\boldsymbol{Z}_s^k\right)^{\mathrm{T}}\boldsymbol{C}_s^k dz\,,\quad \boldsymbol{D}_s = \sum_{k=1}^{N_L}\int_{h_k}^{h_{k+1}}\left(\boldsymbol{Z}_s^k\right)^{\mathrm{T}}\boldsymbol{C}_s^k\boldsymbol{Z}_s^k dz\,,$$

$$m_1 = \sum_{k=1}^{N_L}\int_{h_k}^{h_{k+1}}\rho^k dz\,,\quad \boldsymbol{m}_2 = \sum_{k=1}^{N_L}\int_{h_k}^{h_{k+1}}\rho^k\boldsymbol{Z}_r^k dz\,,$$

$$\boldsymbol{m}_3 = \sum_{k=1}^{N_L}\int_{h_k}^{h_{k+1}}\left(\boldsymbol{Z}_r^k\right)^{\mathrm{T}}\rho^k dz\,,\quad \boldsymbol{m}_4 = \sum_{k=1}^{N_L}\int_{h_k}^{h_{k+1}}\left(\boldsymbol{Z}_r^k\right)^{\mathrm{T}}\rho^k\boldsymbol{Z}_r^k dz \tag{6.12}$$

where, h_k and h_{k+1} are the thickness coordinates of the bottom and top surfaces of k^{th} layer. Introducing Eq. (6.11) in the extended Hamilton's principle (Eq. (2.11)), the elemental governing equations of motion can be obtained. These elemental equations can then be assembled into global equations of motion of the overall plate as given in Eq. (6.13).

$$\int_{t_1}^{t_2}\left(\delta T_K-\delta T_P\right)dt = 0 \tag{2.11}$$

$$M\ddot{X}+\left(K_b+K_s\right)X = P_c\,p(t) \tag{6.13}$$

where, $\boldsymbol{M}$ is the global mass matrix; $\boldsymbol{K}_b$ and $\boldsymbol{K}_s$ are the bending and shear counterparts of the global stiffness matrix; $\boldsymbol{X}$ and $\boldsymbol{P}_c$ are the global nodal displacement and load-coefficient vectors, respectively.

The transverse harmonic point-load is considered in the form of, $p(t) = p_0 e^{j\omega t}$ ($j = \sqrt{-1}$; p_0 and ω are the load-amplitude and operating frequency, respectively). For the corresponding linear steady state vibration of the overall plate, the equations (Eq. (6.13)) of motion can be reduced as (Meirovitch, 1997),

$$\left[-\omega^2 \boldsymbol{M} + \left(\boldsymbol{K}_b + \boldsymbol{K}_s\right)\right]\tilde{X} = \boldsymbol{P}_c p_0 \tag{6.14}$$

where, $\tilde{X}$ is a complex nodal displacement vector, and its absolute value represents the nodal displacement-amplitude vector.

6.3 Estimation of damping in the overall plate

The viscoelastic material is modelled using the complex stiffness method, and thus Eq. (6.14) can be written as,

$$\left[-\omega^2 \boldsymbol{M} + \left(\boldsymbol{K}_b^R + \boldsymbol{K}_s^R\right) + j\left(\boldsymbol{K}_b^I + \boldsymbol{K}_s^I\right)\right]\tilde{X} = \boldsymbol{P}_c p_0 \tag{6.15}$$

where, the superscripts R and I indicate real and imaginary counterparts of a complex quantity. For free vibration ($p_0 = 0$) of the overall plate, Eq. (6.15) can be written as,

$$\left\langle (\boldsymbol{K}_b^R + \boldsymbol{K}_s^R) + j(\boldsymbol{K}_b^I + \boldsymbol{K}_s^I)\right\rangle \boldsymbol{\psi}_i = \omega_i^2 \boldsymbol{M} \boldsymbol{\psi}_i \tag{6.16}$$

where, $\boldsymbol{\psi}_i$ and ω_i are the complex eigen vector and natural frequency, respectively for the i^{th} mode of vibration. The complex natural frequency (ω_i) can be expressed in terms of the natural frequency (ω_i^0) and the modal loss factor (η_i) as given in Eq. (3.29).

$$(\omega_i)^2 = (\omega_i^0)^2 \langle 1 + j\eta_i \rangle, \quad \eta_i = \mathrm{Im}(\omega_i)^2 / \mathrm{Re}(\omega_i)^2 \tag{3.29}$$

Now, for the assumption of, $\boldsymbol{K}_s^I = \boldsymbol{0}$ ($\boldsymbol{K}_b^I \neq \boldsymbol{0}$) or $\boldsymbol{K}_b^I = \boldsymbol{0}$ ($\boldsymbol{K}_s^I \neq \boldsymbol{0}$), the damping in the plate appears due to the in-plane or the transverse shear strains, respectively in the viscoelastic phase of the constrained 0-3 VEC layers. The corresponding modal loss factor is denoted by η_e or η_s. Without any assumption, the modal loss factor for the total passive damping in the overall plate is denoted by η.

6.4 Results and discussions

In this section, the numerical results are presented for investigating the passive damping characteristics of the overall plate particularly for the inclusions of

graphite-wafers within the constrained viscoelastic layer. Unless otherwise mentioned, the numerical results are evaluated considering one ($n_z = 1$) 0-3 VEC layer within a specified thickness (h_d) of the constrained damping layer as shown in Fig. 6.2. The geometrical and material properties of the overall plate are given in Table 6.1. The edges of the overall plate are assumed to be simply-supported edges ($v_0 = 0$, $w_0 = 0$, $\beta_i = 0$ at $x = 0$ and a; $u_0 = 0$, $w_0 = 0, \alpha_i = 0$ at $y = 0$ and b).

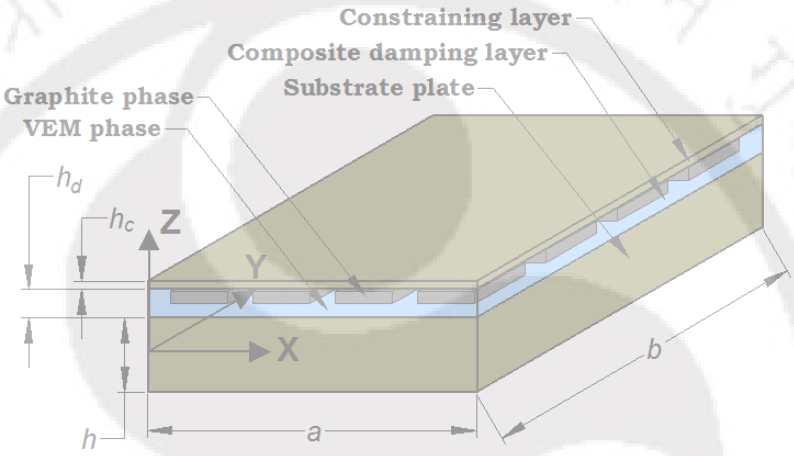

Fig. 6.2 A substrate plate integrated with a constrained 0-3 VEC layer.

Table 6.1 Geometrical and material properties of the overall plate.

Layer	Geometrical properties		
	a (m)	b (m)	h (mm)
Substrate plate	0.4	0.4	4
Constraining layer	0.4	0.4	0.25
Constrained layer	0.4	0.4	0.5
Layer (material)	Material properties		
	E (Pa)	ν	ρ (kg/m^3)
Substrate plate (Al)	69e9	0.3	2740
Constraining layer (Al)	69e9	0.3	2740
0-3 VEC (graphite)	250e9	0.3	1400
0-3 VEC (viscoelastic)	15e6(1+0.6j)	0.49	920

In order to verify the present FE formulation, the natural frequencies and the corresponding modal loss factors (η) are computed in the absence of the inclusions within the constrained viscoelastic layer. These results are compared with the similar results available in the literature (Cupial and Niziol, 1995).

Table 6.2 illustrates this comparison, and it may be observed that the present FE results are in close agreement with the available analytical results (Cupial and Niziol, 1995). This comparison verifies the accuracy of the present FE formulation.

Table 6.2 Verification of the present FE formulation ($\omega_{m,n}$ (Hz) is the natural frequency, $\eta_{m,n}$ is the modal loss factor, m and n are the mode numbers along the x and y directions, respectively, Ref.: Cupiał and Niziół, 1995).

Mode (m,n)	Ref.		Present FE results	
	$\omega_{m,n}$	$\eta_{m,n}$	$\omega_{m,n}$	$\eta_{m,n}$
(1,1)	60.3	0.19	60.5045	0.1901
(1,2)	115.4	0.203	115.8125	0.2034
(2,1)	130.6	0.199	131.0654	0.1991
(2,2)	178.7	0.181	179.1823	0.1806

The damping in the overall plate appears due to the time-varying strains in the constrained viscoelastic layer. So, the change of damping in the overall plate due to the graphite-inclusions can be estimated through the corresponding alterations in the characteristics of the strains within the constrained layer. It is presently studied by evaluating the strains at a transverse (xz) plane and a horizontal (xy) plane of the simply-supported overall plate under a transverse point-load $(a/2, b/2, -h/2)$. The geometry of the overall plate (Fig. 6.2) is considered as, $h_d = 1$ mm, $n_x = n_y = 4$, $\Delta_x = \Delta_y = 10$ mm, $h_v = 0.3$ mm, $h_m = 0.4$ mm. The transverse (xz) plane is taken through the middle points of a row of rectangular graphite-wafers in the x-direction (Fig. 6.2) as shown in Fig. 6.3(a). The same plane in the absence of the inclusions is shown in Fig. 6.3(b). The aforesaid horizontal (xy) plane (for the evaluation of strains) is taken through the viscoelastic phase over the top surface of the middle 1-3 VEC layer of the constrained 0-3 VEC layer (Fig. 6.2/ Fig. 6.1(a)).

The distributions of the transverse shear (γ_{xz}) and extensional (ε_x) strains over the transverse (xz) plane (Fig. 6.3(a) or Fig. 6.3(b)) are illustrated in Fig. 6.4. Similarly, the distributions of the strains ($\varepsilon_x, \gamma_{xy}, \gamma_{xz}$) on the aforesaid xy-plane are demonstrated in Fig. 6.5. Similar to the results for 1-3 VEC layer (Fig. 2.5), it may be observed from Figs. 6.4 and 6.5 that the maximum magnitudes of the strains indicatively increase due to the inclusions of graphite-

wafers within the constrained viscoelastic layer. It should be noted here that the characteristics of the strain components $\varepsilon_y / \gamma_{yz}$ appear similar to those of the $\varepsilon_x / \gamma_{xz}$, and thus the distributions of ε_y and γ_{yz} are not furnished here.

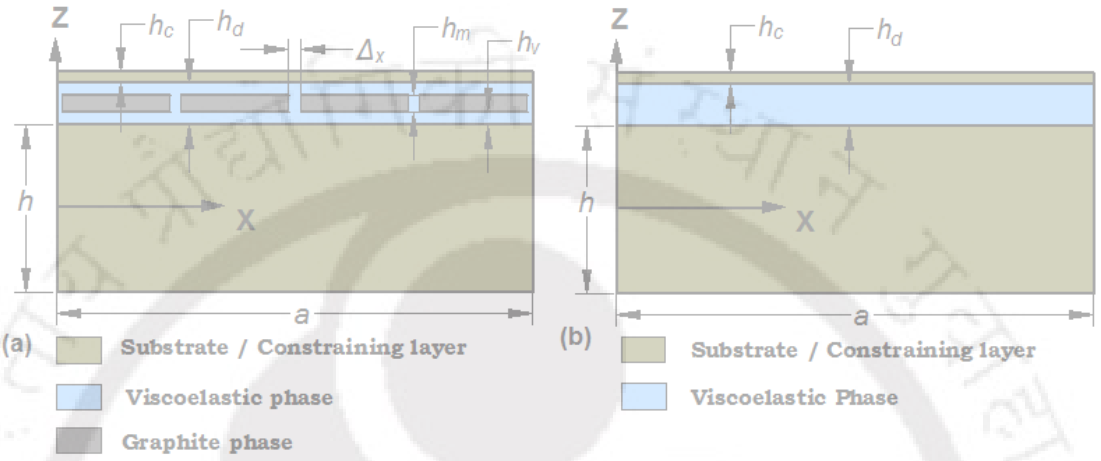

Fig. 6.3 (a) Distributions of materials over a typical XZ-plane through the middle points of a row of rectangular wafers in X-direction; (b) the same plane as in (a) without inclusions or for monolithic VEM layer

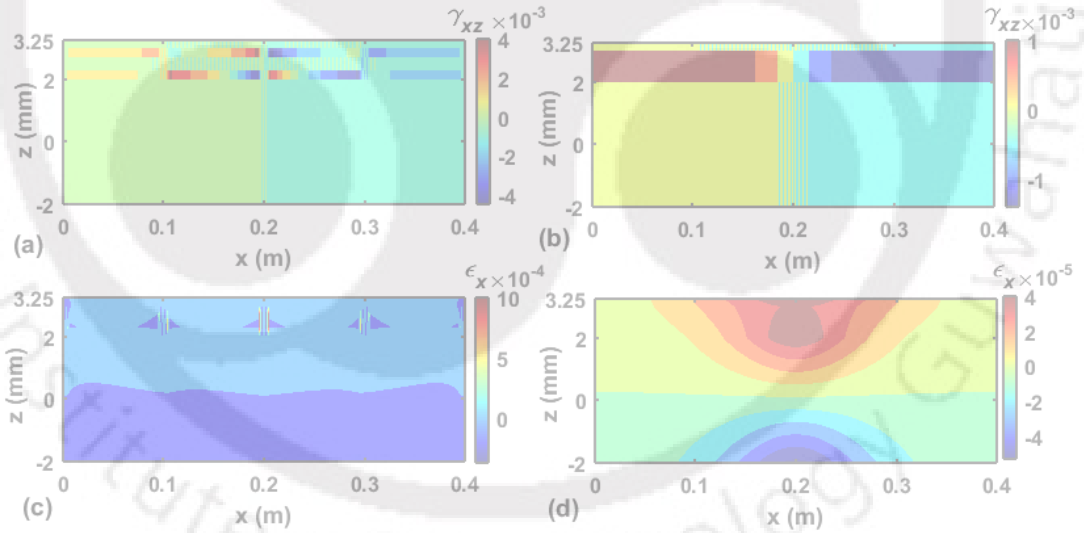

Fig. 6.4 Distributions of the strains (γ_{xz}, ε_x) in the XZ-plane; (a),(c) for the XZ-plane in Fig. 6.3(a); (b),(d) for the XZ-plane in Fig. 6.3(b).

It is important to note here that the magnitudes of all the in-plane and transverse strain components ($\varepsilon_x, \varepsilon_y, \gamma_{xy}, \gamma_{xz}, \gamma_{yz}$) within the viscoelastic phase increase for the case of 0-3 VEC layer, while similar enhancement appears for few strain components ($\varepsilon_x, \gamma_{xz}$) in case of the 1-3 VEC layer (Fig. 2.5). So, the

damping in the overall plate is supposed to improve for the enhanced magnitudes of the strains in the viscoelastic phase of the 0-3 VEC layer, and also the effectiveness of 0-3 VEC layer is expected to be more than that of the 1-3 VEC layer. This estimation is quantified in the following section.

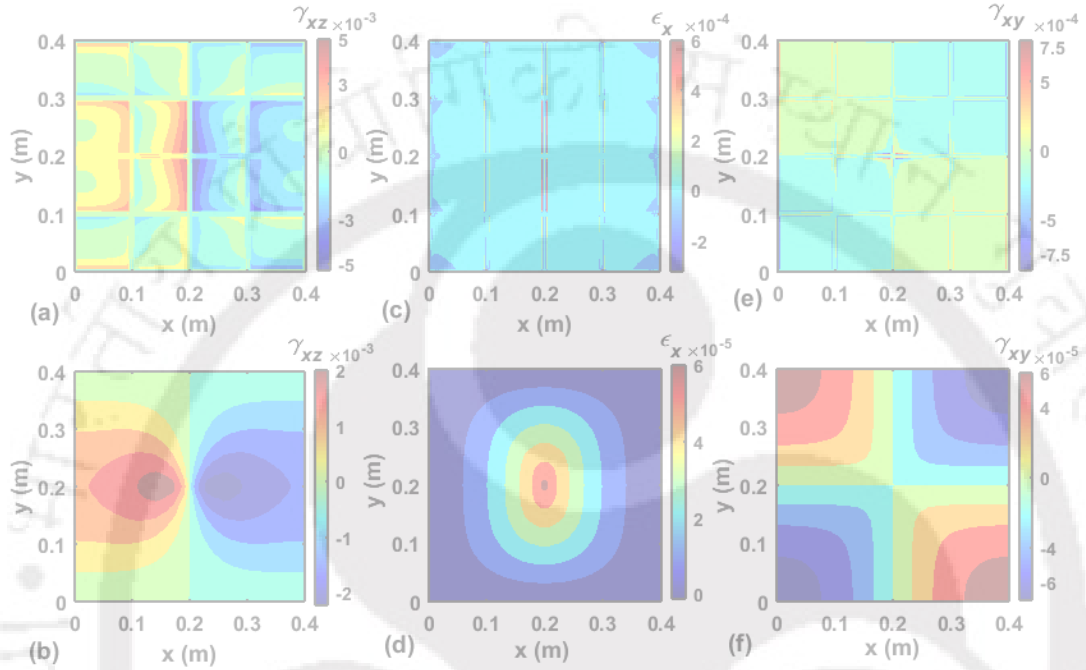

Fig. 6.5 Distributions of strains ($\gamma_{xz}, \varepsilon_x, \gamma_{xy}$) on an xy-plane through the viscoelastic phase over the 1-3 VEC layer or graphite-wafers within the constrained 0-3 VEC layer; (a), (c), (e) in the presence of inclusions; (b), (d), (f) in the absence of inclusions.

6.4.1 Analysis of damping in the overall plate

The damping characteristics of the overall plate are studied in this section by means of varying the geometrical parameters ($h_v, \Delta_x, \Delta_y, n_x, n_y$ (Fig. 6.1)) in the arrangement of the rectangular graphite-wafers. Figure 6.6 illustrates the variations of the modal loss factor (η) and its two counterparts (η_e and (η_s) with the thickness (h_v, Fig. 6.1(a)) of the viscoelastic phase over the top/bottom surfaces of graphite-wafers within the constrained 0-3 VEC layer. The thickness (h_d) of the constrained layer remains constant, while the thickness (h_v) is varied in a ratio as, h_v / h_d. The other geometric parameters are considered as, $n_x = n_y =$ 6, $\Delta_x = \Delta_y =$ 50 μm, n_z=1. The modal loss factor ($\eta / \eta_e / \eta_s$) is computed corresponding to the fundamental mode of vibration of the overall plate. Figure 6.6 also contains similar results for the consideration of the graphite-strips

instead of the graphite-wafers. The gaps (Δ_y) in every row of the graphite-wafers along the y-direction are removed ($\Delta_y = 0$) by the same material (graphite) for achieving the graphite-strips. The variations of the loss factors (η, η_e, η_s) in the absence of the graphite-wafers/graphite-strips within the constrained viscoelastic layer are also presented in Fig. 6.6.

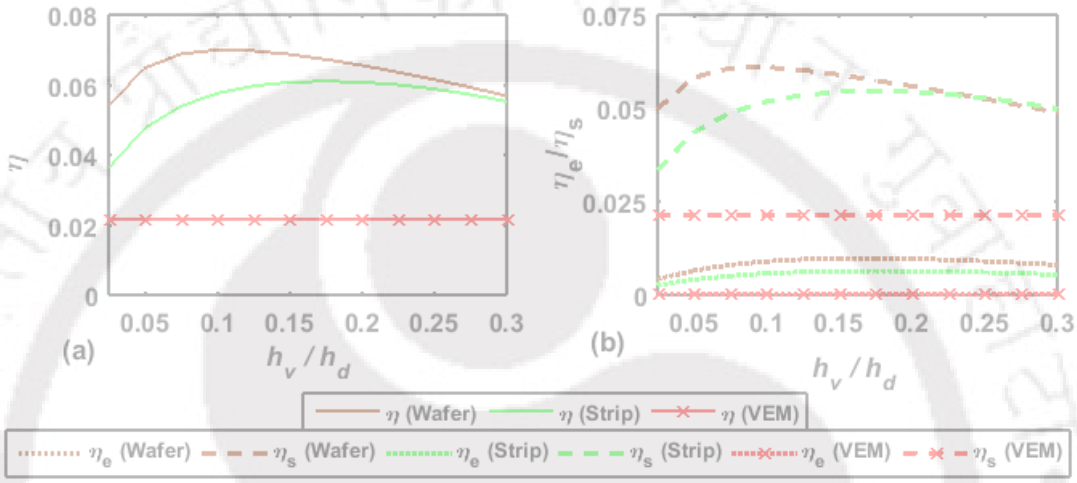

Fig. 6.6 Variations of modal loss factors ((a) for η, (b) for η_e and η_s) with the thickness (h_v) of the viscoelastic phase in the constrained layer.

For the use of pure VEM layer, it may be observed from Fig. 6.6(b) that the damping in the overall plate appears due to its (VEM) transverse shear strains ($\eta_e \approx 0$). Although it is a known fact, the magnitudes of η_e and η_s improve indicatively for the inclusions of graphite-wafers/graphite-strips. So, the total damping (η) significantly increases (Fig. 6.6(a)). It may also be observed from Fig. 6.6 that the damping in the overall plate does not appear in a similar manner for two different forms (wafer and strip) of the inclusions. This result (Fig. 6.6) recommends graphite-wafers with a low thickness (h_v) of the viscoelastic phase within the constrained layer for having maximum improvement of damping in the overall plate.

Figure 6.7 illustrates the variations of the modal loss factors (η, η_e, η_s) at the fundamental mode with the in-plane axial gap between any two consecutive graphite-wafers/graphite-strips. The graphite-wafers are considered to be equally spaced in both the x and y directions ($\Delta_x = \Delta_y = \Delta$), while the graphite-strips are also considered to be equally spaced in the x-direction ($\Delta_x = \Delta$). The

gap (Δ) is gradually increased keeping the same number of graphite-wafers/graphite-strips in any direction. The other dimensions of the constrained layer are taken as, $h_v / h_d = 0.1$, $n_x = n_y = 6$, $n_z = 1$.

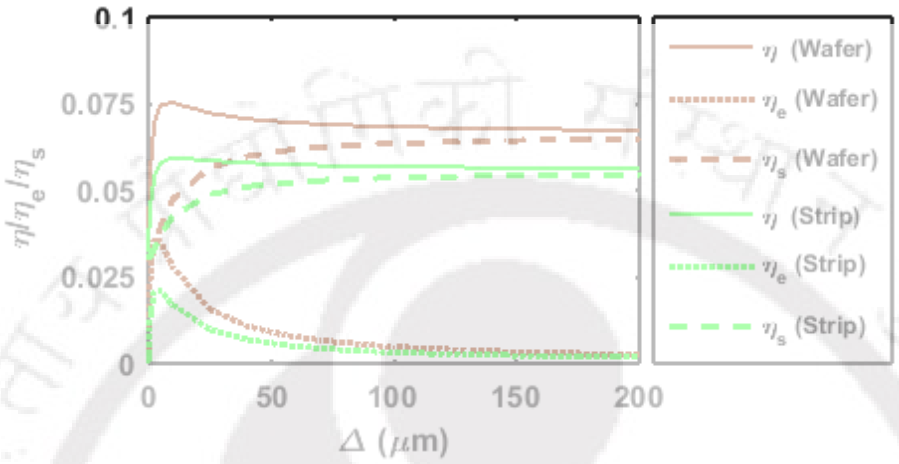

Fig. 6.7 Variations of modal loss factors (η, η_e, η_s) with the in-plane axial gap (Δ) in the constrained VEC layer.

It may be observed from Fig. 6.7 that the magnitude of η_e is almost equal to zero for a graphite-layer ($\Delta_x = \Delta_y = 0$). But it (η_e) increases steeply for the use of graphite-wafers/graphite-strips with a small gap (Δ) and then decreases to a constant value as the gap (Δ) increases. In parallel to this variation of (η_e), the magnitude of (η_s) decreases steeply and then increases to a constant value as the gap (Δ) increases from its zero value. As a result of these variations of η_e and η_s, the damping (η) in the plate significantly increases when the graphite-wafers/graphite-strips are taken instead of a graphite-layer ($\Delta_x = \Delta_y = 0$). For any form (layer/wafer/strip) of the graphite-inclusions, the damping in the overall plate increases over that in the use of the conventional monolithic VEM layer. But, the maximum improvement of damping appears for the inclusions of graphite-wafers (Fig. 6.7).

For the fundamental mode of vibration of the overall plate, Fig. 6.8 illustrates the variations of the modal loss factors (η, η_e, η_s) with the number of graphite-wafers/graphite-strips. The number of graphite wafers ($n_x = n_y = n_f$) in the x and y directions are gradually increased keeping a constant gap ($\Delta_x = \Delta_y = \Delta$, Δ=50 μm). The same strategy is also followed in the use of the

graphite-strips. The other dimensions of the constrained VEC layer are taken as, $h_v / h_d = 0.1,\ n_z = 1$.

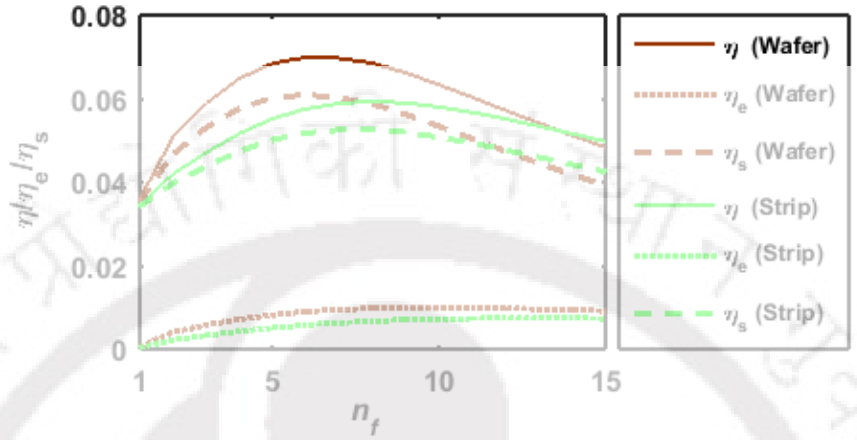

Fig. 6.8 Variations of modal loss factors (η, η_e, η_s) with the number (n_f) of graphite-wafers/strips in the constrained layer.

It may be observed from Fig. 6.8 that the damping in the plate significantly depends on the number (n_f) of graphite-wafers/graphite-strips. Also, there would be an optimal number of graphite-wafers/graphite-strips for maximum improvement of damping. In the previous results (Figs. 6.6-6.8), one VEC layer ($n_z = 1$) is taken within the thickness (h_d) of constrained layer. For the consideration of several layers ($n_z > 1$, Fig. 6.1(b)) within a constant thickness (h_d) of the constrained layer, the corresponding variation of damping in the overall plate is illustrated in Fig. 6.9.

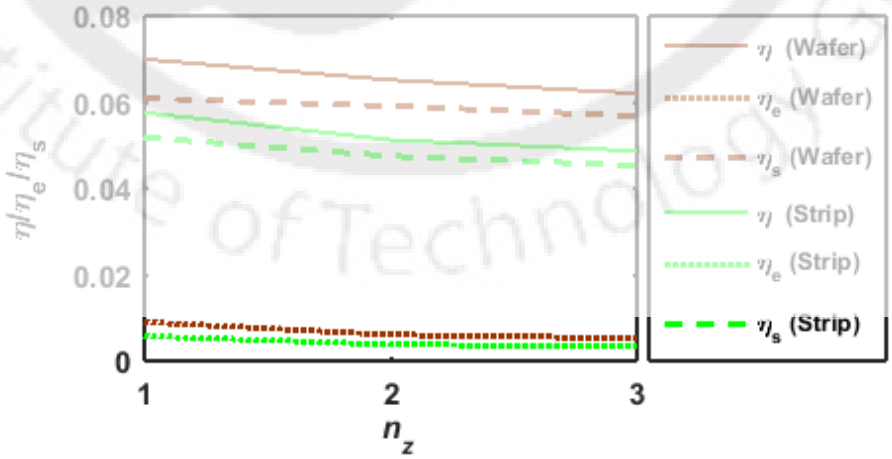

Fig. 6.9 Variations of modal loss factors (η, η_e, η_s) with the number (n_z) of VEC layers within a constant thickness (h_d) of the constrained layer.

The total thickness (h_d) of the constrained layer is considered as, 0.5 mm, while the other geometric parameters of every VEC layer are taken as, $h_v / h_d =$ 0.1, $n_x = n_y$=6 and Δ=50 μm. It may be observed from Fig. 6.9 that there is no significant change of damping in the overall plate for the consideration of several VEC layers within a constant thickness (h_d) of the constrained layer.

6.4.2 Optimal configuration of the constrained 0-3 VEC layer

The foregoing results suggest one VEC layer within the thickness of the constrained layer, and it would also be made of graphite-wafers or 0-3 VEC layer. The damping capacity of this 0-3 VEC layer significantly depends on its geometric parameters (h_v, Δ and n_f (Figs. 6.6-6.8)). Thus, for maximum augmentation of damping, these parameters are to be configured in an optimal manner, and it is carried out in this section by choosing the modal loss factor (η) as the objective function of the geometric parameters ($h_v / h_d, \Delta, n_f$). Presently, the fundamental mode of vibration of the overall plate is considered, and thus the identical rectangular graphite-wafers are spaced uniformly ($\Delta_x = \Delta_y = \Delta$) in both the x and y directions. Under this consideration, the modal loss factor (η) is maximized with respect to the geometric parameters ($h_v / h_d, \Delta, n_f$). According to the present FE procedure, a direct search method (Deb, 2012) is utilized by identifying the bounds of the parameters from the previous results (Figs. 6.6-6.8) as, $0.05 \le (h_v / h_d) \le 0.3$, $15\,\mu\text{m} \le \Delta \le 500\,\mu\text{m}$, $1 \le n_f \le 15$. Within these bounds, a three-dimensional grid is generated, and the magnitudes of the modal loss factor (η) at all the grid-points are computed. The results are plotted in Fig. 6.10, and it may be observed from this figure that the modal loss factor (η) appears with its indicative magnitudes at the low values of the gap (Δ) for any set of values of h_v / h_d and n_f. But, a very small gap (Δ) may cause the difficulties in the fabrication of the VEC layer. So, presently a value of the gap (Δ) is chosen as 50 μm. On the plane of $\Delta = 50$ μm, the maximum value of η is bracketed by the other two parameters ($h_v / h_d, n_f$) as, $0.025 \le (h_v / h_d) \le 0.2$ and $4 \le n_f \le 12$. In each of these two-dimensional planes of h_v / h_d and n_f (at $\Delta = 50$ μm), a two-dimensional grid is generated, and the

corresponding contour of η is evaluated as shown in Fig. 6.11. This contour of η clearly shows its (η) maximum value, and the corresponding values of h_v / h_d and n_f are taken as their optimal values. So, the optimal geometric configuration of the constrained 0-3 VEC layer (Fig. 6.2) is obtained as, h_v / h_d = 0.075, $n = 8$, $\Delta = 50$ μm for $h_d = 0.5$ mm.

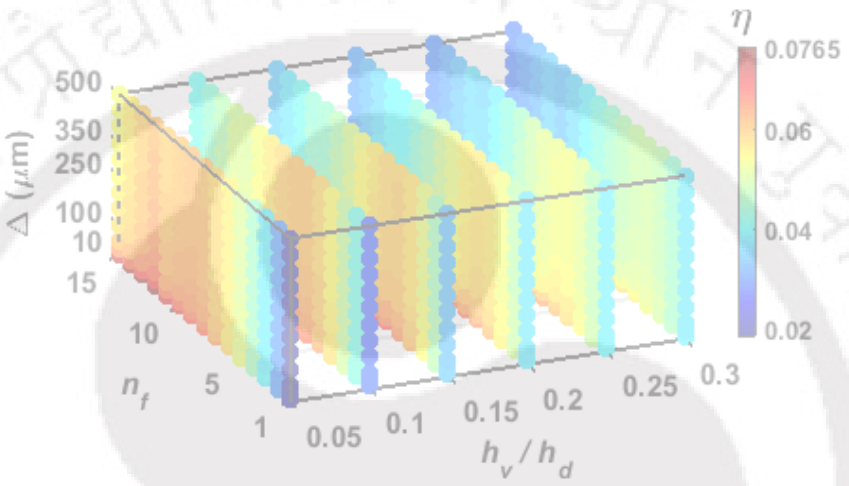

Fig. 6.10 The contour of modal loss factor (η) in a three-dimensional domain of the geometric parameters (h_v / h_d, Δ, n_f) of the constrained 0-3 VEC layer.

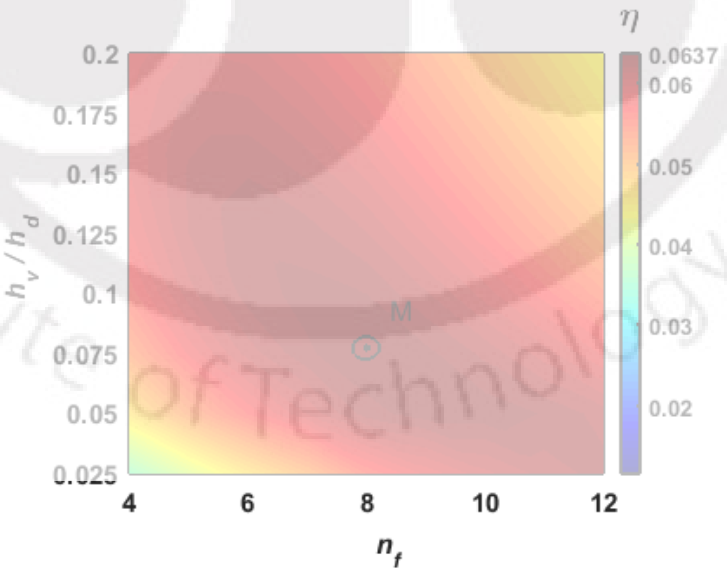

Fig. 6.11 The contour of modal loss factor (η) within a two-dimensional domain of the geometric parameters (h_v / h_d, n_f) of the constrained 0-3 VEC layer (M indicates the maximum value of η).

6.4.3 Frequency responses of the overall plate

On the basis of the optimally configured constrained 0-3 VEC layer as decided in the previous section, the frequency responses of the overall plate under a transverse harmonic point-load are evaluated around the fundamental natural frequency. Similar responses in the absence of the inclusions are also evaluated and presented in Fig. 6.12.

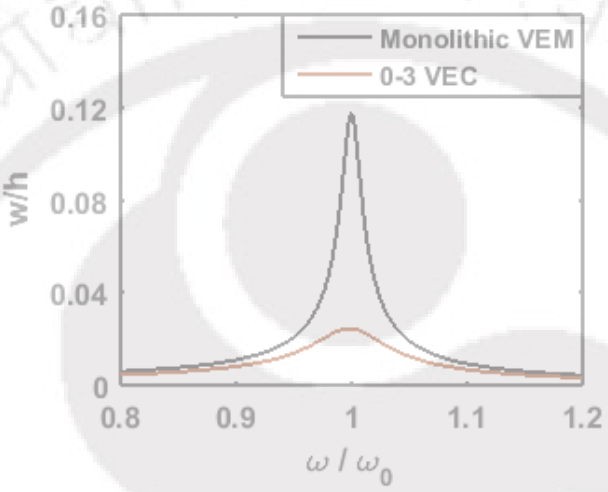

Fig. 6.12 Frequency responses of the overall plate around its fundamental natural frequency (ω_0 is the fundamental natural frequency).

It may be observed from Fig. 6.12 that the damping in the overall plate increases significantly when the constrained layer is made of the present 0-3 VEC instead of the conventional monolithic VEM. These results indicate that the damping capability of the constrained monolithic VEM layer can be improved significantly by inserting a rectangular array of the thin rectangular graphite-wafers through its middle surface (Fig. 6.1(a)).

6.5 Summary

In this chapter, a new 0-3 VEC layer is presented for augmented constrained layer damping of structural vibration. The 0-3 VEC layer is comprised of a rectangular array of thin rectangular graphite-wafers embedded within the viscoelastic matrix. The rectangular graphite-wafers are in the macroscale and evenly spaced with a gap in micro-scale. This 0-3 VEC layer is utilized as a constrained damping layer over the top surface of a simply-supported rectangular plate, and its passive damping capacity is investigated by developing

an FE model of the overall plate based on the layer-wise shear deformation theory. First, a bending analysis of the overall plate is performed, and the characteristics of the transverse shear and in-plane strains within the constrained 0-3 VEC layer are studied. This study reveals significantly improved magnitudes of the transverse shear strains in the viscoelastic phase of the 0-3 VEC layer, while the in-plane strains in the same phase also appear with reasonable magnitudes. These observations infer the improved passive damping in the overall plate through both the transverse shear and in-plane strains, and it is subsequently verified through the evaluation of modal loss factor of the overall plate at its fundamental natural mode of vibration. The modal loss factor of the overall plate is computed for different sets of values of geometrical parameters in the arrangement of the graphite-wafers. These results reveal an indicative increase of damping in the overall plate due to the inclusions of the graphite-wafers within the constrained viscoelastic layer in the form of a 0-3 VEC layer. The same results also indicate to consider appropriate geometric dimensions in the arrangement of the graphite-wafers for the maximum improvement of damping in the overall plate. So, the graphite-wafers in the 0-3 VEC layer are set up in an optimal manner with an objective of the maximum modal loss factor at the fundamental mode of vibration of the overall plate. Using this optimally configured 0-3 VEC layer, the forced frequency responses of the overall plate are evaluated around its fundamental frequency. These responses reveal significant improvement in the attenuation of vibration-amplitude of the overall plate for the inclusion of a rectangular array of the thin graphite-wafers within the constrained viscoelastic layer in an optimal manner. Thus, the present 0-3 VEC layer is a potential damping layer in the CLD treatment of plates, and it may be utilized in place of the conventional monolithic viscoelastic layer for improved damping capacity of the CLD treatment.

Chapter 7

Performance of a graphite wafer-reinforced viscoelastic composite layer for active-passive damping of plate vibration

7.1 Introduction

A new 0-3 VEC layer is designed in the previous chapter (Chapter 6) for the damping layer in the CLD treatment. The CLD treatment is used for suppression of vibration of plates, and it is observed that the passive damping capacity of the treatment improves significantly when the conventional monolithic viscoelastic material (VEM) layer in the CLD treatment is replaced by the 0-3 VEC layer although this VEC layer is to be configured in an appropriate manner. This improved damping capacity of the CLD treatment motivates to extend the study for ACLD treatment of plates using the 0-3 VEC layer, and it is presented in this chapter (Kumar et al., 2017b) considering a smart plate as shown in Fig. 7.1.

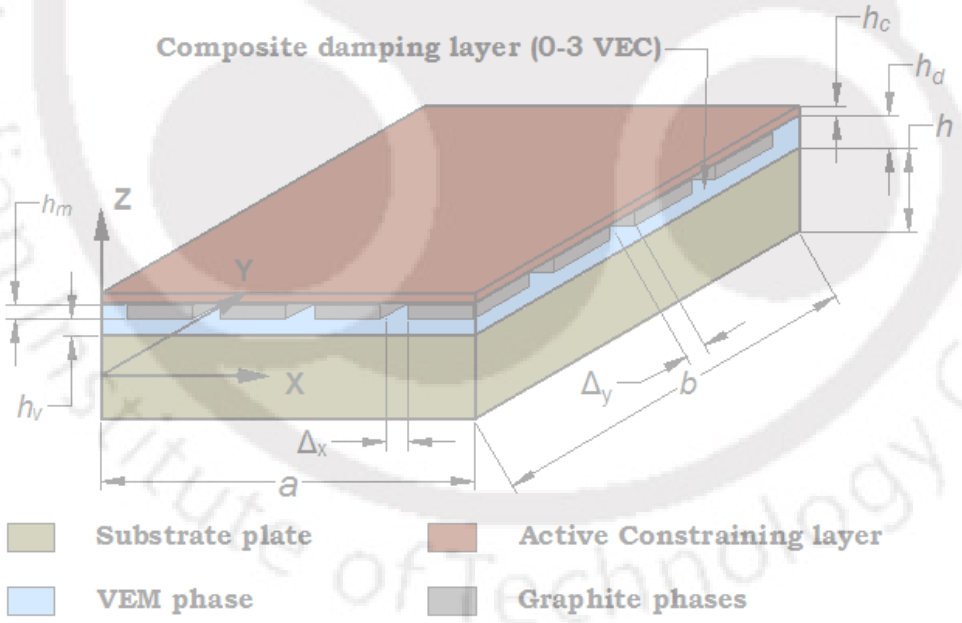

Fig. 7.1. Schematic diagrams of a substrate plate integrated with the actively constrained 0-3 VEC layer.

Figure 7.1 illustrates a substrate plate integrated with an ACLD layer at its top surface where the constrained damping layer is made of the present 0-3 VEC layer. The constraining layer is made of a piezoelectric material (PZT5H).

The poling direction of this piezoelectric constraining layer is the thickness direction, and it acts as an actuator when the external voltage across its top and bottom fully electrode-surfaces is supplied according to the velocity feedback control strategy.

As the overall plate undergoes bending deformation, the viscoelastic phase at the in-plane axial gap between any two consecutive rectangular graphite-wafers experiences reasonable in-plane extensional strain. Concurrently, the viscoelastic phase at the transverse gap between the graphite-wafers and the constraining layer/base plate-surface undergoes transverse shear deformation. So, the constrained 0-3 VEM layer experiences transverse shear strains along with the reasonable in-plane strains. Although this fact is revealed in the case of the CLD treatment of bending mode of vibration of the plates in the previous chapter (Chapter 6), it is again verified in this chapter for the case of ACLD treatment, and then the changes of active-passive damping in the overall plate for the use of 0-3 VEC layer instead of the pure VEM layer are investigated. In the following sections, first, an FE model of the overall plate is derived based on the layer-wise shear deformation theory. Next, the distributions of the aforesaid strains within the actively constrained 0-3 VEC layer are illustrated for the bending deformation of the overall plate. Subsequently, the active-passive damping in the overall plate is quantified to investigate damping characteristics of the overall plate on the basis of the appearing strains in the viscoelastic phase of 0-3 VEC layer. The effects of different geometrical parameters of the 0-3 VEC layer on the active-passive damping in the overall plate are evaluated, and the influential geometric parameters are optimised for maximum active-passive damping in the overall plate. Based on this optimal geometric configuration of the 0-3 VEC layer, the frequency responses of the overall plate are evaluated, and the change in the control capability of the ACLD treatment due to the inserts of graphite-wafers within the actively constrained viscoelastic layer is presented.

7.2 FE model of the smart plate

The middle plane of the substrate plate (Fig. 7.1) is considered as the reference plane, and one corner of this plane is considered as the origin of the reference rectangular coordinate (xyz) system. The length, width and thickness of the substrate plate (Fig. 7.1) are denoted by, a, b and h, respectively. The thicknesses of the constrained damping layer and the piezoelectric constraining

layer are designated by, h_d and h_c, respectively. The thicknesses of the pure viscoelastic layers and the 1-3 VEC layer within the 0-3 VEC layer (Fig. 6.1(a) or Fig. 7.1) are denoted by, h_v and h_m, respectively. The in-plane axial gap between any two consecutive graphite-wafers along the x or y direction is symbolized by, Δ_x or Δ_y, respectively. Also, the number of rows of the rectangular array of graphite-wafers is denoted by, n_x or n_y along the x or y direction, respectively. The overall plate (Fig. 7.1) is considered as a stack of five layers namely one substrate layer, one 1-3 VEC layer, two pure viscoelastic layers and one piezoelectric constraining layer. These layers are denoted by the symbol, k starting from the bottom substrate plate as $k=1$. As the overall plate is comprised of very thin layers of different materials (Fig. 7.1), its (overall plate) kinematics of deformation is defined according to the layer-wise first-order shear deformation theory as given in Eq. (6.1).

$$u^k(x,y,z,t) = u_0(x,y,t) + z_i^k\,\alpha_i(x,y,t)\,,$$
$$v^k(x,y,z,t) = v_0(x,y,t) + z_i^k\,\beta_i(x,y,t)$$
$$w^k(x,y,z,t) = w_0(x,y,t) \tag{6.1}$$

where, z_i^k stands for the thickness coordinates of different layers, and it can be obtained from Eq. (6.2) as follows,

$$z_1^k = z \text{ or } (h/2) \text{ for } k=1 \text{ or } k>1$$
$$z_2^k = 0 \text{ or } (z-h/2) \text{ or } h_v \text{ for } k<2 \text{ or } k=2 \text{ or } k>2$$
$$z_3^k = 0 \text{ or } (z-h/2-h_v) \text{ or } h_m \text{ for } k<3 \text{ or } k=3 \text{ or } k>3$$
$$z_4^k = 0 \text{ or } (z-h/2-h_v-h_m) \text{ or } h_v \text{ for } k<4 \text{ or } k=4 \text{ or } k>4$$
$$z_5^k = 0 \text{ or } (z-h/2-2h_v-h_m) \text{ for } k<5 \text{ or } k=5 \tag{7.1}$$

According to the displacement field (Eq. (6.1)), a state of deformation ($\boldsymbol{d}^k$) of k^{th} layer can be written following Eq. (6.3) as,

$$\boldsymbol{d}^k = \begin{Bmatrix} u^k & v^k & w^k \end{Bmatrix}^{\mathrm{T}},\ \boldsymbol{d}^k = (\boldsymbol{d}_t + \boldsymbol{Z}_r^k \boldsymbol{d}_r),\ \boldsymbol{d}_t = \begin{Bmatrix} u_0 & v_0 & w_0 \end{Bmatrix}^{\mathrm{T}},$$

$$\boldsymbol{Z}_r^k = \begin{bmatrix} \boldsymbol{Z}_1^k & \boldsymbol{Z}_2^k & \boldsymbol{Z}_3^k & \boldsymbol{Z}_4^k & \boldsymbol{Z}_5^k \end{bmatrix},\ \boldsymbol{Z}_i^k = \begin{bmatrix} z_i^k & 0 & 0 \\ 0 & z_i^k & 0 \end{bmatrix}^{\mathrm{T}},$$

$$\boldsymbol{d}_r = \{\boldsymbol{d}_{r1} \quad \boldsymbol{d}_{r2} \quad \boldsymbol{d}_{r3} \quad \boldsymbol{d}_{r4} \quad \boldsymbol{d}_{r5}\}^{\mathrm{T}},\ \boldsymbol{d}_{ri} = \{\alpha_i \quad \beta_i\} \tag{7.2}$$

The state of deformation ($\boldsymbol{d}^k$) of any layer can also be expressed in terms of the generalized displacement vector ($\boldsymbol{d}$) as follows,

$$\boldsymbol{d}^k = (\boldsymbol{T}_t + \boldsymbol{Z}_r^k \boldsymbol{T}_r)\boldsymbol{d},$$

$$\boldsymbol{d} = \{u_0 \quad v_0 \quad w_0 \quad \alpha_1 \quad \alpha_2 \quad \alpha_3 \quad \alpha_4 \quad \alpha_5 \quad \beta_1 \quad \beta_2 \quad \beta_3 \quad \beta_4 \quad \beta_5\}^{\mathrm{T}} \tag{7.3}$$

where, $\boldsymbol{T}_t$ and $\boldsymbol{T}_r$ are the transformation matrices. The state of strain and the state of stress at any point within the overall plate can be expressed under the plane stress assumption as given in Eq. (6.5)

$$\boldsymbol{\varepsilon}_b = \{\varepsilon_x \quad \varepsilon_y \quad \varepsilon_{xy}\}^{\mathrm{T}},\ \boldsymbol{\varepsilon}_s = \{\varepsilon_{xz} \quad \varepsilon_{yz}\}^{\mathrm{T}},$$

$$\boldsymbol{\sigma}_b = \{\sigma_x \quad \sigma_y \quad \sigma_{xy}\}^{\mathrm{T}},\ \boldsymbol{\sigma}_s = \{\sigma_{xz} \quad \sigma_{yz}\}^{\mathrm{T}} \tag{6.5}$$

The strain-displacement relations for k^{th} layer is given by Eq. (6.6a).

$$\boldsymbol{\varepsilon}_b^k = (\boldsymbol{\varepsilon}_{bL} + \boldsymbol{Z}_b^k \boldsymbol{\kappa}_b),\ \boldsymbol{\varepsilon}_s^k = (\boldsymbol{\varepsilon}_{sL} + \boldsymbol{Z}_s^k \boldsymbol{\kappa}_s)$$

$$\boldsymbol{\varepsilon}_{bL} = \left\{\frac{\partial u_0}{\partial x} \quad \frac{\partial v_0}{\partial y} \quad \left(\frac{\partial u_0}{\partial y} + \frac{\partial v_0}{\partial x}\right)\right\}^{\mathrm{T}},\ \boldsymbol{\varepsilon}_{sL} = \left\{\frac{\partial w_0}{\partial x} \quad \frac{\partial w_0}{\partial y}\right\}^{\mathrm{T}},$$

$$\boldsymbol{\kappa}_b = \{\boldsymbol{\kappa}_b^1 \quad \boldsymbol{\kappa}_b^2 \quad \boldsymbol{\kappa}_b^3 \quad \boldsymbol{\kappa}_b^4 \quad \boldsymbol{\kappa}_b^5\}^{\mathrm{T}},\ \boldsymbol{\kappa}_s = \{\boldsymbol{\kappa}_s^1 \quad \boldsymbol{\kappa}_s^2 \quad \boldsymbol{\kappa}_s^3 \quad \boldsymbol{\kappa}_s^4 \quad \boldsymbol{\kappa}_s^5\}^{\mathrm{T}},$$

$$\boldsymbol{\kappa}_b^i = \left\{\frac{\partial \alpha_i}{\partial x} \quad \frac{\partial \beta_i}{\partial y} \quad \left(\frac{\partial \alpha_i}{\partial y} + \frac{\partial \beta_i}{\partial x}\right)\right\},\ \boldsymbol{\kappa}_s^i = \{\alpha_i \quad \beta_i\},$$

$$\boldsymbol{Z}_b^k = \left[\boldsymbol{z}_{b1}^k \quad \boldsymbol{z}_{b2}^k \quad \boldsymbol{z}_{b3}^k \quad \boldsymbol{z}_{b4}^k \quad \boldsymbol{z}_{b5}^k\right],\ \boldsymbol{Z}_s^k = \left[\boldsymbol{z}_{s1}^k \quad \boldsymbol{z}_{s2}^k \quad \boldsymbol{z}_{s3}^k \quad \boldsymbol{z}_{s4}^k \quad \boldsymbol{z}_{s5}^k\right],$$

$$\boldsymbol{z}_{bi}^k = \boldsymbol{I}_{3\times 3} \otimes z_i^k,\ \boldsymbol{z}_{si}^k = \boldsymbol{I}_{2\times 2} \otimes (\partial z_i^k / \partial z) \tag{6.6a}$$

The generalized strain vectors in Eq. (6.6a) can be expressed in terms of the generalized displacement vector ($\boldsymbol{d}$) following Eq. (7.4) as follows

$$\boldsymbol{\varepsilon}_{bL} = \boldsymbol{L}_{bL}\boldsymbol{T}_t\boldsymbol{d},\ \boldsymbol{\kappa}_b = \boldsymbol{L}_{b\kappa}\boldsymbol{T}_r\boldsymbol{d},$$

$$\boldsymbol{\varepsilon}_{sL} = \boldsymbol{L}_{sL}\boldsymbol{T}_t\boldsymbol{d},\ \boldsymbol{\kappa}_s = \boldsymbol{L}_{s\kappa}\boldsymbol{T}_r\boldsymbol{d},$$

$$\boldsymbol{L}_{sL} = \begin{bmatrix} 0 & 0 & \partial/\partial x \\ 0 & 0 & \partial/\partial y \end{bmatrix},\quad \boldsymbol{L}_{b\kappa} = \boldsymbol{I}_{5\times 5} \otimes \boldsymbol{l}_{b\kappa},\quad \boldsymbol{L}_{s\kappa} = \boldsymbol{I}_{5\times 5} \otimes \boldsymbol{l}_{s\kappa}$$

$$\boldsymbol{L}_{bL}=\begin{bmatrix} \partial/\partial x & 0 & 0 \\ 0 & \partial/\partial y & 0 \\ \partial/\partial y & \partial/\partial x & 0 \end{bmatrix},\quad \boldsymbol{l}_{b\kappa}=\begin{bmatrix} \partial/\partial x & 0 \\ 0 & \partial/\partial y \\ \partial/\partial y & \partial/\partial x \end{bmatrix},\quad \boldsymbol{l}_{s\kappa}=\begin{bmatrix} 1 & 0 \\ 0 & 1 \end{bmatrix} \tag{7.4}$$

where, $\boldsymbol{I}_{(5\times5)}$ is a unity matrix of size (5×5). The constitutive relations for a material within the substrate $(k=1)$ and damping layer $(k=2,3,4)$ can be expressed according to Eq. (6.7).

$$\boldsymbol{\sigma}_b^k=\boldsymbol{C}_b^k\boldsymbol{\varepsilon}_b^k,\quad \boldsymbol{\sigma}_s^k=\boldsymbol{C}_s^k\boldsymbol{\varepsilon}_s^k,$$

$$\boldsymbol{C}_b^k=\frac{E^k}{1-\left(\nu^k\right)^2}\begin{bmatrix} 1 & \nu^k & 0 \\ \nu^k & 1 & 0 \\ 0 & 0 & \frac{1}{2}\left(1-\nu^k\right) \end{bmatrix},\quad \boldsymbol{C}_s^k=\frac{E^k}{2\left(1+\nu^k\right)}\begin{bmatrix} 1 & 0 \\ 0 & 1 \end{bmatrix} \tag{6.7}$$

The viscoelastic material in the constrained layer $(k=2,3,4)$ is modelled by the complex stiffness method. So, the stiffness matrices $(\boldsymbol{C}_b^k,\boldsymbol{C}_s^k)$ for the viscoelastic material are complex matrices. The poling direction of the piezoelectric constraining layer is considered as the transverse direction, and the external voltage (V) is supplied across its top and bottom fully electrode-surfaces. For this arrangement of the surface-electrodes, the transverse electric field component (E_z) at any point in the active constraining layer may be assumed as, $E_z=-V/h_c$, while the other components (E_x and E_y) of the electric field are assumed as, $E_x\approx0$ and $E_y\approx0$. According to these electric field components at any point within the thin piezoelectric constraining layer ($k=5$), its constitutive relations under the plane stress assumption can be written as,

$$\boldsymbol{\sigma}_b^k=\boldsymbol{C}_b^k\boldsymbol{\varepsilon}_b^k-\boldsymbol{e}_b^kE_z,\quad \boldsymbol{\sigma}_s^k=\boldsymbol{C}_s^k\boldsymbol{\varepsilon}_s^k,\quad k=5$$

$$D_z^k=\left(\boldsymbol{e}_b^k\right)^{\mathrm{T}}\boldsymbol{\varepsilon}_b^k+\in_{33}^kE_z,$$

$$\boldsymbol{C}_b^k=\begin{bmatrix} \bar{C}_{11}^k & \bar{C}_{12}^k & 0 \\ \bar{C}_{12}^k & \bar{C}_{22}^k & 0 \\ 0 & 0 & C_{66}^k \end{bmatrix},\quad \boldsymbol{C}_s^k=\begin{bmatrix} C_{55}^k & 0 \\ 0 & C_{44}^k \end{bmatrix},\quad \boldsymbol{e}_b^k=\begin{Bmatrix} \bar{e}_{31}^k \\ \bar{e}_{32}^k \\ 0 \end{Bmatrix},$$

$$\bar{C}_{11}^k = \left\langle C_{11}^k - \left(C_{13}^k\right)^2 / C_{33}^k \right\rangle,\ \bar{C}_{22}^k = \left\langle C_{22}^k - \left(C_{23}^k\right)^2 / C_{33}^k \right\rangle,$$

$$\bar{C}_{12}^k = \left\langle C_{12}^k - C_{13}^k C_{23}^k / C_{33}^k \right\rangle,$$

$$\bar{e}_{31}^k = \left\langle e_{31}^k - C_{13}^k e_{33}^k / C_{33}^k \right\rangle,\ \bar{e}_{32}^k = \left\langle e_{32}^k - C_{23}^k e_{33}^k / C_{33}^k \right\rangle \tag{7.5}$$

In Eq. (7.5), C_{ij}^k, e_{ij}^k and $\in_{ij}^k$ are the stiffness, piezoelectric and dielectric coefficients, respectively for the piezoelectric constraining layer ($k=5$). The overall plate is considered to operate under a uniformly distributed transverse harmonic load ($p(t)$). For the corresponding vibration of the overall plate, the principle of virtual work gives,

$$\delta T_p = \int_0^a \int_0^b \left[\sum_{k=1}^{5} \int_{h_k}^{h_{k+1}} \left\langle (\delta\boldsymbol{\varepsilon}_b^k)^{\mathrm{T}} \boldsymbol{\sigma}_b^k + (\delta\boldsymbol{\varepsilon}_s^k)^{\mathrm{T}} \boldsymbol{\sigma}_s^k \right\rangle dz - \int_{h_k}^{h_{k+1}} (\delta E_z)^{\mathrm{T}} D_z^k \Big|_{k=5} dz \right] dy dx \\ - \left\langle \delta w\left(p(t)\right) \right\rangle_{z=-h/2} \tag{7.6}$$

$$\delta T_K = \int_0^a \int_0^b \left[\sum_{k=1}^{5} \int_{h_k}^{h_{k+1}} \left\langle \left\{ \delta\dot{u}^k \quad \delta\dot{v}^k \quad \delta\dot{w}^k \right\} \rho^k \left\{ \dot{u}^k \quad \dot{v}^k \quad \dot{w}^k \right\}^{\mathrm{T}} \right\rangle dz \right] dy dx \tag{7.7}$$

Where, δT_p and δT_k are the first variations of the total potential energy and the total kinetic energy respectively at any instant of time (t), δ is an operator for the first variation; ρ^k is the mass density of the k^{th} layer. For deriving the FE model of the overall plate, the sides of the rectangular plane of the plate are divided to generate the FE mesh using nine-node quadrilateral element where every element is in the shape of the rectangle with the edges in parallel to the in-plane axial directions. It may be noted here that the serendipity (eight nodes) and Lagrange (nine nodes) plate elements are the popular ones for the bending analysis of plates using FE procedure (Cook, 2007). Although both the elements perform well, the Lagrange element (nine nodes) is usually preferred because of its faster convergence towards the accurate values (Dhainaut, 1997). So, presently the nine-node quadrilateral element is utilized. The two different materials within 1-3 VEC layer yield two kinds of elemental stacking sequences in the FE mesh. In the first one, the material for the 1-3 VEC layer ($k=3$) is graphite, and the element is denoted by Element#1. In the other one, the material for the same layer ($k=3$) is the viscoelastic material, and this element is designated by Element#2. The materials of other layers ($k=1,2,4,5$) remain

the same for both the elements (Element#1 and Element#2). The generalized displacement vector ($\boldsymbol{d}$) at any point within an element can be expressed in terms of the shape function matrix ($\boldsymbol{N}$) and the elemental nodal displacement vector ($\boldsymbol{d}^e$) as given in Eq. (6.10)

$$
\begin{gathered}
d = N d^e \,,\;\; d^k = (T_t + Z_r^k T_r) N d^e \,, \\
\boldsymbol{\varepsilon}_{bL} = \boldsymbol{B}_{bL} \boldsymbol{d}^e \,,\;\; \boldsymbol{\kappa}_b = \boldsymbol{B}_{\kappa b} \boldsymbol{d}^e \,, \\
\boldsymbol{\varepsilon}_{sL} = \boldsymbol{B}_{sL} \boldsymbol{d}^e \,,\;\; \boldsymbol{\kappa}_s = \boldsymbol{B}_{\kappa s} \boldsymbol{d}^e \\
\boldsymbol{B}_{bL} = \boldsymbol{L}_{bL} \boldsymbol{T}_t \boldsymbol{N} \,,\;\; \boldsymbol{B}_{\kappa b} = \boldsymbol{L}_{b\kappa} \boldsymbol{T}_r \boldsymbol{N} \,, \\
\boldsymbol{B}_{sL} = \boldsymbol{L}_{sL} \boldsymbol{T}_t \boldsymbol{N} \,,\;\; \boldsymbol{B}_{\kappa s} = \boldsymbol{L}_{s\kappa} \boldsymbol{T}_r \boldsymbol{N}
\end{gathered}
\tag{6.10}
$$

Substituting Eqs. (6.7), (7.5), (6.6a) and (6.10) in Eqs. (7.6) and (7.7), the following simplified expressions for first variations of the total potential energy (δT_p^e) and the total kinetic energy (δT_k^e) for a typical element can be obtained,

$$
\delta T_P^e = \left(\delta \boldsymbol{d}^e\right)^{\mathrm{T}} \left\{ \left(\boldsymbol{K}_b^e + \boldsymbol{K}_s^e\right) \boldsymbol{d}^e - \boldsymbol{P}_E^e V - \boldsymbol{P}_c^e \, p(t) \right\} \,,\;\; \delta T_K^e = \left(\delta \dot{\boldsymbol{d}}^e\right)^{\mathrm{T}} \boldsymbol{M}^e \dot{\boldsymbol{d}}^e \tag{7.8a}
$$

In Eq. (7.8a), various matrices and vectors are as follows,

$$
\begin{gathered}
\boldsymbol{K}_b^e = \int_{A^e} \left[\left(\boldsymbol{B}_{bL}\right)^{\mathrm{T}} \left(\boldsymbol{A}_b \boldsymbol{B}_{bL} + \boldsymbol{B}_{L1} \boldsymbol{B}_{\kappa b}\right) + \left(\boldsymbol{B}_{\kappa b}\right)^{\mathrm{T}} \left(\boldsymbol{B}_{L2} \boldsymbol{B}_{bL} + \boldsymbol{D}_L \boldsymbol{B}_{\kappa b}\right) \right] dA^e \,, \\
\boldsymbol{K}_s^e = \int_{A^e} \left[\left(\boldsymbol{B}_{sL}\right)^{\mathrm{T}} \left(\boldsymbol{A}_s \boldsymbol{B}_{sL} + \boldsymbol{B}_{s1} \boldsymbol{B}_{\kappa s}\right) + \left(\boldsymbol{B}_{ks}\right)^{\mathrm{T}} \left(\boldsymbol{B}_{s2} \boldsymbol{B}_{sL} + \boldsymbol{D}_s \boldsymbol{B}_{\kappa s}\right) \right] dA^e \,, \\
\boldsymbol{P}_E^e = \int_{A^e} \left[\left(\boldsymbol{B}_{bL}\right)^{\mathrm{T}} \boldsymbol{A}_{be} + \left(\boldsymbol{B}_{\kappa b}\right)^{\mathrm{T}} \boldsymbol{B}_{be} \right] dA^e \,, \\
\boldsymbol{P}_c^e = \int_{A^e} \left[\boldsymbol{N}^{\mathrm{T}} \boldsymbol{T}_t^{\mathrm{T}} \{0 \quad 0 \quad 1\}^{\mathrm{T}} \right] dA^e \,, \\
\boldsymbol{M}^e = \int_{A^e} \left[\boldsymbol{N}^{\mathrm{T}} \left\langle (\boldsymbol{T}_t)^{\mathrm{T}} m_1 \boldsymbol{T}_t + (\boldsymbol{T}_t)^{\mathrm{T}} \boldsymbol{m}_2 \boldsymbol{T}_r + (\boldsymbol{T}_r)^{\mathrm{T}} \boldsymbol{m}_3 \boldsymbol{T}_t + (\boldsymbol{T}_r)^{\mathrm{T}} \boldsymbol{m}_4 \boldsymbol{T}_r \right\rangle \boldsymbol{N} \right] dA^e
\end{gathered}
\tag{7.8b}
$$

In Eq. (7.8b), different rigidity matrices, electro-elastic coupling vectors and mass parameters per unit area are given in Eq. (7.8c).

$$
A_b = \sum_{k=1}^{5} \int_{h_k}^{h_{k+1}} C_b^k dz \;\;,\;\; B_{L1} = \sum_{k=1}^{5} \int_{h_k}^{h_{k+1}} C_b^k Z_b^k dz \,,
$$

$$
\boldsymbol{B}_{L2} = \sum_{k=1}^{5} \int_{h_k}^{h_{k+1}} \left(\boldsymbol{Z}_b^k\right)^{\mathrm{T}} \boldsymbol{C}_b^k dz \,,\;\; \boldsymbol{D}_L = \sum_{k=1}^{5} \int_{h_k}^{h_{k+1}} \left(\boldsymbol{Z}_b^k\right)^{\mathrm{T}} \boldsymbol{C}_b^k \boldsymbol{Z}_b^k dz \,,
$$

$$\boldsymbol{A}_s = \sum_{k=1}^{5} \int_{h_k}^{h_{k+1}} \boldsymbol{C}_s^k dz\,,\ \boldsymbol{B}_{s1} = \sum_{k=1}^{5} \int_{h_k}^{h_{k+1}} \boldsymbol{C}_s^k \boldsymbol{Z}_s^k dz\,,$$

$$\boldsymbol{B}_{s2} = \sum_{k=1}^{5} \int_{h_k}^{h_{k+1}} \left(\boldsymbol{Z}_s^k\right)^{\mathrm{T}} \boldsymbol{C}_s^k dz\,,\ \boldsymbol{D}_s = \sum_{k=1}^{5} \int_{h_k}^{h_{k+1}} \left(\boldsymbol{Z}_s^k\right)^{\mathrm{T}} \boldsymbol{C}_s^k \boldsymbol{Z}_s^k dz\,,$$

$$m_1 = \sum_{k=1}^{5} \int_{h_k}^{h_{k+1}} \rho^k dz\,,\ \boldsymbol{m}_2 = \sum_{k=1}^{5} \int_{h_k}^{h_{k+1}} \rho^k \boldsymbol{Z}_r^k dz\,,$$

$$\boldsymbol{m}_3 = \sum_{k=1}^{5} \int_{h_k}^{h_{k+1}} \left(\boldsymbol{Z}_r^k\right)^{\mathrm{T}} \rho^k dz\,, \boldsymbol{m}_4 = \sum_{k=1}^{5} \int_{h_k}^{h_{k+1}} \left(\boldsymbol{Z}_r^k\right)^{\mathrm{T}} \rho^k \boldsymbol{Z}_r^k dz\,,$$

$$\boldsymbol{A}_{be} = \int_{h_k}^{h_{k+1}} \left\langle \boldsymbol{e}_b^k (1/h_c) \right\rangle_{k=5} dz\,,\ \boldsymbol{B}_{be} = \int_{h_k}^{h_{k+1}} \left\langle \left(\boldsymbol{Z}_b^k\right)^{\mathrm{T}} \boldsymbol{e}_b^k (1/h_c) \right\rangle_{k=5} dz \qquad (7.8c)$$

Introducing Eq. (7.8a) in the extended Hamilton's principle (Eq. (2.11)), the elemental governing equations of motion can be obtained as given in Eq. (7.9).

$$\int_{t_1}^{t_2} \left(\delta T_K - \delta T_P\right) dt = 0 \qquad (2.11)$$

$$\boldsymbol{M}^e \ddot{\boldsymbol{d}}^e + \left(\boldsymbol{K}_b^e + \boldsymbol{K}_s^e\right)\boldsymbol{d}^e = \boldsymbol{P}_E^e V + \boldsymbol{P}_c^e\, p(t) \qquad (7.9)$$

Assembling the elemental equations (Eq. (7.9)), the following global equations of motion of the overall plate can be obtained,

$$\boldsymbol{M}\ddot{\boldsymbol{X}} + \left(\boldsymbol{K}_b + \boldsymbol{K}_s\right)\boldsymbol{X} = \boldsymbol{P}_E V + \boldsymbol{P}_c\, p(t) \qquad (7.10)$$

where, $\boldsymbol{M}$ is the global mass matrix; $\boldsymbol{K}_b$ and $\boldsymbol{K}_s$ are the bending and transverse shear counterparts of the global stiffness matrix; $\boldsymbol{P}_E$ is the global nodal electro-elastic coefficient vector; $\boldsymbol{P}_c$ is the global nodal mechanical load coefficient vector; $\boldsymbol{X}$ is the global nodal displacement vector.

The piezoelectric constraining layer is activated by taking the feedback of transverse velocity ($\dot{w}_s$) at the middle point on the top surface of the overall plate. This transverse velocity ($\dot{w}_s$) is fed back in the form of voltage (V) across the top and bottom surface-electrodes of the piezoelectric constraining layer as,

$$V = -k_d \dot{w}_s \qquad (7.11)$$

where, k_d is the velocity feedback control-gain. It would be noted here that the present analysis of damping in the overall plate is carried out considering its (overall plate) fundamental bending mode of vibration. As the maximum

magnitude of the corresponding transverse velocity ($\dot{w}_s$) appears at the middle point of the plate, the feedback of transverse velocity is taken at the same point. Equation (7.11) can also be expressed in terms of the global nodal velocity vector ($\dot{\boldsymbol{X}}$) through a transformation vector ($\boldsymbol{N}_T$) as follows,

$$\dot{w}_s = \boldsymbol{N}_T \dot{\boldsymbol{X}} \tag{7.12}$$

Introducing Eqs. (7.11) and (7.12) in Eq. (7.10), the following equation can be obtained,

$$\boldsymbol{M}\ddot{\boldsymbol{X}} + \boldsymbol{C}\dot{\boldsymbol{X}} + \left(\boldsymbol{K}_b + \boldsymbol{K}_s\right)\boldsymbol{X} = \boldsymbol{P}_c\, p(t),\ \boldsymbol{C} = \boldsymbol{P}_E k_d \boldsymbol{N}_T \tag{7.13}$$

Equation (7.13) represents the FE equations of motion of the overall plate under a uniformly distributed transverse harmonic load. This harmonic load is considered as, $p(t) = p_0 e^{j\omega t}$ ($j = \sqrt{-1}$), where p_0 and ω are the load-amplitude and operating frequency, respectively. The corresponding solution of Eq. (7.13) for the linear steady state vibration of the overall plate may be written as (Meirovitch, 1997), $X = \bar{X} e^{j\omega t}$ where $\bar{X}$ is a complex nodal displacement vector. The absolute value of $\bar{X}$ provides the nodal displacement-amplitude vector. Substituting this solution into Eq. (7.13), the governing equations of motion can be reduced as,

$$\left[-\omega^2 \boldsymbol{M} + j\omega \boldsymbol{C} + \left(\boldsymbol{K}_b^R + \boldsymbol{K}_s^R\right) + j\left(\boldsymbol{K}_b^I + \boldsymbol{K}_s^I\right)\right]\bar{\boldsymbol{X}} = \boldsymbol{P}_c p_0 \tag{7.14}$$

where, the superscripts R and I indicate the real and imaginary counterparts of a complex quantity.

7.3 Estimation of active-passive damping in the overall plate

For the free vibration of the overall plate ($p_0 = 0$), Eq. (7.14) represents a complex quadratic eigenvalue problem as follows,

$$\left\langle (\boldsymbol{K}_b^R + \boldsymbol{K}_s^R) + j(\boldsymbol{K}_b^I + \boldsymbol{K}_s^I + \omega \boldsymbol{C}) \right\rangle \boldsymbol{\psi}_i = \omega_i^2 \boldsymbol{M} \boldsymbol{\psi}_i \tag{7.15}$$

where, $\boldsymbol{\psi}_i$ is the complex nodal displacement vector for i^{th} natural mode having the complex natural frequency of ω_i. This complex natural frequency can be expressed in terms of the natural frequency (ω_i^0) of the overall plate and the modal loss factor (η_i) as given in Eq. (3.29).

$$(\omega_i)^2 = (\omega_i^0)^2 \langle 1 + j\eta_i \rangle,\ \eta_i = Im(\omega_i)^2 / Re(\omega_i)^2 \tag{3.29}$$

Now, if one assumes $\boldsymbol{K}_s^I = \mathbf{0}$ and $\boldsymbol{K}_b^I = \mathbf{0}$, the corresponding modal loss factor (η_i) would appear due to the active damping in the overall plate, and it arises due to the modelling of the piezoelectric actuation force in the form of viscous damping force. Along with this active damping, the passive damping due to the transverse shear strains of the viscoelastic phase in the constrained 0-3 VEC layer can be accounted by assuming, $\boldsymbol{K}_s^I \neq \mathbf{0}$ and $\boldsymbol{K}_b^I = \mathbf{0}$. The corresponding modal loss factor is presently denoted by, η_s. Similarly, for the assumptions of $\boldsymbol{K}_s^I = \mathbf{0}$ and $\boldsymbol{K}_b^I \neq \mathbf{0}$, the passive counterpart of the total active-passive damping in the overall plate appears due to the in-plane strains of the viscoelastic phase of the constrained 0-3 VEC layer. Without any of the aforesaid assumptions, the modal loss factor (η) indicates the total active-passive damping in the overall plate. The difference between η and η_s means the contributions of in-plane strains of the viscoelastic phase of 0-3 VEC layer to the total active-passive damping in the overall plate. In order to determine these modal loss factors (η, η_s), the complex quadratic eigenvalue problem (Eq. (7.15)) is presently solved using direct iteration method by writing the equation as follows,

$$\left\langle (\boldsymbol{K}_b^R + \boldsymbol{K}_s^R) + j(\boldsymbol{K}_b^I + \boldsymbol{K}_s^I + \boldsymbol{C}\omega_i^{prev}) \right\rangle \boldsymbol{\psi}_i = \left(\omega_i^{curr}\right)^2 \boldsymbol{M}\boldsymbol{\psi}_i \qquad (7.16)$$

In Eq. (7.16), the superscripts *prev* and *curr* indicate the values of ω_i corresponding to the previous and current iterations, respectively. The iteration starts with $\omega_i^{prev} = 0$. In every iteration, a complex linear eigenvalue problem is solved for ω_i^{curr} with an assigned value of ω_i^{prev} obtained from the previous iteration. If the value of ω_i^{curr} becomes in well agreement with the value of ω_i^{prev} according to convergence criteria, the iteration is terminated with the solution as, $\omega_i^{curr} = \omega_i^{prev} = \omega_i$.

7.4 Results and discussions

In this section, the numerical results are presented for investigating the active-passive damping characteristics of the overall plate particularly for the inclusions of rectangular graphite-wafers within the actively constrained viscoelastic layer. The geometrical properties of the substrate plate and the constraining layer are considered as, a = 0.4 m, b = 0.4 m, h = 4 mm, h_c = 0.25

mm. The material for the substrate plate is considered as Aluminum ($E = 69$ GPa, $\nu = 0.3$, $\rho = 2740$ kg/m^3), while the graphite-wafers within the constrained layer possess the properties of, $E = 250$ GPa, $\nu = 0.3$, $\rho = 1400$ kg/m^3 (Jones, 1999). The piezoelectric constraining layer is made of PZT-5H (Smith and Auld, 1991) having the properties of, $C_{11} = 151$ GPa, $C_{12} = 98$ GPa, $C_{13} = 96$ GPa, $C_{33} = 124$ GPa, $C_{44} = 24$ GPa, $\rho = 7500$ kg/m^3, $e_{31} = -5.1$ C/m^2, $e_{33} = 27$ C/m^2, $e_{15} = 17$ C/m^2. The viscoelastic material in the 0-3 VEC layer or for the pure viscoelastic layer is considered as Butyl Rubber (Jones, 2001). The properties of this viscoelastic material change with the operating frequency and temperature. The present analysis is carried out at a temperature of 35^o C, and the damping characteristics of the overall plate are investigated at an eigen frequency of fundamental bending mode of vibration the plate. Also, the frequency responses of the overall plate are evaluated within a narrow frequency-range around the eigen frequency of fundamental bending mode of vibration of the plate. As it is observed that the properties of the viscoelastic material (Butyl Rubber (Jones, 2001)) do not vary in significant manner within this narrow frequency-range, average properties of the viscoelastic material within the same frequency-range are considered as, $E = 15(1+0.6j)$ MPa, $\nu = 0.49$, $\rho = 920$ kg/m^3. Although the consideration of varied properties of the viscoelastic material would yield more practical results, the assumption of constant properties of the viscoelastic material may be made for the analysis at an eigen frequency of a mode of vibration of the plate as the similar considerations are reported in the review reports on the ACLD treatment (Benjeddou, 2001; Trindade and Benjeddou, 2002). The boundary edges of the overall plate are considered as the simply-supported edges ($v_0 = 0$, $w_0 = 0$, $\beta_i = 0$ at $x = 0$ and a; $u_0 = 0$, $w_0 = 0$, $\alpha_i = 0$ at $y = 0$ and b).

In order to achieve sufficient numerical accuracy in the present FE results, an FE mesh-convergence study is performed where the fundamental natural frequency of the overall plate is computed by increasing the number of rectangular elements. The corresponding results are illustrated in Table 7.1. Table 7.1 indicates the minimum number of elements in the FE mesh of the overall plate for sufficient accuracy in the numerical results. So, the FE mesh of the plate is decided following this study for evaluation of further numerical results.

The present FE formulation is verified considering passively ($V = 0$) constrained pure viscoelastic layer since the results for the present 0-3 VEC layer are not available in the literature. The first four natural frequencies of the overall plate are evaluated, and these results are compared with the similar results available in (Lall et al., 1987). This comparison is illustrated in Table 7.2.

Table 7.1 FE mesh-convergence study (ω_o : fundamental natural frequency in rad/s, N_e^{FE} : number of rectangular elements).

N_e^{FE}	121	256	441	676	961	1296	1681
ω_o	142.234	140.528	140.476	140.467	140.463	140.460	140.458

Table 7.2 Verification of the present FE formulation (m and n are the natural mode numbers along x and y directions, respectively).

Natural mode (m,n)	Natural frequency (rad/s)	
	Ref. (Lall et al., 1987)	Present
(1,1)	975	974.7
(1,2)	2350.83	2348
(2,1)	2350.83	2348
(2,2)	3725.6	3718.2

It may be observed from Table 7.2 that the present FE results are in good agreement with the similar results in (Lall et al., 1987) thus verifying the present FE formulation. In order to verify the present FE formulation for modelling the electro-elastic coupling in the piezoelectric layer, the damping layer is considered to have a negligibly small thickness ($h_d \approx 0$) so that the overall plate is comprised of the substrate plate and a piezoelectric layer. This smart plate is supposed to be subjected to a transverse point-load of 200 N at the middle point over its (smart plate) bottom surface in the presence of an external voltage (V) across the thickness of the piezoelectric layer. The corresponding transverse deflection at the point of loading is evaluated by developing an FE model of the smart plate in the ANSYS software. The SOLID186 and SOLID226 elements are utilized for discretization of the volumes of substrate plate and piezoelectric layer, respectively. A mesh convergence study is first carried out to obtain the minimum number of elements of the FE model for sufficient numerical accuracy in the results, and it (minimum number of elements) is obtained as 1682.

Subsequently, the transverse deflection (w_o) at the point of loading is computed in the ANSYS software for different values of the applied voltage (V). Similar results are also calculated using the present FE model of the smart plate, and these results are illustrated in Table 7.3 together with the ANSYS results. It may be observed from Table 7.3 that the present FE results are in good agreement with the similar results obtained from the analysis of the smart plate in ANSYS software. This comparison (Table 7.3) verifies the present FE formulation for handling the electro-elastic coupling in the piezoelectric layer.

Table 7.3 Verification of the present FE formulation for modelling the electro-elastic coupling in the piezoelectric actuator layer.

V (volts)	w_o (m×1e-4)	
	ANSYS	Present FEM
100	7.661	7.575
200	7.401	7.320
400	6.952	6.809
800	6.054	5.788

Table 7.4 Verification of the present iterative procedure for solving the complex quadratic eigenvalue problem (η_{iter} : modal loss factor estimated by the present iterative procedure; η_{resp} : modal loss factor determined by half-power bandwidth method).

	VEM		0-3 VEC	
k_d	η_{resp}	η_{iter}	η_{resp}	η_{iter}
0	0.014	0.014	0.062	0.0619
100	0.1152	0.115	0.0149	0.1488
200	0.219	0.2179	0.2394	0.2379

In order to verify the present iterative procedure for the solution of the complex quadratic eigenvalue problem (Eq. (7.15)), the overall plate is considered to operate under a transverse harmonic load. The corresponding variation of the transverse displacement-amplitude at the middle point over the bottom surface of the overall plate is evaluated within a frequency-range around the fundamental natural frequency. This frequency response of the overall plate is utilized to estimate its (plate) modal loss factor at the fundamental bending mode using the half-power bandwidth method (ASTM, 2010). The modal loss factor at the fundamental bending mode of the overall plate is also evaluated through the solution of the quadratic eigenvalue problem (Eq. (7.15)) using the

present iterative procedure. These results are illustrated in Table 7.4, and it may be observed from this table that the results obtained from the iterative procedure are in good agreement with the similar results obtained from the half-power bandwidth method. This comparison verifies the present iterative procedure for solving the complex quadratic eigenvalue problem (Eq. (7.15)).

7.4.1 Distributions of strains in the actively constrained damping layer

In this section, a bending analysis of the overall plate is performed to study the distributions of transverse shear and in-plane strains within the actively constrained 0-3 VEC layer. Mainly, the changes in the characteristics of the strains within the constrained viscoelastic layer are identified due to the inclusions of the graphite-wafers. The geometrical properties of the overall plate are considered as, $h = 4$ mm, $a = b = 400$ mm, $h_c = 0.25$mm, $h_d = 1$ mm, $n_x = n_y = 4$, $\Delta_x = \Delta_y = 10$ mm, $h_v = 0.3$ *mm*, $h_m = 0.4$ *mm*. The piezoelectric constraining layer is activated by supplying a voltage of 100 volts across its top and bottom fully electrode-surfaces, while a transverse point-load of 100 N is applied at the middle point on the underside surface of the overall plate. The strains in the actively constrained damping layer are illustrated considering its two different planes. The first plane is a xy-plane through the viscoelastic phase of the 0-3 VEC layer over the top surface of the middle 1-3 VEC layer (Fig. 6.1(a) and Fig. 7.1). A schematic diagram of the top surface of the 1-3 VEC layer is shown in Fig. 7.2(a).

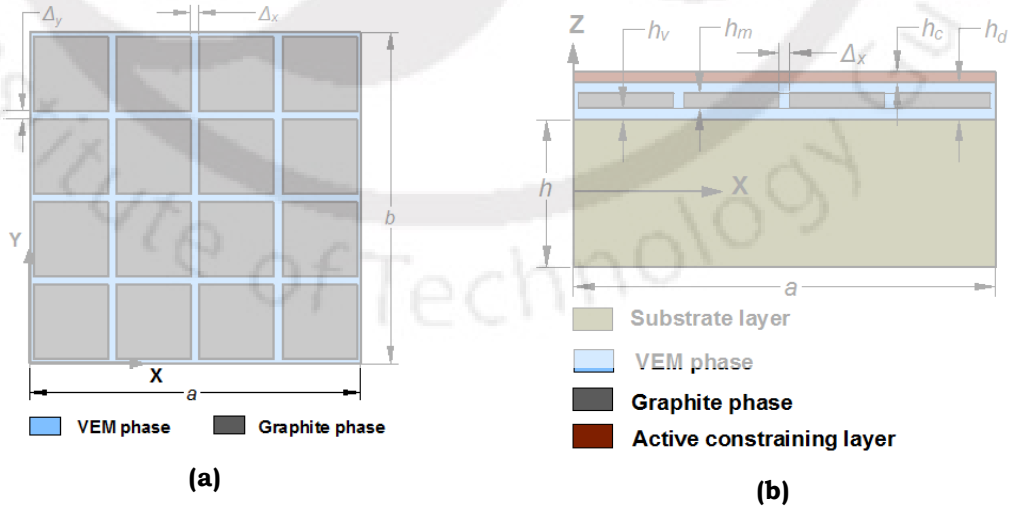

Fig. 7.2. (a) The top surface of the 1-3 VEC layer within the 0-3 VEC layer and (b) a xz-plane through the middle points of a row of the rectangular graphite-wafers.

The second plane is taken as a xz-plane through the middle points of a row of rectangular graphite-wafers. The distribution of different materials over this xz-plane is shown in Fig. 7.2(b). For the bending deformation of the overall plate under the transverse point-load and the activated piezoelectric constraining layer, the distributions of the in-plane strains $(\varepsilon_x, \gamma_{xy})$ on the aforesaid xy-plane are shown in Figs. 7.3(a)-(b). Similar results in the absence of the inclusions within the constrained viscoelastic layer are also shown in Figs. 7.3(c)-(d).

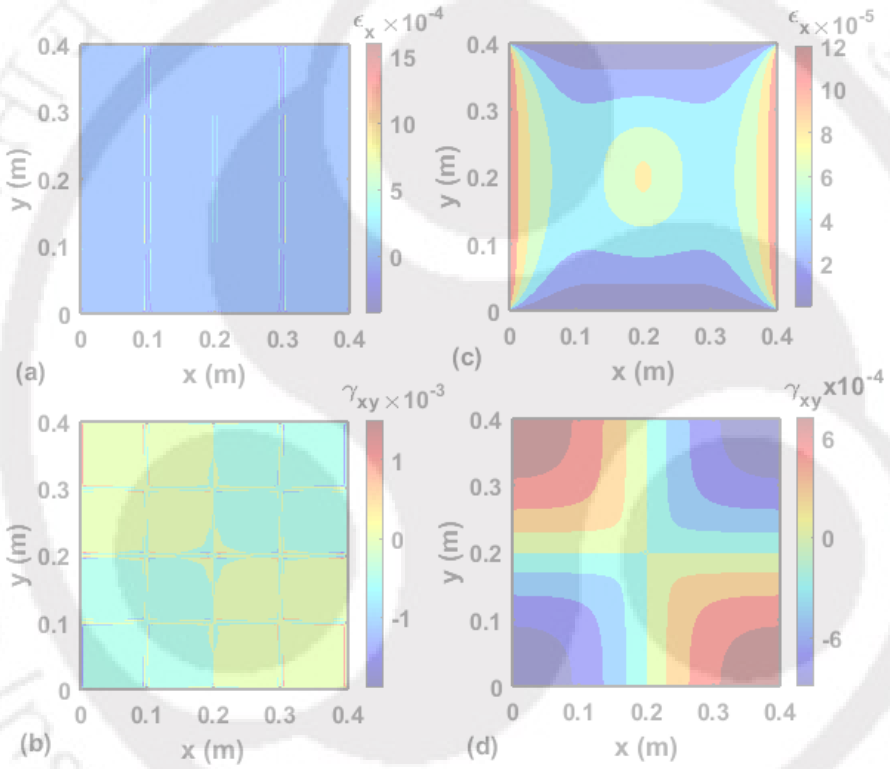

Fig. 7.3. Distributions of the in-plane (a) extensional strain (ε_x) and (b) shear strain (γ_{xy}) over a xy-plane through the viscoelastic phase above the top surface (Fig. 7.2(a)) of the middle 1-3 VEC layer; (c)-(d) distributions of the strains $(\varepsilon_x, \gamma_{xy})$ on the same xy-plane in the absence of the graphite-wafers within the actively constrained viscoelastic layer.

The distributions of the transverse shear and normal strains $(\varepsilon_x, \gamma_{xz})$ on the aforesaid xz-plane are demonstrated in Figs. 7.4(a)-(b). Similar distributions of the strains $(\varepsilon_x, \gamma_{xz})$ for the absence of the inclusions within the constrained viscoelastic layer are also illustrated in Figs. 7.4(c)-(d). It may be observed from Figs. 7.3(a), 7.3(c), 7.4(a) and 7.4(c) that the maximum magnitude of the in-

plane axial strain (ε_x) in the viscoelastic phase increases indicatively due to the inclusion of graphite-wafers and this improved magnitude appears at the axial gap between any two consecutive graphite-wafers. The maximum magnitude of the in-plane shear strain (γ_{xy}, Figs. 7.3(b) and 7.3(d)) also increases for the inclusions of graphite-wafers. It may also be observed from Figs. 7.4(b) and 7.4(d)) that the maximum magnitude of the transverse shear strain (γ_{xz}) in the viscoelastic phase increases for the inclusions of graphite-wafers. This improved magnitude of the shear strain (γ_{xz}) appears at the top and bottom viscoelastic layers within the 0-3 VEC layer (Figs. 7.1 and 7.2(b)).

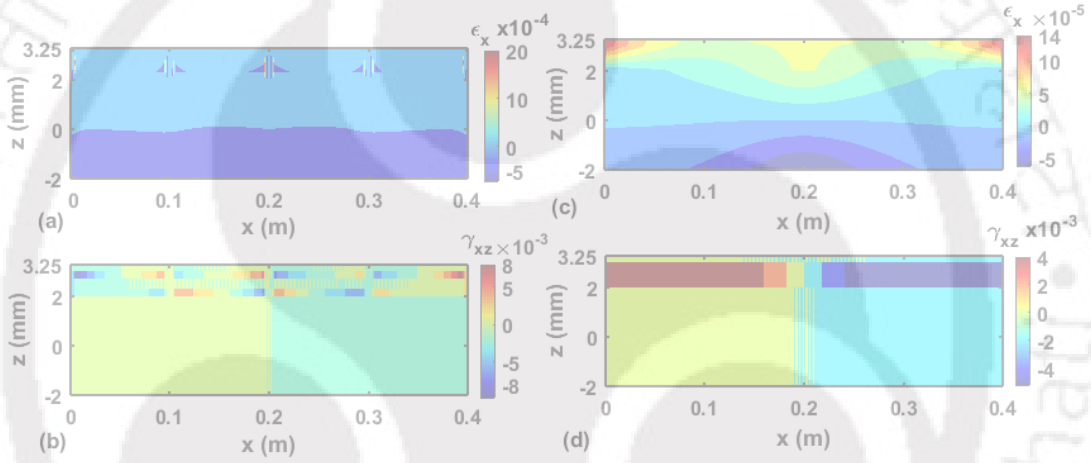

Fig. 7.4. Distributions of the (a) normal strain (ε_x) and (b) shear strain (γ_{xz}) over the xz-plane (Fig. 7.2(b)); (c)-(d) distributions of the strains ($\varepsilon_x, \gamma_{xz}$) over the same xz-plane in the absence of the graphite-wafers.

It should be noted here that the characteristics of the strains ε_y and γ_{yz} are similar to those for ε_x and γ_{xz}, respectively since the bending deformation of the overall plate is symmetric with respect to the xz / yz plane through the middle point of the substrate plate. Similar to the previous results (Figs. (6.4) and (6.5)), Figs. 7.3 and 7.4 indicate that the maximum magnitudes of the strains in the actively constrained viscoelastic layer increase indicatively due to the insertion of an array of graphite-wafers. These improved magnitudes of the strains are supposed to enhance the active-passive damping in the overall plate, and it (damping) is quantified through the dynamic analysis of the overall plate in the following sections.

7.4.2 Active-passive damping characteristics of the overall plate

In this section, the active-passive damping characteristics of the overall plate are investigated by computing the modal loss factor at its (overall plate) fundamental bending mode of vibration. The piezoelectric actuation force is modelled as an active damping force through the velocity feedback control strategy. In addition to this active damping, the passive damping in the overall plate arises due to the mechanical strains of the viscoelastic phase within the 0-3 VEC layer. For the analysis of this total active-passive damping in the overall plate, the modal loss factors (η_s and η) are computed by solving the complex quadratic eigenvalue problem (Eq. (7.15)) as the corresponding procedure is illustrated in the forgoing section. Figure 7.5 shows the variations of the loss factors (η, η_s) with the thickness (h_v) of the viscoelastic phase over the top and bottom surfaces of the middle 1-3 VEC layer within the constrained 0-3 VEC layer (Fig. 7.1). The thickness (h_v) is varied in a ratio of (h_v / h_d) where the constrained layer is taken with a constant thickness (h_d). The velocity feedback control-gain (k_d) and the other geometrical properties of the 0-3 VEC layer are taken as, $k_d = 100$, $n_x = n_y = 6$, $\Delta_x = \Delta_y = 100$ μm. In the case of the pure viscoelastic (VEM) layer, the variation of h_v or h_v / h_d does not cause any change in the geometric configuration of the material for the constrained damping layer. So, the magnitudes of the loss factors (η, η_s) do not vary with the thickness (h_v) (Fig. 7.5).

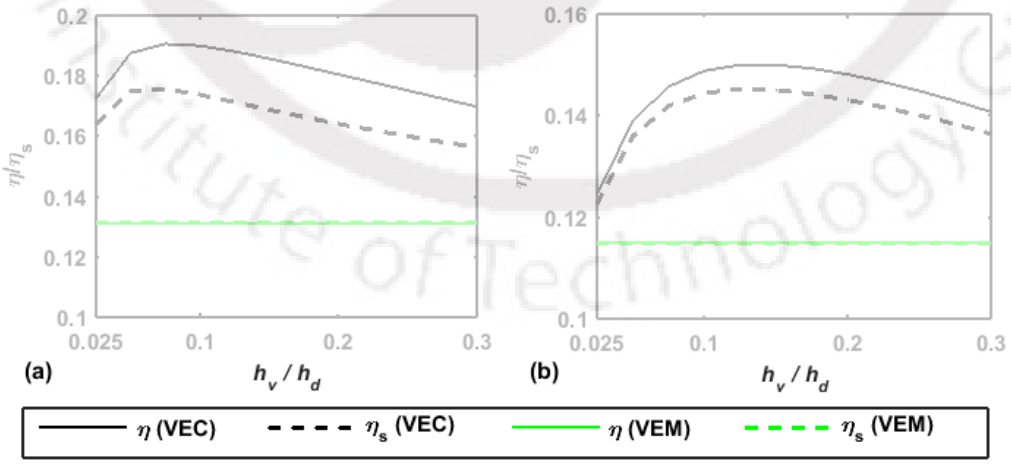

Fig. 7.5. Variations of the modal loss factors (η, η_s) with the thickness (h_v) of the viscoelastic phase over the top/bottom surface of the 1-3 VEC layer within the 0-3 VEC layer, (a) $h_d = 1$ mm and (b) $h_d = 0.5$ mm.

It may also be observed from Fig. 7.5 that the magnitudes of the modal loss factors (η, η_s) increase significantly when the conventional VEM layer is replaced by the present 0-3 VEC layer. It is important to observe that there is no difference between the magnitudes of η and η_s for the pure VEM layer. But, this difference appears significantly for the present 0-3 VEC layer. So, the in-plane strains in the actively constrained VEM layer have no contribution to the damping in the overall plate. But, it appears indicatively for the present 0-3 VEC layer. Figure 7.5 infers augmented active-passive damping in the overall plate due to the replacement of the conventional pure viscoelastic layer by the present 0-3 VEC layer. This augmented active-passive damping appears not only due to the enhanced transverse shear deformation of the damping layer but also due to its (damping layer) reasonable in-plane strains.

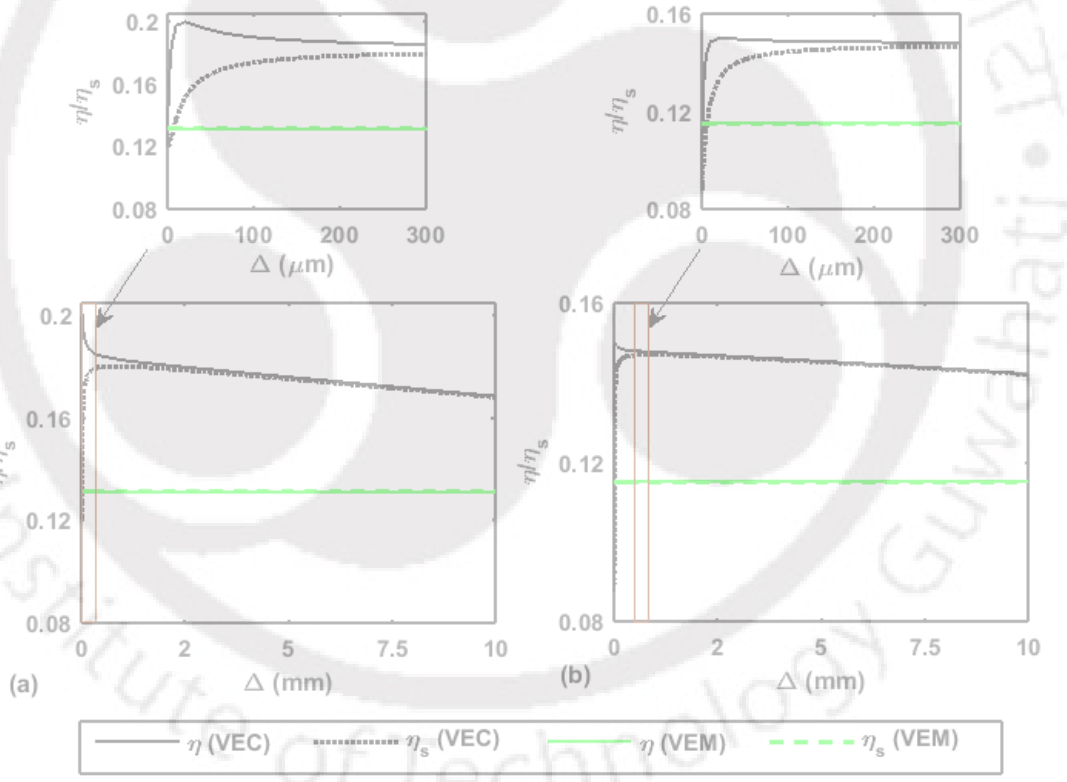

Fig. 7.6. Variations of the modal loss factors (η, η_s) with the in-plane axial gap ($\Delta_x = \Delta_y = \Delta$) between any two consecutive rectangular graphite-wafers, (a) h_d = 1 mm and (b) h_d = 0.5 mm.

Figure 7.6 illustrates the variations of the modal loss factors (η, η_s) with the in-plane axial gap (Δ_x / Δ_y) between any two consecutive rectangular

graphite-wafers. The rectangular graphite-wafers are considered to be spaced uniformly ($\Delta_x = \Delta_y = \Delta$) in both the in-plane axial directions, and this gap (Δ) is increased gradually so that the size of the rectangular wafers decreases. The thickness-ratio (h_v / h_d) is chosen from the previous result (Fig. 7.5) as 0.1, while the same values of the control-gain and other geometric properties of the 0-3 VEC layer are retained as those were considered in the previous result (Fig. 7.5). It may be observed from Fig. 7.6 that the active-passive damping in the plate increases significantly when the graphite layer ($\Delta = 0$) is divided in the form of an array of rectangular graphite-wafers ($\Delta \neq 0$). It may also be observed that the transverse gap between the curves for η and η_s decreases with the increasing gap (Δ), while the total damping (η) in the overall plate is also decreasing. Thus, the rectangular array of graphite-wafers is to be used instead of a graphite layer for the augmented damping in the overall plate. But, the graphite-wafers are to be spaced with a sufficiently small gap (Δ) that may be decided in an optimal manner.

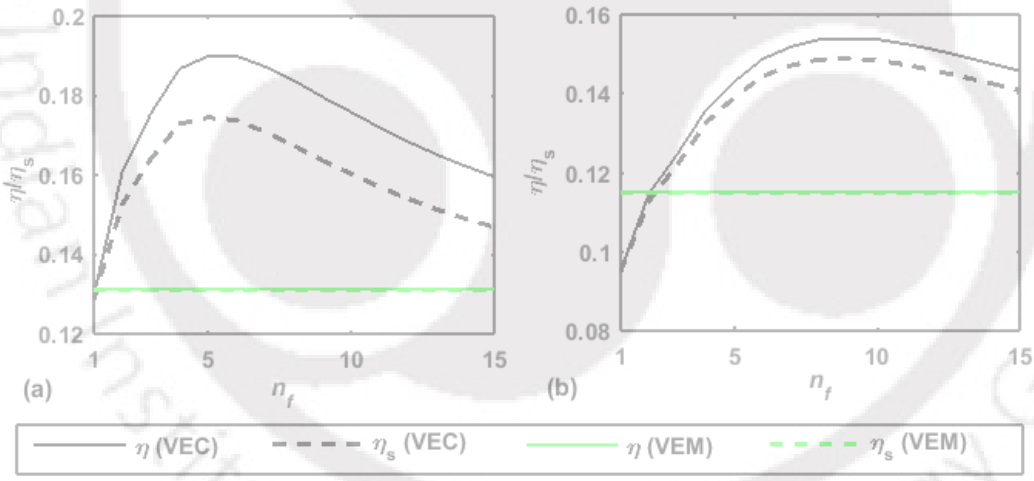

Fig. 7.7. Variations of the modal loss factors (η, η_s) with the number of graphite-wafers ($n_x = n_y = n_f$) within the constrained damping layer, (a) $h_d = 1$ mm and (b) $h_d = 0.5$ mm.

Figure 7.7 illustrates the variations of the modal loss factors (η, η_s) with the number (n_x / n_y) of graphite-wafers along the in-plane axial direction. A square array ($n_x = n_y = n_f$) of the graphite-wafers is considered with a gap ($\Delta_x = \Delta_y = \Delta$) of 100 μm. The values of the control-gain and the other geometric

parameters of the overall plate are not altered from those for the previous result (Fig. 7.6). It may be observed from Fig. 7.7 that the active-passive damping in the overall plate first increases and then decreases as the number (n_f) of graphite-wafers increases from 1. This result indicates an optimal number of graphite-wafers for achieving maximum damping in the overall plate.

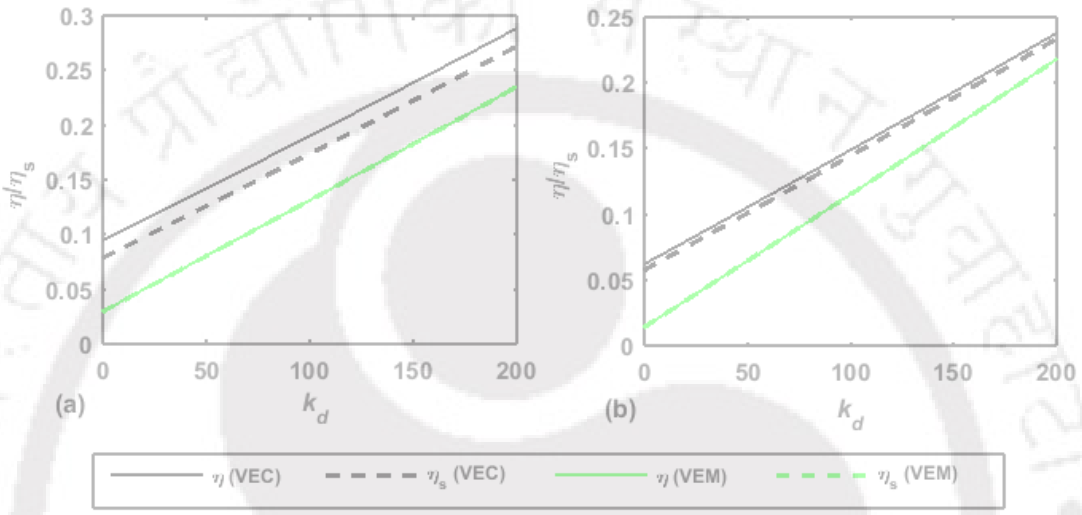

Fig. 7.8. Variations of the modal loss factors (η, η_s) with the velocity feedback control-gain (k_d), (a) $h_d = 1$ mm and (b) $h_d = 0.5$ mm.

Figure 7.8 illustrates the variations of the modal loss factors (η, η_s) with the velocity feedback control-gain (k_d) when the constrained damping layer is made of a pure viscoelastic material or 0-3 VEC. The geometrical properties of the 0-3 VEC layer are considered as, $n_x = n_y = 6$, $\Delta_x = \Delta_y = 100$ μm and h_v / h_d =0.1. It may be observed from Fig. 7.8 that the active-passive damping in the overall plate increases linearly with the increasing value of the control-gain (k_d). But, the rate of change of damping with the increasing control-gain is lesser for the 0-3 VEC layer than that for the pure viscoelastic layer. So, at a high value of the velocity feedback control-gain (k_d), the damping in the overall plate may not improve indicatively for the use of 0-3 VEC layer instead of the pure viscoelastic layer particularly when the damping layer is of small thickness (h_d).

7.4.3 Optimized configuration of the actively constrained 0-3 VEC layer

Figures 7.5-7.7 indicate that the damping capacity of the actively constrained 0-3 VEC layer indicatively depends on its geometric parameters like h_v / h_d, Δ_x, Δ_y,

n_x and n_y. So, these geometric parameters would be configured in an optimal manner for achieving the maximum damping capability of the 0-3 VEC layer. This optimal configuration of the 0-3 VEC layer is decided in this section by maximizing the modal loss factor (η) at the fundamental mode of vibration with respect the geometric parameters ($h_v/h_d, \Delta, n_f$). For the fundamental bending mode shape of the rectangular plate, it (plate) deforms symmetrically with respect to the xz/yz plane through its middle point. So, the geometric parameters are reduced as, $\Delta_x = \Delta_y = \Delta$ and $n_x = n_y = n_f$, and the modal loss factor (η) is taken as the objective functions of the geometric parameters as, h_v/h_d, Δ and n_f. As per the present FE formulation for the complex quadratic eigenvalue problem, the exhaustive search method (Deb, 2012) is utilized to find the maximum value of the modal loss factor (η) with respect to the geometric parameters ($h_v/h_d, \Delta, n_f$). The exhaustive search method is implemented following the procedure as that is presented in the section 6.4.2. The bounds of the geometric parameters ($h_v/h_d, \Delta, n_f$) are obtained from the previous results (Figs. 7.5-7.7) as, $1 \le n_f \le 15$, $0 \le \Delta \le 300\,\mu m$, $0.05 \le (h_v/h_d) \le 0.3$ for h_d =1 mm and $1 \le n_f \le 18$, $0 \le \Delta \le 300\,\mu m$, $0.05 \le (h_v/h_d) \le 0.3$ for h_d =0.5 mm. Within these bounds of the three parameters ($h_v/h_d, \Delta, n_f$), a three-dimensional grid is generated, and the values of the modal loss factor (η) are computed at every grid point by solving the complex quadratic eigenvalue problem (Eq. (7.15)). The corresponding results are plotted in Fig. 7.9 which represents the contour of the modal loss factor (η) within the bounds of the parameters ($h_v/h_d, \Delta, n_f$).

It may be observed from this figure that the magnitude of the modal loss factor increases with the decrease of the gap (Δ) for any set of the values of other parameters (h_v/h_d, n_f). But, this gap (Δ) would not be removed ($\Delta = 0$) as the corresponding results show an indicative reduction of the magnitude of the modal loss factor (η). According to the results in Fig. 7.9 or Fig. 7.6, a very small gap (Δ) is required as the similar observation was also obtained in the previous case (Fig. 6.10). As a very small gap may cause the difficulties in fabrication of the 0-3 VEC layer, presently a value for the gap (Δ) in the constrained 0-3 VEC

layer of ACLD treatment is chosen as 100 μm. At this value of the gap (Δ=100 μm), the maximum magnitude of the modal loss factor is bracketed by the other parameters ($h_v / h_d, n_f$) as, $0.01 \le (h_v / h_d) \le 0.2$, $1 \le n_f \le 18$ for h_d = 0.5 mm and $0.01 \le (h_v / h_d) \le 0.2$, $1 \le n_f \le 15$ for h_d =1 mm. Within these bounds of the parameters (h_v / h_d, n_f) for every thickness (h_d = 0.5 mm or 1 mm) of the constrained 0-3 VEC layer, two-dimensional grid points are generated, and the same procedure is followed to plot the contour of the modal loss factor as shown in Fig. 7.10.

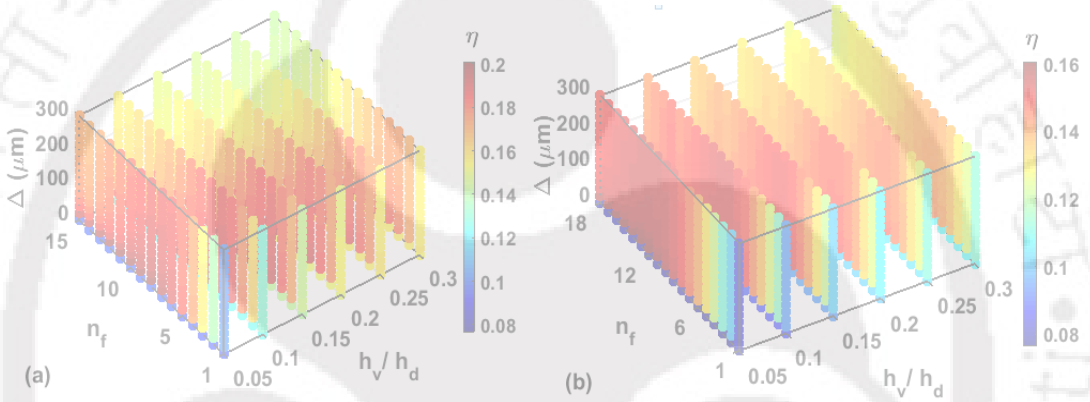

Fig 7.9. The contour of modal loss factor (η) in a three-dimensional domain of the geometric parameters (h_v / h_d, Δ, n_f), (a) h_d =1 mm or (b) h_d =0.5 mm (k_d =100).

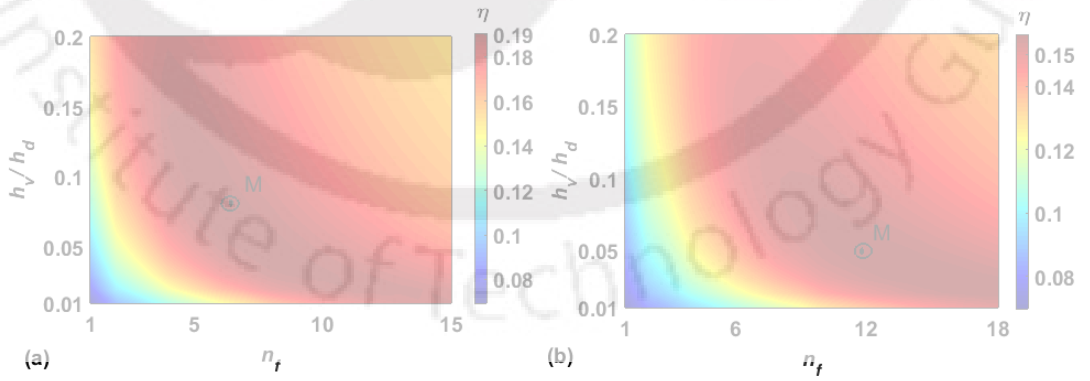

Fig 7.10. The contour of modal loss factor (η) in a two-dimensional domain of the geometric parameters (h_v / h_d, n_f), (a) h_d =1 mm or (b) h_d =0.5 mm (Δ = 50 μm, k_d =100) (M is the point for maximum magnitude of η).

From these contours of the modal loss factor, its maximum magnitude is identified for every thickness of the constrained 0-3 VEC layer, and the corresponding values of the geometric parameters are taken as their optimal values. These optimal values of the parameters are obtained as, $h_v / h_d = 0.05$, $n_f = 12$, $\Delta = 100\ \mu m$ for $h_d = 0.5$ mm and $h_v / h_d = 0.08$, $n_f = 6$, $\Delta = 100\ \mu m$ for $h_d = 1$ mm.

7.4.4 Controlled frequency responses of the overall plate

The actively constrained 0-3 VEC layer within the overall plate is configured with the optimal values of its (0-3 VEC) geometric parameters, and the forced frequency responses of the overall plate are evaluated within a range of the operating frequency of the uniformly distributed transverse harmonic load around the fundamental natural frequency. These results are presented in Fig. 7.11. Figures 7.11(a) and 7.11(b) illustrate the variations of the transverse displacement-amplitude at the middle point of the overall plate and the corresponding required control-voltage, respectively for two different values of the thickness (h_d) of the constrained damping layer.

Figure 7.11 also contains similar responses of the overall plate for the pure viscoelastic layer (without inclusions of graphite-wafers). For any thickness (h_d) of the damping layer, it may be observed from this figure that the attenuation of the vibration-amplitude increases significantly when the traditional pure viscoelastic layer is replaced by the 0-3 VEC layer. This improved attenuation of the vibration-amplitude also appears with less control-voltage. Also, the attenuation of vibration-amplitude increases for a higher thickness of the 0-3 VEC layer. So, 0-3 VEC layer would always be preferred with a high thickness whenever it is allowed as per the design requirements. In order to verify the change in the active action of the piezoelectric layer due to the inclusion of graphite wafers, the loss factor of the viscoelastic phase of the VEC layer is taken with zero value. Then, the frequency responses of the plate are evaluated with and without considering the graphite wafers within the constrained viscoelastic layer as shown in Figs. 7.11(c) and 7.11(d). It may be observed from this figure that the attenuation of transverse displacement-amplitude increases as the graphite wafers are provided within the viscoelastic layer. This may be due to the fact that the inclusion of graphite wafers causes higher effective stiffness of the constrained viscoelastic layer. This increased

stiffness of the constrained viscoelastic layer causes enhanced transfer of active action of the piezoelectric constraining layer to the substrate plate resulting in improved attenuation of its (plate) transverse displacement-amplitude.

These results (Fig. 7.11) suggest 0-3 VEC layer instead of the traditional viscoelastic layer for the improved active-passive control of vibration of plates at the expense of less control-voltage. But, this 0-3 VEC layer is to be taken with its appropriate geometric configuration within the allowable thickness for the constrained damping layer. It may be noted here that the replacement of VEM layer by the 0-3 VEC layer causes an increase of weight of the overall structure since the density of the graphite-wafers is more than that of the viscoelastic phase. The inclusion of graphite wafers also causes the change of natural frequencies of the overall plate. Additionally, the cost of the damping (ACLD) treatment may increase due to the use of 0-3 VEC layer instead of the conventional VEM layer.

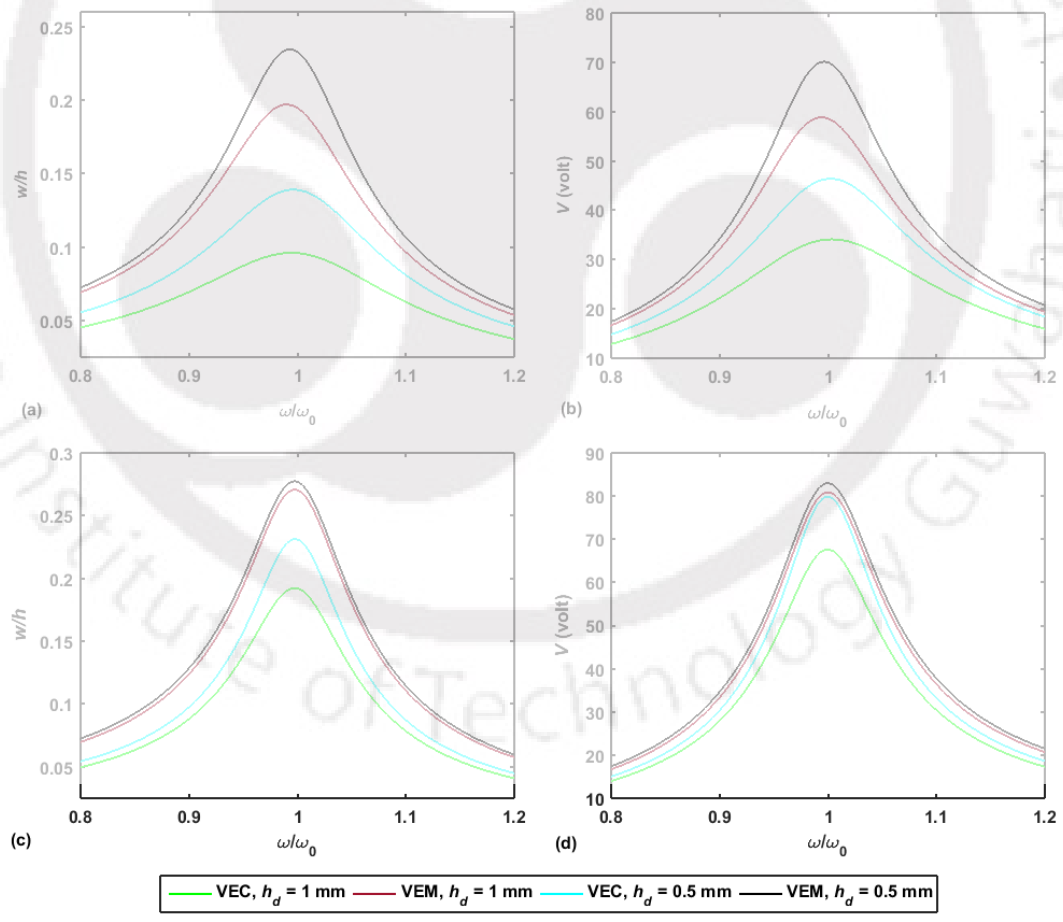

Fig. 7. 11. Variations of (a) the transverse displacement-amplitude and (b) the corresponding required control-voltage within a range of the operating

frequency around the fundamental natural frequency (ω_0) of the overall plate (k_d =100).

Despite these disadvantages, one may prefer the present 0-3 VEC layer as a damping layer of ACLD treatment because of the significantly augmented active-passive damping capacity of the treatment as demonstrated in the aforesaid results.

7.5 Summary

An analysis of active-passive damping in plates integrated with the actively constrained 0-3 VEC layer is presented in this chapter. The new 0-3 VEC layer is utilized as an actively constrained damping layer over the top surface of a substrate rectangular plate, and the active-passive damping characteristics of the overall plate are investigated particularly for the inclusions of the graphite-wafers within the actively constrained viscoelastic layer. The active constraining layer is made of PZT5H, and it acts as an extension mode piezoelectric actuator when the external voltage is supplied across its top and bottom fully electrode-surfaces according to the velocity feedback control strategy. For the analysis of active-passive damping in the overall plate, an FE model is developed based on the layer-wise first-order shear deformation theory. Using this FE model, first, a bending analysis of the overall plate is performed where the strains in the viscoelastic phase of the actively constrained damping layer are evaluated in the absence and the presence of the graphite-wafers. These results reveal significant improvement of maximum magnitudes of the transverse shear strains in the constrained viscoelastic layer due to the inclusions of graphite-wafers. Along with this enhanced transverse shear strain, in-plane strains in the constrained viscoelastic layer also arise with their reasonable magnitudes due to the inclusions of graphite-wafers. These observations from the static results provide an initial estimation of the augmented active-passive damping in the overall plate, and it is further investigated by computing the modal loss factor at the fundamental mode of vibration of the overall plate. The modal loss factor is computed for different sets of values of the velocity feedback control-gain and the geometric parameters of the 0-3 VEC layer. These results reveal the significantly improved magnitude of the modal loss factor for the inclusions of graphite-wafers within the viscoelastic layer in the form of a 0-3 VEC layer. The modal loss factor increases indicatively with the increasing velocity feedback

control-gain, but the corresponding rate of change of the modal loss factor decreases for the inclusions of graphite-wafers. The same results also reveal indicative influences of the geometric parameters of the 0-3 VEC layer on its damping capacity, and thus an optimal geometric configuration of the 0-3 VEC layer is presented for maximum active-passive damping in the overall plate. In order to verify the corresponding performance of the actively constrained 0-3 VEC layer to control the vibration-amplitude, the frequency responses of the overall plate are evaluated in the presence and the absence of the graphite-wafers within the viscoelastic layer. These results reveal that the attenuation of vibration-amplitude significantly increases in expense of less control-voltage when the graphite-wafers are inserted within the actively constrained viscoelastic layer. So, the present 0-3 VEC layer may be a potential damping layer in the active constrained layer damping treatment of structural vibration. But, it has to be configured in an optimal manner for an application.

Chapter 8

Conclusions and scope of future work

8.1 Conclusions

This dissertation deals with the design of viscoelastic composite (VEC) layers for improved passive and active-passive damping of vibration of basic structural elements (beams, plates, shells). First, a beam integrated with the conventional UCLD/PCLD treatment is considered, and the graphite-wafers are inserted through the middle surface of the viscoelastic layer within the arrangement of the UCLD/PCLD treatment. This inclusion of graphite-wafers within the viscoelastic layer yields a 1-3 VEC layer, and the corresponding changes in the passive damping characteristics of the overall beam are studied through its static and dynamic bending analyses using FE procedure. Subsequently, the 1-3 VEC layer is utilized as the damping layer in the ACLD treatment of beams where a transversely polarized monolithic piezoelectric (PZT5H) layer is taken to constrain the 1-3 VEC layer over the top surface of the host beam. This active constraining layer is considered to be activated by supplying the external voltage across its thickness according to the velocity feedback control strategy. For the bending deformation of the overall beam under the active piezoelectric constraining layer, the characteristics of the strains in the constrained viscoelastic layer are studied in the presence and the absence of the graphite-wafers, and the effects of these strains in the viscoelastic phase on the active-passive damping characteristics of the overall beam are evaluated.

Next, this concept of 1-3 VEC layer is implemented for CLD treatment of circular cylindrical shell structures. The cylindrical shell is constructed in the form of a sandwich shell with the viscoelastic core, and the graphite-strips are axially inserted through the middle surface of the viscoelastic core so that the 1-3 VEC core appears. First, the changes in the damping mechanisms of the CLD treatment due to the inclusion of graphite-strips within the viscoelastic core are studied, then the passive damping in the sandwich shell are evaluated. The variation of the passive damping in the sandwich shell corresponding to different geometric configurations of the graphite-strips are investigated, and an optimal geometric configuration of the 1-3 VEC core is presented for effective control of all the bending modes of vibration of the shell within an operating

frequency range of interest. In this optimization procedure, a weighted average loss factor of modal loss factors of excited modes is taken as the objective function that is maximized for optimal size and circumferential distribution of the graphite-strips. The weights of excited modes are taken based on the resonant-amplitudes appearing in the use of the traditional monolithic viscoelastic core.

The performance of the 1-3 VEC layer as a damping layer of ACLD treatment is also investigated for attenuation of vibration of a substrate FG circular cylindrical shell. The ACLD layer is considered to be distributed throughout the outer surface of the substrate shell while its (ACLD) conformability with the curved host-surface is ensured by the use of the vertically/radially reinforced 1-3 PFC constraining layer. The surfaces of this active constraining layer are printed with electrode-patches for effective control of several modes of vibration of the shell by the use of the ACLD treatment in layer-form. A fruitful strategy for the arrangements of electrode-patches and velocity-sensors is presented for effective control of several modes of vibration of the shell within an operating frequency range. The properties of the substrate FG shell vary from its inner ceramic rich surface to its outer metal rich surface for the consideration of a high temperature at the inner concave surface, while the overall FG shell vibrates under an external mechanical harmonic excitation. A geometrically nonlinear electro-visco-elastic incremental FE model of the overall FG shell is developed, and its controlled frequency responses are evaluated to investigate the active-passive damping in the overall shell in attenuation of its all the bending modes of vibration within an operating frequency range.

Besides the 1-3 VEC layer, a new 0-3 VEC layer is proposed by means of inserting a rectangular array of thin rectangular graphite-wafers through the middle surface of a viscoelastic layer. The performance of this 0-3 VEC layer in the PCLD arrangement over a plate is investigated by analysing the bending deformation/vibration of the overall plate. The bending analysis of the overall plate reveals the characteristics of strains in the viscoelastic phase of the 0-3 VEC layer, and the corresponding passive damping characteristics of the overall plate are quantified subsequently. The effects of geometrical properties in the arrangement of graphite-wafers on the passive damping in the overall plate are investigated, and an optimal geometric arrangement of the graphite inclusions is

demonstrated for the maximum damping in the overall plate. The fruitfulness of this optimal configuration of the 0-3 VEC layer is substantiated by evaluating the frequency responses of the overall plate. This study is subsequently extended for the ACLD treatment of the plate where the active constraining layer is considered to be made of a transversely polarized monolithic piezoelectric material (PZT5H). The active layer is activated by means of velocity feedback control strategy, and the corresponding active-passive damping characteristics of the overall plate are studied.

The following main observations are obtained from the aforesaid studies in this thesis.

1. The bending analysis of a substrate beam integrated with the UCLD/PCLD layer reveals that the extensional and transverse shear strains in the viscoelastic phase increase indicatively due to the graphite inclusions in the viscoelastic layer in the form of a 1-3 VEC layer. These improved stains result in augmented passive damping in the overall beam although this augmentation of passive damping significantly depends on the geometrical parameters in the arrangement of graphite inclusions within the viscoelastic layer.

2. The analysis of a substrate beam integrated with the actively constrained 1-3 VEC layer (ACLD) reveals the same viscoelastic damping mechanisms as those were obtained for the passively constrained 1-3 VEC layer (PCLD). The active-passive damping capacity of the ACLD treatment increases indicatively in the suppression of bending modes of vibration of beams. Similar to the UCLD/PCLD treatment, the augmentation of active-passive damping capacity of ACLD treatment indicatively depends on the geometrical properties of the 1-3 VEC layer.

3. The results for the analysis of circular cylindrical sandwich shell exhibit significantly improved passive damping in the shell for the use of the present 1-3 VEC core instead of the traditional monolithic viscoelastic core. This improved damping arises due to the embedded graphite-strips which indicatively enhance transverse shear as well as extensional strains within the viscoelastic core. For an effective improvement of passive damping in the sandwich shell, the size and circumferential distribution of the graphite-strips are to be taken in an appropriate manner.

4. The study on the optimal geometric configuration of the 1-3 VEC core of the circular cylindrical sandwich shell reveals significantly improved modal damping over the damping in the use of the traditional monolithic viscoelastic core. This improvement of damping at different excited modes of vibration appears following the assigned relative importance (weights) of the excited modes. As these weights are taken in proportion to the resonant-amplitudes appearing in the use of pure viscoelastic core, the difference among these resonant-amplitudes significantly reduces due to the optimally configured 1-3 VEC core.

5. From the study on the performance of the 1-3 VEC layer as the damping layer of ACLD treatment of vibration of an FG circular cylindrical shell, the important observations are obtained as, (a) the damping capacity of the ACLD layer significantly increases due to the use of the present 1-3 VEC layer instead of the pure viscoelastic layer, (b) the improved ACLD treatment holds for any volume fraction index of the constituents of the substrate FG shell, (c) the improved ACLD treatment appears mainly due to an enhanced transverse shear strain of the viscoelastic phase, (d) the increase in the circumferential span of the graphite-strips (with a constant gap between any two consecutive graphite-strips) may not improve the damping characteristics of the ACLD layer, (e) the temperature in the substrate FG shell does not have much effect on the damping characteristics of the ACLD layer even though it (FG shell) undergoes indicative thermal deformation, (f) the equilibrium position of vibration of the overall FG shell is almost equal to its (overall shell) thermal deformation and it (equilibrium position) does not change indicatively with the operating frequency, (g) the present strategy for arrangement of the patches of surface-electrode provides effective control of all the modes of vibration of the overall shell within an operating frequency range of interest, (h) the vertically reinforced 1-3 PFC constraining layer possesses good actuation capability in control of bending modes of vibration of the circular cylindrical shell structure even though it is primarily known as a material of distributed actuator for control of thickness mode of deformation/vibration.

6. For the inclusion of graphite-strips in the form of 1-3 VEC, the magnitudes of certain strain components in the viscoelastic phase improve, and these

strain components lie in a transverse plane of the principal material coordinate system. However, the design of 0-3 VEC layer yields the enhancement of all the strains in the viscoelastic phase of VEC damping layer under the bending deformation.

7. The bending analysis of a substrate plate integrated with a passively constrained 0-3 VEC layer exhibits significantly improved magnitudes of all the transverse shear strains in the viscoelastic phase along with the reasonable magnitudes of all the in-plane strains in the same phase. So, the passive damping in the plate improves due to the inclusion of an array of graphite-wafers although the inclusions are to be arranged in an appropriate geometrical configuration. The optimal configuration of the 0-3 VEC layer results in a significant magnitude of modal loss factor at the fundamental bending mode of the overall plate and the study recommends 0-3 VEC layer instead of 1-3 VEC layer for effective passive damping of vibration of plates.
8. The consideration of an active piezoelectric layer to constrain the 0-3 VEC layer (ACLD) over a substrate plate does not yield any alteration of the damping mechanisms from those obtained in the use of the passive constraining layer. But, the active-passive damping in the overall plate indicatively increases due to the presence of the inclusion of graphite-wafers. The optimal geometrical properties of the rectangular array of rectangular graphite-wafers yield a significant control capability of the active-passive damping (ACLD) treatment, and this damping treatment may be utilized instead of the traditional ACLD treatment for superior control of vibration of plates.

8.2 Scope of future work

Although preceding chapters of this thesis fulfil the objectives of the present dissertation, further research may still be carried out for improvement of damping in the UCLD, PCLD and ACLD treatments of structural vibration. Some of the future works which may be readily undertaken in line with the present work are as follows.

1. Design of 0-3 VEC damping layer for UCLD, PCLD and ACLD treatments of vibration of shell structures especially for suppression of multiple modes of vibration using one configuration of the VEC layer.

2. Development of active-passive damping layer using the piezoelectric inclusions within the viscoelastic matrix.
3. Development of a theoretical methodology for optimal distributions of stiffness and damping properties within the domain of the damping layer especially for suppression of one or multiple modes of vibration of a substrate structure.
4. The experimental verifications of the theoretical models developed in this thesis are also an important scope for further research work.

References

Adhikari S, Woodhouse J. Quantification of non-viscous damping in discrete linear systems. Journal of Sound and Vibration 2003; 260(3):499-518.

Alam N, Asnani NT. Vibration and damping analysis of multilayered rectangular plates with constrained viscoelastic layers. Journal of Sound and Vibration 1984a; 97(4):597-614.

Alam N, Asnani NT. Vibration and damping analysis of a multilayered cylindrical shell, Part I: Theoretical analysis. AIAA journal 1984; 22(6):803-810.

Al-Ajmi MA, Bourisli RI. Optimum design of segmented passive-constrained layer damping treatment through genetic algorithms. Mechanics of Advanced Materials and Structures 2008; 15(3-4):250-257.

Alibeigloo A. Thermo elasticity solution of functionally graded, solid, circular, and annular plates integrated with piezoelectric layers using the differential quadrature method. Mechanics of Advanced Materials and Structures 2017; 1-19.

Alvelid M, Enelund M. Modelling of constrained thin rubber layer with emphasis on damping. Journal of Sound and Vibration 2007; 300(3):662-675.

Amabili M. Nonlinear vibrations and stability of shells and plates. Cambridge University Press; 2008.

Arafa M, Baz A. Dynamics of active piezoelectric damping composites. Composites Part B: Engineering. 2000 Jun 30;31(4):255-264.

Araújo AL, Carvalho VS, Soares CM, Belinha J, Ferreira AJ. Vibration analysis of laminated soft core sandwich plates with piezoelectric sensors and actuators. Composite Structures 2016; 151:91-98.

ASTM E756-2005. Standard Test Method for Measuring Vibration-Damping Properties of Materials. American Society of Test Materials, West Conshohocken. 2010.

Azvine B, Tomlinson GR, Wynne RJ. Use of active constrained-layer damping for controlling resonant vibration. Smart Materials and Structures 1995; 4(1):1.

Bailey T, Hubbard JE. Distributed piezoelectric-polymer active vibration control of a cantilever beam. Journal of Guidance, Control, and Dynamics 1985; 8(5):605-611.

Balamurugan V, Narayanan S. Shell finite element for smart piezoelectric composite plate/shell structures and its application to the study of active vibration control. Finite Elements in Analysis and Design 2001; 37(9):713-738.

Balamurugan V, Narayanan S. Active–passive hybrid damping in beams with enhanced smart constrained layer treatment. Engineering structures 2002; 24(3):355-363.

Batra RC, Liang XQ, Yang JS. The vibration of a simply supported rectangular elastic plate due to piezoelectric actuators. International Journal of Solids and Structures 1996; 33(11):1597-1618.

Baz AM. Method and device for active constrained layer damping for vibration and sound control. U.S. Patent No. 5485053, 1996.

Baz A, Chen T. Boundary Control of Axi-Symmetric Vibrations of Cylindrical Shell Using Active Constrained Layer Damping. AIAA paper # 97- 0360, 35th AJAA Aerospace Sciences Conference, Reno, Nevada; 1997.

Baz A, Poh S. Performance of an active control system with piezoelectric actuators. Journal of sound and Vibration 1988; 126(2):327-343.

Baz A, Ro J. Partial treatment of flexible beams with active constrained layer damping. ASME Applied Mechanics Division-Publications-AMD. 1993; 167:61.

Baz A, Ro J. Performance characteristics of active constrained layer damping. Shock and Vibration 1995; 2(1): 33-42.

Baz A, Tempia A. Active piezoelectric damping composites. Sensors and Actuators A: Physical 2004; 112(2):340-350.

Bent AA. Active fiber composites for structural actuation. PhD thesis, Massachusetts Institute of Technology; 1997.

Benjeddou A. Advances in hybrid active-passive vibration and noise control via piezoelectric and viscoelastic constrained layer treatments. Journal of Vibration and Control 2001; 7(4):565-602.

Bert CW. Material damping: An introductory review of mathematic measures and experimental technique. Journal of Sound and Vibration 1973; 29(2):129-153.

Biot MA. Linear thermodynamics and the mechanics of solids. Cornell Aeronautical Lab., Inc., Buffalo; 1958.

Bruant I, Gallimard L, Nikoukar S. Optimal piezoelectric actuator and sensor location for active vibration control, using genetic algorithm. Journal of Sound and Vibration 2010; 329(10):1615-1635.

Cady WG. Piezoelectricity: an introduction to the theory and applications of electromechanical phenomena in crystals. McGraw-Hill; 1946.

Cai C, Zheng H, Liu GR. Vibration analysis of a beam with PCLD patch. Applied Acoustics 2004; 65(11):1057-1076.

Cao XT, Zhang ZY, Hua HX. Free vibration of circular cylindrical shell with constrained layer damping. Applied Mathematics & Mechanics 2011; 32(4).

Cao X, Hua H, Zhang Z. Acoustic Radiation From Stiffened Cylindrical Shells With Constrained Layer Damping. Journal of Vibration and Acoustics 2013; 135(1):011005.

Cento PF, Kawiecki G. Finite element modeling of segmented active constrained damping layers including bonding layer effect. Modal Analysis 2002; 8(6):805-832.

Chaudhry Z, Rogers C. Actuators for smart structures. Fiber optic smart structures (A 95-34976 09-39), New York, NY, John Wiley & Sons, Inc. 1995; 497-536.

Chawla KK, Meyers MA. Mechanical behavior of materials. Prentice Hall; 1999.

Chee CYK. Static shape control of laminated composite plate smart structure using piezoelectric actuators. PhD thesis, The University of Sydney; 2000.

Chee CY, Tong L, Steven GP. A review on the modelling of piezoelectric sensors and actuators incorporated in intelligent structures. Journal of Intelligent Material Systems and Structures 1998; 9(1):3-19.

Chen T, Baz A. Performance characteristics of active constrained layer damping versus passive constrained layer damping with active control. Smart Structures & Materials 1996; 256-268.

Chen LH, Huang SC. Vibrations of a cylindrical shell with partially constrained layer damping (CLD) treatment. International Journal of Mechanical Sciences 1999; 41(12):1485-1498.

Chen LH, Huang SC. Vibration attenuation of a cylindrical shell with constrained layer damping strips treatment. Computers & Structures 2001; 79(14):1355-1362.

Chen YC, Huang SC. An optimal placement of CLD treatment for vibration suppression of plates. International Journal of Mechanical Sciences 2002; 44(8):1801-1821.

Cheng L, Lapointe R. Vibration attenuation of panel structures by optimally shaped viscoelastic coating with added weight considerations. Thin-walled structures 1995; 21(4):307-326.

Choi SB, Han YM. Piezoelectric actuators: control applications of smart materials. CRC Press; 2016.

Christensen RM. Theory of Viscoelasticity: An Introduction. New York: Academic Press; 1982.

Cook RD. Concepts and applications of finite element analysis. John Wiley & Sons; 2007.

Cortés F, Elejabarrieta MJ. Structural vibration of flexural beams with thick unconstrained layer damping. International Journal of Solids and Structures 2008; 45(22):5805-5813.

Crawley E, Luis DE. Use of piezoelectric actuators as elements of intelligent structures. AIAA journal 1987; 25(10):1373-1385.

Crawley EF, Lazarus KB. Induced strain actuation of isotropic and anisotropic

plates. AIAA journal 1991; 29(6):944-951.

Cunha-Filho AG, de Lima AM, Donadon MV, Leão LS. Flutter suppression of plates using passive constrained viscoelastic layers. Mechanical Systems and Signal Processing 2016; 79:99-111.

Cupiał P, Nizioł J. Vibration and damping analysis of a three-layered composite plate with a viscoelastic mid-layer. Journal of Sound and Vibration 1995; 183(1):99-114.

Datta P, Ray MC. Three-dimensional fractional derivative model of smart constrained layer damping treatment for composite plates. Composite Structures 2016; 156:291-306.

Deb K. Optimization for engineering design: Algorithms and examples. PHI Learning Pvt. Ltd.; 2012.

Della CN, Shu D. The performance of 1–3 piezoelectric composites with a porous non-piezoelectric matrix. Acta Materialia. 2008; 56(4):754-761.

Dhainaut M. A comparison between serendipity and Lagrange plate elements in the finite element method. International Journal for Numerical Methods in Biomedical Engineering 1997; 13(5):343-353.

Douglas BE, Yang JC. Transverse compressional damping in the vibratory response of elastic-viscoelastic-elastic beams. AIAA journal 1978; 16(9):925-930.

Douglas B. E. Compressional damping in three-layer beams incorporating nearly incompressible viscoelastic cores. Journal of Sound and Vibration 1986; 104:343–347.

Du C, Li Y. Nonlinear resonance behavior of functionally graded cylindrical shells in thermal environments. Composite Structures 2013; 102:164-174.

El-Sabbagh A, Baz A. Topology optimization of unconstrained damping treatments for plates. Engineering Optimization. 2014; 46(9):1153-1168.

Ferreira AJ, Araújo AL, Neves AM, Rodrigues JD, Carrera E, Cinefra M, Soares CM. A finite element model using a unified formulation for the analysis of viscoelastic sandwich laminates. Composites Part B: Engineering 2013; 45(1):1258-1264.

Filippi M, Carrera E, Regalli AM. Layerwise Analyses of Compact and Thin-Walled Beams Made of Viscoelastic Materials. Journal of Vibration and Acoustics 2016; 138(6):064501.

Ganapathi M, Patel BP, Boisse P, Polit O. Flexural loss factors of sandwich and laminated composite beams using linear and nonlinear dynamic analysis. Composites Part B: Engineering 1999; 30(3):245-256.

Gandhi F, Munsky BE. Comparison of the mechanism and effectiveness of position and velocity feedback in active constrained-layer damping treatments. In Proceedings of the SPIE The International Society for Optical Engineering 2000; 3989:61-72.

Gao JX, Liao WH. Vibration analysis of simply supported beams with enhanced self-sensing active constrained layer damping treatments. Journal of Sound and Vibration 2005; 280(1):329-357.

Garrison MR, Miles RN, Sun JQ, Bao W. Random response of a plate partially covered by a constrained layer damper. Journal of Sound and Vibration 1994; 172(2):231-245.

Gentilman RL, Fiore DF, Pham HT, French KW, Bowen LJ. Fabrication and properties of 1-3 PZT-polymer composites. American Ceramic Society, Westerville, OH (United States); 1994.

Ghoneim H. Electromechanical surface damping using constrained layer and shunted piezoelectric. In North American Conference on Smart Structures and Materials 1993; 78-89.

Ghoneim H. Application of the electromechanical surface damping to the vibration control of a cantilever plate. Transactions-American Society Of Mechanical Engineers, Journal Of Vibration And Acoustics 1996; 118:551-557.

Golla DF, Hughes PC. Dynamics of viscoelastic structures—a time-domain, finite element formulation. ASME Journal of Applied Mechanics 1985; 52(4):897-906.

Granger D, Ross A. Effects of partial constrained viscoelastic layer damping parameters on the initial transient response of impacted cantilever beams: Experimental and numerical results. Journal of Sound and Vibration 2009; 321(1):45-64.

Grootenhuis P. The control of vibrations with viscoelastic materials. Journal of Sound and Vibration 1970; 11(4):421-433.

Haghighi G, Malekzadeh P, Afshari M. Inverse internal pressure estimation of functionally graded cylindrical shells under thermal environment. Acta Mechanica 2014; 225(12):3377.

Hagood NW, von Flotow A. Damping of structural vibrations with piezoelectric materials and passive electrical networks. Journal of Sound and Vibration 1991; 146(2):243-268.

Hagood NW, Bent AA. Development of piezoelectric fiber composites for structural actuation. Proc. of AIAA/ASME/ASCE/AHS/ASC 34th Structures, Structural Dynamics, and Materials Conference (La Jolla, CA, April, 1993) 3625-3638.

Hamdaoui M, Robin G, Jrad M, Daya EM. Optimal design of frequency dependent three-layered rectangular composite beams for low mass and high damping. Composite Structures 2015; 120:174-182.

Herdic PC, Houston BH, Marcus MH, Williams EG, Baz AM. The vibro-acoustic response and analysis of a full-scale aircraft fuselage section for interior noise reduction. The Journal of the Acoustical Society of America 2005; 117(6):3667-3678.

High JW, Wilkie WK. Method of fabricating NASA-standard macro-fiber composite piezoelectric actuators. National Aeronautics and Space Administration, Langley Research Center; 2003.

Hu H, Belouettar S, Potier-Ferry M. Review and assessment of various theories for modeling sandwich composites. Composite Structures; 84(3):282-292.

Huang SC, Inman DJ, Austin EM. Some design considerations for active and passive constrained layer damping treatments. Smart Materials and Structures 1996; 5(3):301.

Huang PY, Reinhall PG, Shen IY, Yellin JM. Thickness deformation of constrained layer damping: an experimental and theoretical evaluation. Journal of Vibration and Acoustics 2001; 123(2):213-221.

Illaire H, Kropp W. Quantification of damping mechanisms of active constrained layer treatments. Journal of sound and vibration 2005; 281(1):189-217.

Imaino W, Harrison JC. A comment on constrained layer damping structures with low viscoelastic modulus. Journal of sound and vibration 1991; 149(2):354-359.

Jalili N. Piezoelectric-Based Systems Modeling. In Piezoelectric-Based Vibration Control. Springer US; 2010:183-232.

Jin G, Yang C, Liu Z, Gao S, Zhang C. A unified method for the vibration and damping analysis of constrained layer damping cylindrical shells with arbitrary boundary conditions. Composite Structures 2015; 130:124-142.

Johnson CD, Kienholz DA. Finite element prediction of damping in structures with constrained viscoelastic layers. AIAA journal. 1982; 20(9):1284-1290.

Johnson CD, Kienholz DA, Rogers LC. Finite element prediction of damping in beams with constrained viscoelastic layer. Shock Vibration Bulletin 1991; 51(1):71–81.

Jones IW, Salerno VL. The effect of structural damping on the forced vibrations of cylindrical sandwich shells. Journal of Engineering for Industry 1966; 88(3):318-323.

Jones CJ, Thompson DJ. Rolling noise generated by railway wheels with visco-elastic layers. Journal of sound and vibration 2000; 231(3):779-790.

Jones DI. Handbook of viscoelastic vibration damping. John Wiley & Sons; 2001.

Jones RM. Mechanics of composite materials. Tailor and Francis; 1999.

Kalamkarov AL, Savi MA. Micromechanical modeling and effective properties of the smart grid-reinforced composites. Journal of the Brazilian Society of Mechanical Sciences and Engineering 2012; 34:343-351.

Kapuria S, Hagedorn P. Unified efficient layerwise theory for smart beams with segmented extension/shear mode, piezoelectric actuators and sensors.

Journal of Mechanics of Materials and Structures 2007; 2(7):1267-1298.

Kapuria S, Kumari P. Three-dimensional isofield micromechanics model for effective electrothermoelastic properties of piezoelectric composites. Journal of Mechanics of Materials and Structures 2011; 6(1):249-265.

Kerwin Jr EM. Damping of flexural waves by a constrained viscoelastic layer. The Journal of the Acoustical society of America 1959; 31(7):952-962.

Kerwin EM. Macromechanisms of damping in composite structures. In Internal Friction, Damping, and Cyclic Plasticity. ASTM International; 1965.

Khalfi B, Ross A. Influence of partial constrained layer damping on the bending wave propagation in an impacted viscoelastic sandwich. International Journal of Solids and Structures 2013; 50(25):4133-4144.

Khalfi B, Ross A. Transient and harmonic response of a sandwich with partial constrained layer damping: A parametric study. Composites Part B: Engineering. 2016; 91:44-55.

Kiehl MZ, Jerzak CP. Modeling of passive constrained layer damping as applied to a gun tube. Shock and Vibration 2001; 8(3-4):123-9.

Koh B. Hybrid active-passive constrained layer damping treatments in beams, plates and shells. PhD thesis, University of Southampton; 2016.

Koizumi, M. The concept of FGM. 1993; 3-10.

Korjakin A, Rikards R, Altenbach H, Chate A. Free damped vibrations of sandwich shells of revolution. Journal of Sandwich Structures & Materials. 2001; 3(3):171-196.

Kulkarni K, Singh BN, Maiti DK. Analytical solution for bending and buckling analysis of functionally graded plates using inverse trigonometric shear deformation theory. Composite Structures 2015; 134:147-157.

Kundu CK, Maiti DK, Sinha PK. Post buckling analysis of smart laminated doubly curved shells. Composite structures 2007; 81(3):314-322.

Kumar A, Panda S. Design of a 1-3 viscoelastic composite layer for improved free/constrained layer passive damping treatment of structural vibration. Composites Part B: Engineering 2016; 96:204-214.

Kumar A, Panda S. Optimal Damping in Circular Cylindrical Sandwich Shells With a Three-Layered Viscoelastic Composite Core. Journal of Vibration and Acoustics 2017; 139(6):061003.

Kumar A, Panda S, Narsaria V, Kumar As. Augmented constrained layer damping in plates through the optimal design of a 0-3 viscoelastic composite layer. 2017a; First review report obtained and the revised manuscript has been submitted to Journal of Vibration and Control.

Kumar A, Panda S, Kumar As, Narsaria V. Performance of a graphite wafer-reinforced viscoelastic composite layer for active-passive damping of plate vibration. 2017b; First review report obtained and the revised manuscript

has been submitted to Composite Structures.

Kumar AMS, Panda S, Chakraborty D. Harmonically exited nonlinear vibration of heated functionally graded plates integrated with piezoelectric composite actuator. Journal of Intelligent Material Systems and Structures 2015a; 26(8):931–951.

Kumar AP, Panda S, Reddy NH. Smart damping of vibration of annular plates by the design of a cylindrically orthotropic piezoelectric fiber-reinforced composite actuator. Acta Mechanica 2015b; 1–26.

Kumar N, Singh SP. Vibration and damping characteristics of beams with active constrained layer treatments under parametric variations. Materials & Design 2009; 30(10):4162-4174.

Kumar N, Singh SP. Experimental study on vibration and damping of curved panel treated with constrained viscoelastic layer. Composite structures 2010; 92(2):233-243.

Kumar S, Sehgal R, Kumar R. Active Vibration Control of Beams By Combining Precompressed Layer Damping and ACLD Treatment: Theory and Experimental Implementation. Journal of Vibration and Acoustics 2011; 133(6):061013.

Kumar S, Kumar R, Sehgal R. Enhanced ACLD treatment using stand-off-layer: FEM based design and experimental vibration analysis. Applied Acoustics 2011a; 72(11):856-872.

Kumar R. Enhanced active constrained layer damping (ACLD) treatment using stand-off-layer: robust controllers design, experimental implementation and comparison. Journal of Vibration and Control 2013; 19(3):439-460.

Kung SW, Singh R. Vibration analysis of beams with multiple constrained layer damping patches. Journal of Sound and Vibration 1998; 212(5):781-805.

Kwak MK, Heo S. Active vibration control of smart grid structure by multiinput and multioutput positive position feedback controller. Journal of Sound and Vibration 2007; 304(1):230-245.

Kwak SK, Washington G, Yedavalli RK. Active and passive vibration control of landing gear components. Adaptive Structures and Materials Systems-ASME. 1999;59.

Lall AK, Asnani NT, Nakra BC. Vibration and damping analysis of rectangular plate with partially covered constrained viscoelastic layer. Journal of vibration, acoustics, stress, and reliability in design 1987; 109(3):241-247.

Lall AK, Asnani NT, Nakra BC. Damping analysis of partially covered sandwich beams. Journal of Sound and Vibration. 1988; 123(2):247-259.

Lam MJ, Saunders WR, Inman DJ. Modeling active constrained layer damping using Golla-Hughes-McTavish approach. Smart Structures and Materials 1995; 2445:86-97.

Lam MJ, Inman DJ, Saunders WR. Vibration control through passive constrained layer damping and active control. Journal of Intelligent Material Systems and Structures 1997; 8(8):663-677.

LaPlante WA. Vibration control of fluid-loaded cylindrical shells using active constrained layer damping. PhD thesis, Catholic University of America; 1998.

Lee BC, Kim KJ. Consideration of both extensional and shear strain of core material in modal property estimation of sandwich plates. In Proceedings of the American Society of Mechanical Engineers Design Technical Conferences. Boston, MA 1995; 701-708.

Lee DH, Hwang WS. Layout Optimization of Unconstrained Viscoelastic Layer On Beams Using Fractional Derivative. In 10th AIAA/ISSMO Multidisciplinary Analysis and Optimization Conference 2004.

Le Maout N, Verron E, Bègue J. Simultaneous geometrical and material optimal design of hybrid elastomer/composite sandwich plates. Composite Structures 2011; 93(3):1153-1157.

Lepoittevin G, Kress G. Optimization of segmented constrained layer damping with mathematical programming using strain energy analysis and modal data. Materials & Design. 2010; 31(1):14-24.

Lesieutre GA, Bianchini E. Time Domain Modeling of Linear Viscoelasticity Using Anelastic Displacement Fields. Transactions of the ASME 1995; 117:424-430.

Lesieutre GA, Lee U. A finite element for beams having segmented active constrained layers with frequency-dependent viscoelastics. Smart Materials and Structures. 1996 Oct;5(5):615.

Li FM, Kishimoto K, Wang YS, Chen ZB, Huang WH. Vibration control of beams with active constrained layer damping. Smart Materials and Structures 2008; 17(6):065036.

Li J, Narita Y. Vibration suppression for laminated cylindrical panels with arbitrary edge conditions. Journal of Vibration and Control 2013; 19(4):626-640.

Liao WH, Wang KW. A new active constrained layer configuration with enhanced boundary actions. Smart Materials and Structures 1996; 5(5):638.

Librescu L, Meirovitch L, Song O. Integrated structural tailoring and control using adaptive materials for advanced aircraft wings. Journal of Aircraft 1996; 33(1):203-213.

Liao WH, Wang KW. Analysis of edge elements for a new active constrained layer treatment. Passive Damping and Isolation 1997;70.

Lifshitz JM, Leibowitz M. Optimal sandwich beam design for maximum viscoelastic damping. International Journal of Solids and Structures 1987; 23(7):1027-1034.

Lin CH, Muliana A. Micromechanics models for the effective nonlinear electro-mechanical responses of piezoelectric composites. Acta Mechanica 2013; 224(7):1471.

Liu Y, Wang KW. Enhanced active constrained layer damping treatment with symmetrically and non-symmetrically distributed edge elements. Smart Structures & Materials 1998; 61-72.

Liu Y, Wang KW. Active-passive hybrid constrained layer for structural damping augmentation. Journal of vibration and acoustics 2000; 122(3):254-262.

Liu Y, Wang KW. Damping optimization by integrating enhanced active constrained layer and active-passive hybrid constrained layer treatments. Journal of sound and vibration 2002; 255(4):763-775.

Lu J, Wang P, Zhan Z. Active vibration control of thin-plate structures with partial SCLD treatment. Mechanical Systems and Signal Processing 2017; 84:531-550.

Lu J, Xiang Y, Huang Y, Li X, Ni Q. Transfer matrix method for analyzing vibration and damping characteristics of rotational shell with passive constrained layer damping treatment. Acta Mechanica Solida Sinica 2010; 23(4):297-311.

Lu YP. Forced vibrations of damped cylindrical shells filled with pressurized liquid. AIAA Journal 1977; 15(9):1242-1249.

Lu YP, Killian JW, Everstine GC. Vibrations of three layered damped sandwich plate composites. Journal of Sound and Vibration 1979; 64(1):63-71.

Lu YP, Roscoe AJ, Douglas BE. Analysis of the response of damped cylindrical shells carrying discontinuously constrained beam elements. Journal of sound and vibration 1991; 150(3):395-403.

Lumsdaine A, Scott RA. Shape optimization of unconstrained beam and plate damping layers. In Proceedings of the American Society of Mechanical Engineers 15th Biennial Conference on Mechanical Vibration and Noise, Boston, MA 1995.

Lumsdaine A, Scott RA. Shape optimization of unconstrained viscoelastic layers using continuum finite elements. Journal of sound and vibration 1998; 216(1):29-52.

Lunden R. Optimum distribution of additive damping for vibrating beams. Journal of Sound and Vibration. 1979; 66(1):25-37.

Madeira JF, Araújo AL, Soares CM, Soares CM, Ferreira AJ. Multiobjective design of viscoelastic laminated composite sandwich panels. Composites Part B: Engineering 2015; 77:391-401.

Mallik N, Ray MC. Effective coefficients of piezoelectric fiber-reinforced composites. AIAA journal 2003; 41(4):704-710.

Manconi E, Mace BR. Estimation of the loss factor of viscoelastic laminated panels from finite element analysis. Journal of Sound and Vibration 2010;

329(19):3928-3939.

Marcelin JL, Trompette P, Smati A. Optimal constrained layer damping with partial coverage. Finite elements in Analysis and Design 1992; 12(3-4):273-280.

Markus S. Damping mechanism of beams partially covered by constrained viscoelastic layer. Acta Technica CSAV 1974; 19(2):179-194.

Markus S. Damping properties of layered cylindrical shells, vibrating in axially symmetric modes. Journal of Sound Vibration 1976; 48:511-524.

Marsh ER, Hale LC. Damping of flexural waves with imbedded viscoelastic materials. Journal of Vibration and Acoustics Transaction ASME 1998; 120(1):188-193.

Masti RS, Sainsbury MG. Vibration damping of cylindrical shells partially coated with a constrained viscoelastic treatment having a standoff layer. Thin-walled structures 2005; 43(9):1355-1379.

McTavish DJ, Hughes PC. Finite element modeling of linear viscoelastic structures: the GHM method. In Proceedings of the 33rd AIAA/ASME/ASCE/AHS/ASC Structures, Structural Dynamics and Materials Conference, Dallas, TX, 1992; 13-15.

Mead DJ, Markus S. The forced vibration of a three-layer, damped sandwich beam with arbitrary boundary conditions. Journal of sound and vibration. 1969; 10(2):163-175.

Mead DJ, Pearce TG. The optimum use of unconstrained layer damping treatments. Southampton Univ (England) Dept Of Aeronautics And Astronautics, 1961.

Mead DJ. The measurement of the loss factors of beams and plates with constrained and unconstrained damping layers: A critical assessment. Journal of sound and vibration 2007; 300(3):744-762.

Meirovitch L. Principles and techniques of vibrations. New Jersey: Prentice Hall; 1997.

Merideno I, Nieto J, Gil-Negrete N, Landaberea A, Iartza J. Constrained layer damper modelling and performance evaluation for eliminating squeal noise in trams. Shock and Vibration 2014.

Meunier M, Shenoi RA. Forced response of FRP sandwich panels with viscoelastic materials. Journal of sound and vibration 2003; 263(1):131-151.

Moita JS, Araújo AL, Martins PG, Soares CM, Soares CA. Analysis of active-passive plate structures using a simple and efficient finite element model. Mechanics of Advanced Materials and Structures 2011; 18(2):159-169.

Moreira RA, Rodrigues JD, Ferreira AJ. A generalized layerwise finite element for multi-layer damping treatments. Computational Mechanics 2006; 37(5):426.

Nakra BC. Vibration control with viscoelastic materials. III. The Shock and Vibration Digest 1984; 16(5):17-22.

Nakra BC. Vibration control in machines and structures using viscoelastic damping. Journal of sound and vibration 1998; 211(3):449-466.

Nakra BC. Structural dynamic modification using additive damping. Sadhana 2000; 25(3):277-289.

Narayanan S, Verma JP, Mallik AK. Free vibration of thin-walled open section beams with unconstrained damping treatment. Journal of Applied Mechanics 1981; 48(1):169-173.

Nashif AD, Jones DI, Henderson JP. Vibration damping. John Wiley & Sons; 1985.

Newnham RE. Composite electroceramics. Ferroelectrics 1986; 68(1):1-32.

Ni Q, Xiang Y, Huang Y, Lu J. Modeling and dynamics analysis of shells of revolution by partially active constrained layer damping treatment. Acta Mechanica Solida Sinica 2013; 26(5):468-479.

Noda N. Thermal stresses in functionally graded materials. Journal of Thermal Stresses 1999; 22(4-5):477-512.

Nokes DS, Nelson FC. Constrained layer damping with partial coverage. Shock and Vibration Bulletin 1968; 38:5-10.

Oberst H, Frankenfeld K. Damping of the bending vibrations of thin laminated metal beams connected through adherent layer. Acustica 1952; 2:181-194.

Okazaki A, Tatemichi A, Mirza S. Damping properties of two-layered cylindrical shells with an unconstrained viscoelastic layer. Journal of sound and vibration 1994; 176(2):145-161.

Pan HH. Axisymmetrical vibrations of a circular sandwich shell with a viscoelastic core layer. Journal of Sound and Vibration. 1969; 9(2):338-348.

Panda S, Kumar A. A design of active constrained layer damping treatment for vibration control of circular cylindrical shell structure. Journal of Vibration and Control 2016; 1077546316670071.

Panda S, Ray MC. Active control of geometrically nonlinear vibrations of functionally graded laminated composite plates using piezoelectric fiber reinforced composites. Journal of Sound and Vibration 2009a; 325(1):186-205.

Panda S, Ray MC. Control of Nonlinear Vibrations of Functionally Graded Plates Using 1-3 Piezoelectric Composite. AIAA Journal 2009b; 47(6):1421-1434.

Papagiannopoulos GA, Hatzigeorgiou GD. On the use of the half-power bandwidth method to estimate damping in building structures. Soil Dynamics and Earthquake Engineering 2011; 31(7):1075-1079.

Parthasarathy G, Reddy CV, Ganesan N. Partial coverage of rectangular plates by unconstrained layer damping treatments. Journal of sound and vibration 1985; 102(2):203-216.

Park CH, Inman DJ, Lam MJ. Model reduction of viscoelastic finite element models. Journal of Sound and Vibration 1999; 219(4):619-637.

Park CH, Baz A. Vibration control of bending modes of plates using active constrained layer damping. Journal of Sound and vibration 1999; 227(4):711-734.

Park CH, Baz A. Comparison between finite element formulations of active constrained layer damping using classical and layer-wise laminate theory. Finite Elements in Analysis and Design 2001; 37(1):35-56.

Parke S. Logarithmic decrements at high damping. British Journal of Applied Physics 1966; 17(2):271.

Plattenburg J, Dreyer JT, Singh R. Active and passive damping patches on a thin rectangular plate: a refined analytical model with experimental validation. Journal of Sound and Vibration 2015; 353:75-95.

Plunkett R, Lee CT. Length optimization for constrained viscoelastic layer damping. The Journal of the Acoustical Society of America 1970; 48(1B):150-161.

Pradyumna S, Gupta A. Nonlinear dynamic stability of laminated composite shells integrated with piezoelectric layers in thermal environment. Acta mechanica 2011; 218(3):295-308.

Praveen GN, Reddy JN. Nonlinear transient thermoelastic analysis of functionally graded ceramic-metal plates. International Journal of Solids and Structures. 1998; 35(33):4457-4476.

Pradhan SC, Loy CT, Lam KY, Reddy JN. Vibration characteristics of functionally graded cylindrical shells under various boundary conditions. Applied Acoustics 2000; 61(1):111-1129.

Raja S, Ikeda T. Concept and electro-elastic modeling of shear actuated fiber composite using micro-mechanics approach. Journal of Intelligent Material Systems and Structures 2008; 19(10):1173-1183.

Ramesh TC, Ganesan N. A finite element based on a discrete layer theory for the free vibration analysis of cylindrical shells. Computers & structures 1992; 43(1):137-143.

Ramesh TC, Ganesan N. A finite element based on a discrete layer theory for the free vibration analysis of conical shells. Journal of sound and vibration 1993; 166(3):531-538.

Ramesh TC, Ganesan N. Finite element analysis of cylindrical shells with a constrained viscoelastic layer. Journal of Sound and Vibration 1994; 172(3):359-370.

Ramesh TC, Ganesan N. Vibration and Damping Analysis of Cylindrical Shells With Constrained Damping Treatment--A Comparison of Three Theories. Transactions-ASME Journal Of Vibration And Acoustics 1995; 117:213.

Rao MD, Echempati R, Nadella S. Dynamic analysis and damping of composite structures embedded with viscoelastic layers. Composites Part B: Engineering 1997; 28(5-6):547-554.

Rao MD. Recent applications of viscoelastic damping for noise control in automobiles and commercial airplanes. Journal of Sound and Vibration 2003; 262(3):457-474.

Rao MD, He S. Dynamic analysis and design of laminated composite beams with multiple damping layers. AIAA journal 1993; 31(4).

Ravi SS, Kundra TK, Nakra BC. Reanalysis of plates modified by free damping layer treatment. Computers & structures 1996; 58(3):535-541.

Ray MC, Batra RC. A single-walled carbon nanotube reinforced 1–3 piezoelectric composite for active control of smart structures. Smart Materials and Structures 2007; 16(5):1936.

Ray MC, Batra RC. Smart constrained layer damping of functionally graded shells using vertically/obliquely reinforced 1–3 piezocomposite under a thermal environment. Smart Materials and Structures 2008; 17(5):055007.

Ray MC, Baz A. Optimization of energy dissipation of active constrained layer damping treatments of plates. Journal of Sound and Vibration 1997; 208(3):391-406.

Ray M, Chen T, Baz A. Vibration control of cylindrical shells using active constrained layer damping. In Smart Structures and Material Conference 1997; 293-314.

Ray MC, Oh J, Baz A. Active constrained layer damping of thin cylindrical shells. Journal of sound and vibration 2001; 240(5):921-935.

Ray MC, Mallik N. Analysis of piezoelectric fiber reinforced composites as new smart materials for active control of flexible structures. In Smart Materials II, International Society for Optics and Photonics 2002; 4934:1-12.

Ray MC, Pradhan AK. The performance of vertically reinforced 1–3 piezoelectric composites in active damping of smart structures. Smart materials and structures 2006; 15(2):631.

Ray MC, Pradhan AK. On the use of vertically reinforced 1-3 piezoelectric composites for hybrid damping of laminated composite plates. Mechanics of Advanced Materials and Structures 2007; 14(4):245-261.

Ray MC, Reddy JN. Optimal control of thin circular cylindrical laminated composite shells using active constrained layer damping treatment. Smart Materials and Structures 2004; 13(1):64.

Ray MC, Reddy JN. Performance of piezoelectric fiber-reinforced composites for active structural-acoustic control of laminated composite plates. IEEE transactions on ultrasonics, ferroelectrics, and frequency control 2004a; 51(11):1477-1490.

Ray MC, Reddy JN. Active control of laminated cylindrical shells using

piezoelectric fiber reinforced composites. Composites Science and Technology 2005; 65(7):1226-1236.

Reader W, Sauter D. Piezoelectric composites for use in adaptive damping concepts. In DAMPING'93 Conference 1993; GBB-1.

Reddy CV. Some studies on the effect of damping treatment on the vibration and noise attenuation in structures. Ph. D. Thesis, IIT Madras; 1979.

Reddy JN. Mechanics of laminated composite plates and shells: theory and analysis. CRC press; 2004.

Rogers L, Parin M. 'Experimental Results for Stand-off Passive Vibration Damping Treatment. Passive Damping and Isolation, Proceedings SPIE Smart Structures and Materials 1995; 2445:374-383.

Kerwin Jr EM. Damping of flexural waves by a constrained viscoelastic layer. The Journal of the Acoustical society of America 1959; 31(7):952-962.

Roy PK, Ganesan N. Dynamic studies on plates with unconstrained layer treatment. Computers & structures 1993; 49(3):473-480.

Roy PK, Ganesan N. Dynamic studies on beams with unconstrained layer damping treatment. Journal of Sound and Vibratio. 1996; 195(3):417-427.

Sakthivel M, Arockiarajan A. Thermo-electro-mechanical response of 1-3-2 piezoelectric composites: effect of fiber orientations. Acta Mechanica 2012; 223(7):1353.

Saravanan C, Ganesan N, Ramamurti V. Study on energy dissipation pattern in vibrating fluid filled cylindrical shells with a constrained viscoelastic layer. Computers & Structures 2000; 75(6):575-591.

Saravanan C, Ganesan N, Ramamurti V. Semianalytical finite element analysis of active constrained layer damping in cylindrical shells of revolution. Computers & Structures 2001; 79(11):1131-1145.

Scanlan RH. Linear damping models and causality in vibrations. Journal of Sound and Vibration 1970; 13(4):499-503.

Seubert SL, Anderson TJ, Smelser RE. Passive damping of spinning disks. Journal of Vibration and Control 2000; 6(5):715-725.

Shen IY. Intelligent constrained layer- An innovative approach(active and passive vibration damping). Intelligent structures, materials, and vibrations. 1993:75-82.

Shen IY. Hybrid damping through intelligent constrained layer treatments. Journal of Vibration and Acoustics, Transactions of the ASME 1994; 116(3):341-349.

Shen HS. Thermal postbuckling behavior of functionally graded cylindrical shells with temperature-dependent properties. International Journal of Solids and Structures 2004; 41(7):1961-1974.

Shi Y, Hua H, Sol H. The finite element analysis and experimental study of beams with active constrained layer damping treatments. Journal of sound and vibration 2004; 278(1): 343-363.

Shi J, Song Q, Liu Z, Wan Y. Formulating a numerically low-cost method of a constrained layer damper for vibration suppression in thin-walled component milling and experimental validation. International Journal of Mechanical Sciences 2017.

Shin YS, Maurer GJ. Vibration response of constrained viscoelastically damped plates: Analysis and experiments. Finite elements in analysis and design 1991; 7(4):291-297.

Shin WH, Lee SJ, Oh IK, Lee I. Thermal post-buckled behaviors of cylindrical composite shells with viscoelastic damping treatments. Journal of Sound and Vibration 2009; 323(1):93-111.

Sisemore CL, Darvennes CM. Transverse vibration of elastic-viscoelastic-elastic sandwich beams: compression-experimental and analytical study. Journal of Sound and Vibration 2002; 252(1):155-167.

Smith WA, Auld BA. Modeling 1-3 composite piezoelectrics: thickness-mode oscillations. IEEE transactions on ultrasonics, ferroelectrics, and frequency control 1991; 38(1):40-47.

Stanway R, Rongong JA, Sims ND. Active constrained-layer damping: a state-of-the-art review. Proceedings of the Institution of Mechanical Engineers, Part I: Journal of Systems and Control Engineering 2003; 217(6):437-456.

Sun J, Kari L. Coating Methods to Increase Material Damping of Compressor Blades—Measurements and Modeling. ASME Paper No. GT2010-44014. 2010.

Sun CT, Sankar BV, Rao VS. Damping and vibration control of unidirectional composite laminates using add-on viscoelastic materials. Journal of Sound and Vibration 1990; 139(2):277-287.

Sun D, Tong L. A compressional-shear model for vibration control of beams with active constrained layer damping. International journal of mechanical sciences 2004; 46(9):1307-1325.

Swallow W. An improved method of damping panel vibrations. British Patent Specification. 1939; 513:171.

Sylwan O. Shear and compressional damping effects of constrained layered beams. Journal of sound and vibration 1987; 118(1):35-45.

Teng TL, Hu NK. Analysis of damping characteristics for viscoelastic laminated beams. Computer methods in applied mechanics and engineering 2001; 190(29):3881-3892.

Tian S, Xu Z, Wu Q, Qin C. Dimensionless Analysis of Segmented Constrained Layer Damping Treatments with Modal Strain Energy Method. Shock and Vibration 2016.

Tiersten HF. Linear Piezoelectric Plate Vibrations. New York: Plenum Press; 1969.

Thomson W. Theory of vibration with applications, CRC Press; 1996.

Tomlinson GR. The use of constrained layer damping in vibration control. International Journal of Mechanical Sciences 1990; 32(3):233-242.

Tomlinson GR. An overview of active/passive damping techniques employing viscoelastic materials. In Proceedings-Spie The International Society For Optical Engineering 1996; 656-669.

Torvik PJ, Strickland DZ. Damping additions for plates using constrained viscoelastic layers. The Journal of the Acoustical Society of America 1972; 51(3B):985-991.

Trindade MA, Benjeddou A, Ohayon R. Finite element modelling of hybrid active–passive vibration damping of multilayer piezoelectric sandwich beams—part I: Formulation. International Journal for Numerical Methods in Engineering 2001 Jul; 51(7):835-854.

Trindade MA, Benjeddou A. Hybrid active-passive damping treatments using viscoelastic and piezoelectric materials: review and assessment. Modal Analysis 2002; 8(6):699-745.

Trompette P, Fatemi J. Damping of beams. Optimal distribution of cuts in the viscoelastic constrained layer. Structural and Multidisciplinary Optimization 1997; 13(2):167-171.

Tsai MH, Chang KC. A study of the modal strain energy method for viscoelastically damped structures. Journal of the Chinese Institute of Engineers 2001; 24(3):311-320.

Tzou HS, Gadre M. Theoretical analysis of a multi-layered thin shell coupled with piezoelectric shell actuators for distributed vibration controls. Journal of Sound and Vibration 1989; 132(3):433-450.

Ungar EE. Loss factors of viscoelastically damped beam structures. The Journal of the Acoustical Society of America 1962; 34(8):1082-1089.

Ungar EE, Kerwin Jr EM. Loss factors of viscoelastic systems in terms of energy concepts. The Journal of the acoustical Society of America 1962; 34(7):954-957.

Ungar EE, Kerwin Jr EM. Plate damping due to thickness deformations in attached viscoelastic layers. The Journal of the Acoustical Society of America 1964; 36(2):386-392.

Van Nostrand WC, Knowles GJ, Inman DJ. Finite element model for active constrained-layer damping. In 1994 North American Conference on Smart Structures and Materials 1994; 126-137.

Vasques CM, Mace BR, Gardonio P, Rodrigues JD. Arbitrary active constrained layer damping treatments on beams: Finite element modelling and experimental validation. Computers & structures 2006; 84(22):1384-1401.

Veley DE, Rao SS. A comparison of active, passive and hybrid damping in structural design. Smart Materials and Structures 1996; 5(5):660.

Wagner P. Damped Response of Shells by a Constrained Visooelastio Layer. Journal of Applied Mechanics 1986; 53:903.

Wan H, Li Y, Zheng L. Vibration and damping analysis of a multilayered composite plate with a viscoelastic midlayer. Shock and Vibration 2016.

Wang Q, Wang CM. Optimal placement and size of piezoelectric patches on beams from the controllability perspective. Smart Materials and Structures 2000; 9(4):558.

Wang HJ, Chen LW. Finite element dynamic analysis of orthotropic cylindrical shells with a constrained damping layer. Finite Elements in Analysis and Design 2004; 40(7):737-755.

Wang M, Fang Z. Spectral strip-element method for beams treated with active constrained layer damping. Mechanics Research Communications 2005; 32(6):704-716.

Whittier JS. The effect of configurational additions using Viscoelastic interfaces on the damping of a cantilever beam. Wright Air Development Command, US Air Force; 1959.

Wilson CJ, Carnevali P, Morris RB, Tsuji Y. Viscoelastic damping calculations using a p-type finite element code. Trans. ASME, J. Appl. Mechanics 1992; 59:696-699.

Woo J, Meguid SA. Nonlinear analysis of functionally graded plates and shallow shells. International Journal of Solids and structures 2001; 38(42):7409-7421.

Xu C, Lin S, Yang Y. Optimal design of viscoelastic damping structures using layerwise finite element analysis and multi-objective genetic algorithm. Computers & Structures 2015; 157:1-8.

Xiang Y, Huang YY, Lu J, Yuan LY, Zou SZ. New matrix method for analyzing vibration and damping effect of sandwich circular cylindrical shell with viscoelastic core. Applied mathematics and mechanics 2008; 29(12):1587-1600.

Xie Z, Shepard WS. An enhanced beam model for constrained layer damping and a parameter study of damping contribution. Journal of Sound and Vibration 2009; 319(3):1271-1284.

Yang C, Jin G, Liu Z, Wang X, Miao X. Vibration and damping analysis of thick sandwich cylindrical shells with a viscoelastic core under arbitrary boundary conditions. International Journal of Mechanical Sciences 2015; 92:162-177.

Yellin JM, Shen IY. A self-sensing active constrained layer damping treatment for a Euler-Bernoulli beam. Smart materials and structures 1996; 5(5):628.

Yi S, Hilton HH. Dynamic finite element analysis of viscoelastic composite plates

in the time domain. International Journal for Numerical Methods in Engineering 1994; 37(23):4081-4096.

Yildiz A, Stevens K. Optimum thickness distribution of unconstrained viscoelastic damping layer treatments for plates. Journal of Sound and Vibration 1985; 103(2):183-199.

Yin TP, Kelly TJ, Barry JE. A quantitative evaluation of constrained-layer damping. Journal of Engineering for Industry 1967; 89(4):773-782.

Yu YY. Viscoelastic damping of vibrations of sandwich plates and shells. Polytechnic Institute of Brooklyn NY; 1963.

Yuan L, Xiang Y, Huang Y, Lu J. A semi-analytical method and the circumferential dominant modal control of circular cylindrical shells with active constrained layer damping treatment. Smart Materials and Structures 2010; 19(2):025010.

Zang X, Yu D, Yao L, Yan R. Optimization of thickness distribution of unconstrained damping layer based on mode shapes. Zhongguo Jixie Gongcheng (China Mechanical Engineering) 2010; 21:515-518.

Zhang SH, Chen HL. A study on the damping characteristics of laminated composites with integral viscoelastic layers. Composite Structures 2006; 74(1):63-69.

Zheng H, Cai C, Pau GS, Liu GR. Minimizing vibration response of cylindrical shells through layout optimization of passive constrained layer damping treatments. Journal of Sound and Vibration 2005; 279(3):739-756.

Zheng L, Zhang D, Wang Y. Vibration and damping characteristics of cylindrical shells with active constrained layer damping treatments. Smart Materials and Structures 2011; 20(2):025008.

Zheng L, Qiu Q, Wan H, Zhang D. Damping analysis of multilayer passive constrained layer damping on cylindrical shell using transfer function method. Journal of Vibration and Acoustics 2014; 136(3):031001.

Zheng H, Tan XM, Cai C. Damping analysis of beams covered with multiple PCLD patches. International journal of mechanical sciences 2006; 48(12):1371-1383.

Zheng H, Pau GS, Wang YY. A comparative study on optimization of constrained layer damping treatment for structural vibration control. Thin-walled structures 2006; 44(8):886-896.

List of Publications

The work presented in this thesis has led to the following publications:

1. Kumar A, Panda S. Design of a 1-3 viscoelastic composite layer for improved free/constrained layer passive damping treatment of structural vibration. Composites Part B: Engineering 2016; 96:204-214.
2. Panda S, Kumar A. A design of active constrained layer damping treatment for vibration control of circular cylindrical shell structure. Journal of Vibration and Control 2016; 1077546316670071.
3. Kumar A, Panda S. Optimal Damping in Circular Cylindrical Sandwich Shells With a Three-Layered Viscoelastic Composite Core. Journal of Vibration and Acoustics 2017; 139(6):061003.
4. Kumar A, Panda S, Narsaria V, Kumar As. Augmented constrained layer damping in plates through the optimal design of a 0-3 viscoelastic composite layer. Journal of Vibration and Control 2018; 1077546318756502.
5. Kumar A, Panda S, Kumar As, Narsaria V. Performance of a graphite wafer-reinforced viscoelastic composite layer for active-passive damping of plate vibration. Composite Structures 2018; 186:303-314.